Dissertation zur Erlangung des Doktorgrades

der Fakultät für Chemie und Pharmazie

der Ludwig-Maximilians-Universität München

Mechanistic insights into the DNA repair factors MRN and ATM

von

Erik van de Logt

aus

Köln, Deutschland

2023

Erklärung

Diese Dissertation wurde im Sinne von §7 der Promotionsordnung vom 28. November 2011 von Herrn Prof. Dr. Karl-Peter Hopfner betreut.

Versicherung an Eides statt

Diese Dissertation wurde eigenständig und ohne unerlaubte Hilfe erarbeitet.

_____

Erik van de Logt München, den 22. Mai 2023

Dissertation eingereicht am:	22.05.2023
1. Gutachter:	Prof. Dr. Karl-Peter Hopfner
2. Gutachter:	Prof. Dr. Roland Beckmann
Mündliche Prüfung am:	10.08.2023

This thesis has been prepared from November 2019 to April 2023 in the laboratory of Prof. Dr. Karl-Peter Hopfner at the Gene Center of the Ludwig-Maximilians-University in München, Germany.

This is a cumulative thesis based on the following publications:

Kristina Stakyte*, Matthias Rotheneder*, Katja Lammens*, Joseph D. Bartho*, Ulrich Grädler, Thomas Fuchß, Ulrich Pehl, Aaron Alt, Erik van de Logt, Karl-Peter Hopfner, **Molecular basis of human ATM kinase inhibition**, *Nature Structural and Molecular Biology*, Volume 28, October 2021, Pages 789-798

Fabian Gut*, Lisa Käshammer*, Katja Lammens, Joseph D. Bartho, Anna-Maria Boggusch, Erik van de Logt, Brigitte Kessler, Karl-Peter Hopfner, **Structural mechanism of endonucleolytic processing of blocked DNA ends and hairpins by Mre11-Rad50**, *Molecular Cell*, Volume 18, September 2022, Pages 3513-3522

Matthias Rotheneder*, Kristina Stakyte*, Erik van de Logt*, Joseph D. Bartho*, Katja Lammens, Yilan Fan, Aaron Alt, Brigitte Kessler, Christophe Jung, Wynand P. Roos, Barbara Steigenberger, Karl-Peter Hopfner, **Cryo-EM structure of the Mre11-Rad50-Nbs1 complex reveals the molecular mechanism of scaffolding functions**, *Molecular Cell*, Volume 83, January 2023, Pages 167-185

* These authors contributed equally

Table of contents

Summary

The genetic material in every living organism, DNA, faces various endogenous and exogenous threats which damage its structure or sequence. The most deleterious lesions are double strand breaks (DSBs), potentially resulting in large chromosome aberrations, cell death or tumorigenesis. To repair this type of DNA damage, two main pathways emerged: Non-homologous end joining (NHEJ) and homologous recombination (HR). In the course of NHEJ, both broken DNA strands together are directly re-ligated in an error-prone manner. HR requires extensive resection of the broken DNA strands, leaving a single stranded DNA (ssDNA) overhang used for homology search in the sister chromatid followed by template dependent repair. This pathway is considered error-free whilst being restricted to the S/G2-phase of the cell cycle. The protein complex Mre11-Rad50-Nbs1 (MRN) acts in the very first steps of HR by recognizing and tethering DNA ends as well as initiating the resection. It consists of the manganese dependent nuclease Mre11, the ATPase Rad50 and the eukaryote specific, regulatory subunit Nbs1. To initiate the DNA damage response (DDR), MRN recruits and activates the signalling kinase Ataxia-Telangiectasia Mutated (ATM).

ATM belongs to the evolutionary well-conserved phosphoinositide 3-kinase related kinases (PIKK) family, with most of the members being involved in different stress responses. Targeting one of these stress responses, the DDR, represents a promising way to develop novel cancer therapies with ATM as a central element. In the first part of this thesis, two potential therapeutic human ATM inhibitors were biochemically characterized and their inhibitory mechanism solved with structural analysis. Both inhibitors, the first-generation inhibitor KU-55933 and the more recently developed, pharmacokinetically improved inhibitor M4076, compete with the substrate ATP. They show high specificity towards ATM while displaying reduced inhibition to other PIKK family members such as mTOR, DNA-PK or ATR. High resolution cryo-electron microscopy (EM) structures of ATM with either KU-55933, M4076 or ATPγS bound explain these high specificities in a comparison of the catalytic centres to other PIKKs and checkpoint kinase (CHK)2 structures. Binding of these inhibitors reduced the total flexibility and therefor a higher overall resolution was obtained. This allowed for resolving the near-complete ATM protein, revealing two novel zinc-binding sites, mapping cancer mutation sites, and paving the path for future structure-based drug design.

In contrast to the highly regulated eukaryotic HR process with all its additional regulatory factors and posttranslational modifications, the bacterial system displays a simplified yet in the core steps conserved system. In prokaryotes, the MR complex consists of only the catalytically active components, Mre11 and Rad50, lacking the regulatory subunit Nbs1. The second part of this thesis answers the question how a single complex, MR, can enzymatically process a variety of DNA substrates occurring after DSBs: free DNA ends, blocked DNA strands or hairpin structures. For all substrates, a unified mechanism underlies, solved by cryo-EM analysis and supported by biochemical data. Hereby, DNA is bound in the cleft between two Rad50 proteins, the Mre11 dimer translocates from the top of the head complex towards the designated cutting site, i.e. a free DNA end, the hairpin or an internal site for blocked ends.

While the work on bacterial MR is able to explain large parts of the nuclease reaction mechanism, the other main MRN function, tethering and scaffolding of DNA, remained elusive. Integrating these two different aspects into a combined model is discussed in the third part of this thesis. Using cryo-EM analysis, MRN's catalytic head domain in its ATPγS bound state was resolved for the *Chaetomium thermophilum* complex. The complex resides in an autoinhibited conformation: Mre11's nuclease is blocked by Rad50's ATPase domains and the DNA binding site in between two Rad50 proteins is occluded by a closed conformation of the coiled-coils, forming a linear, rod-like structure protruding

from the head. A newly characterized, eukaryote specific additional DNA binding site at the Mre11 C-terminus allows binding to internal DNA sites, whereas the canonical Rad50 DNA binding site strongly prefers DNA ends in an ATP-dependent manner. A single Nbs1 wraps asymmetrically around the Mre11 dimer, potentially further locking the complex in a rigid conformation. This rigidity allowed to resolve large parts of the coiled-coil domains, which are interrupted by several interaction points. Combining cryo-EM data with a crystal structure visualized a zinc hook dimerization motif between the apices of two distinct Rad50 coiled-coils, thereby forming larger assemblies with the ability to tether distant DNA ends. *In vivo* DSB repair assays bolster the biological importance of this interaction.

With the first full-length MRN structure solved, a mechanistic model for MRN activation can be proposed. Combining the insights of the ATM and MRN studies, one can deduce a possible mechanism for the highly discussed question of MRN-mediated ATM activation.

1. Introduction

1.1 DNA

The molecule deoxyribonucleic acid (DNA) contains the genetic instructions essential for all known organisms[1]. Life on earth stores, maintains, reads and replicates DNA for functioning, development, and reproduction purposes. This polymer is built of repeating units of nucleotides, with each nucleotide consisting of 2-deoxyribose sugar, a phosphate at the fifth carbon, and one of the four nucleobases Adenin (A), Thymin (T), Cytosin (C) and Guanin (G) attached to the first carbon of each sugar moiety. These nucleotides are covalently joined via phosphoester bonds between the third carbon of the sugar and the adjacent phosphate group, forming the sugar-phosphate backbone. Each DNA strand therefore has a polarity, ranging from the terminal 5'-phosphate group to the terminal 3'-hydroxyl group. Two complement DNA strands pair up over specific hydrogen bonds (Watson-Crick base pairing) between the nucleobases to build a double-stranded helix in an antiparallel manner with stacked, complementary bases in the centre and the backbone wrapping around[2].

1.1.1 DNA damage

While DNA is considered as a relatively stable macromolecule, various sources lead to alterations of its structure or sequence[3]. Although being an important evolutionary driving force, DNA damage can have very detrimental effects on living organisms, ranging from tumorigenesis to genetic instability, cell death and premature aging[4-6]. Therefore, effective repair pathways to counter all types of DNA damages have emerged (summarized in **Figure 1**)[7]. DNA damage originates from exogenous sources, present in the environment, and endogenous sources that arise from cellular processes[8].

Exogenous sources itself can be divided into high-energetic radiation or diverse chemicals. Ionizing radiation (IR), such as γ- or X-rays, leads to direct strand breakages and the generation of reactive oxygen species (ROS), subsequently damaging nearby molecules. For DNA, this damage comprises single strand breaks (SSB), double strand breaks (DSB) and base oxidations, such as 8-oxo guanine or 8-oxo adenine[9]. The less energetic ultraviolet (UV) radiation excites molecular bonds, including carbon-carbon π-bonds occurring in pyrimidines, resulting in covalent linkages of adjacent bases[10]. Extensive exposure to UV light represents the major cause for skin cancer[11].

Alkylating agents are a large class of DNA damaging chemicals, arising from e.g. tobacco smoke but also used in chemotherapy[12,13]. One typical alkylating agent, acetaldehyde, found in smoke or food, reacts with the nucleobases to induce DNA interstrand crosslinks and base alterations[14,15]. Diverse chemotherapeutics utilize the ability of intra- or interstrand crosslinking to evoke enough DNA damage to repair-deficient cancer cells, leading to their death. Examples are cisplatin, cyclophosphamide or busulfan[16-18]. Some crosslinking agents like nitrogen mustard additionally introduce DNA-protein crosslinks (DPCs), these large adducts interfere with numerous chromatin processes[19]. The class of intercalating chemicals, mostly polycyclic planar molecules, with members like ethidium, aflatoxins or the chemotherapeutic daunorubicin insert non-covalently between the planar bases inside the double helix[20-22]. This distorts the helix structure, hindering the transcription and replication processes with the latter being the source for their mutagenic effect[23].

Endogenous agents are no less detrimental to cells as their exogenous counterparts. While one can to some extend avoid environmental sources, DNA damage arising from cellular process cannot be circumvented, be it due to basic underlying statistical problems such as the error rate of replication polymerases, spontaneous hydrolysis or various essential metabolic processes producing reactive

compounds[24-26]. As DNA is built up by a row of condensation reactions, this process can be reverted in spontaneous hydrolysis reactions. Purine bases as a well-suited leaving group are lost this way, leading to the formation of apurinic sites. This occurs roughly 2,000-10,000 times per day in a human cell[27]. Pyrimidines are also lost in a similar way, but at a much lower rate. The nucleobases itself are as well damaged by hydrolysis reactions. In the process of deamination, for example cytosine is converted to uracil. Single-stranded DNA, occurring during transcription or replication, is especially susceptible to deamination[27].

Different cellular processes, such as oxidative phosphorylation in the mitochondria, peroxisomal lipid metabolism or certain stress responses can as well generate ROS[28,29]. To protect itself and maintain a certain redox-homoeostasis, cells employ a variety of protective mechanisms and contain antioxidants such as glutathione or vitamin C[30]. These protective mechanisms also include compartmentalisation, spatially separating the ROS generating processes from DNA in the nucleus[31]. Although most reactive oxygen species are very short-lived and react in their direct vicinity, they are a major endogenous cause for SSBs[31].

Next to metabolic by-products such as ROS, different compounds utilized in regular cellular processes also have DNA-damaging properties. S-adenosylmethionine (SAM) is an endogenous methyl donor, which unspecifically alkylates DNA bases and therefore influences base pairing[31]. Other metabolites such as choline or betaine act in the same way, leading to point mutations after replication.

However, metabolites or spontaneous reactions are not the only endogenous source for DNA damage. The DNA structure faces topological stress after unwinding in transcription or replication[32]. In order to relax the tensed strands, topoisomerases introduce SSBs (type I) or DSBs (type II), the free strand ends rotate to relieve the torsional stress after which the strands are resealed again. During the relaxation step, topoisomerases stay covalently bound to the 3' DNA termini. If the catalytic cycle of these enzymes fails to complete, due to DNA distortions (damaged bases or abasic sites) or topoisomerase poisons (e.g. camptothecin), SSBs or DSBs in combination with DPCs occur[33].

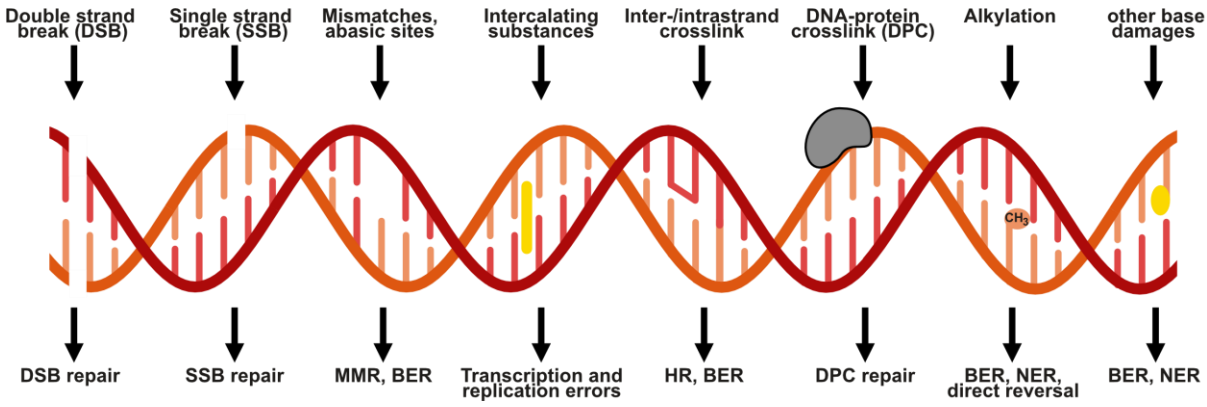

Figure 1: Types of DNA damage and their repair pathways. MMR: Mismatch repair, BER: Base excision repair, HR: Homologous recombination, NER: Nucleotide excision repair.

1.1.2 DNA double strand breaks

Compared to other DNA lesions, DSBs are quite rare with around 10 lesions during one human cell division[34]. Nevertheless, they represent the most genotoxic damage as DSBs lead to chromosome

breakage and rearrangements, thereby possibly disrupting or mutating genes. Unrepaired DSBs might result in cell death or tumorigenesis[35].

The sources for DSBs are as well diverse. Next to ionizing radiation and abortive type II topoisomerases, a major source for DSBs arises during replication. When the common lesion of a SSB is left unrepaired, the replication fork stalls and collapses at this alteration, eventuating in a DSB[36].

Apart from accidentally induced DSBs, organisms developed ways to increase their genetic variability over programmed DSB intermediates. During meiotic recombination, a dimer of Spo11 proteins introduces a DNA DSB in one chromatid, the homologous chromatid is then used for repair which will eventually result in exchange of genetic material[37]. Lymphocytes employ a specialized type of recombination, denoted V(D)J recombination, to generate a highly diverse amount of different immunoreceptors and antibodies for the adaptive immune system. In this case, recombination-activating genes (RAG) protein complexes create the breaks and the repair is facilitated homolog independent to additionally introduce a higher variability[38].

1.2 DNA repair

With the pleiotropy of different DNA lesions, it is no surprise that a variety of repair mechanisms have evolved. They range from very simple pathways involving just a few proteins to highly complex networks with dozens of tightly regulated proteinaceous factors and the integration of other genome parts as repair templates.

1.2.1 Direct reversal

Direct reversal is a group of simple repair mechanism which revert a chemical base modification without the need of a template and are specific for only one type of damage. Thus, O^6-methylguanine is reverted to normal guanine by the protein O^6-methylguanine-DNA methyltransferase. Interestingly, the methyltransferase reacts stoichiometrically and not catalytically, therefor the protein is used up after a single reaction[39]. Pyrimidine dimers can as well be repaired to single pyrimidines by direct reversal through an enzyme called photolyase. The light-activated photolyase further utilizes visible light for its catalytic mechanism called photoreactivation. However, placental mammals evolutionary lost functional photolyases and rely on excision pathways to resolve pyrimidine dimers[40].

1.2.2 Excision pathways

For chemically more complex lesions, direct reversal reactions do not suffice. To overcome the issue of directly reverting a variety of damages by an equal number of specifically reverting enzymes, cells have evolved three different so-called excision pathways. Commonly in these cases, base alterations are recognized and excised due to their induced distortion of the helical structure instead of a mere chemical change. For a single stranded damage, the undamaged strand can then act as a repair template to replace the excised parts.

Damaged bases are mostly repaired by base-excision repair (BER). Hereby, a glycosylase removes the damaged base, leaving an abasic site. Apurinic/apyrimidinic (AP) endonuclease then introduces a SSB at this site, recognized by DNA polymerase (Pol) β or λ[41]. With their intrinsic exonuclease activity, the

polymerases first resect the abasic nucleotide and secondly resynthesize the strand with the complementary strand as template. A ligase seals the gap[42].

Nucleotide excision repair (NER) is used to repair bulky lesions or intrastrand crosslinks. The major difference to BER lies in the recognition of the damaged strand by additional, non-enzymatic factors (XPC-RAD23B) and the endonucleolytical processing by XPF/ERCC1 and XPG a few bases up- and downstream of the actual damage, resulting in a small stretch of ssDNA[43].

A similar mechanism is employed by the third excision pathway, the mismatch repair (MMR). This pathway recognizes and repairs base mismatches, as well as small insertions and deletions, which occur during replication, recombination or repair[44]. As these lesions are per se no damage to bases nor the backbone of DNA, cells need to discriminate the strand to be corrected and the template strand for repair. In gram-negative bacteria, newly synthesized DNA transiently exists unmethylated, thereby determining the strand specificity of MMR[45]. For other prokaryotes and eukaryotic cells with no such system, the daughter strands are identified due to internal nicks. These nicks originate in replication with the use of RNA primers which are excised and leave two disconnected strands. Over a yet unclear mechanism, the mismatch recognizing factor MSH detects these nicks and together with MLH introduces an SSB close to the mismatch on the faulty strand[45]. An exonuclease resects a short DNA stretch, leaving a single stranded template strand. This gap is filled by a polymerase and sealed with a ligase[46].

1.2.3 DNA-protein crosslink repair

DNA-protein crosslinks are repaired by interplaying repair mechanisms tackling its 3 components: The DNA, the protein and the crosslink[33]. Whereas small protein adducts might still be directly repaired by NER, this excision pathway fails for proteins larger than 15 kDa[33]. To overcome this issue, different DNA-dependent proteases have evolved, with Wss1/SPRTN being the best characterized. These highly regulated proteases are activated upon recognition of DNA structures with ssDNA and dsDNA features in combination with a ubiquitin switch: The inactive form resides monoubiquitylated, upon DPC induction the inhibitory ubiquitin is removed[47]. An additional autocatalytic cleavage activity exerts the off-switch[47]. Proteasomal cleavage of DPCs occurs DNA independent, but requires prior substrate ubiquitylation[48]. Next to proteolysis, certain DPCs can be resolved by directly reverting the crosslink. Tyrosyl-DNA phosphodiesterases (TDP) 1 and 2 hydrolyse the chemically defined DPC between the active site tyrosine of covalently trapped topoisomerase (TOP) 1 and 2 with DNA respectively[49]. To gain access to the crosslink, proteolysis or remodelling of the bound topoisomerase is required[50]. When DPCs occur at DSBs, for example due to trapped TOP2 or Spo11, nucleases involved in DSB repair pathways (covered in 1.2.5 in detail) will clip off the crosslinked DNA strand, thereby removing the DPC[51].

1.2.4 Single strand break repair

Being one of the most common DNA lesions, single strand breaks require a rapid and accurate repair to enable transcription and prevent double strand break formation during replication. Mainly the poly (ADP-ribose) polymerase 1 (PARP1) detects and signals direct breaks by generating chains of poly (ADP-ribose) (PAR) onto itself and other chromatin factors[52]. This strong signal is recognized by the scaffolding protein XRCC1, which recruits and stimulates downstream factors. Poly (ADP-ribose) glycohydrolase (PARG) quickly degrades the PAR chains to restore PARP1 and limit the signalling

cascade[53]. With the broad source of SSBs, the chemically diverse, abnormal DNA termini require different enzymes to clean the breaks and pave the way for the following gap filling and ligation steps. 5'-deoxyribose phosphate (dRP) residues are processed by Pol β, polynucleotide kinase 3'-phosphatase (PNKP) removes 3' phosphates and adds 5' phosphates, apurinic–apyrimidinic endonuclease I (APE1) resects nucleotide residues containing modified phosphates[53]. Aprataxin processes abortive ligation products, 5'-AMP–SSBs[53]. The gaps are closed by Pol β, either by insertion of the single nucleotide which was resected before (short-patch repair), or by synthesizing and displacing two or more nucleotides (long-patch repair)[31]. The displaced strand is nucleolytically cleaved by FEN1 and the nicks sealed by ligase I or IIIα[54].

1.2.5 Double strand break repair

The particularly hazardous DNA double strand breaks rely on three different pathways for repair: classical non-homologous end-joining (C-NHEJ), alternative end-joining (A-EJ) and homologous recombination (HR)[36]. As the nature of a DSB disallows to directly use the existing complementary strand as a repair template, the choice of repair pathways is cell cycle dependent. During S/G2-phase, a sister chromatid is present and used as a template in HR, resulting in an error-free repair. In other cell cycle phases, the chromatids reside as single copies and end-joining pathways repair DSBs[55].

1.2.5.1 End-joining pathways

C-NHEJ is the main end-joining pathway and functions throughout the whole cell cycle (**Figure 2**, left side). In the first step, a Ku70/80 dimer binds to DSBs and determines the pathway choice towards C-NHEJ[56]. The DNA-dependent protein kinase catalytic subunit (DNA-PKcs), a phosphatidylinositol 3-kinase-related kinase (PIKK) family member, joins the Ku-bound ends, thereby forming the DNA-PK complex[57]. This complex holds both DNA ends in close proximity, activates the processing nuclease Artemis by phosphorylation and recruits polymerases μ/λ[56]. Analogous to SSBs, most DSBs have incompatible ends for a direct ligation, either due to chemical abnormal termini or mismatching ssDNA overhangs. Artemis cleaves overhangs exo- and endonucleolytically, whereas Pol μ/λ fill up ssDNA patches and can also extend the ends template-independently[58]. These two potential mutagenic processes, Artemis-mediated short resection and synthesis often produce short microhomologies (≤4 nucleotides), which are used to guide end-joining. Deletions and random insertions originate in this step. After processing, the ends are positioned by binding of XRCC4 and XLF to DNA-PK and ligated by ligase IV[56].

If C-NHEJ fails to repair DSBs in the G1-phase due to missing or mutated components, the alternative end-joining pathway complements DSB repair (**Figure 2**, right side)[59]. This backup pathway, also referred as microhomology mediated end-joining (MMEJ), is normally suppressed by a high abundance and very strong affinity of the C-NHEJ determining factor Ku70/80 towards DSBs[60]. A-EJ starts with the recognition of the DNA ends by PARP1 and their resection by the MRN/CtIP complex, creating 3' overhangs between 15-100 nucleotides long[60]. Microhomologies in these overhangs, ranging from 2 to 20 nucleotides, pair to re-join both DNA ends. This typically leaves ssDNA flaps which are consecutively cleaved by XPF/ERCC1[59]. Pol θ fills the gaps and ligase III in complex with XRCC1 closes the SSBs[59]. Due to the pronounced resection step, A-EJ is highly mutagenic and leads to genomic instability.

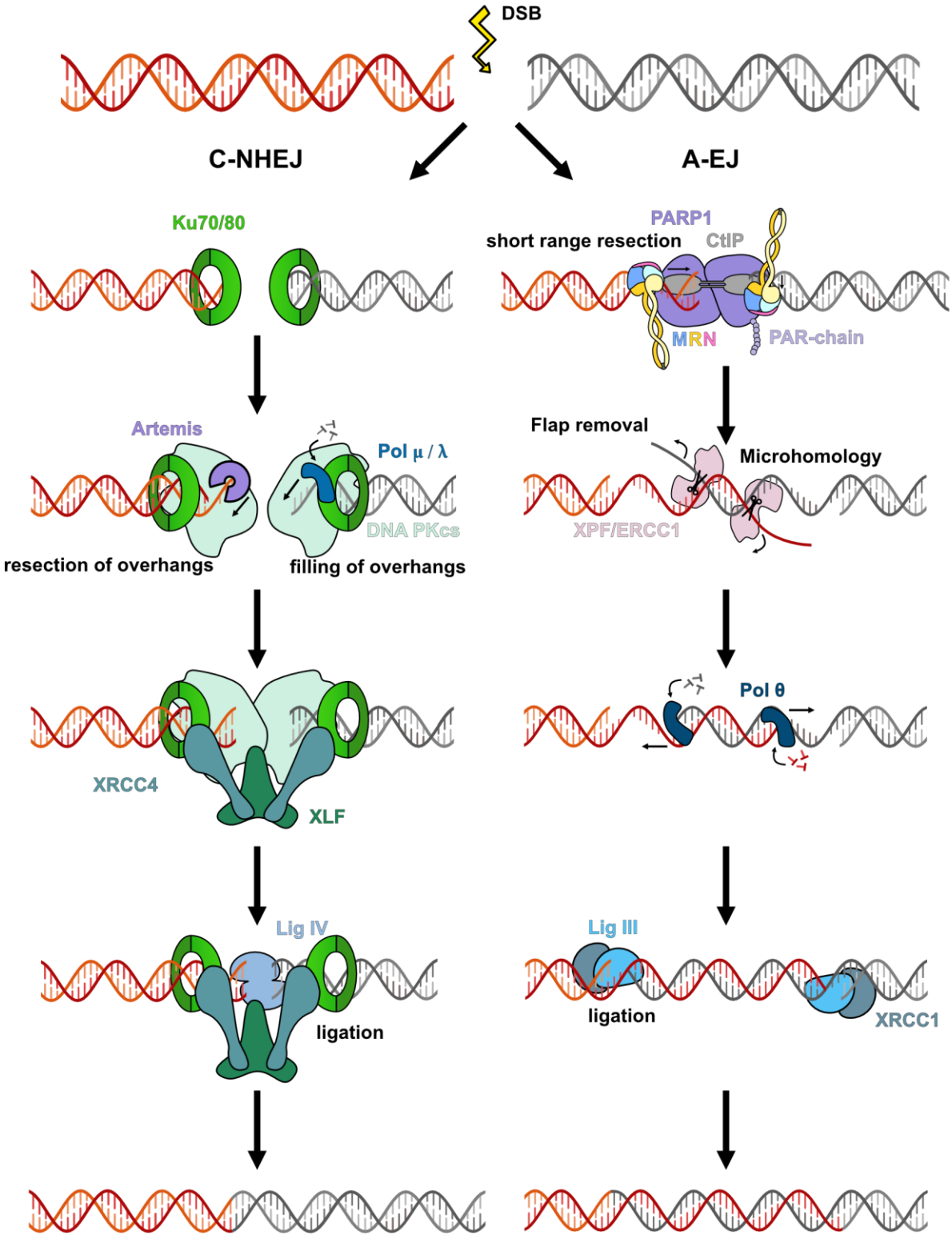

Figure 2: Overview of end-joining pathways. Ionizing radiation or other factors (yellow arrow) can lead to DSBs (orange and grey strands). In C-NHEJ, the DNA ends are recognized and protected by a Ku70/80 dimer. DNA-PKcs bind to DNA with Ku70/80 attached, recruit the nuclease Artemis or polymerases μ/λ to resect or fill incompatible overhangs. The ends are bridged additionally by XRCC4/XLF. After DNA-PKcs leave the DSB, a ligase IV dimer reseals both strands together. A-EJ starts with the recognition of the DSB by PARP1, which recruits the MRN complex. Together with the bridging factor CtIP, MRN resects the DNA ends towards the break, leaving short single stranded DNA stretches. Microhomologies in the overhangs can then pair, potential flaps of protruding unpaired stretches are removed by XPF/ERCC1. Pol θ fills the gaps between the microhomologous

site and the remaining, unresected double strand. Ligase III in complex with the scaffolding protein XRCC1 closes the nicks.

1.2.5.2 Homologous recombination

In contrast to the error-prone end-joining pathways, HR uses the already replicated homologous sister chromatid as a template for error-free DSB repair. Therefore, HR is a tightly regulated process, restricted to the S/G2-phase[55]. Besides providing an accurate repair mechanism for all sorts of DSBs, HR is also utilized by germ cells to increase the genetic variability in the process of crossover of chromosome parts[61].

HR follows similar principles and steps of most DNA repair pathways discussed so far: DNA damage recognition, lesion processing, re-synthesis of processed nucleotides and eventual ligation of the sugar-phosphate backbone. In addition to excision pathways, which directly use the complementary strand as the repair template or end-joining pathways which skip the need of a template, HR relies at the core on a fifth, crucial step: the search for a homologous template.

To reach this step, DNA ends are initially recognized by the multifunctional MRN complex (**Figure 3**)[62]. The C-terminal binding protein interacting protein (CtIP) then binds and activates MRN's nuclease Mre11[63]. This very first step is highly regulated to prevent unwanted resection. CtIP requires different cell-cycle dependent phosphorylations by CDK, most importantly at T847, to act as a cofactor for MRN[55]. MRN introduces an endonucleolytic cut roughly 30 nucleotides upstream of the DNA ends and further resects the incised strand exonucleolytically 3' – 5' towards the break[63]. In the first steps, CtIP as well as MRN are thought to bridge the DNA ends together to limit their diffusion[64,65]. MRN recruits the DNA damage response (DDR) signalling kinase ATM, which in turn phosphorylates a pleiotropy of targets to orchestrate the course of HR and to initiate cell cycle arrest or apoptosis in case of extensive DSBs[66]. Following the initial short-range resection, the 3' ssDNA overhangs are further extended by the action of the long-resection processive nucleases DNA2 and Exo1[67]. DNA2 depends on the helicases Bloom-Syndrom (BLM) or Werner-Syndrom (WRN) to melt the dsDNA prior to nucleolytic attack[68]. The heterotrimeric single-strand binding protein Replication protein A (RPA) strongly associates with the overhangs, thereby dictating the directionality of long-range resection and protecting the ssDNA from further nucleolytic degradation[69]. Breast cancer type 2 susceptibility protein (BRCA2) recruits Rad51 monomers to ssDNA and mediates the displacement of RPA with the recombinase[70]. The ATPase Rad51 interacts with ssDNA in its ATP-bound state and forms helical nucleofilaments, promoted as well by BRCA2[71]. In the next crucial and unique step, the ssDNA-Rad51 filaments search for homology in the neighbouring sister chromatid by invading the dsDNA. The complementary strand is scanned during this process in 3-nucleotide increments in a distance of <1 kb up to >70 kb apart from the break[71]. The displaced template strand forms the so-called displacement (D-) loop. The homology search ends with a complementary base pairing of roughly 15 nucleotides and Pol η begins to accurately extend the invading strand[72]. This leads to the formation of a cross-shaped DNA structure, referred to as single Holliday-junction[73].

Depending on the cell type, the junction is resolved by two possible mechanisms. In mitotic cells, DSBs are accidental lesions and require repair without transferring genetic material between chromatids. They mostly resolve single Holliday junctions with a mechanism denoted strand-displacement annealing (SDSA). Hereby, the junction spatially translocates due to DNA extension and disengages the invading strand from the sister chromatid. The displaced strand then anneals to the second end of the resected DSB. Eventually, the gaps are filled and the single strand breaks ligated by Ligase I to produce non-crossover DNA[73]. During meiotically programmed DSBs, the purpose of increasing

genetic variability favours the other junction resolving pathway, simply referred as double strand break repair (DSBR). In this mechanism, the other resected end invades the displaced strand as well, thereby forming a double Holliday junction. Both sister chromatid strands are consecutively utilized as synthesis templates for Pol η. For somatic cells, alternative to SDSA, double Holliday junctions are dissolved by the BTR complex, consisting of the BLM helicase, Topoisomerase IIIα and RecQ-mediated genome instability (RMI) 1 and 2 through a topoisomerase cleavage and ligation step, resulting in non-crossover products[74]. To produce crossover products, the different dimeric resolvases GEN1, MUS81-EME1, SLX1-SLX4, pairwise cut cross-shaped DNA into two nicked DNA duplexes, which can be directly repaired by ligases[74].

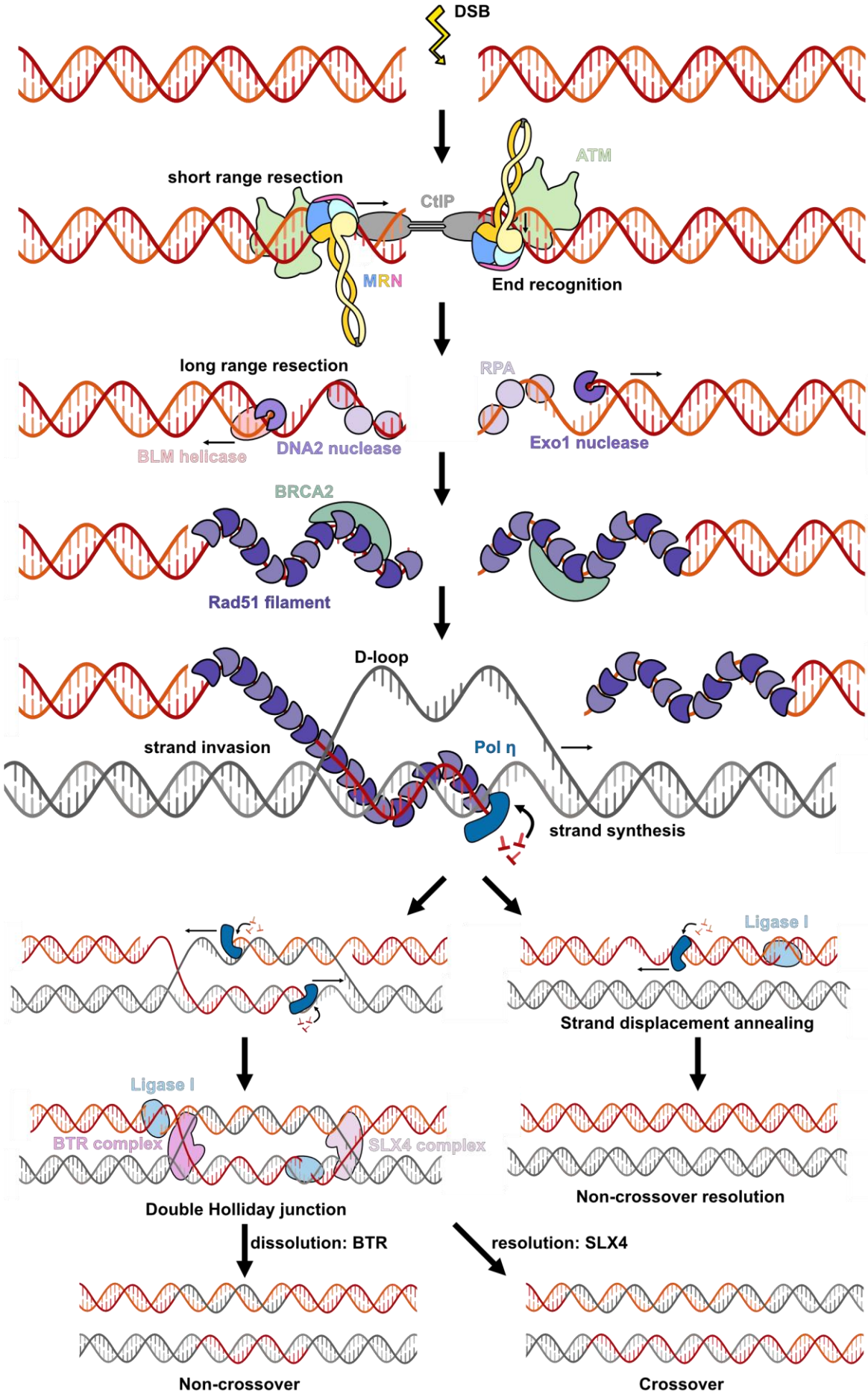
DSB
short range resection
CtIP
ATM
MRN
End recognition
long range resection
RPA
BLM helicase
DNA2 nuclease
Exo1 nuclease
BRCA2
Rad51 filament
D-loop
strand invasion
Pol η
strand synthesis
Ligase I
Strand displacement annealing
Ligase I
BTR complex
SLX4 complex
Double Holliday junction
Non-crossover resolution
dissolution: BTR
resolution: SLX4
Non-crossover
Crossover

Figure 3: Overview of HR. As a first step, MRN senses DSBs, and together with the bridging and activating factor CtIP, introduces an endonucleolytic incision upstream of the break. The following short-range resection towards the ends leaves brief 3' overhangs. To initiate the DDR and coordinate the repair sequence, the kinase ATM is recruited and activated by MRN. The short single stranded overhangs are bound by RPA and further extended by two nucleases: DNA2 (in combination with the BLM helicase) and Exo1. BRCA2 displaces RPA by Rad51, the so-formed filaments invade the sister chromatid (grey) in the search for homology and form a displacement loop (D-loop). Pol η extends the strand in 5' to 3' direction, changing the D-loop to a cross-shaped Holliday junction. At this stage, the junction can be resolved by 2 ways: In the course of strand-displacement annealing (SDSA, right side), the junction spatially translocates due to DNA synthesis and displaces the invading strand from the template. The displaced strand anneals to the other end of the resected break. Eventually, the gaps are filled and the single strand breaks ligated to produce non-crossover DNA. The other Holliday-junction resolving pathway, referred as double strand break repair (DSBR, left side), involves the other 3' overhang to anneal to the other homologous strand, thereby forming a double Holliday junction. This structure can be either resolved by the BTR complex, resulting in non-crossover products or dissolved by resolvase complexes (e.g. SLX4) to yield crossovers.

1.2.5.3 Cell cycle dependency of DSB repair

The mitotic cell cycle possesses two major phases: DNA synthesis (S-phase) and division into two separate daughter cells (mitosis, M-phase). Following the S-phase, the genome exists duplicated and the cell growths rapidly in the gap phase 2 (G2-phase)[75]. After M-phase, the two daughter cells enter the G1-phase or exit the cell cycle in a state of replicative dormancy (G0-phase)[75]. The cell cycle needs to be tightly regulated to ensure the availability of enough materials and to prevent genetically incomplete daughter cells. Progression in the cell cycle mainly depends on the interplay of non-catalytic cyclins and the kinases they bind to and activate, Cyclin-dependent kinases (CDK)[76]. CDK protein levels remain constant during the different phases, whereas cyclin levels oscillate periodically in a cell-cycle dependent manner[77]. One of the many CDK targets are proteins involved in DSB repair[55].

With two very different, main DSB repair pathways in the repertoire, cells need to decide to either use the potential erroneous NHEJ or the error-free HR. While at the first glimpse HR would be the better choice to protect genomic stability, the requirement of a sister chromatid as template restricts this pathway to late S and G2-phase. Moreover, the extensive DNA end resection could result in a variety of mutations if HR is timed wrong and no template is available as in G1-phase. Therefore, this first catalytic step in HR (and A-EJ), is the critical node for regulation of DSB repair choices[55]. While resection simultaneously inhibits NHEJ, particularly through hampering Ku70/80 binding, it promotes HR and settles the competition between the two DSB repair pathways (**Figure 4**)[55].

Shortly after a DSB occurs, MRN is one of the first factors that binds dsDNA ends and activates ATM[78]. Cell cycle independently, ATM phosphorylates the histone variant H2AX and the scaffold protein MDC1[78]. MDC1 binds to phosphorylated H2AX, denoted γH2AX, and accumulates more ATM in a positive feedback loop to amplify the signal[79]. In addition, MDC1 recruits the E3-uibiquitin ligase RNF8, which further recruits the E3-ubiquitin ligase RNF168[80]. The latter then ubiquitylates histone H2A at Lys15[81]. Tumor suppressor p53-binding protein 1 (53BP1) recognizes these ubiquitylation marks as well as pre-existing methylations on H4 Lys20 and becomes phosphorylated by ATM[55]. N-terminally phosphorylated 53BP1 interacts with the factors Rif1 and PTIP, eventually inhibiting the resection ability of MRN[55]. In post replicative chromatin, H4 Lys20 exists unmethylated, thereby hindering 53BP1 recruitment[82].

On top of different histone modifications, the action of CDKs play the other major part in regulating the choice of DSB repair pathways. In late S and G2-phase, the respective cyclin levels rise (E in S-phase entry, A in G2-phase), and activate CDK2[76]. This kinase phosphorylates one of the main regulatory

switches for end resection: CtIP. While CtIP contains multiple CDK phosphoresidues, the extensively investigated tyrosine 847 (human CtIP) is of special interest (see section 1.4.1 for more details)[83]. Several studies attend phosphorylated T847 to be essential to activate MRN nuclease, in combination with an ATM phosphorylation at T859 even a small CtIP fragment suffices to promote end resection *in vitro*[84,85]. Other CDK mediated CtIP phosphosites proved to be important for the CtIP-BRCA1 interaction, which antagonizes 53BP1 inhibitory effect on resection[55,86]. A direct CDK phosphorylation of the nucleases DNA2 and Exo1 as well as the Nbs1 part of MRN, positively regulates their activity[55]. In an indirect manner, CDK phosphorylation of the resection limiting factor HELB exports this factor from the nucleus, hence releasing its inhibitory function[55].

During G1-phase, cyclin A and E levels remain low, which renders CDK2 inactive and inhibits end resection. Additionally, H4 Lys20 residues are methylated and promote 53BP1 recruitment. Reversely, NHEJ is utilized for DSB repair.

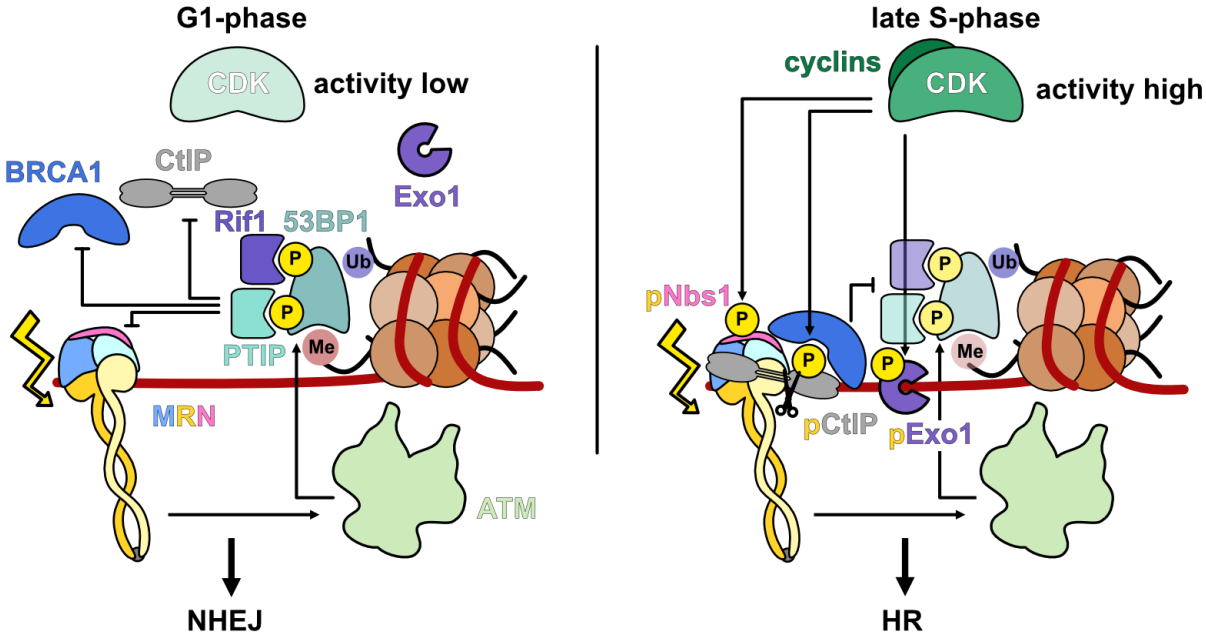

Figure 4: Cell cycle dependent choice of DSB repair pathways. In G1-phase (left), CDK activity is low, CtIP, Nbs1 and Exo1 exist unphosphorylated at certain key residues. Upon DSBs, histones in the vicinity are specifically modified (methylation at H4 Lys20 and ubiquitylation at H2A Lys15) and accumulate 53BP1. MRN activates ATM, phosphorylating 53BP1 which in turn recruits Rif1 and PTIP, these factors inhibit end resection. The cell utilizes NHEJ for repair. During the late S- and G2-phase (right), cellular cyclin levels rise, and CDKs are rendered active. Phosphorylated CtIP, constantly by CDK and during DSB repair temporarily by ATM, associates with BRCA1, prevents the inhibitory action of Rif1 and PTIP onto MRN and further activates the Mre11 nuclease. Recruitment of 53BP1 to DSBs is hampered after replication due to missing H4 Lys20 methylation (transparent). After initial end resection, CDK phosphorylated Exo1 facilitates long-range resection, determining the pathway choice towards HR.

1.3 MRN

As a central player in the initial HR steps, MRN fulfils a multitude of functions. MRN recognizes DSBs, integrates various regulatory signals, initiates end resection and starts the DDR by recruiting the master regulator ATM[87]. Therefore, MRN combines sensing, scaffolding, and enzymatic functions in a single protein complex by a yet poorly understood mechanism. Besides the tasks in DNA repair, this

multifaceted complex also plays important roles in telomere maintenance and meiotic recombination[62,88]. While the two enzymatically active parts, meiotic recombination 11 (Mre11) as the Mn^{2+}-dependent nuclease, and the ATPase radiation sensitivity 50 (Rad50) are evolutionarily highly conserved, eukaryotes have a third, regulatory component, Nijmegen breakage syndrome 1 (Nbs1) (also referred to as Nibrin or Xrs2 in yeast)[89]. Interestingly, this conservation extends from all three domains of life, prokaryotes, archaea and eukaryotes to some phages[90]. Dimeric Mre11 and Rad50 form the conserved core complex in a heterotetrametric assembly (M_2R_2), joined by one or two Nbs1 proteins in eukaryotes[91,92].

1.3.1 Mre11

Mre11 consists of an N-terminal nuclease domain with the di-metal active centre, followed by the capping domain to form the catalytic core (**Figure 5**)[93]. The nuclease centre is built by two Mn^{2+} ions, coordinated by several histidines, aspartates and an asparagine[93]. A short, flexible linker connects the Rad50 coiled-coils binding helix-loop-helix (HLH) motif to the well-structured N-terminal part[94]. The C-terminus is evolutionary less conserved and forms a mainly unstructured extension in eukaryotes (roughly 200 residues in human Mre11), harbouring DNA binding activities[95,96]. Mre11 dimerizes over conserved helical bundles between the nuclease domains and together with the capping domains forms a U-shape with a Rad50/DNA binding cleft[97,98].

Mre11 on its own possesses 3' – 5' dsDNA exonuclease activity[99]. In complex with Rad50, this activity is stimulated and further Mre11 is able to process ssDNA and DNA hairpins endonucleolytically as well[99,100]. To form 3' overhangs, as occurring in HR, MR introduces an endonucleolytic incision approximately 20 bp from a DNA end and then processively resects the incised strand 3' – 5' towards the break[63,101]. In the eukaryotic system, CtIP and Nbs1 promote this ATP-dependent endonuclease cut[63]. For clearing protein-blocked DNA ends, e.g. due to abortive topoisomerases or Spo11, the endonuclease activity is essential to remove the block prior to repair[97]. Mre11 is an essential protein in vertebrates and mutations, in the nuclease domain as well as other parts, are associated with different types of cancer[102,103].

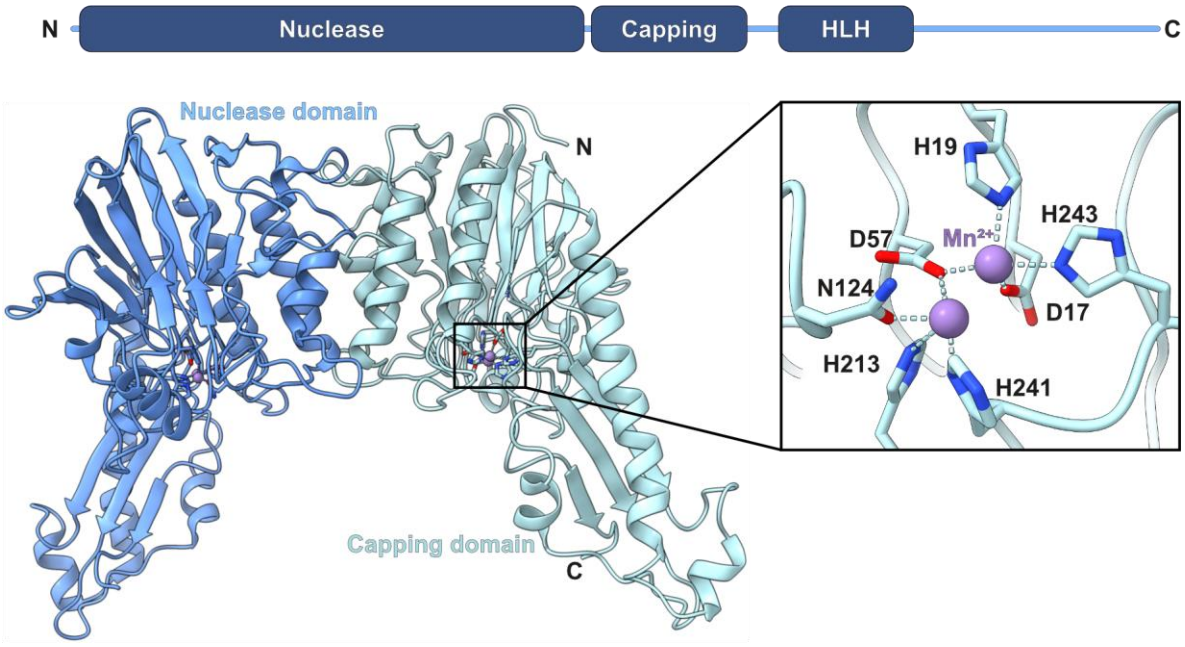

Figure 5: Mre11 domain architecture and structure. Mre11 consists of an N-terminal nuclease domain, followed by the capping domain and the helix-loop-helix domain interacting with Rad50. The length of the flexible C-terminal region varies evolutionary. Crystal structure of *Chaetomium thermophilum* (*Ct*)Mre11 dimer (PDB: 4YKE), catalytic domain. One active centre with two coordinated manganese ions (purple) is emphasized.

1.3.2 Rad50

The ATPase Rad50 is part of the structural maintenance of chromosomes (SMC) protein family, a group containing cohesin and condensin as well[104]. SMC proteins display a conserved fold, very N- and C-terminal, globular nucleotide binding domains (NBD) are connected via long coiled-coils in-between (**Figure 6**)[105]. In the case of Rad50, the coiled-coil domain folds backwards halfway to form a long, antiparallel assembly with the NBDs joined together[93]. At the coiled-coil apex, the CXXC motifs from two Rad50 proteins form a dimer interface by tetrahedrally coordinating a single Zn^{2+} ion with four cysteines, referred to as zinc-hook (see also **Figure 8**)[106]. Mre11s HLH motif binds at the very beginning of the coiled-coils (Mre11 binding domain, MBD)[94,107].

The NBDs resemble the structure of ATP-binding cassette (ABC) ATPases[104]. In this conserved fold, the binding of two ATP molecules dimerizes the globular NBD domains of two individual Rad50 proteins[108]. Thereby, ATP is sandwiched in between the dimer interface: The N-terminal NBD Walker A motif and the signature motif originating from the second Rad50 C-terminal NBD coordinate the β-phosphate, whereas the Walker B motif from the first Rad50s C-terminal NBD positions the γ-phosphate and a Mg^{2+} ion[109]. The second ATP is bound in the same way which leads to an opposed positioning of the globular NBDs. Due to the ATP-induced dimerization of the NBDs, a DNA binding cleft is formed between the commencing coiled-coils and the globular head[109]. Indeed, dsDNA greatly increases the ATPase activity of formerly slowly ATP hydrolysing Rad50[110]. In the human system, Nbs1 boosted the ATPase rate of MR as well, while the yeast equivalent Xrs2 was not able to affect the ATPase[110]. In a biological context, the ATPase function of Rad50 is essential. Mutating key residues involved in ATP hydrolysis leads to severe phenotypes, equivalent to deleting Rad50 as whole[111,112]. Next to ATPase activity, the NBDs play important roles in MRN oligomerization, thereby influencing overall DNA binding, nuclease activity and functions in meiotic recombination[113,114].

With the extended coiled-coils, Rad50 contributes unique structural and biochemical features to MRN. Thereby, the length of the coiled-coils varies across the domains of life, with the shortest being around 10 nm in viral Rad50, and the longest extending up to 60 nm in higher eukaryotes. These marked differences in lengths possibly reflect the inherent inter-chromosomal distances and differences in chromosomal organization complexity[115]. While the length may vary across species, truncating the coiled-coils leads to severe defects in meiotic recombination, telomere maintenance and interestingly also in NHEJ[116]. Similar effects can be observed when the zinc-hook is disrupted, which as well points towards important roles of the MRN complex in pathways next to HR[117]. In HR, one of the main functions of MRN is thought to be end recognition and resection, whereas other pathways rely on the DNA tethering functions mediated by coiled-coil interactions.

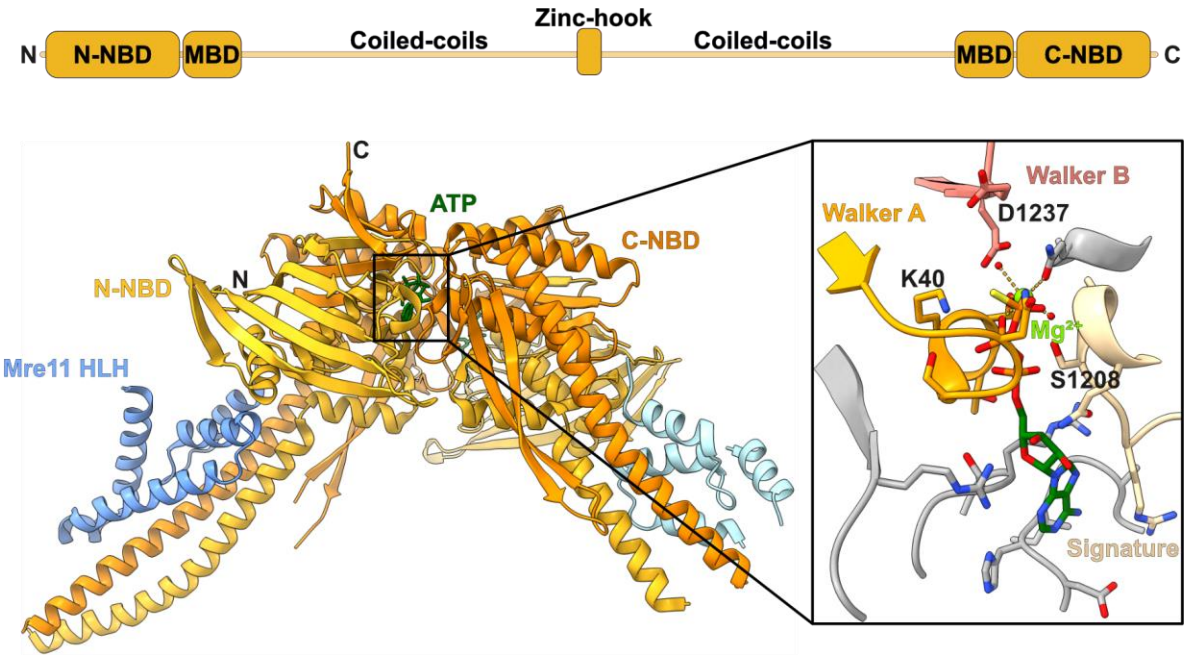

Figure 6: Rad50 domain architecture and structure. Rad50 consists of N- and C-terminal nucleotide binding domains, followed and preceded by short Mre11 binding domains respectively. The two globular terminal parts are joined by long coiled-coils, forming a zinc-hook at their apex. The length of this coiled-coil domain varies between species. Crystal structure of *Ct*Rad50 globular head dimer (orange) with ATPγS (green) and Mre11 HLH (blue) bound (PDB: 5DA9). One ATP binding site in between the dimer is highlighted (phosphates: dark orange, magnesium ion: light green). Thereby the grey coloured peptide chains, the Walker A and the signature motif originate from one protomer, the Walker B motif from the other NBD.

1.3.3 Mre11-Rad50 interplay in end resection

While the majority of previous structural research was limited on Mre11 or Rad50 alone, already very early studies highlighted the importance of the interaction and functional dependence of Mre11 and Rad50[118]. This obstacles in understanding the molecular mechanism of MR(N) function existed mainly due to restrictions for specimen in X-ray crystallography, which requires very defined and rigid samples. Recent advances in cryo-electron microscopy techniques allowed to analyse more flexible and heterogenous specimen, including Rad50 and Mre11 in their full length in combination with DNA. Structurally solving the bacterial MR complex (often denoted SbcCD with SbcC being the equivalent to Mre11 and SbcD Rad50) shed light on how both proteins with their catalytic activity influence each other and visualized the dynamics of the complex (**Figure 7**)[98]. To prevent nucleolytic cleavage inside the intact genome, a Rad50 dimer blocks the active centres of a Mre11 dimer when no DNA end is engaged. In this so-called “resting”- or autoinhibited state, two ATPs are bound to Rad50, and the coiled-coils reside in an open conformation, primed to embed DNA in their binding cleft. When MR recognizes a DNA end, ATP is hydrolysed and ADP bound Rad50 adopts a closed coiled-coil conformation, with both coiled-coils and the globular head clamping the DNA in-between very defined residues. Mre11 translocates from binding Rad50 in its U-shape towards the DNA end and positions one active centre in proximity to the sugar-phosphate backbone. This prepares the complex for DNA cleavage. Disturbing the clamping mechanism by mutating the respective DNA contacting residues greatly inhibits the nuclease activity. In the “cutting”-state, the DNA is slightly bend through a channel formed between $Rad50^{NBD}$ and Mre11. This bending represents a potential end-recognition mechanism as undamaged *Escherichia coli* (*E.coli*) DNA resides negatively supercoiled, a state

counteracting extensive bending[119]. During the large relocation of Mre11, a flexible linker allows the HLH motifs to stay attached to the start of the coiled-coils.

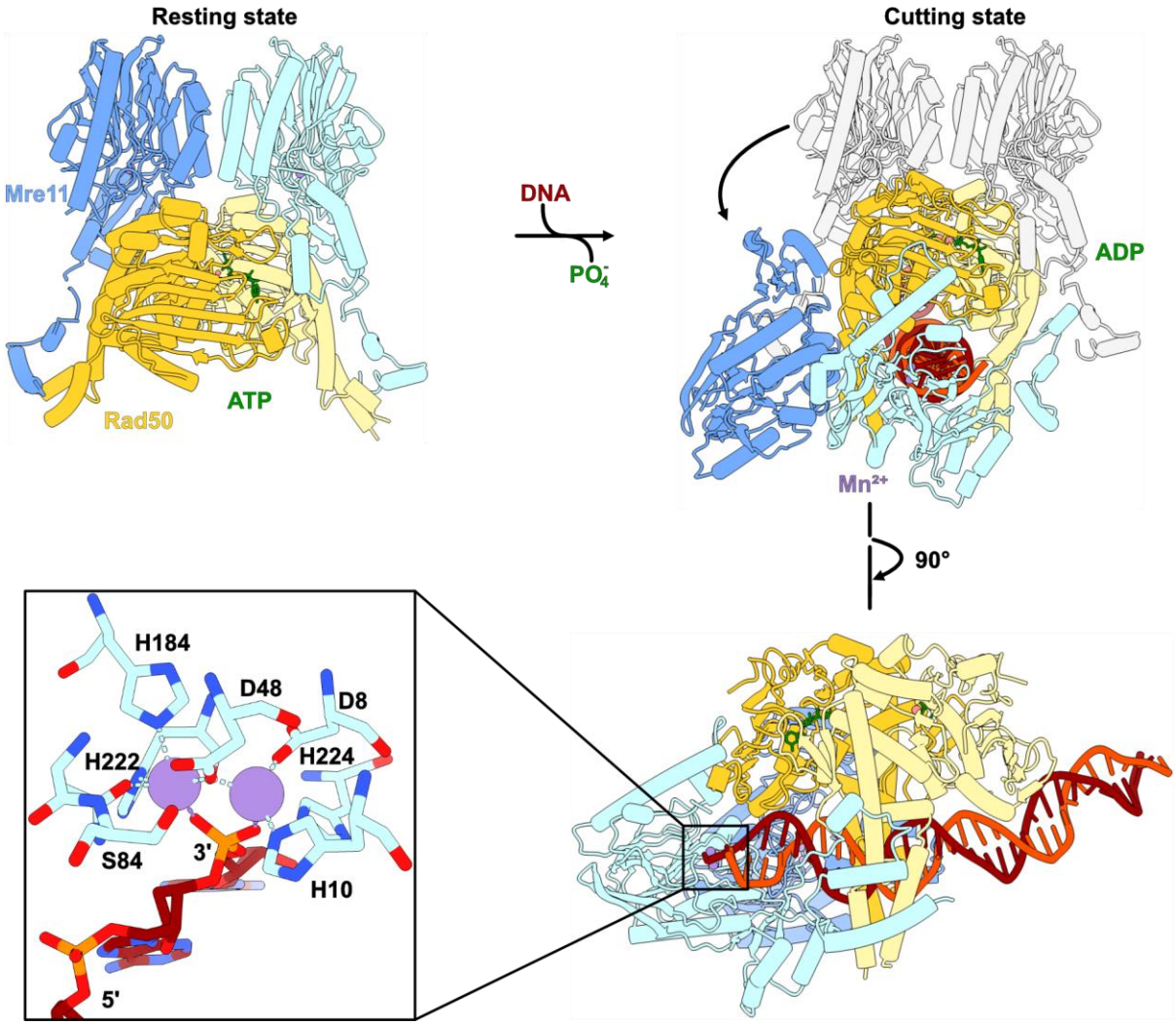

Figure 7: Exonucleolytic DNA processing by *E. coli* (*Ec*)MR. In the ATP-bound (green) resting state, the complex resides in an autoinhibited state: Rad50s globular head domains (orange) block Mre11s nuclease (blue) (PDB: 6S6V). Upon DNA (red) clamping in between the Rad50 coiled-coils and ATP hydrolysis, the Mre11 nuclease dimer translocates to the DNA end and positions one active centre in the vicinity of the sugar-phosphate backbone, poising the DNA for cleavage in this cutting state (highlighted, PDB: 6S85).

1.3.4 Coiled-coil dynamics

Besides the large relocation of the Mre11 dimer, Rad50's coiled-coils undergo an extensive movement during the transition from the resting to cutting state. While the coils display an open conformation in the resting state, they are presumably joined at the zinc-hook to form a ring-like structure (**Figure 8**)[106]. Data from atomic force microscopy (AFM) thereby support the underlying crystal and cryo-EM structures[120-122]. Viewed from the zinc-hook, the coiled-coils from two different Rad50 proteins run in an antiparallel manner. This state would allow the complex to scan along the genome for DSBs with the DNA sliding through the cleft formed by the open coils. The enormous length of the coiled-coils thereby permits MR to bypass even large DNA-bound proteins[123].

In the DNA-bound cutting state, the coiled-coils zip up to form a rod-like shape[98,121]. For bacterial MR, five zipper contact points are predicted to interrupt the strict linear coiled-coils arrangement and to stabilize the dimeric rod-shape. At the apex, the zinc-hook is formed by two parallel coiled-coil domains[124]. AFM studies suggest a higher-ordered oligomerization of closed-coil MRN mediated by zinc-hook contacts, which could explain MRN's DNA tethering ability[121]. Together with the multimerization ability of Rad50^{NBD}, MRN contains at least two sites for transient oligomerization[113]. The coil dynamics during DSB recognition likely play an important role especially for the endonuclease activity. One model postulates that the zipping transduces a force onto the Mre11 dimer, thereby promoting its relocation into the active conformation.

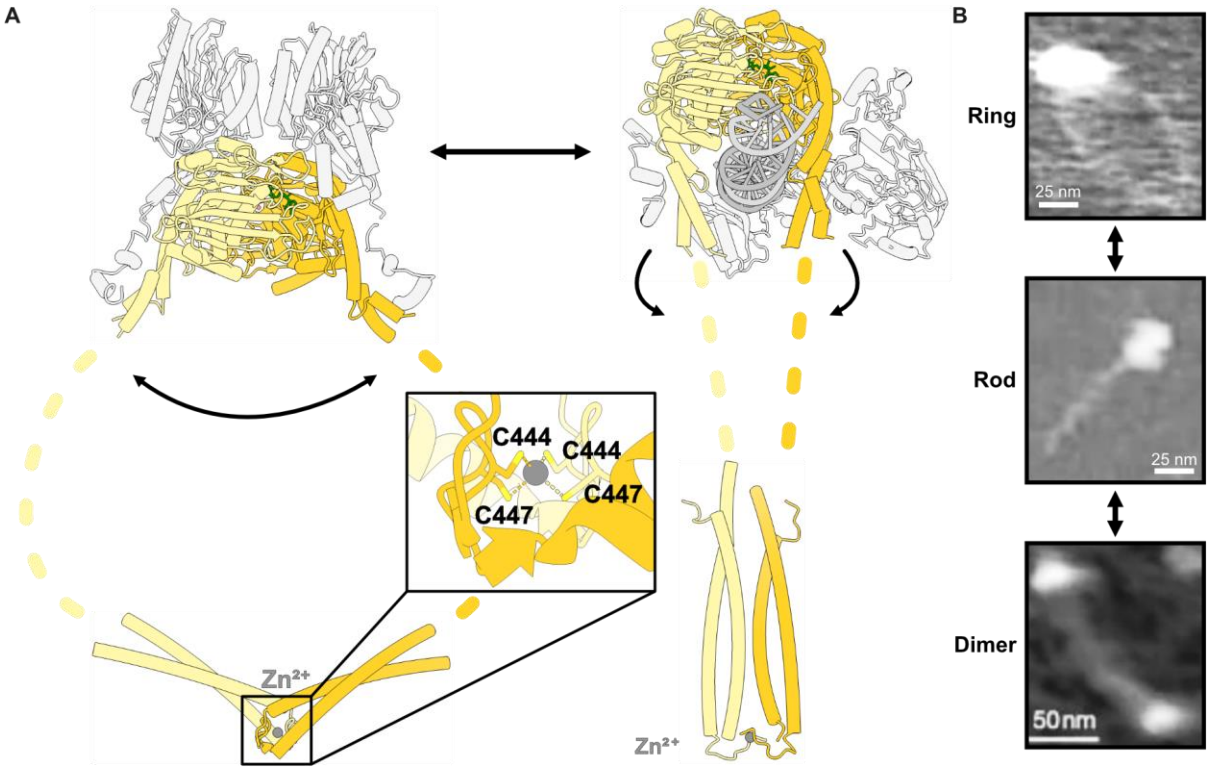

Figure 8: Proposed Rad50 coiled-coil movement during MRNs nuclease cycle. **A**: In the ATP-bound resting state (left side), the coiled-coils adopt an open conformation, and are probably joined at the apical zinc hook in an antiparallel manner (Mre11 greyed out, PDB resting state: 6S6V, PDB *Pyrococcus furiosus* (*Pf*)Rad50 zinc-hook: 1L8D). Upon DNA clamping in between the coiled-coils and ATP hydrolysis (right side), the coiled-coils close to form a rod-like structure. At the apex, the zinc-hook is likely formed by parallel, joined coiled-coils. (PDB cutting state: 6S85, PDB *Pf*Rad50 zinc-hook: 6ZFF). **B**: AFM images of eukaryotic MR(N) show ring-like structures without DNA, the addition of DNA evoked rod-like coiled-coils as well as dimers of two MR(N) molecules, joined presumably at the zinc-hook[120-122].

1.3.5 Nbs1

The eukaryote specific Nbs1 protein holds no enzymatic activity but has important regulatory and scaffolding features. At the well-structured N-terminus, two breast cancer-associated 1 C-terminus (BRCT) domains follow a fork head-associated (FHA) domain via a direct linkage and cease in the large, flexible C-terminal part (**Figure 9**)[125]. FHA as well as BRCT domains are conserved phosphopeptide binding folds, and can recruit a variety of phosphoproteins such as CtIP, BRCA1 and MDC1 to transform MRN into an interaction hub[70,126]. These domains further allows MRN to bind phosphorylated H2AX

histones, an important DSB signal introduced by ATM, to locally accumulate at DNA ends[127]. The C-terminal part harbours the Mre11-binding domain (MBD) with the conserved KNFKxFxx motif binding across the Mre11 dimer interface to further stabilize and thereby regulate the nuclease[92]. Mutational studies assign a 108 amino acid short sequence embracing the MBD domain essential roles to sustain MRN functions[128]. This region further contains the nuclear localisation sequence (NLS), missing in the other components of MRN[129]. An ATM-binding domain (ABD) resides at the very C-terminus, which associated over a conserved FXF/Y motif to the HEAT-repeat domain of ATM (see also **Figure 11**)[130]. This interaction plays important roles in recruiting and activating ATM at DSBs. ATM in turn phosphorylates Nbs1 at multiple sites, in combination with CDK-mediated phosphorylations, this pattern influences Nbs1 complex regulatory role via a yet poorly understood mechanism[131].

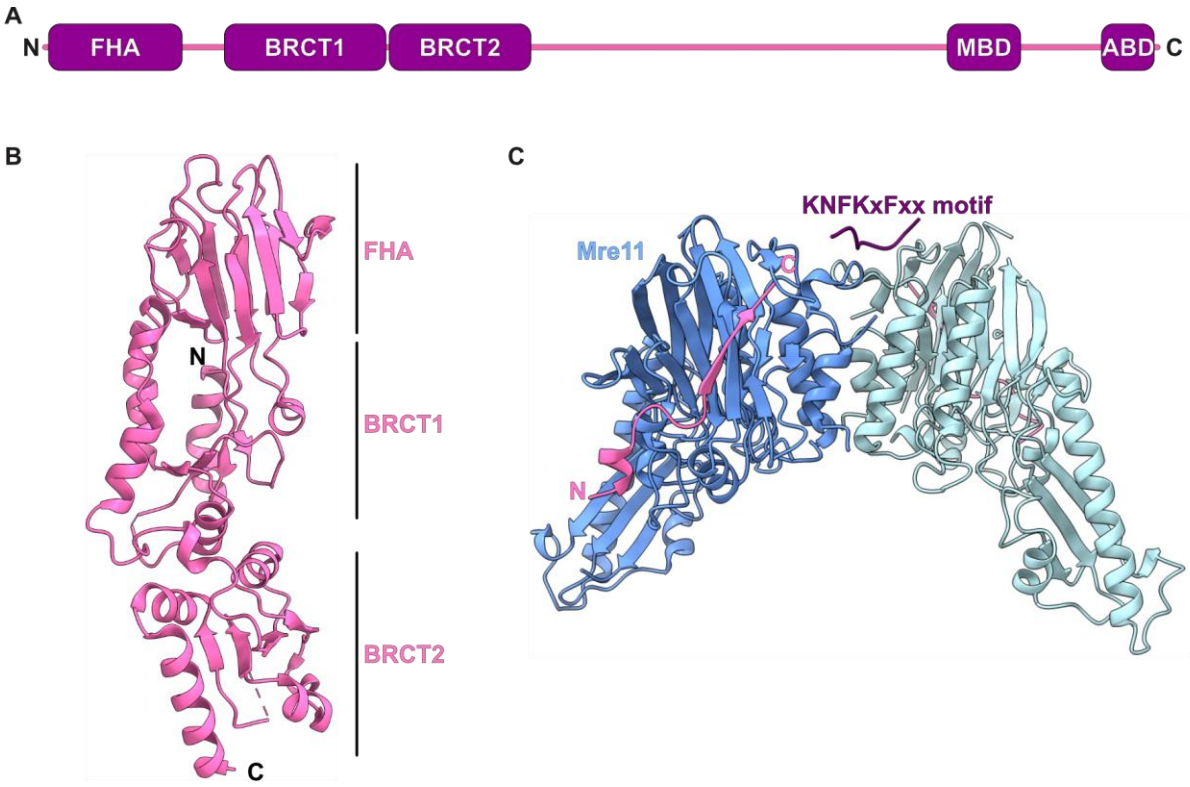

Figure 9: Nbs1 domain architecture and structure. **A**: Nbs1 consists of well-structured N-terminal FHA and tandem BRCT domains succeeded by a long, flexible region harbouring the Mre11 binding domain (MBD) and the ATM binding domain (ABD). **B**: Crystal structure of *Schizosaccharomyces pombe* (*Sp*)Nbs1 FHA-BRCT1/2 domain (PDB: 3HUE). **C**: Crystal structure of *Sp*Mre11 catalytic domain with Nbs1^{MBD} (PDB: 4FBW). Nbs1's conserved KNFKxFxx motif is highlighted in dark purple.

1.3.6 MRN in DNA repair

Besides the already discussed roles of MRN in HR, namely DNA end recognition, resection and signalling, MRN interestingly influences C-NHEJ as well. While in HR MRN's catalytic functions are essential, a nuclease-dead Mre11 mutant was able to rescue a C-NHEJ defective Mre11 deletion, suggesting a more structural than enzymatic role of MRN in NHEJ[132]. Similar to NHEJ, MRN is involved in the specialized repair process during somatic V(D)J recombination, explaining the deficiencies in the adaptive immune system of patients suffering from different MRN mutations[133]. The other type of programmed DSBs, in which during meiotic recombination Spo11 introduces a break and stays covalently attached until repair, requires MRN for repair as well[134]. Thereby, MRN resolves DNA-

protein crosslinks at DSBs by endonucleolytically clipping of the adduct. As a common principle, MRN was shown to rapidly relocate and accumulate at DSBs from a usually uniform nuclear distribution[135]. In accordance, MRN possesses the ability to undergo cooperative oligomerization[113]. This enables a strong signal amplification and high local concentration of downstream factors such as ATM[66].

1.3.7 MRN in telomere maintenance

The eukaryotic genome is divided into multiple linear chromatids. This linearity raises two main challenges for cells: firstly, the nature of replication in one direction, 5' to 3', with one leading and one lagging strand, results in the shortening of the lagging strand after each replication as no new primer can be synthesized at the very ends[136]. Secondly, chromatid ends, denoted telomers, are chemically indistinguishable from DSBs and therefore would trigger the DSB repair and DDR machinery[137]. To overcome the first challenge, chromatids have a repetitive end sequence ($[TTAGGG]_n$ in mammals) which is extended by the ribonucleoprotein telomerase, an enzyme containing a short RNA stretch to serve as a template for terminal DNA extension[138]. As a protective mechanism, telomerase is normally only active in gametes and stem cells to ensure their genome integrity in this frequently dividing cell[139]. Differentiated cells lack telomerase activity and are thus limited in the amount of total cell divisions (Hayflick limit)[140]. Cancer cells overcame this limit by expressing telomerase or alternative pathways[141].

The second challenge is solved by a very specific structure of the telomers. Thereby, the 3' single-stranded overhang of the chromatid end invades upstream repetitive, dsDNA sequences to form a so-called T-loop[142]. The T-loop is stabilized by the shelterin complex, consisting of six proteins in humans, TRF1, TRF2, hRap1, TIN2, TPP1, and POT1[142]. Unfunctional shelterin complexes result in unprotected chromosome ends, which can be recognized by DNA damage sensors, e.g. ATM and eventually lead to NHEJ or HR[143]. A potential outcome of aberrant DSB repair at telomers are chromosome fusions[144].

One of the first discovered MRN functions during telomere maintenance was the observed telomere shortening in yeast cells with dysfunctional MRN[145,146]. MRN facilitates recruitment of telomeric proteins to chromosome ends during telomere replication in the S-phase, including telomerase[147]. However, the 3' overhangs invading the upstream strand and forming the T-loop are most likely generated by Exo1 and Apollo nucleases; roles of MRN as one of the processing nucleases are discussed[148]. In a more scaffolding function, all MRN parts interact with the shelterin component telomeric repeat-binding factor 2 (TRF2)[138]. The Nbs1 interaction is disrupted by CDK2 phosphorylation, thus coupling MRNs role in telomere maintenance to the cell cycle[149]. To prevent nucleolytic digest by MRN at intact telomeres, the telomeric Rif2 protein suppresses MRNs endonuclease activity by directly binding at Rad50 β-sheets[150].

Cancer cells lacking telomerase activity developed an alternative lengthening of telomeres (ALT) pathway, similar to HR[151]. In this process, MRN resects shortened telomeres to generate 3' overhangs, which can invade adjacent homologous, DNA sequences[151]. The invading strand is extended by polymerases and thus the telomere length restored.

1.4 MRN interacting factors

In order to fulfil its diverse range of functions while at the same time integrating multiple regulatory signals, MRN interacts with different additional factors and forms at least short-lived complexes. Evolutionary, many of these proteinaceous factors are exclusively found in eukaryotes, while some

higher eukaryotes such as vertebrates were recently shown to have an additional layer of complexity with even more proteins influencing MRN. This reflects the need for a tighter regulation of DSB repair as well as other processes e.g. telomere maintenance to avoid genetic instability and tumorigenesis.

1.4.1 CtIP

From the variety of MRN interactors, CtIP is one of the most intensively studied examples. The eukaryote specific protein contains a conserved oligomerisation domain at the N-terminus to form tetramers (**Figure 10**). This domain comprises parallel dimerizing coiled-coils, which can contact another dimer over a short hydrophobic interaction to build antiparallel tetramers[152,153]. The tetrameric assembly is crucial for CtIP's function to promote DNA end resection[152]. Following the oligomerization domain, the mainly unstructured middle region of CtIP varies greatly in length across different species, from roughly a hundred amino acids in fungi up to 600 amino acids in humans[154]. The middle part harbours an important CDK phosphorylation site, S327 in humans, to facilitate recruitment to Nbs1 and BRCA1[155]. Binding to Nbs1 in a positively charged pocket of the FHA domain induces a conformational change in Nbs1 with a yet unclear function[125]. The middle region further contains a DNA binding domain and a DNA2 binding site to enhance long-range resection[156]. The conserved and partly structured C-terminal domain (CTD) interacts with and activates MRNs endonuclease depending on the phosphorylation status of the CDK site T847 and the ATM site T859[157]. This regulatory switch ensures efficient end resection only during S/G2-phase and after ATM activation as an additional layer of regulation. Interestingly, CtIP shares the binding interface on Rad50 with the telomeric protein Rif2 which in contrast inhibits the endonuclease activity[150]. ATM-mediated hyperphosphorylation eventually leads to CtIP SUMOylation, in turn a signal for polyubiquitylation and subsequent degradation[158]. This off-switch mechanism limits excessive resection[158]. Altogether, tetrameric CtIP adopts a dumbbell shape with the C-terminal domains facing outwards, joined by the N-terminal coiled-coils. With this structure, CtIP is able to bridge DNA ends[153].

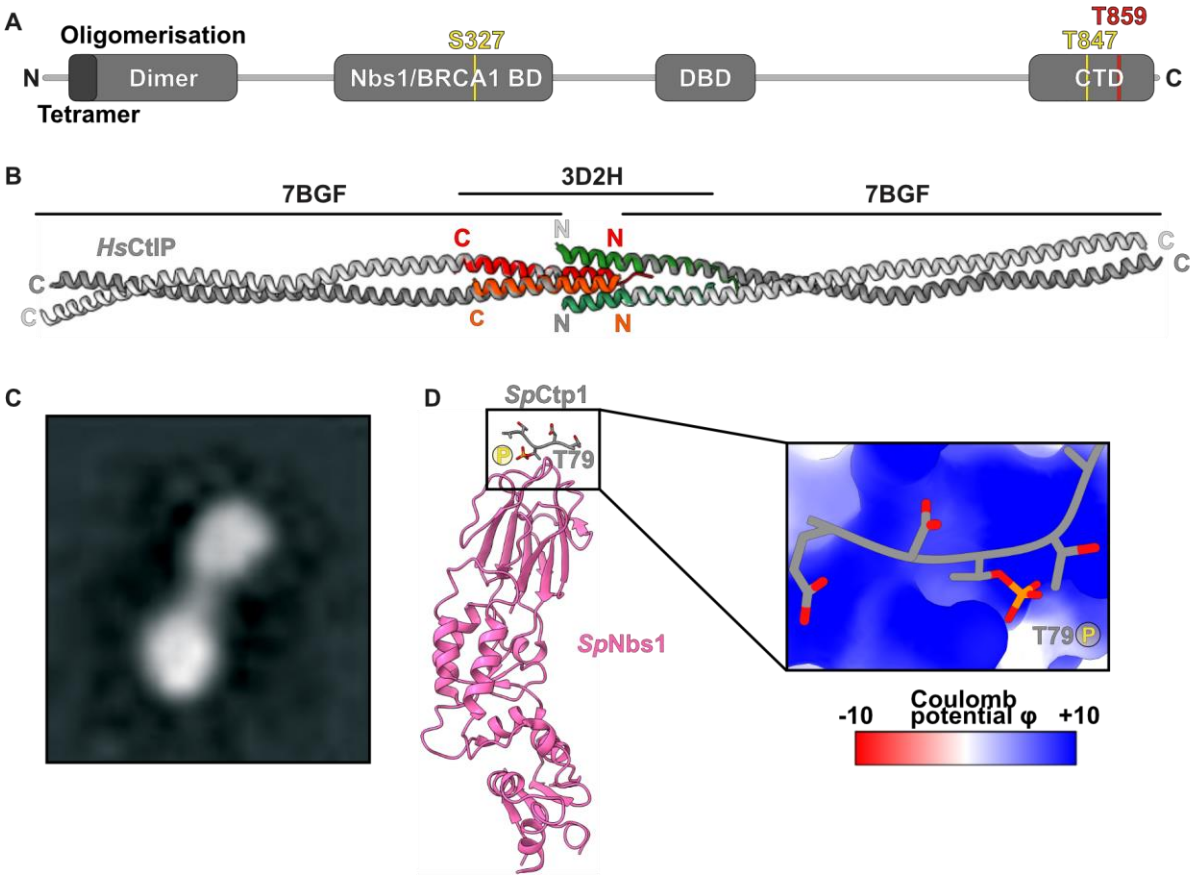

Figure 10: CtIP domain architecture and structure. **A**: CtIP tetramerizes over a short N-terminal motif, directly followed by a dimerization domain to build a well-ordered coiled-coil oligomerization fold. The middle region is mainly unstructured and features a Nbs1/BRCA1 binding domain (BD) with the CDK phosphosite S327 (yellow) followed by a DNA binding domain (DBD). The C-terminal domain (CTD) is partly structured, contains MRN activating features and the phosphosites at T847 (CDK) and T859 (ATM, red). **B**: Crystal structures of *Hs*CtIP with the dimerization domain (grey, PDB: 7BGF) overlaid on the tetramerization motif (one dimer coloured orange, the other green. PDB: 3D2H). **C**: Negative stain electron microscopy revealed a dumbbell shape of the CtIP tetramer[153]. **D**: Crystal structure of *Sp*Nbs1 FHA-BRCT1/2 domain in complex with a short CtIP phosphopeptide (PDB: 3HUF). The phosphate binds into a positively charged pocket (highlighted).

1.4.2 MRNIP

While CtIP mainly upregulates MRNs endonucleolytic capabilities, the exonuclease activity was recently reported to be influenced by the MRN interacting protein (MRNIP). MRNIP, a roughly 40 kDa large, non-enzymatic factor thereby specifically inhibits the exonuclease[159]. During replication fork stalling, DNA is remodelled to form reversed forks, a crucial intermediate step to eventually resolve stalling. In this scenario, the nascent strands need to be protected from Mre11-dependent degradation, mediated by MRNIP[159]. Further studies suggest MRNIP's ability to undergo liquid-liquid phase separation (LLPS) while incorporating MRN inside[160]. Upon DSBs, MRNIP rapidly relocates to the lesion to promote MRN loading and end resection[160,161]. This local MRN accumulation enhances the DDR response via increased ATM activation[161].

1.4.3 ATM

The protein kinase ATM acts in the very first steps of DSB signalling to coordinate the repair and further downstream leads to checkpoint activation and cell cycle arrest[131]. Due to homology in the kinase domain to phosphatidylinositol 3 (PI3) family of kinases (PI3K), ATM is placed in the family of PI3K-like protein kinases (PIKK)[131]. This family contains two other DDR signalling factors, DNA-PKcs, mediating C-NHEJ, and the single-strand break repair factor ataxia-telangiectasia and Rad3–related (ATR)[162]. Other PIKK members include mammalian target of rapamycin (mTor), sensing nutrients and the cellular metabolism, suppressor of morphogenesis in genitalia 1 (SMG-1), which facilitates nonsense-mediated mRNA decay and the pseudo-kinase transformation/transcription domain–associated protein (TRRAP), regulating transcription processes[163-165]. Common to DNA-PK and ATR, ATM preferentially phosphorylates serines and threonines at SQ/TQ sites[162].

The roughly 3,000 amino acids large ATM protein resides as a butterfly-shaped, 700 kDa sized inactive dimer and adopts the conserved PIKK domain architecture (**Figure 11**)[166]. The N-terminus and the largest part of ATM forms so-called HEAT repeats (Huntingtin, elongation factor 3, protein phosphatase 2A, TOR1), which are further divided into the "Spiral" and "Pincer" domain. This domain acts as a scaffold to mediate protein-protein as well as DNA interactions[130,166]. Following the HEAT repeats, the FRAP–ATM–TRRAP (FAT) domain, consisting of three Tetratricopeptide Repeat Domain subdomains (TRD) and a HEAT-repeat subdomain (HRD), harbours the dimer interface with multiple hydrophobic patches. The C-terminal kinase domain is built by an N- and C-lobe, while substrate binding is autoinhibited by the PIKK Regulatory Domain (PRD) from the opposing protomer. The FAT C-terminal (FATC) domain forms the very C-terminus and influences the activation mechanism[167].

Analogous to the tight regulation of the MRN complex, ATM activation requires different inputs to prevent the potential detrimental outcomes cell cycle arrest and apoptosis if no DSB occurred. The main ATM activator, MRN, initially recruits the kinase to DSBs over the Nbs1 C-terminal sequence FXF/Y binding to the HEAT repeats[130,168]. In an ATP-dependent manner, DNA-bound MRN is thought to induce ATM autophosphorylation and thereby monomerization, which greatly increases ATM activity[131]. Monomerization would detach the inhibitory PRD from the opposing protomer and render the active site accessible. This step presumably involves Rad50-ATM contacts, integrating the coiled-coil dynamics into signalling[131]. Mre11's nuclease activity was shown to be dispensable for this positively regulating input[169]. For a robust autophosphorylation, the histone acetyltransferase Tip60/KAT5 additionally needs to acetylate lysine 3016 in the FATC domain[170,171]. Thereby the Tip60 activity is controlled by CDK phosphorylations, coupling DSB induced ATM signalling to the cell cycle[172]. In a positive feedback loop, active ATM then phosphorylates histone H2AX, which in turn recruits Mdc1, to bind and accumulate more ATM at sites of DSBs[79]. Noteworthy, ATM shows a low basal kinase activity also in unperturbed cells[173]. A possible explanation could be the recently emerging role of other DNA damage types to potentially activate ATM, including R-loops (DNA:RNA hybrid and the displaced DNA strand), SSBs, topoisomerase cleavage complexes (TOPcc) and splicing intermediates[174].

Identified in patients suffering from debilitating ataxia due to progressive loss of cerebral neurons and telangiectasia (dilated blood vessels), mutations in ATM further cause severe immune deficiencies, radiosensitivity, and increased rates of malignancies[175]. While the central role of ATM as the signalling kinase in HR explains the radiosensitivity and high malignancies rates, the neuronal loss might be reasoned in the second pathway activating ATM: oxidative stress. Neurons are characterized by a high energy consumption and oxygen metabolism, leading to an increased production of ROS[176]. ATM facing increased oxidative stress forms covalent, disulfide-bond linked dimers, most importantly between cysteines 2991, and is activated in an MRN-independent manner[131]. In a yet poorly

understood mechanism, this covalent linkage then leads to autophosphorylation and phosphorylation of a different subset of targets compared to the DDR to respond to oxidative stress[177]. This includes the downstream upregulated antioxidants production, enhanced mitophagy (autophagy of mitochondria) and pexophagy (autophagy of peroxisomes), to reduce the generation of ROS and maintain cell homeostasis[178-180]. In this context, ATM was observed to have a partly cytoplasmic localisation with yet unclear function[181,182]. Cells with dysfunctional ATM show elevated ROS levels, resulting in an increased SSB rate. This leads to PARP enzyme hyperactivation, with the detrimental outcome of drastically reduced NAD^+ and ATP levels during PAR chain synthesis and the stable aggregation of proteins on these polymers[174]. Both mechanisms contribute to neuronal cell death.

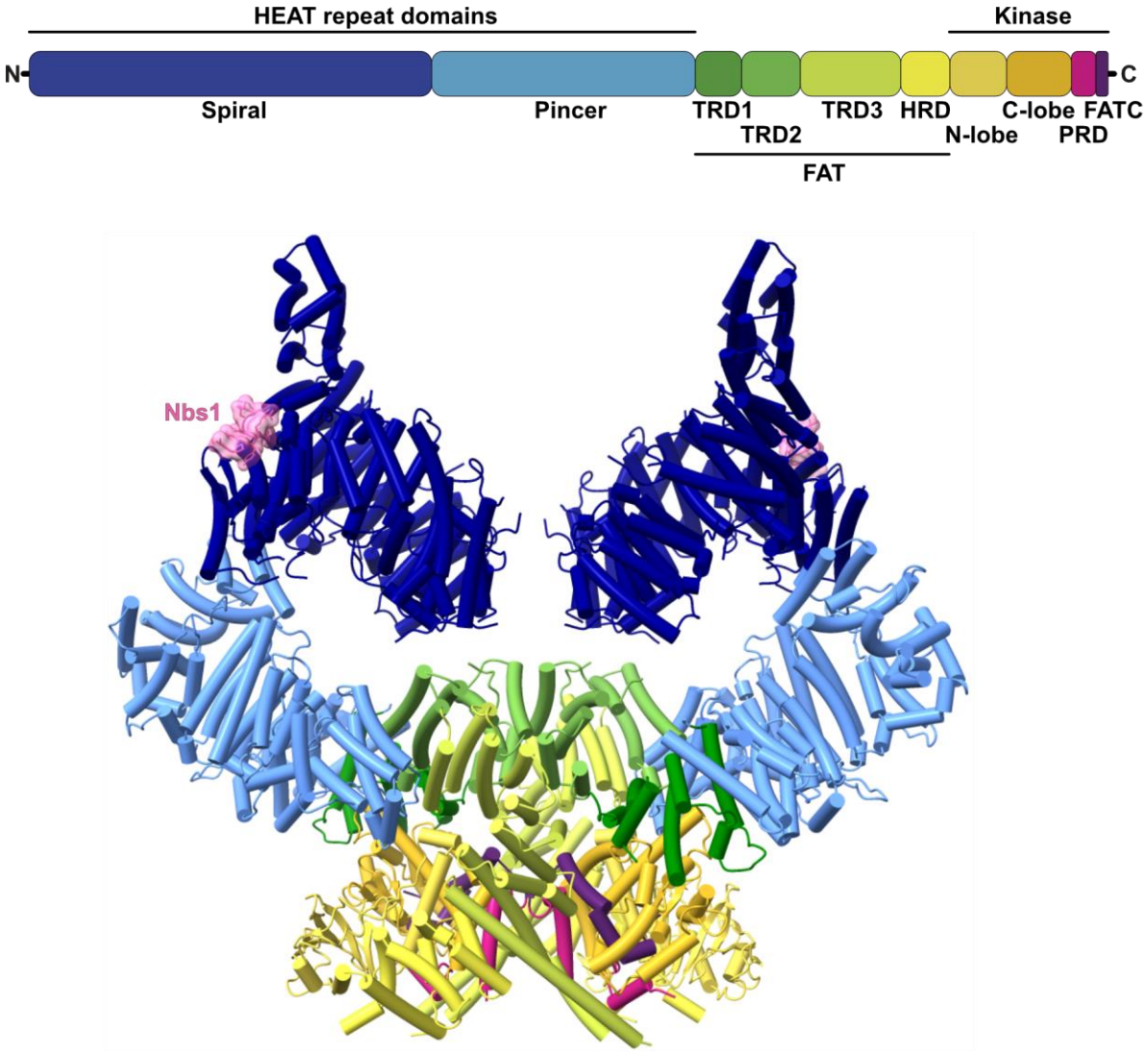

Figure 11: ATM domain architecture and structure. ATM consists of N-terminal HEAT repeat domains, denoted as “Spiral” and “Pincer”. The N-terminal part is followed by the FAT domain harbouring three Tetratricopeptide Repeat Domain subdomains (TRD) and a HEAT-repeat subdomain (HRD). The kinase domain is built by an N- and C-lobe, substrate binding is autoinhibited by the PIKK Regulatory Domain (PRD). A conserved FAT C-terminal (FATC) domain forms the extreme C-terminus. Cryo-EM structure of full-length human ATM (coloured according to domains) in complex with Nbs1 ATM binding domain (pink) (PDB: 7SID).

1.5 DNA damage response

To combat the deleterious effects of DNA damage, cells have evolved a sophisticated DDR network that comprises a series of interconnected signalling pathways to coordinate multiple cellular processes, including DNA damage sensing, DNA repair, signal transduction, cell cycle checkpoints and eventually apoptosis. The DDR is activated upon DNA damage by a cascade of events primarily beginning with the recruitment of PIKK family members ATM, ATR, or DNA-PKcs to the site of damage and activation of PARP enzymes[162,183]. As discussed earlier, PARP enzymes itself recognize single and double stranded DNA breaks, to catalyse the formation of PAR chains onto itself and other proteins[183]. Together with the PARylated environment, the DNA break sensing factors, MRN, Ku70/80 or RPA recruit the respective PIKK signalling kinases[162].

Thereby, ATR senses RPA-coated ssDNA lesion to activate the SSB repair machinery and further halts the cell cycle by phosphorylating and hence activating the checkpoint kinase (Chk)1[184]. In contrast to ATM and DNA-PKcs, ATR activation from RPA-coated ssDNA patches arises from diverse DNA lesions. These structures emerge during stalled replication forks, nucleolytic processing of DNA damage during excision repair pathways or as well in end resection during HR[184]. Therefore, ATR is a broad sensor of genotoxic stress and its ability to activate Chk1 essential for proliferating cells[185]. Active Chk1 promotes proteasomal degradation of the Cdc25 phosphatases, which normally remove inhibitory modifications from CDKs[186]. Reduced CDK activity due to decreasing levels of Cdc25 phosphatases thereby slows or stops cell-cycle progression. As a result, cells have more time to repair DNA damage and premature entry into mitosis is prevented. In cases of extensive damage and prolonged Chk1 activation, this delay can induce senescence or apoptosis[187]. ATR requires the co-factor ATR-interacting protein (ATRIP) to recognize RPA-coated ssDNA. Further, the proteins TopBP1, recruited to RPA-coated ssDNA via the RAD9-RAD1-HUS1 (9-1-1) complex, and ETAA1, directly binding RPA-coated ssDNA, respectively activate ATR[188,189].

In contrast to the primarily signalling functions of ATR, DNA-PKcs' function is extended with a direct role in the NHEJ repair of DSBs: Together with the DNA-PKcs' recruiting factor Ku70/80, the kinase tethers both DNA ends in close proximity and further directly binds and activates downstream repair factors[190,191]. Thereby, the kinase activity orchestrates the course of repair but is thought to be of minor importance for signalling in the presence of the DSB response master regulator, ATM[174,191].

While ATR activation dramatically differs from ATM (covered in 1.4.3), both kinases have similar and overlapping substrates (**Figure 12**). For example, ATM phosphorylates mainly Chk2, with an analogous outcome of ATR-mediated Chk1 activation[192]. In addition, all three PIKK DDR enzymes phosphorylate histone H2AX, a well-established chromatin mark of DNA damage[162]. Besides its function in recruiting repair factors, γH2AX transcriptionally silences the surrounding chromatin to prevent clashes of the transcription machinery with DNA repair[193]. Another common substrate of ATM and ATR is the tumour suppressor p53[194]. This transcription factor underlies constant ubiquitin-dependent proteasomal degradation mediated by the E3 ubiquitin ligase Mdm2 to keep the cellular levels at a minimum[195]. Phosphorylation by ATM and ATR, with the best characterized site serine 15, inhibits the interaction with Mdm2 and thus p53 levels rise[195]. On top, Mdm2 is an ATM substrate as well, phosphorylation renders the ubiquitin ligase inactive[162]. P53 induces the expression of a multitude of genes, to redundantly with Chk activation, stop the cell cycle and possibly initiate apoptosis. This includes the upregulation of the universal CDK inhibitor p21[196]. P21 also blocks DNA replication directly by inhibiting the replication complex PCNA, therefore preventing the S-phase entry[196].

Another class of ATM targets are factors directly involved in the course of DSB repair. In NHEJ, ATM phosphorylates Artemis, XRCC4 and XLF to generally promote DSB repair[197-199]. Intriguingly, DNA-PK is

as well modified by ATM to activate the tethering kinase, whereas DNA-PK-mediated phosphorylation negatively regulates ATM[200,201]. Thus, both PIKKs actively influence each other to steer the DDR. During HR, ATM e.g. modifies CtIP, MRN, BRCA1, Exo1 and the BLM helicase to enable end resection and homology search[174]. To prime the chromatin in vicinity of a DSB for repair, ATM modifies different chromatin remodelers, such as the BRG1 ATPase of SWI/SNF remodeling complexes[202]. The action of chromatin remodelers renders the DNA accessible for repair factors and amplifies the γH2AX foci formation. With its dual role in NHEJ and HR, ATM mediates efficient DSB repair and contributes to the repair pathway choice.

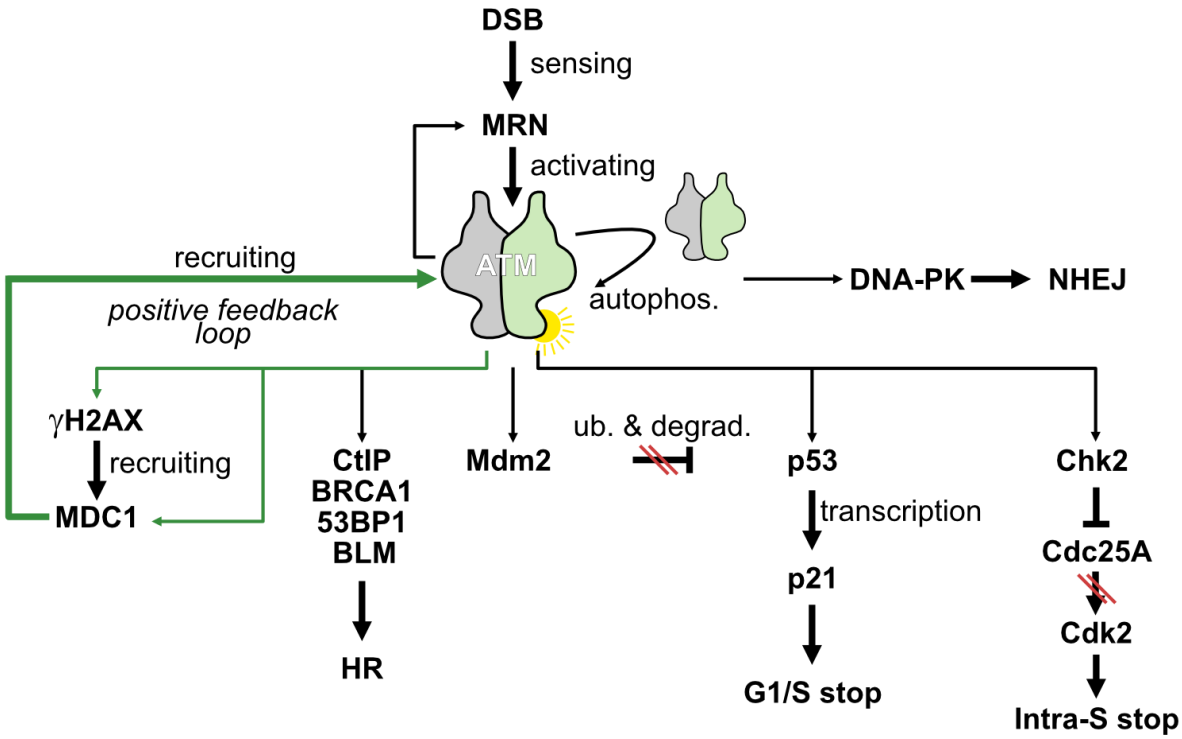

Figure 12: Overview DDR with focus on ATM. Active ATM presumably exists as a monomer (second protomer greyed out), and phosphorylates a pleiotropy of targets (narrow arrows), important ones for DSB repair are highlighted in this scheme. The positive feedback loop is marked with green arrows. Outcomes are implicated with thick arrows, ATM phosphorylations disturbing the respective outcome are crossed out. Ub. = ubiquitination, degrad. = degradation

1.6 ATM in cancer treatment

As a key player in the DDR, ATM and its dysfunctions have been implicated in the pathogenesis of a variety of diseases, including cancer. One of the most important hallmarks of cancer, genomic instability and mutations, is promoted if ATM as the central DSB signalling factor is mutated. To avoid checkpoint activation and apoptosis from elevated DNA damage, cancer cells accumulate further mutations in the DDR. While on the one hand several mutated ATM variants can be found in different types of cancer, on the other hand an increased transcriptional activation of ATM coincides with robust resistance to chemotherapeutica[203]. Therefore, in recent years, there has been significant interest in developing therapeutic strategies to specifically target ATM and thereby selectively kill cancer cells while sparing normal cells.

One approach involves the use of ATM inhibitors, which have been shown to sensitize cancer cells to chemo- and radiation therapy by blocking the DDR pathway and preventing DNA repair[204]. This strategy has been particularly effective in tumours with existing defects in DNA repair, e.g. breast cancer with BRCA1/2 mutations, which are already sensitive to PARP inhibitors, or by evoking efficient synthetic lethality that combines ATM with ATR/PARP inhibition[205-207]. Thereby, both partially redundant pathways are shut down and cells devoid of DSB repair pathways, leading to accumulation of DSBs and cell death. Recently, several small molecule ATM inhibitors have been developed and entered clinical trials in combination with chemo- or radiotherapy. These molecules need to be potent inhibitors, selective for ATM while minimally effecting other targets and show a high bioavailability. All available ATM inhibitors to date such as KU-55933, CP-466722 and AZD0156, are designed to block the active site with a structure similar to ATP[204].

In addition to its role in DNA repair, ATM is involved in the regulation of cellular metabolism and immune response, making it an attractive target for the emerging field of cancer immunotherapy[208]. During immunotherapy, the patient's own immune system is stimulated to clear tumours. ATM inhibitors have been shown to inhibit immune checkpoint pathways and thus promote T cell infiltration into tumours, reducing their growth[209].

1.7 Objectives

MRN and ATM are central factors in HR and involved in a multitude of other cellular processes as well. Over the past two decades, both factors have been extensively studied and many details regarding their structural, cellular and biological functions were uncovered. However, a largely flexible Nbs1 protein and long Rad50 coiled-coils hindered researchers to investigate MRN as whole in X-ray crystallography, restricting the structural knowledge to mostly individual parts of the complex and therefor missing the interplay of MRN's variety in structural and functional features. The ATM protein as an interesting therapeutic target lacked a high-resolution structure which could be used for future structure-based drug design and explain important aspects of its regulation. With the development of high-resolution cryo-EM techniques, partially flexible and heterogenous protein complexes such as MRN and ATM can now be visualized.

Entering the ATM project midway, the goal was to setup an *in vitro* kinase assay to test the efficiency of different inhibitors, KU-55933 and M4076, used in structural studies. Therefore, one of the best studied targets of ATM and a central component in HR, CtIP was cloned, purified and established as a well-suited substrate in a gel-based kinase assay. Structural analysis of inhibitor-bound ATM resulted in a near-complete atomic model of dimeric ATM. With this structure, the selectivity of different inhibitors can be explained on an atomic level. Further, this map allows to localize common ATM mutations in cancer or ataxia-telangiectasia and hypothesize their influence on the protein.

In the MRN project, the first goal was to establish a working nuclease assay for the eukaryotic system. Starting with the simpler, prokaryotic MR, a novel well-based fluorescence-quencher setup was successfully tested and used to characterize MR further. A previous paper visualizing full-length MR in its exonuclease state, raised the question whether the other crucial cutting modalities, endonuclease and hairpin opening, rely on the same mechanism. Solving MR structures bound to a Ku70/80 double-sided blocked DNA and a hairpin DNA unify the mode of action, independent of the substrate. Upon substrate recognition, the Rad50 coiled-coils close and clamp the DNA in between. The Mre11 dimer translocates towards the DNA backbone from its previous autoinhibited conformation and positions one active centre poised to catalyse the hydrolysis reaction.

The eukaryotic MRN complex with its tighter regulation and increased propensity to oligomerize represents a disparate more intricate study subject. Therefore, the major aim of this research project was to obtain a first full-length structure using cryo-EM. To reach this goal, the purification of the *Chaetomium thermophilum* and human MRN was established and both complexes extensively screened for cryo-EM analysis. The *Ct*MRN-ATPγS structure was determined to high-resolution, revealing an autoinhibited Mre11 state, rod-like Rad50 coiled-coils, and asymmetric Nbs1 binding. To verify the structure, crosslinking mass spectrometry was utilized. A comparison with the human Mre11-Nbs1 complex shows a highly conserved fold and therefor allows to deduce features from one organism to the other. To investigate how MRN integrates the enzymatic and tethering functions, the Rad50 zinc-hook was crystallized, displaying a tetrameric, tethering-competent conformation of an MRN-MRN dimer. Disrupting the multimerization interface leads to severe DSB repair deficiencies. Biochemical characterizations of *Ct*MRN DNA binding properties revealed a novel ATP-independent DNA binding motif in the Mre11 C-terminus, which is probably involved in scanning the genome for DSBs. To clarify the role of the eukaryote specific Nbs1 protein, a MR complex lacking Nbs1 was characterized. Nbs1 contributes to the ATP-independent DNA-binding mode as well as stabilizes and locks MRN in a rigid conformation.

2. Publications

2.1 Molecular basis of human ATM kinase inhibition

Kristina Stakyte*, Matthias Rotheneder*, Katja Lammens*, Joseph D. Bartho*, Ulrich Grädler, Thomas Fuchß, Ulrich Pehl, Aaron Alt, Erik van de Logt, Karl-Peter Hopfner, **Molecular basis of human ATM kinase inhibition**, *Nature Structural and Molecular Biology*, Volume 28, October 2021, Pages 789-798, https://doi.org/10.1038/s41594-021-00654-x

* These authors contributed equally.

Summary

In this publication we solved high resolution cryo-EM structures of the human ATM kinase with two different inhibitors or ATPγS bound. Due to reduced flexibility in the inhibited state, we were able to build a near complete atomic model of ATM in its dimeric form, including the N-terminal solenoid region. This allowed us to assign known cancer mutations to the exact position in the protein and thereby inferring their biological effect. The increased resolution compared to previous publications helped us to identify two zinc-binding sites, contributing to the overall stability of ATM while leaving the kinase activity unaltered. In a structural comparison with other PIKK family members, the specificity of ATM inhibitors KU-55933 and M4076 can be explained on a molecular level: Multiple non-conserved residues in the active centre interact specifically with chemical groups of the respective competitive inhibitor. With this publication, we set the foundation for further structure-guided drug design to target this clinically as well as biologically highly relevant kinase.

Author contributions

I cloned and purified the CtIP fragment which I used to establish and perform *in vitro* ATM kinase assays together with Kristina Stakyte. Kristina Stakyte, Matthias Rotheneder and Aaron Alt established the expression and purification of human ATM. Kristina Stakyte and Matthias Rotheneder purified ATM for biochemical assays and prepared cryo-EM grids. All first authors contributed to cryo-EM data collection and processing. Kristina Stakyte, Matthias Rotheneder, Katja Lammens, Joseph D. Bartho and Karl-Peter Hopfner built the 3D models. Ulrich Grädler and Thomas Fuchß were involved in the development of M4076 at Merck KGaA, Darmstadt, Germany. Thomas Fuchß and Ulrich Pehl contributed further biochemical assay and kinase selectivity results. All authors were involved in data analysis and manuscript preparation.

nature structural & molecular biology

ARTICLES

https://doi.org/10.1038/s41594-021-00654-x

Molecular basis of human ATM kinase inhibition

K. Stakyte[1,4], M. Rotheneder[1,4], K. Lammens[1,4] ✉, J. D. Bartho[1,4], U. Grädler[2], T. Fuchß[2], U. Pehl[2], A. Alt[1,3], E. van de Logt[1] and K. P. Hopfner[1] ✉

Human checkpoint kinase ataxia telangiectasia-mutated (ATM) plays a key role in initiation of the DNA damage response following DNA double-strand breaks. ATM inhibition is a promising approach in cancer therapy, but, so far, detailed insights into the binding modes of known ATM inhibitors have been hampered due to the lack of high-resolution ATM structures. Using cryo-EM, we have determined the structure of human ATM to an overall resolution sufficient to build a near-complete atomic model and identify two hitherto unknown zinc-binding motifs. We determined the structure of the kinase domain bound to ATPγS and to the ATM inhibitors KU-55933 and M4076 at 2.8 Å, 2.8 Å and 3.0 Å resolution, respectively. The mode of action and selectivity of the ATM inhibitors can be explained by structural comparison and provide a framework for structure-based drug design.

Cells rely on an efficient DNA damage response (DDR) to maintain genomic stability. Cancer cells, on the other hand, acquire defects in DDR genes to increase the genomic instability and mutation rate while ensuring cancer cell survival. The DDR comprises complex chains of events that result in the efficient repair of various types of DNA damage, including DNA double-strand breaks (DSBs)[1]. DSBs are a hallmark of cancer and particularly harmful to the cell if left unrepaired. Initiation of the DDR leads to activation of checkpoint responses, cell-cycle arrest, recruitment of the DNA repair machinery and chromatin remodeling[2–4]. Persistent DSBs and DDR trigger cellular senescence or apoptosis, thereby helping to remove potentially abnormal cells. However, misrepaired DSBs can result in gross chromosomal aberrations, aneuploidy or loss of genetic information and are linked to cancer development[1,5–7].

Ataxia telangiectasia-mutated (ATM) is a ~350-kDa Ser/Thr kinase that initiates a DDR following DSB formation. On activation, ATM phosphorylates a multitude of downstream transducers and effector proteins at SQ/TQ motifs. Target proteins include the DSB repair factor CtIP, histone variant H2AX, tumor suppressors BRCA1 and p53, and the checkpoint transducing kinase CHK2[4]. ATM belongs to a family of related surveillance kinases known as phosphatidylinositol 3-kinase-related protein kinases (PIKKs). Members of this kinase family also include ATR, the DNA-dependent protein kinase catalytic subunit (DNA-PKcs), mTOR, SMG1 and TRRAP[8,9]. ATM, ATR and DNA-PKcs monitor the cell for DNA damage by sensing DSBs (ATM and DNA-PKcs) or single-stranded DNA (ssDNA; ATR). SMG1 triggers nonsense-mediated messenger RNA (mRNA) decay. TRRAP is involved in epigenetic control of transcription regulation, while mTOR is part of distinct complexes that regulate metabolism, translation and cell growth[10–13]. PIKKs share a fairly conserved domain structure[14–16]. The N-terminal parts of the polypeptide chains are generally composed of HEAT repeats and form 100–300-kDa α-solenoid structures, which are interaction modules for nucleic acids and/or protein cofactors[17]. The C-terminal region known as FATKIN contains the kinase (KIN) domain along with regulatory domains. The latter are denoted as FAT (FRAP, ATM and TRRAP) domain, PRD (PIKK regulatory domain) and FATC (C-terminal part of the FAT domain). The FAT, PRD and FATC wrap around the kinase, regulating substrate recognition.

Cryo-EM provided the first structures of human ATM along with its fungal homologs at low to medium resolution[16,18–21]. ATM resides in the cell as an autoinhibited dimer in all organisms studied. The FATKIN is tightly associated through a fairly hydrophobic interface and keeps the kinase domains side by side in an inactive state[16,18–21]. The structure of human ATM at 4.7 Å showed how the PRD restricts kinase active site access by acting as a pseudo-substrate[16]. More highly resolved fungal Tel1 (ATM ortholog) structures showed details of the kinase active site[19,21]. They also revealed that Tel1 can bind ATP and possesses a properly folded active site geometry, even in the absence of activating ligands[19,21]. Current models of active site access postulate either ligand-induced conformational changes in the ATM dimer, or a dimer-to-monomer transition[22–24].

Although the DDR is important for genome integrity maintenance of healthy cells, it also helps cancer cells to cope with increasing amounts of replication and genotoxic stress, and to develop resistance against DNA-damaging chemo- and/or radiotherapy, thereby favoring tumor growth and survival[25]. Consequently, targeting of proteins involved in the DDR has shown promising effects in cancer therapy[26,27]. Owing to its prominent role in DDR signaling, ATM represents an auspicious target for drug development, predominately as an anticancer therapeutic. Inhibition of ATM increases the sensitivity of cancer cells to DNA-damaging agents and/or ionizing radiation[28–31]. DSB repair is crucial for the survival of malignant tumor cells, especially under DNA-damaging conditions. Thus, the rationale for transient pharmacological ATM inhibition is to impair DSB repair and maintain the extent of unrepaired tumor DNA damage for several hours so as to drive tumor cells ultimately to cell death[27,32,33]. Moreover, based on genetic and pharmacological evidence, inhibition of ATM kinase activity is considered to ameliorate mutant huntingtin (mHTT) toxicity as a potentially novel clinical intervention to treat Huntington's disease[34]. ATM deficiency or reduced expression levels have been identified as a biomarker of sensitivity for selective poly adenosine diphosphate-ribose polymerase (PARP) or ATR inhibition in the treatment of solid tumors[35–38]. ATM inhibitors in combination with ATR or PARP inhibitors induce synthetic lethality in proliferating cancer cell lines as a result of mitotic

[1]Gene Center, Department of Biochemistry, Ludwig-Maximilians-Universität, Munich, Germany. [2]Merck KGaA, Darmstadt, Germany. [3]Present address: Proteros Biostructures GmbH, Martinsried, Germany. [4]These authors contributed equally: K. Stakyte, M. Rotheneder, K. Lammens, J. D. Bartho. ✉e-mail: klammens@genzentrum.lmu.de; hopfner@genzentrum.lmu.de

replication stress and unrepaired DSBs[39]. Initial high-affinity ATM inhibitors (KU-55933 and CP466722) were identified by compound library screens and served as lead structures for the development of compounds with improved pharmacokinetic properties (KU-60019 and KU-59403)[28,29,40,41]. More recently, next generations of inhibitors (AZ31, AZ32, AZD0156 and AZD1390) with up to subnanomolar half-maximum inhibitory concentration (IC_{50}) potencies and suitable pharmacokinetic profiles were identified, demonstrating preclinical in vivo efficacy in rodent cancer models[42–44]. Both ATM inhibitors, AZD0156 and AZD1390, had been selected to enter clinical trials either in combination with cytotoxic chemotherapy, as well as targeted anticancer agents such as the PARP1/2 inhibitor olaparib (Lynparza, AZD2281) for the treatment of solid tumors, or with radiotherapy in the treatment of brain cancers[43–45]. M4076, a subnanomolar potent, ATP-competitive and orally bioavailable ATM inhibitor with excellent human kinase selectivity and physicochemical and pharmacokinetic properties was developed at Merck KGaA[46]. Currently, M4076 is in a phase I clinical trial for the treatment of cancer (ClinicalTrials.gov ID NCT04882917)[31].

Structure-based approaches are an important source of information for the optimization of selective inhibitors, and progress in the resolution capabilities of cryo-EM has opened up this technique to structure-based drug design[47]. Despite the fact that several cryo-EM structures of eukaryotic ATM/Tel1 have been published, high-resolution structures of human ATM enabling structure-based drug design are not yet available[16,18–21]. In this Article, we use cryo-EM to investigate the detailed binding modes of ATM-specific kinase inhibitors KU-55933 and M4076 comprising chemically diverse scaffolds. We present cryo-EM structures of human ATM in complex with KU-55933, M4076 and the non-hydrolysable ATP analog ATPγS at resolution below 3 Å, permitting the distinct fitting of all three compounds. The protein structures provide a detailed view of the kinase domain and the active site conformation in its inhibited state, and clearly explain the distinct ATM kinase inhibition and selectivity profiles of KU-55933 and M4076 based on their binding modes. The quality of the maps allowed us to generate a near-complete atomic model of human ATM, including the more flexible spiral and pincer domains, where we identified two zinc-binding motifs.

Results

Near-complete atomic structure of human ATM. Human ATM was expressed in Expi293F cells and purified using FLAG affinity followed by anion exchange chromatography. Biochemical analysis indicates that the purified protein is an enzymatically active kinase that is capable of phosphorylating its natural substrate, the C-terminal fragment of human CtIP (Fig. 1a). Basal kinase activity was reduced in the presence of the widely used ATM inhibitor KU-55933 (Fig. 1a). To reduce protein flexibility within the kinase domain of human ATM, we incubated the protein sample with KU-55933 before cryo-EM grid preparation[1]. Consistent with the published human ATM cryo-EM structure, which showed distinct dimeric states, we still observed conformational flexibility in the N-terminal α-solenoid domain, but, in contrast, did not observe conformationally 'open' C-terminal domains or monomers in the micrographs (Extended Data Fig. 1a and Supplementary Video 2)[2]. We reconstructed a full-length human ATM structure by using a 2.8-Å-resolution pincer-FATKIN map in combination with 3.0–3.3-Å maps for the spiral and pincer domains (Supplementary Figs. 1 and 2 and Table 1). The overall domain organization is illustrated in Fig. 1b. The quality of the map enabled us to build full side chain models for all secondary structural elements, along with large parts of the loop regions within the FATKIN and pincer domains. We also corrected the sequence assignments at the N-terminal 1,932 residues of earlier structures that were modeled based on lower-resolution maps (Fig. 1b, insets and Extended Data Fig. 1e)[2,3].

Intriguingly, analysis of the sequence and EM density revealed the presence of a zinc-binding motif in the pincer domain (Fig. 1b, top inset and Supplementary Video 1). This motif also validates a newly assigned registry. The zinc-binding site belongs to the classical Cys2 His2 motif zinc finger type and consists of residues H1876, H1895, C1899 and C1900 in a loop region at the C-terminal end of the pincer domain. The zinc-binding motif is pointing towards the spiral domain, which mediates the recruitment of DNA, binding partners such as NBS1 and substrates such as p53[4,5]. The loop stabilized by this motif contains the important cancer mutation T1880R[48]. Because all four zinc coordinating residues are only conserved in certain mammals, an essential, evolutionarily conserved role of this motif for kinase activity is not likely, but it could play an important function in mammalian-specific regulation and ligand or substrate recognition (Extended Data Fig. 1b)[24]. Mutation of the two zinc coordinating cysteine residues did not diminish kinase activity (Extended Data Fig. 1c). However, addition of zinc-specific chelating agents decreased the thermal stability of the ATM (Extended Data Fig. 1d).

To model the N-terminal α-solenoid structure, this region of the density was processed independently by subtracting the density for the C-terminal domains and the other protomer of the dimer to create a map of the N terminus alone (Supplementary Fig. 2). This workflow permitted classification of the structural variation within the N terminus, resulting in a map with an overall resolution of 3.15 Å that allowed atomic modeling of the N terminus. The map displays defined side chain densities until the two most N-terminal helices and indicates a different sequence assignment than previously published (Fig. 1c). This area is of particular interest because the HEAT repeats are believed to provide an interaction hub for components of the DNA repair machinery, such as NBS1, and substrates like p53[49,50]. In the center of the solenoid structure, the HEAT repeat pattern is broken where the loop (amino acids 549–570) between helices 24 and 25 extends to interact with the FATKIN domain loops (residues 2084–2092 and 2107–2123; Extended Data Fig. 2a,d). We note the direct contact between the N-terminal region of the α-solenoid and the FATKIN domain that was not observed in the previously published human ATM structures. However, the equivalent inter-domain interaction was observed in ctTel1[19]. After this FATKIN interacting loop, three short helices 25–28 break the HEAT repeat pattern in the center of the solenoid ring, followed by the 'plug' loop (residues 630–643) which bridges through the center of the solenoid (Extended Data Fig. 2c). This loop is tethered to the edge of the solenoid in a structure that may represent a second zinc-binding motif (Fig. 1c and Supplementary Video 1). The local resolution is insufficient to resolve all residues with confidence, but the density represents a turn-like structure bringing in close proximity two histidines (H635 and H636) with two cysteines (C633 and C790), with an additional density sufficient for a zinc atom. Helix 29 then sits on the opposite side of the solenoid, running nearly parallel to the junction between the N- and C-terminal sections of the solenoid structure, before loop 657–683 passes back across the bottom of the solenoid ring, connecting to helix 30 on the far outer side of the solenoid (Extended Data Fig. 2c). The solenoid then continues with regular HEAT repeats until the hinge region.

The functionally important Tel1/ATM N-terminal (TAN) motif (residues 15–27) and essential residues 91–97 form a continuous interaction site on the solenoid-facing side of the N terminus[48,49]. The proline and hydrophobic residues within this interaction site are more probably conserved for their role in protein folding rather than for ligand interaction. P37 caps helix 3, while the hydrophobic residues form internal contacts between HEAT repeats. The long, unstructured loop (residues 825–879) interacts with R35 of helix 2, directly neighboring the TAN motif. This loop contains the cancer-associated mutation F858L and may be involved in signal transduction or ligand binding at the N terminus (Extended Data Fig. 3)[48].

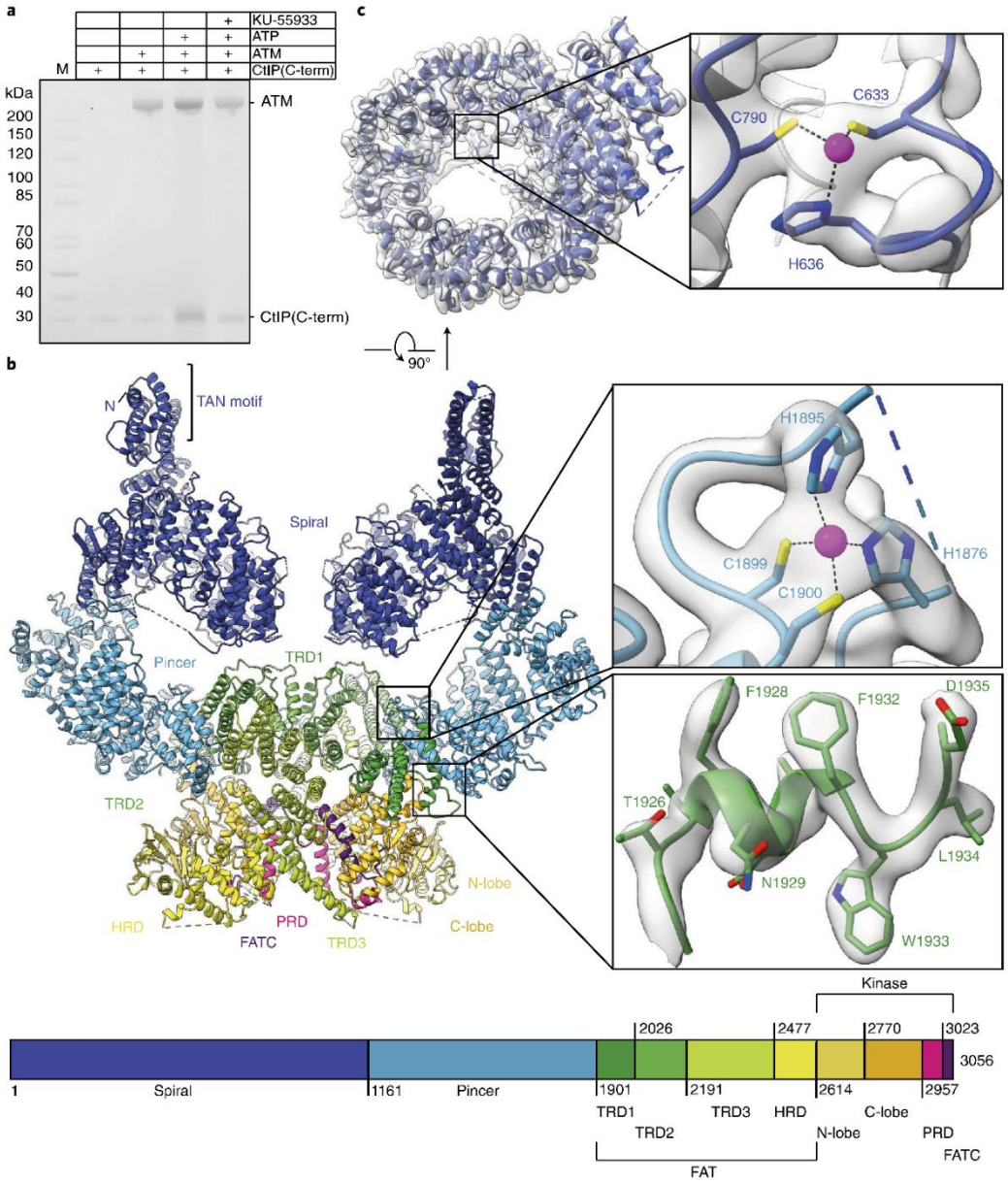

Fig. 1 | Cryo-EM structure and activity of dimeric human ATM. a, Inhibition of basal ATM kinase activity by KU-55933. Phosphorylation of human CtIP C terminus (650–897, phosphomimetic mutant T847E) visualized by phosphoprotein SDS–PAGE staining. The experiment was repeated twice with similar results. The uncropped gel image is available as source data. **b**, Model of KU-55933-bound human ATM. The structural domains are colored according to the schematic shown below the model. This domain color coding will be used throughout this Article. Top inset: pincer zinc-binding motif and map quality in the region. Bottom inset: map quality of the representative region (residues 1926–1935) in TRD1. **c**, Cryo-EM density map of the N-terminal spiral domain at 3.06 Å resolution (contoured at 0.017) with the fitted model in top view. Inset: spiral zinc-binding motif and map quality in the region.

To analyze the orientation of the region N-terminal to the FATKIN domain, we conducted focused three-dimensional (3D) classification on the spiral and pincer domain of all ATM particles (Supplementary Fig. 1). This indicated the presence of three different dimeric classes of ATM (Extended Data Fig. 1a and Supplementary Video 2). The main class, comprising 45% of the particles, belongs to a symmetrically related dimer with a small gap between the two opposing spiral domains, while 31% of the particles show a symmetrically related dimer with the spiral domains in close contact. Only 13% of the data resulted in one flexibly detached spiral domain. The best resolved N-terminal structure with closed spiral domains was refined to a final resolution of 3.41 Å. In addition to the spiral–FATKIN contact described above, we identified a second interface between the spiral domains of the two protomers. The N-terminal inter-domain contact was not seen in other human structures, in which the kinase and FAT domains were exclusively

Table 1 | Cryo-EM data collection and refinement statistics

	#1 ATM (kinase, KU-55933-bound state) (EMD-12343)	#2 ATM (hinge/pincer, KU-55933-bound state) (EMD-12345)	#3 ATM (N-term. spiral/pincer, KU-55933-bound state) (EMD-12346)	#4 ATM (focused N-term. spiral, KU-55933-bound state) (EMD-12347)	#5 ATM (composite map, KU-55933-bound state) (EMD-12351, PDB 7NI5)	#6 ATM (kinase, M4076-bound state) (EMD-12350, PDB 7NI4)	#7 ATM (kinase, ATPγS-bound state) (EMD-12352, PDB 7NI6)
Data collection and processing							
Magnification	130,000	130,000	130,000	130,000	130,000	130,000	130,000
Voltage (kV)	300	300	300	300	300	300	300
Electron exposure (e^-/Å^2)	45	45	45	45	45	45	43
Defocus range (μm)	−1.0 to −2.8	−1.0 to −2.8	−1.0 to −2.8	−1.0 to −2.8	−1.0 to −2.8	−1.0 to −2.8	−1.0 to −2.8
Pixel size (Å)	1.059	1.059	1.059	1.059	1.059	1.059	1.059
Symmetry imposed	*C*1	*C*1	*C*1	*C*1	*C*1	*C*2	*C*1
Initial particle images (no.)	2,679,787	2,679,787	2,679,787	2,679,787	2,679,787	2,346,822	709,013
Final particle images (no.)	826,510	807,127	1,035,906	977,752			
Map resolution (Å)	2.78	3.34	3.10	3.15	Composite Map (#1–4)	3.03	2.78
FSC threshold	0.143	0.143	0.143	0.143		0.143	0.143
Map resolution range (Å)	2.49–8.52	3.14–5.61	2.93–4.71	2.91–4.27		2.57–9.75	2.62–9.75
Refinement							
Initial model used					PDB 6K9L	PDB 7NI5	PDB 7NI5
Model resolution (Å)					2.79	3.3	2.9
FSC threshold					0.5	0.5	0.5
Model resolution range (Å)					2.49–4.27	2.57–4.80	2.62–3.90
Map sharpening *B* factor (Å^2)					0 (LAFTER filtered)	0 (LAFTER filtered)	0 (LAFTER filtered)
Model composition							
Nonhydrogen atoms					45,052	23,236	23,079
Protein residues					5,581	2,864	2,847
Ligands					4 Zn, 2 KU-55933	2 Zn, 2 M4076	2 Zn, 2 Mg, 2 AGS
B factors (Å^2)					22.49/138.51/70.38	59.66/184.03/106.29	24.39/131.44/65.67
Protein					39.77/167.58/48.67	74.15/205.96/78.84	50.79/143.71/69.28
Ligand							
R.m.s. deviations					0.003	0.005	0.003
Bond lengths (Å)					0.500	0.859	0.467
Bond angles (°)							
Validation							
MolProbity score					1.42	1.35	1.15
Clashscore					4.88	6.07	3.60
Poor rotamers (%)					0.02	0.08	0.08
Ramachandran plot							
Favored (%)					97.06	97.95	98.04
Allowed (%)					2.94	2.05	1.96
Disallowed (%)					0.00	0.00	0.00

Different datasets are described.

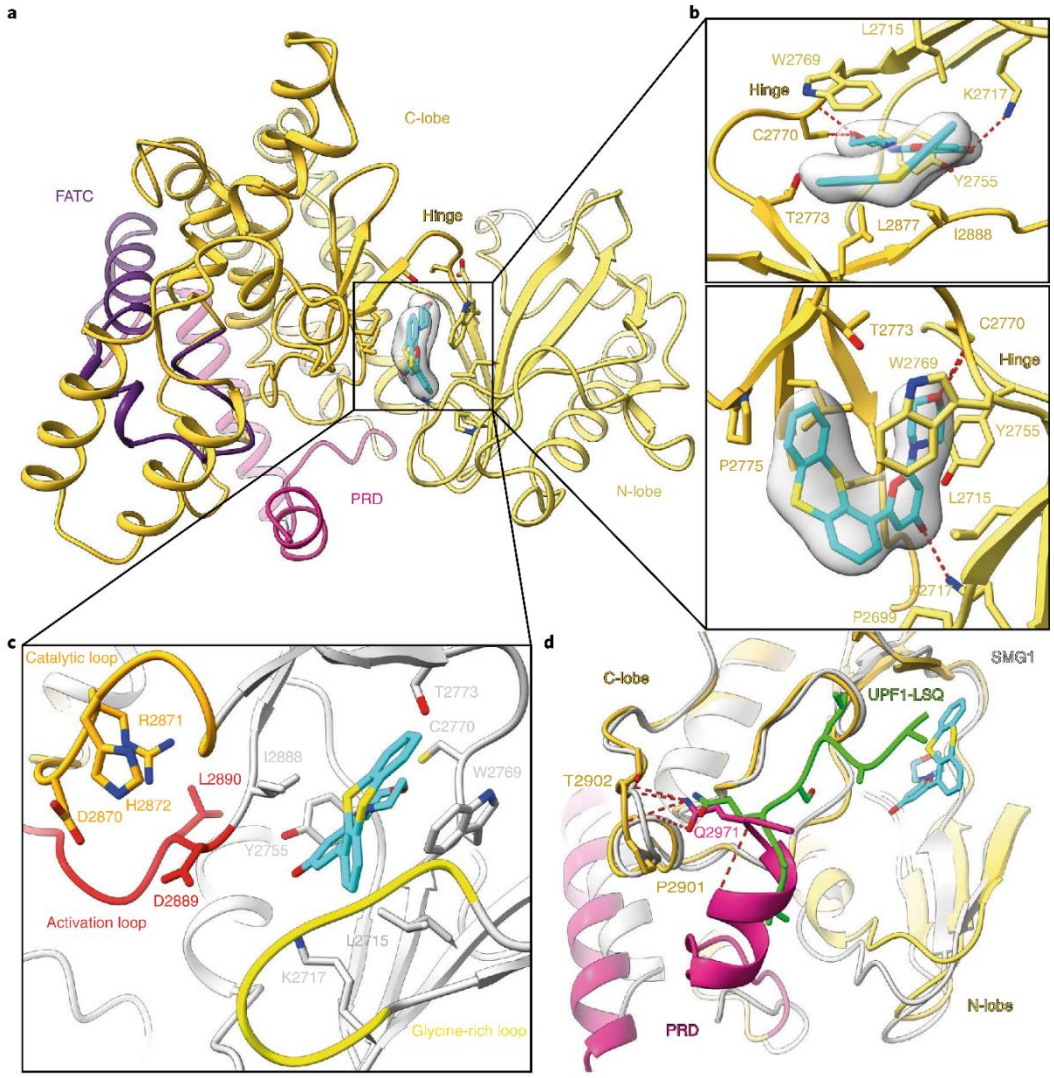

Fig. 2 | Human ATM active site conformation in the KU-55933 bound state. a, KU-55933 (cyan) in 2.8-Å density (contoured at 0.032) bound to the kinase active site. **b**, Detailed binding mode of KU-55933 inhibitor in side and top views. Side chains of inhibitor-proximal residues are shown. Interactions were calculated with ViewContacts and hydrogen bonds are indicated as red dotted lines[57]. **c**, Conformations of the kinase catalytic loop (orange), activation loop (red) and glycine-rich loop (yellow) surrounding the bound inhibitor. **d**, Detailed view of the superimposed substrate-bound (UPF1 substrate in green) SMG1 (PDB ID 6Z3R; gray) and KU-55933-bound ATM (color) kinase domain. Substrate-mimicking Q2971 of PRD (magenta) and its hydrogen bonds (red dotted lines) to the kinase C-lobe residues T2902 and P2901 are indicated.

involved in dimerization[21]. This observation supports the assumption that the inhibitor-bound ATM structure is in a more stable dimeric state (Extended Data Fig. 1a,e). The resolution of the spiral–FATKIN interface loops does not permit unambiguous identification of the interacting residues, but the opposing loops carry charge complementarity, suggesting they may mediate salt bridge formation.

Cancer-associated human ATM mutations. The prevalence of mutations that result in ATM functional deficiency is generally below 5%, but is enhanced for colon adenocarcinoma (11%), cholangiocarcinoma (8.8%) and uterine corpus endometrial carcinoma (6.9%). Other mutations that do not compromise ATM kinase function represent the majority of ATM alterations. (The results published here are in whole or part based upon data generated by the TCGA Research Network at https://www.cancer.gov/tcga.) We mapped the locations of common ATM mutations that were reported more than five times in the COSMIC database (Extended Data Fig. 3)[51]. Although mutations are distributed throughout the entire length of the protein, some mutations cluster in surface regions and may indicate important functional sites. For example, a highly conserved R23, frequently mutated to Q (count of 9), is located in the substrate-binding TAN motif. The very frequent F858L (count of 31) mutation maps to a loop that interacts with the TAN motif, supporting the functional role of this apical region in ATM signaling. R337C/H (count of 93), S707P and S333F (count of 9) mutations affect adjacent solvent-exposed loops of the spiral near the TAN motif, which may be an important interaction site.

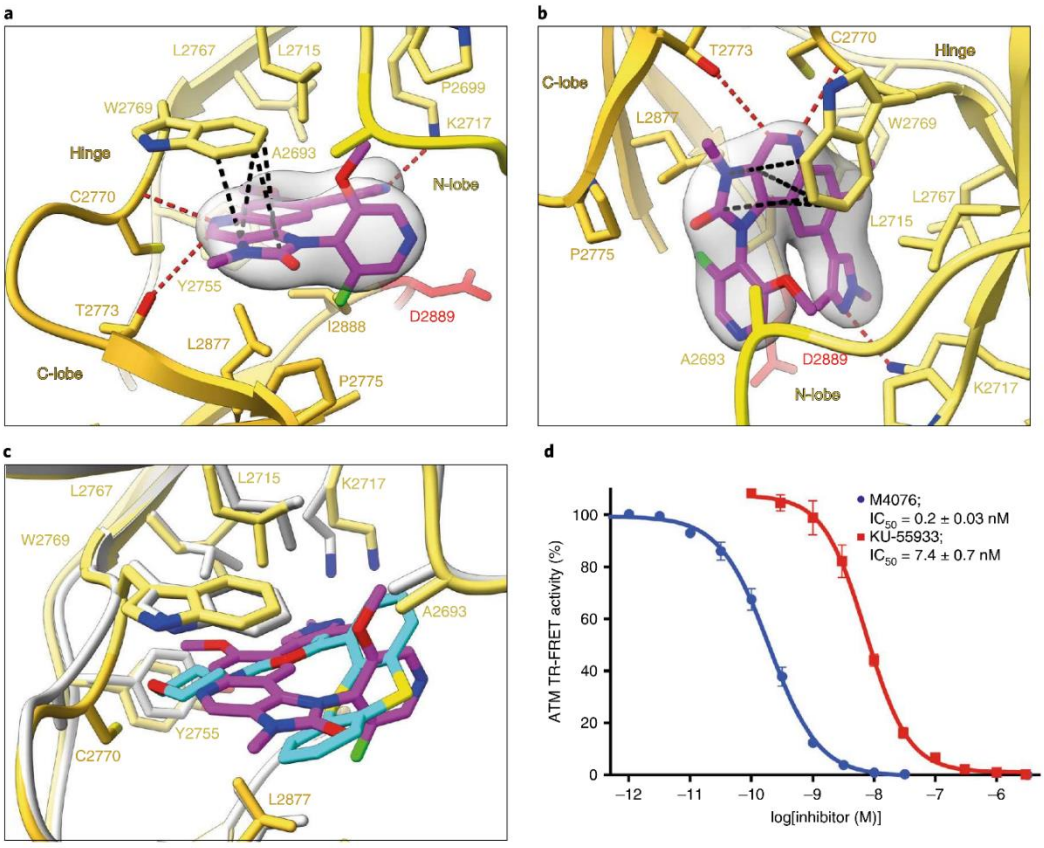

Fig. 3 | Human ATM active site conformation in the M4076-bound state. a, Detailed binding mode of the M4076 inhibitor at a resolution of 3.0 Å (contoured at 0.038). Side chains of inhibitor-proximal residues are shown. Interactions were calculated with ViewContacts[57]. Hydrogen bonds are indicated by red dotted lines and π-stacking interactions are highlighted as black dotted lines. The kinase activation loop is shown in red. **b**, Same as in **a**, but as a side view. **c**, Superimposition of M4076 (magenta, colored model) and KU-55933 (cyan, gray model) bound ATM active sites. **d**, Dose–response curves of enzymatic ATM kinase inhibition by M4076 and KU-55933. Data represent the mean ± s.e.m. from $n = 15$ independent experiments performed in duplicate for M4076 ($IC_{50} = 0.20 \pm 0.03$ nM) and from one experiment performed in duplicate for KU-55933 ($IC_{50} = 7.4 \pm 0.7$ nM). Data for **d** are available as source data.

R337C/H was identified as a 'hotspot' cancer mutation common in colorectal cancer and associated with an ATM loss-of-function phenotype[52]. V410A (count of 20) forms an internal hydrophobic contact with I339 that may influence the stability of the spiral, or may lead to conformational changes. T1880R (count of 7) affects a loop stabilized by the pincer zinc-binding motif and thus could be a substrate/ligand interaction site. Q2442P (count of 7) and R2443Q (count of 21) are located in the helix of the TRD3 that contacts the PRD across a dimer interface. R3008H/C (count of 64) contributes to this interaction from the PRD side. This TRD3–PRD interaction would need to break to enable the conformational change into the open dimer, as reported by Baretic and colleagues[16]. It has been proposed that R3008H substitution impairs the conformational change of PRD-I required for substrate interactions with the catalytic loop[53]. The following disease-associated mutations are located directly within the ATP-binding site: R2691C (count of 11), G2695S (count of 8), R2832C (count of 15), N2875S (count of 8), I2888T (count of 6) and L2890V (count of 7).

ATM active site and KU-55933 binding mode. The overall architecture of the FAT and kinase domains largely resembles the apoenzyme structure reported by Xiao et al. (Extended Data Fig. 4a,c)[22], but the reduced structural flexibility of ATM due to inhibitor binding as compared with the apoenzyme structures allowed for model building of virtually all amino acid side chains in the active site (Extended Data Fig. 4d). Briefly, the catalytic cleft is formed by the N- and C-terminal lobes (N-lobe and C-lobe) which are connected via a hinge region (Fig. 2a). In general, the N-lobe of PIKKs is responsible for nucleotide binding and coordination, and contains the glycine-rich loop (P-loop). The C-lobe of ATM and related kinases includes the catalytic loop with the DRH residues (D2870, R2871, H2872) required for substrate phosphorylation. The catalytic loop is held in place by the activation loop, which contains a DLG motif composed of D2889, L2890 and G2891. This motif plays an important role in substrate recognition and Mg^{2+} coordination, and hence in the regulation of catalysis (Fig. 2c)[54]. In the related kinases DNA-PK, mTOR, ATR and Mec1, the motif consists of DFG, DFN or DFD (see "Understanding of kinase inhibitor selectivity" below). Recently, it was shown that the conserved phenylalanine residue is critical for autoinhibition and activation of Mec1[55]. Mutation to leucine, the amino acid present in ATM and Tel1, leads to a constitutively active Mec1[55]. Consequently, the F-to-L substitution in ATM/Tel1 may explain why no additional activator protein is needed for their basal phosphorylation activity. However, in the

Table 2 | Kinase selectivity of KU-55933 and M4076 inhibitors

Inhibitor	On-target	Primary downstream target	Kinase selectivity						
	ATM IC_{50} (nM)[a]	Cellular pCHK^{Thr68} HCT116 IC_{50} (nM)[b]	DNA-PK IC_{50} (nM)[a]	mTOR IC_{50} (nM)[c]	ATR IC_{50} (nM)[a]	PI3Kα IC_{50} (nM)[a]	PI3Kβ IC_{50} (nM)[a]	PI3Kγ IC_{50} (nM)[a]	PI3Kδ IC_{50} (nM)[a]
KU-55933	7.4	1,100[d]	1,400	9,300[e]	>100,000[e]	2,000	1,900	14,000	1,500
M4076	0.2	10[f]	600	>30,000[c,g]	10,000[a]	8,500[g]	>30,000[g]	>30,000[g]	15,000[g]

Shown are KU-55933 and M4076 biochemical IC_{50} values against kinases ATM, DNA-PK, mTOR, ATR and PI3Ks and cellular IC_{50} values for inhibition of bleomycin- or 2 Gy-induced phosphorylation of CHK2 (pThr68) in HCT116 cells. Source data for Table 2 are presented in Supplementary Data 1. [a]Determined by time-resolved FRET assays with recombinant proteins. [b]In vitro cell-based IC_{50} for inhibition of bleomycin- or 2 Gy-induced phosphorylation of CHK2 (pThr68) in the human colon carcinoma cell line HCT116. [c]Determined by enzymatic mTOR assay. [e]ELISA, bleomycin-induced. [a]As determined by Hicksson et al.[40]. [f]Luminex assay, 2 Gy-induced (Methods). [g]IC_{50} obtained for racemate of M4076.

KU-55933 complex structure, the PRD blocks active site access, as seen in other ATM/Tel1 structures, confirming the autoinhibitory function of the ATM PRD domain in the inhibitor-bound form[19,21]. The PRD is firmly locked in position by interactions with the activation loop of the kinase via hydrogen-bond interactions of Q2971 with the backbone oxygens of P2901 and T2902 and hydrophobic contacts of L2970 (Fig. 2d). Superimposition with the substrate-bound SMG1-8-9 kinase UPF-1 complex structure shows that residue Q2971 occupies the substrate glutamine binding site of the kinase, thus mimicking the glutamine in the substrate SQ/TQ selectivity motifs and precluding substrate access to the catalytic center (Fig. 2d)[19,21,56]. Sequence alignment of the PRD region indicates that the substrate-mimicking inhibitory mechanism is conserved among most ATM orthologs (Extended Data Fig. 4b). Combined structural and sequence analysis of the human ATM C terminus with other human PIKKs suggests that DNA-PK may use a similar substrate-mimicking mechanism. However, the map quality of the other kinases, as well as the low level of sequence conservation in this region, precludes more definitive statements regarding a conserved PRD inhibition mechanism for other PIKK family members (Extended Data Fig. 4b).

A more detailed comparison of the KU-55933-bound and apoenzyme structures reveals that the ATM kinase N-lobe is shifted outwards to accommodate the inhibitor (Extended Data Fig. 4c). KU-55933 is well ordered, which facilitates fitting of the small-molecule inhibitor and all interacting residues within this area (Fig. 2b and Extended Data Fig. 4d). The chemical description of the inhibitor is shown in Extended Data Fig. 4e. KU-55933 forms two distinct hydrogen bonds via the morpholine O atom with C2770 of the hinge region and via the pyran-4-one carbonyl O atom with the catalytically important residue K2717 in the N-lobe (Fig. 2b,c). The non-planar thianthrene ring is involved in extensive van der Waals (vdW) contacts with residues P2699 in the P-loop, L2715, L2767, W2769 in the N-lobe, P2775, L2877 and I2888 in the C-lobe and activation loop, respectively (Extended Data Fig. 4f). We next examined the binding and inhibitory mechanism of a second inhibitor, M4076, with a chemically distinct scaffold to KU-55933.

Towards a more selective and potent ATM inhibitor. KU-55933 is a potent ATM inhibitor (IC_{50} = 7.4 nM) with selectivity towards ATR, mTOR (IC_{50} values above 10 μM) and other kinases, but with residual micromolar potencies on DNA-PK (IC_{50} = 1.4 μM), phosphoinositide 3-kinase (PIK3) isoforms α, β and δ (IC_{50} values ~2 μM) and PI3Kγ (IC_{50} = 14 μM) corresponding to IC_{50} splits above 180-fold towards ATM (Fig. 3d, Table 2 and Extended Data Figs. 5d and 6f)[40]. The ATM inhibitor M4076 is a result of advanced optimization efforts that led to the identification of a candidate drug being evaluated in a phase I trial[31]. In comparison to KU-55933, M4076 is a potent, subnanomolar ATM kinase inhibitor (IC_{50} = 0.2 nM) with strong enzymatic selectivity against ATM's close kinase family members, that is, ~3,000-fold selectivity towards DNA-PK (IC_{50} = 600 nM) and more than 40,000-fold selectivity towards ATR, mTOR and PIK3 isoforms α, β, γ and δ (IC_{50} values above 8.5 μM) (Fig. 3d, Table 2 and Extended Data Figs. 5d and 6c–e). Broader kinase profiling of M4076 revealed a strong overall human kinome selectivity. In a panel of 583 human kinases, no interaction had been observed below an IC_{50} of ~700-fold compared to the on-target enzymatic ATM IC_{50} of 0.2 nM for M4076 (Extended Data Fig. 6g,h and Supplementary Notes)[42,43]. M4076 also showed low nanomolar cellular inhibition of checkpoint kinase 2 (CHK2) Thr68 phosphorylation in HCT116 cells (IC_{50} = 10 nM) as the primary downstream target of ATM, while KU-55933 was only weakly potent (IC_{50} = 1,100 nM) in this readout (Extended Data Fig. 6a,b).

To understand the enhanced biochemical ATM potency of M4076, we determined the cryo-EM structure of human ATM in complex with M4076 to 3.0 Å resolution in the kinase domain (Fig. 3a,b and Extended Data Fig. 5c). Before solving the structure, the inhibitory effect on the purified human ATM sample was verified by a CtIP kinase assay (Extended Data Fig. 5a). The EM density allowed clear binding mode assignment of the inhibitor in the ATM active site cleft. The chemical description of the inhibitor is provided in Extended Data Fig. 5b. The 1,3-dihydro-imidazo[4,5-*c*]quinolin-2-one moiety binds towards the hinge region, indicating a classical hydrogen bond between the N5 atom and C2770, as well as non-classical hydrogen bonds of the 4-CH group to C2770 and T2773 (Fig. 3a,b). Remarkably, the imidazolone ring forms extensive π–π and amide–π stacking interactions towards the W2769 side chain of the hinge region (Fig. 3a,b), as calculated from the atomic coordinates by the software tool ViewContacts[57]. The 7-methoxy group attached to the quinoline ring interacts with the gatekeeper residue L2767 and with L2715 via vdW contacts (Extended Data Fig. 5c). The M4076 1,3-dimethyl-1*H*-pyrazole substituent is in vdW contact with I2888 next to the DLG motif of the activation loop and in hydrogen bond distance to K2717 via the unsubstituted N atom. Cryo-EM density fitting of the 3-fluoro-5-methoxypyridine ring was based on the S_a atropisomeric configuration of this moiety identified by small-molecule X-ray crystallography of M4076[46]. In this orientation, the 3-fluoro-5-methoxypyridine ring indicates vdW contacts of the fluorine atom with P2775 and L2877 on one side and of the methoxy group towards W2769 and A2693 on the other side (Extended Data Fig. 5c).

Understanding of kinase inhibitor selectivity. To understand the inhibitory mechanism and to compare the inhibited structure with the catalytic states of ATM, we also determined the cryo-EM structure of human ATM bound to the non-hydrolysable ATP analog ATPγS to a resolution of 2.8 Å (Extended Data Fig. 7c,d,h). Structural superimposition of all three human ATM structures in complex with compounds KU-55933, M4076 and ATPγS indicate a similar overall ATM conformation, including N-terminal domains, and an almost identical active site cleft geometry (Supplementary Video 3 and Extended Data Figs. 7 and 8). However, one major conformational difference involves residue C2770 of the hinge region, which is shifted by 1.2 Å based on αC-atom distance

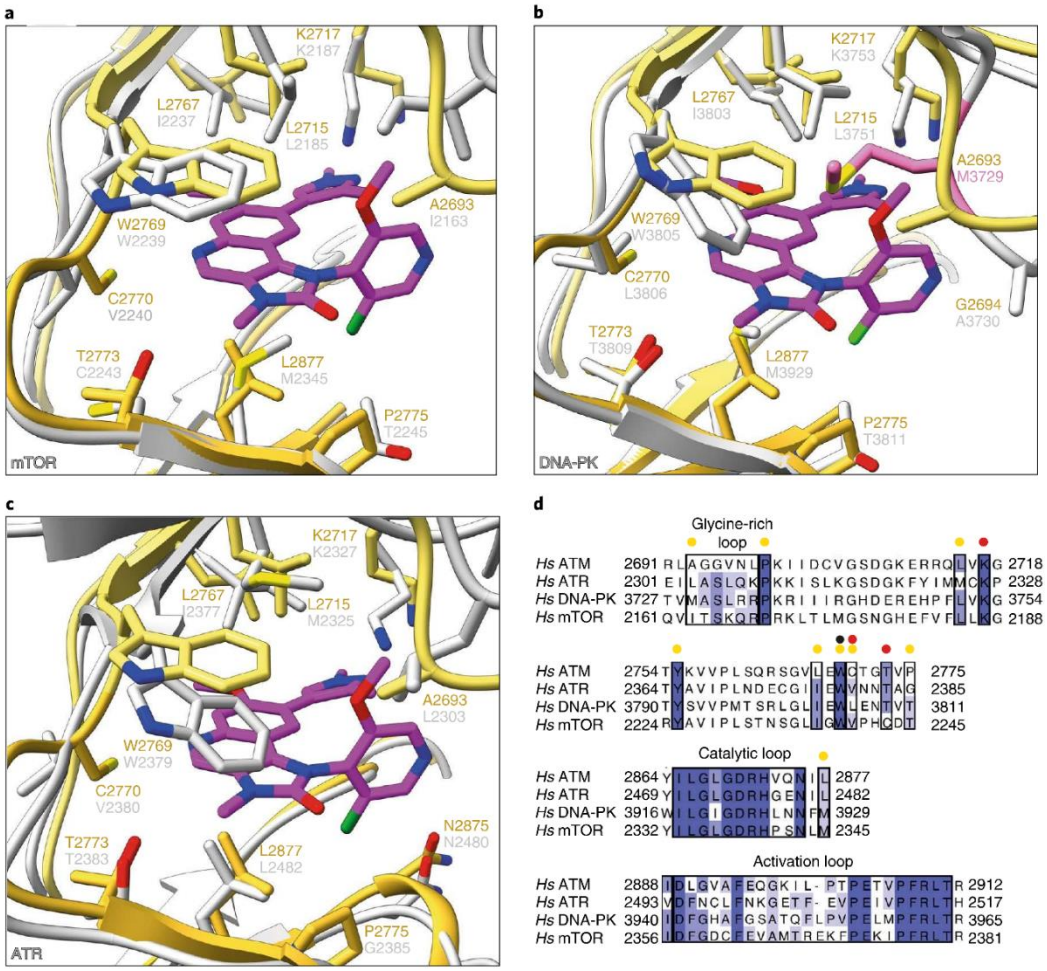

Fig. 4 | Specificity of the inhibitor M4076 towards human ATM kinase over other PIKKs. a, Superimposition of the M4076-bound human ATM active site (color) and apo human mTOR (PDB 4JSN; gray). Residues surrounding the inhibitor are labeled accordingly. **b**, Same as in **a** but with apo DNA-PK (PDB 6ZFP; gray). DNA-PK M3729 is shown in pink. **c**, Same as in **a** but with apo ATR (PDB 5YZ0; gray). **d**, Sequence alignment of the human (*Hs*) ATM, ATR, DNA-PK and mTOR active sites, colored by conservation. Glycine-rich, catalytic and activation loops are labeled. ATM residues forming hydrogen interactions with the inhibitor are marked with red circles, vdW interactions with yellow circles and π-stacking interactions with a black circle.

and 2.2 Å based on the S-atom distance towards the nucleotide binding site in the M4076 and ATPγS structures. This shift is induced by hydrogen bond formation between the C2770 backbone amide NH donor and the 1,3-dihydro-imidazo[4,5-*c*]quinolin-2-one N5 atom of M4076 or with the ATPγS N1 atom, respectively (Fig. 3a and Extended Data Fig. 7c,e,g). Furthermore, the 1,3-dihydro-imidazo[4,5-*c*]quinolin-2-one ring of M4076 overlaps well with the position of the purine ring in the ATPγS structure, creating additional aromatic stacking interactions to the adjacent W2769. The induced fit observed for C2770 together with π–π and amide–π stacking interactions towards the hinge tryptophane might explain the ~35-fold improved biochemical ATM potency as well as the improved selectivity of M4076 towards DNA-PK compared with KU-55933 (Extended Data Fig. 5d). Thus, M4076 perfectly mimics the ATPγS-bound pre-catalysis state of human ATM. Moreover, M4076 adopts additional vdW contacts to the C-lobe and the glycine-rich loop via both the 1,3-dimethyl-1*H*-pyrazole and 3-fluoro-5-methoxypyridine substituents, respectively. Another structural difference exclusively seen in the M4076-bound protein structure is an altered side chain rotamer of residue L2767 to accommodate the 7-methoxy substituent (Fig. 3c).

Structural analysis together with sequence alignment revealed several residues involved in M4076 binding interactions, which are not conserved within the structurally most related kinases ATR, mTOR, DNA-PK and PI3K isoforms: A2693, L2715, L2767, C2770, T2773, P2775 and L2877 (Fig. 4a–d and Extended Data Fig. 6i). The superimposition of ATM cryo-EM structures in complex with KU-55933 and M4076 shows overall similar conformations of these non-conserved residues with few exceptions, including L2767 and C2770 (Fig. 3c). Structural comparison of the M4076-bound ATM with the apoenzyme structures of mTOR, DNA-PK and ATR uncover a rational basis to understand the high selectivity of this inhibitor (Fig. 4a–c). These overlays highlight an important role of the M4076-specific 5-methoxypyridine group in selectivity, which is in vdW contact with A2693 in ATM[58]. This alanine is replaced by the bulkier residues isoleucine, methionine and leucine in mTOR, DNA-PK/PI3Ks and ATR, respectively (Fig. 4a–d and Extended Data Fig. 6i). These larger amino acids might sterically hinder the scaffold of M4076 to obtain an optimal binding position towards

π–π stacking interactions with W2769 as well as hydrogen-bond interactions with C2770 in the hinge region. Sequence variations impairing optimal hinge-binding interactions are also in line with the observed M4076 selectivity against PI3K isoforms, because both W2769 and C2770 are replaced by valines (PIK3α, β and δ) or isoleucine (PIK3γ) and valine, respectively. Additional contributions towards DNA-PK, mTOR and ATR selectivity might be due to second shell residues in ATM (I2701, R2713 and T2771) influencing W2769 side chain flexibility, which are different in DNA-PK (R3737, P3749, E3807), mTOR (K2171, V2183, P2241) and ATR (K2311, I2323, N2381). Finally, residue L2877 below the inhibitor in the C-lobe region is in vdW contact with the imidazolone ring of M4076. This leucine is conserved in ATR but replaced with methionine in DNA-PK, mTOR and PI3Ks, leaving less space for the inhibitor in these kinases.

Discussion

As a key regulator, nuclear ATM kinase orchestrates cellular responses to DNA DSBs. Inhibition of ATM activity sensitizes different tumors to DNA DSB-inducing cancer treatments, such as chemo- and radiotherapy as well as targeted therapies (PARP or ATR inhibition), thereby impeding the ability of cancer cells to evade anticancer therapies[25,32,35,37,59]. A compelling medical need thus exists for the development of ATM inhibitors for anticancer therapies, prompting us to focus on structural studies of ATM. We provide three cryo-EM structures of the human ATM kinase with bound inhibitors and ATPγS. These structures reveal modes of action of small-molecule inhibition of ATM in therapeutic approaches, but also details of kinase active site autoinhibition, as well as an internal pseudo-substrate glutamine in human ATM. The increased conformational rigidity in the inhibited state allowed for atomic modeling of the nearly complete ATM protein. Careful evaluation of the spiral and pincer domain conformations of the KU-55933 inhibitor-bound ATM structure resulted in a cryo-EM density that allowed for a thorough model building of the entire solenoid region. This revealed—unexpectedly—two zinc-binding motifs in the spiral and pincer domains, respectively. These motifs are partially conserved in mammals and appear to either stabilize ATM or be involved in the interaction with other binding partners and/or DNA. Recently, a related zinc-finger motif was discovered in the N-terminal HEAT domain of $Mec1^{ATR}$ checkpoint kinase, which is involved in stabilization of the interface area with the $Mec1^{ATR}$ integral partner $Ddc2^{ATRIP}$ (ref. [55]). In all three structures, the PRD blocks the active site access, confirming the autoinhibitory function of this domain[19,21]. Thereby, the PRD gatekeeper helix is locked in its position by interaction of Q2971 with the activation loop. Overall, the active site cleft geometry of the presented ATM structures is nearly identical except for the hinge region residue C2770 and minor changes in the glycine-rich loop (P-loop) region (Extended Data Fig. 7 and Supplementary Video 3). Together, structures with the bound small-molecule inhibitors uncover the binding mechanisms of two different ATM inhibitor classes and provide further insights into the understanding of their selectivity profiles.

High-resolution ATM structures were not available at the time of discovery of the ATM inhibitor M4076, detailed insights into the binding modalities as well as selectivity determinants towards closely related kinases remained hypothetical[31]. The presented high-resolution cryo-EM structure of ATM now allows detailed insights into the binding mode of M4076. In this regard, we identified extensive π–π and amide–π stacking interactions between the central 1,3-dihydro-imidazo[4,5-*c*]quinolin-2-one scaffold of M4076 towards W2769 in the hinge region of ATM, which are not present in the complex with KU-55933 (Fig. 3a–c). A second major difference between the ATM structures of both inhibitors is the position of C2770, also in the hinge region, which is shifted towards the 1,3-dihydro-imidazo[4,5-*c*]quinolin-2-one moiety of M4076 with respect to the morpholine ring of KU-55933 (Fig. 3c and Supplementary Video 3). The same shifted position of C2770 was observed in the ATM structure with ATPγS, which is considered to correspond to the pre-catalytic state of ATM (Extended Data Fig. 7g). In comparison to KU-55933, M4076 forms additional vdW contacts within the ATP site via its 7-methoxy group as well as with the 3-fluoro-5-methoxypyridine substituent. Together, these additional contacts explain the ~35-fold stronger enzymatic ATM potency of M4076 compared to KU-55933. The enhanced ATM inhibitory potency of M4076 observed in vitro translates well into the in cellulo inhibition of CHK2 phosphorylation at low nanomolar concentrations in HCT116 cells. We note that this inhibitory effect on cellular CHK2 phosphorylation is ~100-fold increased with M4076 compared with KU-55933. Additionally, we identified several non-conserved ATM residues involved in M4076 binding interactions by structural comparison with the DNA-PK, mTOR, ATR and PI3K isoforms. These sequence differences include residues in direct contact with M4076, such as A2693, and in the case of PI3K isoforms also W2769 and C2770. Further sequence differences involve residues in the second shell around W2769, thereby affecting its side chain flexibility to adopt optimal π-stacking interactions with the inhibitor (Fig. 4d and Extended Data Fig. 6i). In this respect, the substitution of A2693 in ATM by bulkier residues in DNA-PK, mTOR, ATR and PI3Ks is considered to be a crucial factor that explains the observed selectivity profile of M4076 towards these closely related kinase family proteins (Table 2).

Taken together, our atomic models of human ATM provide a framework for the evaluation and development of highly specific and potent therapeutics, as well as analyzing the central role and function of human ATM in healthy and cancerogenic cells through structure-informed approaches.

Online content

Any methods, additional references, Nature Research reporting summaries, source data, extended data, supplementary information, acknowledgements, peer review information; details of author contributions and competing interests; and statements of data and code availability are available at https://doi.org/10.1038/s41594-021-00654-x.

Received: 3 February 2021; Accepted: 30 July 2021;
Published online: 23 September 2021

References

1. Hoeijmakers, J. H. Genome maintenance mechanisms for preventing cancer. *Nature* **411**, 366–374 (2001).
2. Matsuoka, S. et al. ATM and ATR substrate analysis reveals extensive protein networks responsive to DNA damage. *Science* **316**, 1160–1166 (2007).
3. Bartek, J. & Lukas, J. Chk1 and Chk2 kinases in checkpoint control and cancer. *Cancer Cell* **3**, 421–429 (2003).
4. Burma, S., Chen, B. P., Murphy, M., Kurimasa, A. & Chen, D. J. ATM phosphorylates histone H2AX in response to DNA double-strand breaks. *J. Biol. Chem.* **276**, 42462–42467 (2001).
5. Roos, W. P. & Kaina, B. DNA damage-induced cell death: from specific DNA lesions to the DNA damage response and apoptosis. *Cancer Lett.* **332**, 237–248 (2013).
6. Mills, K. D., Ferguson, D. O. & Alt, F. W. The role of DNA breaks in genomic instability and tumorigenesis. *Immunol. Rev.* **194**, 77–95 (2003).
7. Kastan, M. B. & Bartek, J. Cell-cycle checkpoints and cancer. *Nature* **432**, 316–323 (2004).
8. Lovejoy, C. A. & Cortez, D. Common mechanisms of PIKK regulation. *DNA Repair (Amst.)* **8**, 1004–1008 (2009).
9. Keith, C. T. & Schreiber, S. L. PIK-related kinases: DNA repair, recombination and cell cycle checkpoints. *Science* **270**, 50–51 (1995).
10. Shiloh, Y. & Ziv, Y. The ATM protein kinase: regulating the cellular response to genotoxic stress, and more. *Nat. Rev. Mol. Cell Biol.* **14**, 197–210 (2013).
11. Zou, L. & Elledge, S. J. Sensing DNA damage through ATRIP recognition of RPA–ssDNA complexes. *Science* **300**, 1542–1548 (2003).

12. Yamashita, A., Ohnishi, T., Kashima, I., Taya, Y. & Ohno, S. Human SMG-1, a novel phosphatidylinositol 3-kinase-related protein kinase, associates with components of the mRNA surveillance complex and is involved in the regulation of nonsense-mediated mRNA decay. *Genes Dev.* **15**, 2215–2228 (2001).
13. McMahon, S. B., Van Buskirk, H. A., Dugan, K. A., Copeland, T. D. & Cole, M. D. The novel ATM-related protein TRRAP is an essential cofactor for the c-Myc and E2F oncoproteins. *Cell* **94**, 363–374 (1998).
14. Yang, H. et al. mTOR kinase structure, mechanism and regulation. *Nature* **497**, 217–223 (2013).
15. Imseng, S., Aylett, C. H. & Maier, T. Architecture and activation of phosphatidylinositol 3-kinase related kinases. *Curr. Opin. Struct. Biol.* **49**, 177–189 (2018).
16. Baretic, D. et al. Structures of closed and open conformations of dimeric human ATM. *Sci. Adv.* **3**, e1700933 (2017).
17. Baretic, D. & Williams, R. L. PIKKs—the solenoid nest where partners and kinases meet. *Curr. Opin. Struct. Biol.* **29**, 134–142 (2014).
18. Sawicka, M. et al. The dimeric architecture of checkpoint kinases Mec1ATR and Tel1ATM reveal a common structural organization. *J. Biol. Chem.* **291**, 13436–13447 (2016).
19. Jansma, M. et al. Near-complete structure and model of Tel1ATM from *Chaetomium thermophilum* reveals a robust autoinhibited ATP state. *Structure* **28**, 83–95 (2020).
20. Xin, J. et al. Structural basis of allosteric regulation of Tel1/ATM kinase. *Cell Res.* **29**, 655–665 (2019).
21. Yates, L. A. et al. Cryo-EM structure of nucleotide-bound Tel1(ATM) unravels the molecular basis of inhibition and structural rationale for disease-associated mutations. *Structure* **28**, 96–104 (2020).
22. Xiao, J. et al. Structural insights into the activation of ATM kinase. *Cell Res.* **29**, 683–685 (2019).
23. Bakkenist, C. J. & Kastan, M. B. DNA damage activates ATM through intermolecular autophosphorylation and dimer dissociation. *Nature* **421**, 499–506 (2003).
24. Guo, Z., Kozlov, S., Lavin, M. F., Person, M. D. & Paull, T. T. ATM activation by oxidative stress. *Science* **330**, 517–521 (2010).
25. Lavin, M. F. & Yeo, A. J. Clinical potential of ATM inhibitors. *Mutat. Res.* **821**, 111695 (2020).
26. Jin, M. H. & Oh, D. Y. ATM in DNA repair in cancer. *Pharmacol. Ther.* **203**, 107391 (2019).
27. Weber, A. M. & Ryan, A. J. ATM and ATR as therapeutic targets in cancer. *Pharmacol. Ther.* **149**, 124–138 (2015).
28. Rainey, M. D., Charlton, M. E., Stanton, R. V. & Kastan, M. B. Transient inhibition of ATM kinase is sufficient to enhance cellular sensitivity to ionizing radiation. *Cancer Res.* **68**, 7466–7474 (2008).
29. Batey, M. A. et al. Preclinical evaluation of a novel ATM inhibitor, KU59403, in vitro and in vivo in p53 functional and dysfunctional models of human cancer. *Mol. Cancer Ther.* **12**, 959–967 (2013).
30. Riches, L. C. et al. Pharmacology of the ATM inhibitor AZD0156: potentiation of irradiation and olaparib responses preclinically. *Mol. Cancer Ther.* **19**, 13–25 (2020).
31. Fuchss, T. et al. Abstract 3500: highly potent and selective ATM kinase inhibitor M4076: a clinical candidate drug with strong anti-tumor activity in combination therapies. *Cancer Res.* **79**, 3500 (2019).
32. Choi, M., Kipps, T. & Kurzrock, R. ATM mutations in cancer: therapeutic implications. *Mol. Cancer Ther.* **15**, 1781–1791 (2016).
33. Dohmen, A. J. C. et al. Identification of a novel ATM inhibitor with cancer cell specific radiosensitization activity. *Oncotarget* **8**, 73925–73937 (2017).
34. Toledo-Sherman, L. et al. Optimization of potent and selective ataxia telangiectasia-mutated inhibitors suitable for a proof-of-concept study in Huntington's disease models. *J. Med. Chem.* **62**, 2988–3008 (2019).
35. Min, A. et al. AZD6738, a novel oral inhibitor of ATR, induces synthetic lethality with ATM deficiency in gastric cancer cells. *Mol. Cancer Ther.* **16**, 566–577 (2017).
36. Perkhofer, L. et al. ATM deficiency generating genomic instability sensitizes pancreatic ductal adenocarcinoma cells to therapy-induced DNA damage. *Cancer Res.* **77**, 5576–5590 (2017).
37. Schmitt, A. et al. ATM deficiency is associated with sensitivity to PARP1- and ATR inhibitors in lung adenocarcinoma. *Cancer Res.* **77**, 3040–3056 (2017).
38. Weston, V. J. et al. The PARP inhibitor olaparib induces significant killing of ATM-deficient lymphoid tumor cells in vitro and in vivo. *Blood* **116**, 4578–4587 (2010).
39. Kantidze, O. L., Velichko, A. K., Luzhin, A. V., Petrova, N. V. & Razin, S. V. Synthetically lethal interactions of ATM, ATR and DNA-PKcs. *Trends Cancer* **4**, 755–768 (2018).
40. Hickson, I. et al. Identification and characterization of a novel and specific inhibitor of the ataxia-telangiectasia mutated kinase ATM. *Cancer Res.* **64**, 9152–9159 (2004).
41. Golding, S. E. et al. Improved ATM kinase inhibitor KU-60019 radiosensitizes glioma cells, compromises insulin, AKT and ERK prosurvival signaling, and inhibits migration and invasion. *Mol. Cancer Ther.* **8**, 2894–2902 (2009).
42. Karlin, J. et al. Orally bioavailable and blood–brain barrier-penetrating ATM inhibitor (AZ32) radiosensitizes intracranial gliomas in mice. *Mol. Cancer Ther.* **17**, 1637–1647 (2018).
43. Pike, K. G. et al. The identification of potent, selective and orally available inhibitors of ataxiatelangiectasia mutated (ATM) kinase: the discovery of AZD0156(8-{6-[3-(dimethylamino)propoxy]pyridin-3-yl}-3-methyl-1-(tetrahydro-2*H*-pyran-4-yl)-1,3-dihydro-2*H*-imidazo[4,5-*c*]quinolin-2-one). *J. Med. Chem.* **61**, 3823–3841 (2018).
44. Durant, S. T. et al. The brain-penetrant clinical ATM inhibitor AZD1390 radiosensitizes and improves survival of preclinical brain tumor models. *Sci. Adv.* **4**, eaat1719 (2018).
45. Morgado-Palacin, I. et al. Targeting the kinase activities of ATR and ATM exhibits antitumoral activity in mouse models of MLL-rearranged AML. *Sci. Signal.* **9**, ra91 (2016).
46. Fuchss, T., Becker, A., Kubas, H. & Graedler, U. Imidazolonylquinoline compounds and therapeutic uses thereof. WO patent 2020/193660 (2020).
47. Boland, A., Chang, L. & Barford, D. The potential of cryo-electron microscopy for structure-based drug design. *Essays Biochem.* **61**, 543–560 (2017).
48. Seidel, J. J., Anderson, C. M. & Blackburn, E. H. A novel Tel1/ATM N-terminal motif, TAN, is essential for telomere length maintenance and a DNA damage response. *Mol. Cell. Biol.* **28**, 5736–5746 (2008).
49. Fernandes, N. et al. DNA damage-induced association of ATM with its target proteins requires a protein interaction domain in the N terminus of ATM. *J. Biol. Chem.* **280**, 15158–15164 (2005).
50. Falck, J., Coates, J. & Jackson, S. P. Conserved modes of recruitment of ATM, ATR and DNA-PKcs to sites of DNA damage. *Nature* **434**, 605–611 (2005).
51. Tate, J. G. et al. COSMIC: the Catalogue Of Somatic Mutations In Cancer. *Nucleic Acids Res.* **47**, D941–D947 (2019).
52. Weber, A. M. et al. Phenotypic consequences of somatic mutations in the ataxia-telangiectasia mutated gene in non-small cell lung cancer. *Oncotarget* **7**, 60807–60822 (2016).
53. Milanovic, M. et al. The cancer-associated ATM R3008H mutation reveals the link between ATM activation and its exchange. *Cancer Res.* **81**, 426–437 (2020).
54. Vivek, M., & Dunbrack, R. L. Defining a new nomenclature for the structures of active and inactive kinases. *Proc. Natl Acad. Sci. USA* **116**, 6818–6827 (2019).
55. Tannous, E. A., Yates, L. A., Zhang, X. & Burgers, P. M. Mechanism of auto-inhibition and activation of Mec1(ATR) checkpoint kinase. *Nat. Struct. Mol. Biol.* **28**, 50–61 (2021).
56. Langer, L. M., Gat, Y., Bonneau, F. & Conti, E. Structure of substrate-bound SMG1-8-9 kinase complex reveals molecular basis for phosphorylation specificity. *eLife* **9**, e57127 (2020).
57. Kuhn, B., Fuchs, J. E., Reutlinger, M., Stahl, M. & Taylor, N. R. Rationalizing tight ligand binding through cooperative interaction networks. *J. Chem. Inf. Model.* **51**, 3180–3198 (2011).
58. Chaplin, A. K. et al. Dimers of DNA-PK create a stage for DNA double-strand break repair. *Nat. Struct. Mol. Biol.* **28**, 13–19 (2021).
59. Armstrong, S. A., Schultz, C. W., Azimi-Sadjadi, A., Brody, J. R. & Pishvaian, M. J. ATM dysfunction in pancreatic adenocarcinoma and associated therapeutic implications. *Mol. Cancer Ther.* **18**, 1899–1908 (2019).

Methods

Expression of human ATM. The pCDNA3.1 vector containing the full-length (1–3056) human ATM gene was ordered from GenScript. Human ATM was designed to comprise an N-terminal FLAG tag (MDYKDDDDK) and codons optimized for protein expression in mammalian cells.

DNA required for transfections was obtained using GigaKit (Macherey-Nagel) and eluted in sterile deionized water. Human ATM was expressed in Expi293F cells (Thermo Fisher Scientific, A14527), as described previously[16].

Human ATM purification. Cell pellet from 500 ml of transfected Expi293F culture was resuspended in 50 ml of pre-cooled buffer A (50 mM HEPES (pH 7.5, 23 °C), 150 mM NaCl, 100 mM L-arginine, 5% (vol/vol) glycerol) supplemented with one tablet of EDTA-free protease inhibitor cocktail (Sigma-Aldrich) and 10 U of TURBO DNase (Thermo Fisher Scientific). The cells were gently lysed using a Dounce homogenizer, followed by sonication for 70 s (50% duty cycle, five-output control) on ice. The cell lysate was cleared by centrifugation at 16,000 r.p.m. for 40 min using an SS-34 rotor. All of the following steps were performed at 8 °C. The soluble fraction of the lysate was filtered using 0.45-µm PVDF membrane filters (Merck Millipore), then 3 ml of anti-FLAG affinity gel resin (Sigma-Aldrich) was equilibrated with buffer A. The cleared lysate was added to the equilibrated beads and incubated in a 2.5 cm × 10 cm glass Econo-Column (Bio-Rad) on a rocking platform for 2 h. After removal of the flow-through, the resin was washed with 50 ml of buffer B (50 mM HEPES (pH 7.5, 23 °C), 150 mM NaCl, 5% (vol/vol) glycerol, 0.5 mM DTT), then 5 ml of buffer B supplemented with 2 mM ATP and 5 mM $MgCl_2$ was added to the resin and incubated for 30 min with rocking. The ATP wash was repeated four times. The resin was washed with 50 ml of buffer B. Elution buffer was prepared by diluting 3× FLAG peptide stock solution (5 mg ml^{-1} 3× FLAG peptide in TBS (50 mM Tris-HCl at pH 7.4, 150 mM NaCl)) in buffer B to reach a final peptide concentration of 200 µg ml^{-1}. The resin was gently resuspended in 3 ml of elution buffer and incubated for 30 min while slowly rocking. In total, 5 × 3-ml elution fractions were obtained in this way. All elution fractions were combined and filtered through a 0.2-µm filter (Merck Millipore) before anion exchange chromatography (AEC). AEC was performed on an AKTA Pure system using a 15-ml loop and a MonoQ 5/50 GL column equilibrated in MonoQ-A buffer (50 mM HEPES (pH 7.5, 23 °C), 150 mM NaCl, 5% (vol/vol) glycerol, 2 mM tris(2-carboxyethyl) phosphine (TCEP)). The column was washed with MonoQ-A buffer following sample application and eluted with a NaCl gradient from 150 mM (MonoQ-A buffer) to 1 M (MonoQ-B buffer (50 mM HEPES (pH 7.5, 23 °C), 1 M NaCl, 5% (vol/vol) glycerol, 2 mM TCEP)). Elution fractions of 0.2 ml were collected. Purified protein was stored at 4 °C and used for cryo-EM grid preparation within 48 h of purification.

Cryo-electron microscopy grid preparation. Freshly purified human ATM was diluted in compensation buffer to obtain a protein concentration of 0.26 mg ml^{-1} in 20 mM HEPES (pH 7.5, 23 °C), 150 mM NaCl and 5 mM $MgCl_2$. The human ATM sample (4 µl) was mixed with 1 µl of 21 µM inhibitor KU-55933 (Sigma-Aldrich) and incubated on ice for at least 5 min. Immediately before plunging, Tween-20 was added to the ATM sample to a final concentration of 0.01%. Grids were prepared using a Leica EM GP plunge freezer (Leica). Tween-20-containing sample (4.5 µl) was deposited onto a plasma-cleaned (GloQube, Quorum) gold grid with a carbon support (Au 200, R2/2, 2 nm C, UltrAufoil). Samples were pre-incubated on the grids for 20 s at 15 °C and 95% humidity and blotted for 2.5 s before plunge-freezing the grid in liquid ethane.

Cryo-electron microscopy data acquisition. Two datasets of ATM-KU-55933 (8,519 and 4,139 micrographs) were acquired on a Titan Krios transmission electron microscope (Thermo Fisher Scientific) operated at 300 kV, with a K2 summit direct electron detector (Gatan) operated in counting mode and an energy filter (Gatan). Data acquisition was automated with the EPU (Thermo Fisher Scientific) software package. Images were recorded at a nominal magnification of ×130,000 (1.059 Å per pixel) with a defocus range of 1.0 µm to 2.8 µm, and total dose of 45 $e^-/Å^2$ over 40 frames. Four datasets of ATM-M4076 (5,287, 1,372, 3,745 and 2,269 micrographs) were acquired using the same set-up as described above. A dataset of ATM-ATPγS containing 5,619 micrographs was collected using the same set-up as described above. Representative micrographs are provided in Supplementary Fig. 7.

Cryo-electron microscopy image processing. Motion correction with MotionCor2 and CTF estimation with CTFFind4 were performed on the fly for all datasets using an in-house-developed pipeline[60,61].

Further processing of ATM-KU-55933 data was carried out using RELION-3.0.7/3.1.0[62]. Particles were picked automatically using a previously obtained low-resolution map of human ATM filtered to 20 Å as a 3D reference (unpublished). A total of 5,333,298 particles were extracted using a box size of 320 × 320 pixels and binned four times to speed up the initial processing. Extracted particles were subjected to a few rounds of 2D classification followed by a selection of 'clean' 2D classes. The resulting 2,679,787 particles were used in 3D classification and another round of 'cleanup' selection was done. The best 3D class with 891,295 particles was selected and used for two rounds of 3D refinement, followed by CTF refinement and Bayesian polishing. A set of polished particles was cleaned by 2D classification. The remaining 826,510 particles were 3D-refined and post-processed with automatic *B*-factor determination. The final map showed an overall resolution of 2.78 Å according to the gold-standard Fourier shell correlation 0.143 criterion (used hereafter unless otherwise stated).

To better resolve the conformational flexibility of the N-terminal HEAT repeat region of ATM, we started by 3D-refining, CTF-refining and Bayesian-polishing all 2,679,787 particles. Polished particles were cleaned by 2D classification and further 3D-refined. The resulting 2,651,173 particles were subjected to a 3D classification, followed by a focused (N-terminal) 3D classification with fixed angles, selectively masking for the N-terminal domains. Masks for the regions of interest were created using UCSF Chimera[63]. Three distinct 3D classes with different N-terminal solenoid confirmation emerged. All three classes were processed individually by focused 3D classification with fixed angles and 3D refinement (for details see the processing scheme in Supplementary Fig. 1). An analogous approach was used to resolve the conformational flexibility of the N-terminal region of M4076- and ATPγS-bound ATM (Extended Data Fig. 8).

To improve the resolution of the N terminus and pincer regions, subtracted maps were prepared. Using the 3D refinement of all 2,679,787 CTF-refined and polished particles, one complete monomer of the ATM dimer and the C-terminal portion of the other were subtracted. Two particle sets were prepared with the pincer region either included or subtracted. The particles were re-centered on the remaining N-terminal density and cropped to 200 × 200 pixels. Maps from the subtracted particles were produced using relion_reconstruct, and used to prepare masks and as references for 3D classifications with local angular searches. Dominant classes appeared containing 1,075,217 particles (excluding pincer) and 1,117,056 particles (including pincer). These classes were refined and post-processed to overall resolutions of 3.06 Å (excluding pincer) and 3.15 Å (including pincer). The 3D classifications with fixed angles were performed using masks for the pincer region and very N-terminal HEAT repeats, and the best classes refined with local searches using the same targeted masks. This resulted in a map of the N-terminal HEAT repeats from 1,035,906 particles to a resolution of 3.10 Å, and a map of the pincer region from 807,127 particles to a resolution of 3.34 Å (Supplementary Fig. 3).

Processing of the ATM-M4076 dataset was continued in CryoSparc by using Topaz for automated particle picking on the motion-corrected micrographs[64,65]. After four rounds of Topaz training and 2D classification cleaning, 455,866 particles were used for ab initio reconstruction and homogeneous refinement. Local refinement masking for the C-terminal half of ATM resulted in a final map with a resolution of 2.99 Å (the processing scheme is depicted in Supplementary Fig. 4).

ATM-ATPγS particles were picked in CryoSparc by using Topaz (as described above) in combination with template-based automated particle picking performed in Relion using a previously obtained human ATM-KU-55933 map filtered to 20 Å as a 3D reference. Particle coordinates were transferred between CryoSPARC and Relion using UCSF pyEM, CryoSparc and Relion picked particles were combined in Relion, removing duplicates, and cleaned by 2D classification. The resulting 709,013 particles were subjected to 3D refinement, CTF refinement and Bayesian polishing. Polished particles were cleaned by 2D classification and the selected 701,857 particles were 3D-refined and 3D-classified using fixed angles, then 690,548 particles from the best 3D class were 3D-refined, masking for the C-terminal half and using local search angles, and post-processed with automatic *B* factor determination (Supplementary Fig. 5). The final map showed an overall resolution of 2.78 Å (Supplementary Fig. 6).

Some maps were filtered using LAFTER in the CCPEM interface[66,67]. Maps with different origins were aligned and resampled using UCSF Chimera where appropriate. Phenix combine-focused-maps was used to generate an overall map of ATM-KU-55933, combining the highest-resolution components of each focused map[63,68].

Model building and refinement. An existing model of *Hs*ATM (PDB 6K9L) was rigid-body-fitted to the ATM-KU-55933 map density using UCSF Chimera. Model building and refinement were performed using Coot[63,69]. The existing *Hs*ATM model was used as a template for building of the C-terminal region, from which sequences were fitted, corrected and extended. However, all existing models were shown to be incorrect for the N-terminal and pincer regions, so these regions were built manually, assisted by secondary-structure predictions from JPred 4[70]. The multiple maps with different focal positions were used to provide the highest resolution at each point in the protein sequence and ensure the model was built in the correct register, before fitting to individual maps. LAFTER filtered maps provided the clearest densities for model building[66]. Loops with poor density were only built where well-defined anchor points and traceable density limited positioning errors. Some side chains were omitted in poorly resolved loops.

For modeling the lower-resolution N-terminal regions of the overall maps, the spiral and hinge models from the high-resolution subtracted maps were rigid-body-fitted into the density, followed by real-space refinement with local restraints. All structures were refined by iterative rounds of model building with Coot and refinement using Phenix real-space refine[71]. Models were validated using Phenix comprehensive validation (cryo-EM)[68]. Figures were generated using UCSF ChimeraX[72].

Sequence alignments of the C-terminal 236 amino acids of human ATM with other PIKK family members and ATM orthologs were carried out using the program clustalW2.

Human CtIP fragment expression and purification for kinase assays. A truncated version of human CtIP consisting of the C-terminal residues 650–897 and the phosphomimetic mutant T847E was cloned into a pET47b vector together with an N-terminal 6× His tag, followed by an MBP tag and an HRV3C protease cleavage site. Transfected *Escherichia coli* Rosetta cells (Novagen) were cultured in Turbo medium at 37 °C, 140 r.p.m. until reaching an optical density at 600 nm of ~1.2. Recombinant protein expression was induced with 0.2 mM IPTG and carried out at 18 °C, 140 r.p.m. for 16 h. Cells were collected by centrifugation at 4,000*g*, 10 min, 4 °C. The cell pellet from a 2-l culture was resuspended in 50 ml of pre-cooled lysis buffer (50 mM HEPES, pH 7.5, 300 mM NaCl, 10% (vol/vol) glycerol, 0.5 mM TCEP, 10 μM $ZnCl_2$, 10 mM imidazole, 0.5% NP-40) supplemented with one tablet of EDTA-free protease inhibitor cocktail (Sigma-Aldrich). Lysis was performed by three rounds of sonication for 5 min each (50% duty cycle, eight-output control) on ice. The cell lysate was cleared by centrifugation at 17,000 r.p.m. for 1 h using an SS-34 rotor. The supernatant was further filtered using 0.45-μm PVDF membrane filters (MERCK Millipore). All of the following steps were performed at 8 °C. A 10 ml volume of Ni-NTA beads (Machery Nagel), equilibrated with buffer A (50 mM HEPES pH 7.5, 300 mM NaCl, 10% (vol/vol) glycerol, 0.5 mM TCEP, 10 μM $ZnCl_2$, 10 mM imidazole), was added to the cleared lysate and incubated in a 2.5 cm × 10 cm glass Econo-Column (Bio-Rad) on a rocking platform for 1 h. The flow-through was removed and the beads washed three times with buffer A, twice with 5% buffer B (buffer A, containing 500 mM imidazole), once with 10% buffer B and once with 15% buffer B. CtIP was eluted four times with 50% buffer B. The fractions were pooled and dialyzed against buffer containing 50 mM HEPES pH 7.5, 150 mM NaCl, 10% (vol/vol) glycerol, 0.5 mM TCEP, 10 μM $ZnCl_2$ and 5 mM imidazole overnight after self-made PreScission protease was added. The dialyzed sample was applied to the same amount of Ni-NTA beads, pre-equilibrated with dialysis buffer and incubated while rotating for 1 h. The flow-through, containing cleaved CtIP, was collected and excess protease removed with a glutathione bead (Thermo Scientific) pulldown. After concentrating the sample using a centrifugal filter (30-kDa molecular weight cutoff, Amicon) to ~8 mg ml^{-1}, 500 μl was injected onto a Superdex 75 10/300 column (GE Healthcare) connected to an ÄKTA Pure system, pre-equilibrated in SEC buffer (20 mM HEPES, pH 7.5, 150 mM NaCl, 10 μM $ZnCl_2$, 0.5 mM TCEP). CtIP was eluted at 1.5 mg ml^{-1} with some minor degradation products, aliquoted, flash-frozen in liquid nitrogen and stored at −80 °C.

Gel-based kinase assay. The kinase activity of freshly purified full-length human ATM (50 mM HEPES (pH 7.5, 23 °C), 160 mM NaCl, 5% (vol/vol) glycerol, 2 mM TCEP) was assessed using human CtIP peptide substrate at a final concentration of 2.4 μM. The final concentration of human ATM used was 0.35 μM. The reactions were carried out in buffer containing 20 mM HEPES (pH 7.5, 23 °C), 150 mM NaCl, 5 mM $MgCl_2$, 1 mM $MnCl_2$, 0.01 mM $ZnCl_2$, 5% (vol/vol) glycerol and 0.5 mM TCEP at a final volume of 15 μl. The ATM-specific inhibitors KU-55933 (Sigma-Aldrich) and M4076 (Merck) were dissolved in dimethyl sulfoxide and used in a final concentration of 10 μM. The reactions were started by the addition of 1 mM adenosine 5′-triphosphate (ATP) followed by 30-min incubation at 30 °C. The reactions were stopped by adding 4× sodium dodecyl sulfate polyacrylamide gel electrophoresis (SDS–PAGE) loading buffer. An aliquot of 15 μl from each reaction was loaded on a 4–20% RunBlue SDS gel (Expedion) and resolved by SDS–PAGE. The gel was stained using Pro-Q Diamond Phosphoprotein gel stain (Thermo Fisher Scientific) and analyzed using a Typhoon FLA 9000 laser scanner (GE Healthcare). In addition, gel was stained with Coomassie (InstantBlue, Expedion) to assure consistent sample loading.

Thermal shift assay. 1,10-Phenanthroline, *N,N,N′,N′*-tetrakis-(2-pyridylmethyl) ethylenediamine (TPEN) and EGTA (Sigma-Aldrich) were prepared by dissolving appropriate amounts of chelating agents in ethanol to reach 500 mM concentration, then further diluted with MonoQ-A buffer to generate 100 mM (100×) stock of chelating agents. The 100× stocks were further diluted with MonoQ-A buffer to 10× concentration before mixing chelating agents with protein.

A volume of 9 μl of freshly purified full-length human ATM at 0.6 μM concentration was mixed with 1 μl of 10× (10 mM) chelating agents. In the control reaction, the same amount of ATM was mixed with 1 μl of buffer prepared in the same way as chelating agents. Following a 10-min incubation of ATM with chelating agents, changes in the intrinsic fluorescence (at 330 nm and 350 nm) with respect to increasing temperature were measured using a Tycho NT.6 system (NanoTemper). The measurements were performed in standard capillaries (NanoTemper).

Recombinant proteins for biochemical kinase activity assays. The following recombinant proteins used in the biochemical kinase activity assays (except Fig. 1a and Extended Data Figs. 1c and 5a) were purchased from Eurofins: human full-length FLAG-tagged ATM (GenBank ID NM_000051; item no. 14-933-K, lot no. 2447914) expressed in a mammalian cell line; human full-length FLAG-tagged ATR (GenBank ID NM_001184.3) and human full-length ATRIP (GenBank ID AF451323.1) co-expressed in a mammalian cell line (item no. 14-953M, lot no. D14HP005NB); N-terminal FLAG-tagged human mTOR amino acids 1362-end (GenBank ID NM_004958.2; item nos. 14-769, 14-769-K and 14-769M, lot no. 1607837) expressed by baculovirus in Sf21 insect cells; PI3K p110α/p85α (complex of N-terminal 6His-tagged full-length p110α and untagged full-length p85α; GenBank U79143(PI3Ka)/GenBank XM_043865(p85a)) (item nos. 14-602, 14-602-K and 14-602M, lot no. WAB0319), expressed by baculovirus in Sf21 insect cells; PI3K p110β/p85α (complex of N-terminal 6His-tagged full-length p110β and untagged full-length p85α; GenBank NM_006219(PI3Kb)/GenBank XM_043865(p85a)) (item nos. 14-603, 14-603-K and 14-603M, lot no. WAD0867), expressed by baculovirus in Sf21 insect cells; PI3K p120γ (N-terminal 6His-tagged full-length PI3-kinase (p120γ); GenBank AF327656) (item nos. 14-558, 14-558-K and 14-558M, lot no. 2298365) and PI3K p110δ/p85α (complex of N-terminal 6His-tagged full-length p110δ and untagged full-length p85α; GenBank NM_005026(PI3Kδ)/GenBank XM_043865(p85α)) (item nos. 14-604, 14-604-K and 14-604M, lot no. WAE0320), expressed by baculovirus in Sf21 insect cells.

DNA-PK was prepared from HeLa nuclear cell extract (Cilbiotech) by Merck KGaA, which was diluted to a final concentration of 40 mM KCl and applied to ion exchange chromatography (AIEX Fractogel DEAE) in buffer A (40 mM KCl, 20 mM HEPES, 1 mM EDTA, 1 mM EGTA, 1 mM DTT, 10% glycerol, 0.02% Tween-20, pH 7.9). Increasing KCl concentrations were applied for a stepwise elution. Fractionation of active DNA-PK was achieved at 300 mM KCl. All steps were performed at 4 °C. Aliquots were frozen in liquid nitrogen and stored at −80 °C. Western blot analysis was used to confirm the DNA-PK catalytic subunit, Ku85 and Ku70. The final protein concentration was determined by Bradford assay (details are provided in the Supplementary Information).

Time-resolved FRET-based ATM kinase assay. The enzymatic ATM assay was carried out as a time-resolved FRET (TR-FRET; homogeneous time-resolved fluorescence (HTRF), Cisbio Bioassays) based 384-well assay. In the first step, purified human recombinant ATM (Eurofins) was incubated in assay buffer for 15 min with the ATM inhibitor at various concentrations and without test substance (as a negative or neutral control). The assay buffer comprised 25 mM HEPES pH 8.0, 10 mM $Mg(CH_3COO)_2$, 1 mM $MnCl_2$, 0.1% BSA, 0.01% Brij 35 and 5 mM DTT. The inhibitor solutions were dispensed into the microtiter plates using an ECHO 555 handler (Labcyte). In the second step, purified human recombinant c-myc-labeled p53 (human p53, full length, GenBank ID BC003596, expressed in Sf21 insect cells, Eurofins) and ATP were added, and the reaction mixture was incubated at 22 °C for 35 min. The final concentrations in the assay during incubation of the reaction mixture were 0.3 nM ATM, 75 nM p53 and 10 μM ATP (final reaction volume of 5 μl). The enzymatic reaction was stopped by the addition of EDTA. The formation of phosphorylated p53 as the result of the ATM-mediated reaction in the presence of ATP was detected via specific antibodies (labeled with the fluorophore europium (Eu) as donor and d2 as acceptor (Cisbio Bioassays)), which enabled FRET. A volume of 2 μl of antibody-containing stop solution (12.5 mM HEPES pH 8.0, 125 mM EDTA, 30 mM NaCl, 300 mM KF, 0.006% Tween-20, 0.005% Brij 35, 0.21 nM anti-phospho-p53(ser15)-Eu antibody and 15 nM anti-cmyc-d2 antibody) was added to the reaction mixture. After 2 h of incubation for signal development, the plates were analyzed in a plate reader (EnVision, PerkinElmer or Pherastar, BMG Labtech) using the TRF mode (and with laser excitation). After excitation of the donor Eu at a wavelength of 340 nm, the emitted fluorescence light both of the acceptor d2 at 665 nm and of the donor Eu at 615 nm was measured. The amount of phosphorylated p53 was directly proportional to the quotient of the amounts of light emitted, that is, the relative fluorescence units at 665 nm and 615 nm. The measurement data were processed by means of GraphPad Prism software. IC_{50} determinations were carried out by fitting a response curve to the data points by means of nonlinear regression analysis.

ATR–ATRIP kinase assay. The ATR–ATRIP enzymatic assay was performed as a TR-FRET (HTRF, Cisbio Bioassays) based 384-well assay. In a first step, purified human recombinant ATR–ATRIP (Eurofins) was incubated in assay buffer for 15 min at 22 °C with inhibitor at different concentrations or without test compound (as a negative control). The assay buffer contained 25 mM HEPES pH 8.0, 10 mM $Mg(CH_3COO)_2$, 1 mM $MnCl_2$, 0.1% BSA, 0.01% Brij 35 and 5 mM DTT. An ECHO 555 handler (Labcyte) was used to dispense compound solutions. In a second step, purified human recombinant cmyc-tagged p53 (human p53, full length, GenBank ID BC003596, expressed in Sf21 insect cells, Eurofins) and ATP were added, and the reaction mixture was incubated for 25–35 min, typically 25 min, at 22 °C. The pharmacologically relevant assay volume was 5 μl. The final concentrations in the assay during incubation of the reaction mixture were 0.3–0.5 nM (typically 0.3 nM) ATR–ATRIP, 50 nM p53 and 0.5 μM ATP. The enzymatic reaction was stopped by the addition of EDTA. The generation of phosphorylated p53 as a result of the ATR-mediated reaction in the presence of ATP was detected by using specific antibodies (labeled with the fluorophores Eu as donor and d2 as acceptor (Cisbio Bioassays)), enabling FRET. For this purpose, 2 μl of antibody-containing stop solution (12.5 mM HEPES pH 8.0, 125 mM EDTA, 30 mM NaCl, 300 mM KF, 0.006% Tween-20, 0.005% Brij 35, 0.21 nM anti-phospho-p53(Ser15)-Eu antibody,

15 nM anti-cmyc-d2 antibody) were added to the reaction mixture. Following signal development for 2 h, the plates were analyzed in an EnVision (PerkinElmer) microplate reader using the TRF mode with laser excitation. Following excitation of the donor Eu at 340 nm, the emitted fluorescence light of the acceptor d2 at 665 nm as well as from the donor Eu at 615 nm was measured. The amount of phosphorylated p53 was directly proportional to the ratio of the amounts of emitted light, that is, the ratio of the relative fluorescence units at 665 nm and 615 nm. Data were processed using GraphPad Prism software. IC_{50} values were determined in the usual manner by fitting a dose–response curve to the data points using nonlinear regression analysis.

DNA-PK assay. The DNA-PK kinase assay was performed as an HTRF (Cisbio Bioassays) based 384-well assay. In a first step, DNA-PK protein complex from HeLa nuclear extract pre-incubated with DNA from calf thymus and staurosporine was incubated with or without test compound for 15–20 min at 22 °C. After addition of the STK-substrate 1-biotin (Cisbio Bioassays) and Mg-ATP, the reaction mixture was incubated for 60–70 min (depending on the activity of the DNA-PK protein complex) at 22 °C. An ECHO 555 handler (Labcyte) or a Biomek FX handler (Beckman Coulter) was used for dispensing of compound solutions. The assay buffer consisted of 25 mM HEPES pH 7.4, 11 mM $MgCl_2$, 80 mM KCl, 0.45 mM EDTA and 0.5 mM EGTA, and contained 1 mM DTT, 0.17% BSA and 0.01% Tween-20. The pharmacologically relevant volume was 5 or 5.5 µl. The final concentrations in the assay during incubation of the reaction mixture were 100–235 ng DNA-PK protein complex per well (depending on the activity of the DNA-PK protein complex), 1 µM STK substrate 1-biotin (Cisbio Bioassays), 10 or 20 µM Mg-ATP, 80 ng DNA from calf thymus per well and 1 µM staurosporine. The enzymatic reaction was stopped by the addition of EDTA. The generation of phosphorylated STK-substrate 1-biotin as a result of the DNA-PK-mediated reaction was detected via a specific anti-phospho STK-antibody (Cisbio Bioassays) labeled with Eu as donor and streptavidin labeled with XL665 (Cisbio Bioassays) as acceptor, allowing FRET. For this purpose, 4 µl of antibody- and streptavidin-containing stop solution (50 mM HEPES pH 7.0, 800 mM KF, 20 mM EDTA, 0.1% BSA, 0.179 or 8.95 nM anti-phospho-STK antibody, 160 or 200 nM streptavidin-XL665) were added to the reaction mixture. Following signal development for 1 h, the plates were analyzed on a Rubystar or Pherastar (BMG Labtech) or on an Ultra Evolution (Tecan) microplate reader. The amount of phosphorylated substrate was directly proportional to the ratio of fluorescence units (excitation wavelength of 337 or 320 nm) at the emission wavelengths of 665 nm (phosphopeptide-sensitive wavelength/emission of XL665) to fluorescence units at 620 nm (reference wavelength Eu). IC_{50} values were calculated using GraphPad Prism software[73].

mTOR kinase assay. The DiscoveRx KINOMEscan assay (Eurofins) was used for mTOR selectivity profiling of inhibitors. Recombinant human mTOR protein (Eurofins) was incubated in assay buffer containing 50 mM HEPES pH 7.5, 1 mM EGTA, 0.01% Tween-20, 2 mg ml^{-1} substrate, 3 mM $MnCl_2$ and [γ-^{33}P-ATP] (specific activity ~500 c.p.m. $pmol^{-1}$, [ATP] = 70 µM in the assay). The reaction was initiated by the addition of Mn-ATP solution. The reaction was stopped by the addition of 3% phosphoric acid after 40-min incubation at room temperature. A volume of 10 µl of reaction solution was pipetted on P30 filters and washed three times for 5 min in 75 mM phosphoric acid and once in methanol, dried, and measured by scintillation counting. IC_{50} values were calculated using GraphPad Prism software.

PI3K HTRF-based assay. The DiscoveRx KINOMEscan assay (Eurofins) was used for PI3K selectivity profiling of inhibitors. The following human recombinant proteins expressed by baculovirus in Sf21 insect cells (Eurofins) were used: PI3K p110α/p85α, PI3K p110β/p85α, PI3K p120γ and PI3K p110δ/p85α. The following HTRF-based assay protocol was used for all PI3K isoforms with ATP concentrations at the respective K_m values (PI3K p110α/p85α, ATP K_m = 193 µM, [ATP] = 200 µM in assay; PI3K p110β/p85α ATP K_m = 235 µM, [ATP] = 200 µM in assay; PI3K p120γ ATP K_m = 109 µM, [ATP] = 100 µM in assay; p110δ/p85α ATP K_m = 321 µM, [ATP] = 200 µM in assay). Recombinant human PI3K protein was incubated in assay buffer containing 10 µM phosphatidylinositol-4,5-bisphosphate. The reaction was initiated by the addition of a Mg-ATP solution at K_m concentration (see above). After incubation for 30 min at room temperature, the reaction was stopped by the addition of EDTA and biotinylated phosphatidylinositol-3,4,5-trisphosphate. Finally, detection buffer was added, containing Eu-labeled anti-GST monoclonal antibody, GST-tagged GRP1 PH domain and streptavidin allophycocyanin. The plate was then read in time-resolved fluorescence mode and the HTRF signal was determined according to the formula HTRF = 10,000 × (Em 665 nm/Em 620 nm). Mg-ATP, magnesium 5′-*O*-[hydroxy[(hydroxyphosphinato)oxy]-phosphinato]-oxy)-phosphoryl] adenosine; $MgCl_2$, magnesium dichloride; EGTA, ethylenglycole-bis(aminoeth ylether)-*N*,*N*,*N*′,*N*′-tetra acetic acid; Tween-20, Polysorbate 20.IC_{50} values were calculated using GraphPad Prism software.

In vitro kinase selectivity profiling assay for M4076. The Reaction Biology Corporation (RBC) HotSpot kinase profiling service (http://www.reactionbiology.com) was used for in vitro selectivity profiling of M4076 in single-dose singlicate mode at a concentration of 1 µM against 583 kinases. Dose–response curves of M4076 were determined for 10 kinases and their mutants (22 kinases in total), which showed activity values below 50% tested at 1 µM M4076 in the in vitro kinase selectivity profile against 583 kinases. For IC_{50} determination, M4076 was tested in duplicate in a 10-dose IC_{50} mode with three-fold serial dilution starting at 10 µM. Staurosporine was used as control compound and tested in 10-dose IC_{50} mode with four-fold serial dilution starting at 20 µM. Reactions were carried out at K_m ATP concentrations of individual kinases according to the RBC K_m binning structure. Kinases inhibitory activities were assessed by the HotSpot assay platform, which contained specific kinase/substrate pairs along with the required cofactors. Base reaction buffer: 20 mM HEPES (pH 7.5), 10 mM $MgCl_2$, 1 mM EGTA, 0.02% Brij 35, 0.02 mg ml^{-1} BSA, 0.1 mM Na_3VO_4, 2 mM DTT and 1% DMSO. M4076 was dissolved in 100% DMSO to a specific concentration. The serial dilution was conducted by Integra Viaflo Assist in DMSO. The reaction mixture containing the examined compound M4076 and ^{33}P-ATP (specific activity 0.01 µCi $µl^{-1}$ final) was incubated at room temperature for 2 h, and radioactivity was detected by the filter-binding method. In detail, reactions were spotted onto P81 ion exchange paper (Whatman cat. no. 3698-915) and filters were extensively washed in 0.75% phosphoric acid. Kinase activity data were expressed as the percent remaining kinase activity in test samples compared to vehicle (dimethyl sulfoxide) reactions. IC_{50} values and curve fits were obtained using GraphPad Prism software.

Cellular pCHK2 Thr68 Luminex. Cellular levels of pCHK2 were detected in a Luminex-based assay format. HCT116 cells (ATCC CCL-247, authenticated by STR analysis) were seeded in medium with 10% fetal calf serum (FCS) in 12-well plates. The next day, the medium was removed and 100 µl of fresh medium including a serial dilution of inhibitor M4076 was added per well 1 h prior to the irradiation of 2 Gy by the CellRad irradiator. The irradiation was performed by adjusting the tube voltage to 120 kV_p; 5 mA and positioning the plates inside circle 2 at plate height position 2. A copper filter was used to reduce the intensity of particular wavelengths from the beam. At 1 h after irradiation, the cells were washed once with PBS, and cell lysates were prepared by using HGNT lysis buffer (20 mM HEPES pH 7.4, 150 mM NaCl, 2 mM EDTA, 25 mM NaF, 10% glycerol and 1% Triton X-100; plus 1% phosphatase inhibitor Cocktail Set II and 0.2% protease inhibitor Cocktail Set III) and analyzed for the level of pCHK2 Thr68 applying a Luminex-based assay. After adding the diluted bead suspension (3,000 beads in BR (Roche 11112589001 + 0.1% Tween)) with coupled antibodies against total CHK2 (Chk2 (D9C6) XP rabbit mAb; Cell Signaling Technology cat. no. 6334BF) to 25 µg of total protein in HGNT, the plate was incubated overnight at 4 °C. The beads were washed three times with TBST (Pierce/Thermo 28358 + 0.05% Tween) and 25 µl of BR as well as 25 µl of antibody dilution of the detection antibody coupled to biotin were added in BR (tCHK2: Chk2 (1C12) mouse mAb; Cell Signaling Technology cat. no. 3440BF, pCHK2: pChk2 (Thr68) (C13C1) rabbit mAb; Cell Signaling Technology cat. no. 2197BF, final concentration 1.5 µg ml^{-1}). After 1 h of incubation at room temperature, the beads were washed again with TBST and 25 µl BR and the streptavidin-phycoerythrin dilution (25 µl, Moss cat. no. 001NB, 1:1,000 diluted in BR) were added for 45 min at room temperature. After washing and adding 100 µl of BR, the probes were analyzed in a Magpix instrument (Thermo Fisher Scientific) following the instruction manual. The instrument settings were as follows: sample volume, 35 µl; count, 50; unit, MFI. To control the Luminex assay, different concentrations of recombinant CHK2 protein (R&D cat. no. 1358-KS) were used as standard and were analyzed in parallel. After background correction, the signals for the phosphorylated proteins were normalized to signals of the total protein. Basal levels were set to 0% and irradiated samples without compound were set to 100%. Samples were measured in singlicate and the experiment was repeated three times. IC_{50} values were calculated using GraphPad Prism software.

Cellular pCHK2 Thr68 enzyme-linked immunosorbent assay. HCT116 cells (ATCC CCL-247) were seeded in 100 µl of culture medium (MEM Alpha, with 10% FCS) in the range of 5×10^4 cells per well in 96-well plates to achieve a defined cell density. The plates were then incubated for 24 h at 37 °C and 10% CO_2. The next day, the medium was removed and 100 µl of fresh medium containing KU-55933 inhibitor in various concentrations (10 nM to 25 µM) plus a constant concentration of 10 µM bleomycin and without test substance as DMSO and bleomycin controls was added per well and incubation was continued for a further 6 h. The medium was removed and cells were lysed using HGNT lysis buffer (20 mM HEPES pH 7.4, 150 mM NaCl, 2 mM EDTA, 25 mM NaF, 10% glycerol and 1% Triton X-100; plus 1% phosphatase inhibitor Cocktail Set II and 0.2% protease inhibitor Cocktail Set III) and incubated at 4 °C overnight. Levels of pCHK2 were determined by ELISA (all reagents from Cell Signaling, cat. no. 7037; PathScan kit) with capture antibody specific for pCHK2 (Thr68) and detection antibody against total CHK2 protein. Anti-mouse immunoglobulin-G, horseradish peroxidase-linked antibody was then used to recognize the bound detection antibody. Horseradish peroxidase substrate (TMB) was added to develop color. The magnitude of the absorbance for the developed color is proportional to the amount of CHK2 phosphorylated at Thr68. Absorbance was measured at 450 nm for 4 s using a Tecan Sunrise reader. IC_{50} values were calculated using GraphPad Prism software.

Reporting Summary. Further information on research design is available in the Nature Research Reporting Summary linked to this Article.

Data availability

The 3D cryo-EM density maps reported in this Article have been deposited in the EMD under accession nos. EMD-12352 (ATM-ATPyS), EMD-12350 (ATM-M4076), EMD-12343 (ATM-KU-55933, Kinase), EMD-12347 (ATM-KU-55933, Spiral), EMD-12345 (ATM-KU-55933, Pincer) and EMD-12346 (ATM-KU-55933, Spiral–Pincer). The corresponding models have been deposited in the Protein Data Bank under IDs 7NI6 (ATM-ATPyS), 7NI4 (ATM-M4076) and 7NI5 (ATM-KU-55933). Raw micrographs are archived at the LRZ of the Bavarian Academy of Science and Humanities and can be accessed for legitimate research purposes upon reasonable request to K.P.H. (hopfner@genzentrum.lmu.de). Any requests for additional data by qualified scientific and medical researchers for legitimate research purposes will be subject to the Merck KGaA, Darmstadt, Germany Data Sharing Policy. All requests should be submitted in writing to the Merck KGaA, Darmstadt, Germany data-sharing portal (https://www.emdgroup.com/en/research/our-approach-to-research-and-development/healthcare/clinical-trials/commitment-responsible-data-sharing.html). When Merck KGaA, Darmstadt, Germany has a co-research, co-development, or co-marketing or co-promotion agreement, or when the product has been out-licensed, the responsibility for disclosure might be dependent on the agreement between parties. Under these circumstances, Merck KGaA, Darmstadt, Germany, will endeavor to gain agreement to share data in response to requests. Source data are provided with this paper.

References

60. Zheng, S. Q. et al. MotionCor2: anisotropic correction of beam-induced motion for improved cryo-electron microscopy. *Nat. Methods* **14**, 331–332 (2017).
61. Rohou, A. & Grigorieff, N. CTFFIND4: fast and accurate defocus estimation from electron micrographs. *J. Struct. Biol.* **192**, 216–221 (2015).
62. Zivanov, J. et al. New tools for automated high-resolution cryo-EM structure determination in RELION-3. *eLife* **7**, e42166 (2018).
63. Pettersen, E. F. et al. UCSF Chimera—a visualization system for exploratory research and analysis. *J. Comput. Chem.* **25**, 1605–1612 (2004).
64. Punjani, A., Rubinstein, J. L., Fleet, D. J. & Brubaker, M. A. cryoSPARC: algorithms for rapid unsupervised cryo-EM structure determination. *Nat. Methods* **14**, 290–296 (2017).
65. Bepler, T. et al. Positive-unlabeled convolutional neural networks for particle picking in cryo-electron micrographs. *Nat. Methods* **16**, 1153–1160 (2019).
66. Ramlaul, K., Palmer, C. M. & Aylett, C. H. S. A local agreement filtering algorithm for transmission EM reconstructions. *J. Struct. Biol.* **205**, 30–40 (2019).
67. Wood, C. et al. Collaborative computational project for electron cryo-microscopy. *Acta Crystallogr. D Biol. Crystallogr.* **71**, 123–126 (2015).
68. Liebschner, D. et al. Macromolecular structure determination using X-rays, neutrons and electrons: recent developments in Phenix. *Acta Crystallogr. D Struct. Biol.* **75**, 861–877 (2019).
69. Emsley, P. & Cowtan, K. Coot: model-building tools for molecular graphics. *Acta Crystallogr. D Biol. Crystallogr.* **60**, 2126–2132 (2004).
70. Drozdetskiy, A., Cole, C., Procter, J. & Barton, G. J. JPred4: a protein secondary structure prediction server. *Nucleic Acids Res.* **43**, W389–W394 (2015).
71. Afonine, P. V. et al. Real-space refinement in PHENIX for cryo-EM and crystallography. *Acta Crystallogr. D Struct. Biol.* **74**, 531–544 (2018).
72. Pettersen, E. F. et al. UCSF ChimeraX: structure visualization for researchers, educators and developers. *Protein Sci.* **30**, 70–82 (2020).
73. Kashishian, A. et al. DNA-dependent protein kinase inhibitors as drug candidates for the treatment of cancer. *Mol. Cancer Ther.* **2**, 1257–1264 (2003).

Acknowledgements

EM data were collected at the Cryo-EM Core Facility of the Gene Center, Department of Biochemistry, LMU, Munich. B. Kessler, a technician at the Gene Center, LMU, provided support with cloning and protein purification. We are grateful for support from B. Blume and H. Dahmen, both employees of Merck KGaA, Darmstadt, Germany, for providing cellular pCHK2 results. Funding was provided by the Deutsche Forschungsgemeinschaft (CRC1054 to K.L.; CRC1361, CRC1064, Gottfried Wilhelm Leibniz-Prize and GRK1721 to K.P.H.) and a PhD fellowship from Boehringer Ingelheim Fonds (BIF) to E.v.d.L. This research was supported by the healthcare business of Merck KGaA, Darmstadt, Germany (CrossRef Funder ID 10.13039/100009945), which provided solid material of inhibitor M4076, free of charge.

Author contributions

J.D.B., K.S., M.R., A.A. and E.v.d.L. were involved in protein production and kinase assays. K.S., M.R., K.L. and J.D.B. carried out structural studies. T.F. was the project leader and principal inventor of M4076 at Merck KGaA, Darmstadt, Germany. U.G. was involved in the structure-based design of M4076 and cryo-EM structural refinement efforts. T.F. and U.P. contributed biochemical assay and kinase selectivity results and graphs. Together with K.L., K.S., M.R., J.D.B., T.F. and U.G. contributed to manuscript preparation. K.P.H. and all authors were involved in the interpretation of data, final manuscript preparation and approval.

Competing interests

K.S., M.R., K.L., J.D.B., E.v.d.L. and K.-P.H. declare no competing interests. A.A. contributed as an employee at the Gene Center, Department of Biochemistry, LMU at the time of the study and is currently an employee of Proteros Biostructures. U.G., T.F. and U.P. are employees of Merck KGaA, Darmstadt, Germany. Proteros Biostructures was contracted by Merck KGaA, Darmstadt, Germany, to determine the cryo-EM structure of ATM in complex with M4076.

Additional information

Extended data is available for this paper at https://doi.org/10.1038/s41594-021-00654-x.

Supplementary information The online version contains supplementary material available at https://doi.org/10.1038/s41594-021-00654-x.

Correspondence and requests for materials should be addressed to K. Lammens or K. P. Hopfner.

Peer reveiw information *Nature Structural & Molecular Biology* thanks Xiaodong Zhang and the other, anonymous, reviewer(s) for their contribution to the peer review of this work. Peer reviewer reports are available. Anke Sparmann and Beth Moorefield were the primary editors on this article and managed its editorial process and peer review in collaboration with the rest of the editorial team.

Reprints and permissions information is available at www.nature.com/reprints.

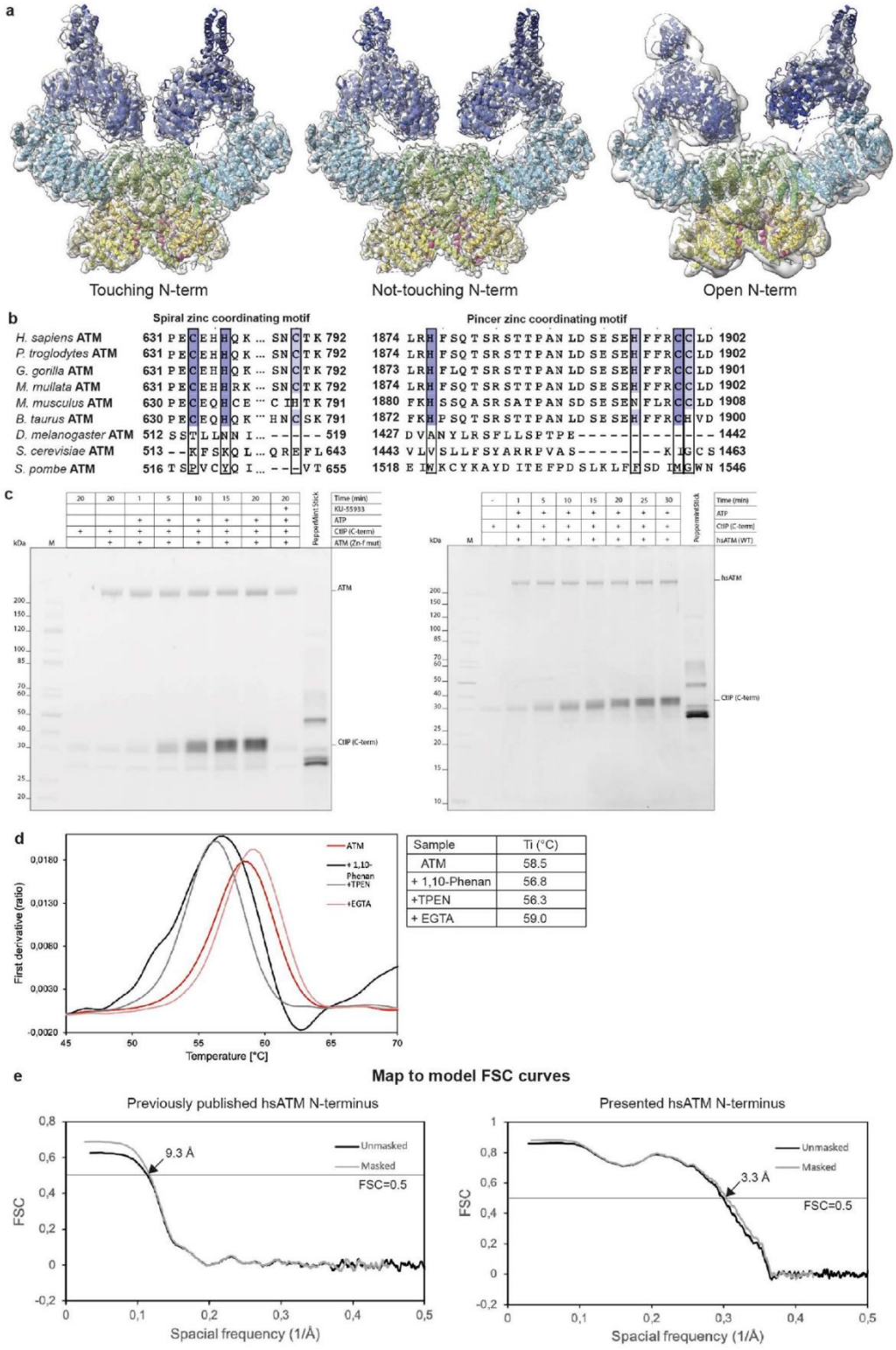

Extended Data Fig. 1 | See next page for caption.

Extended Data Fig. 1 | Features of the N-terminal Spiral domain of human ATM. (**a**) Cryo-EM density maps and models representing three conformational states of N-terminal Spiral-Pincer domains. Left: N-terminal Spiral domains are touching. Middle: N-terminal Spiral domains are not touching. Right: One N-terminal Spiral domain is resolved, the other one is more flexible. (**b**) Sequence alignment of zinc-binding motifs of ATM from different species. ATM residues involved in zinc coordination are highlighted and coloured by conservation. (**c**) Kinase activity time-course of zinc-binding motif mutant (C1899A, C1900A, left) and WT (right) ATM. Kinase activity on CtIP C-terminus (650–897, phosphomimic mutation T847E) visualized by phosphoprotein SDS-PAGE staining. Uncropeed gel image is available in Source Data: Extended Data Fig. 1. (**d**)Effects of chelating agents on the thermal stability of ATM. 1,10-phenanthroline (black) and TPEN (grey) are more specific to Zn2+. ATM only (red) and EGTA (pink) were used as controls. (**e**) Comparison of map to model FSC curves of previously published Spiral (PDB ID: 5NP0) and here presented Spiral domain model.

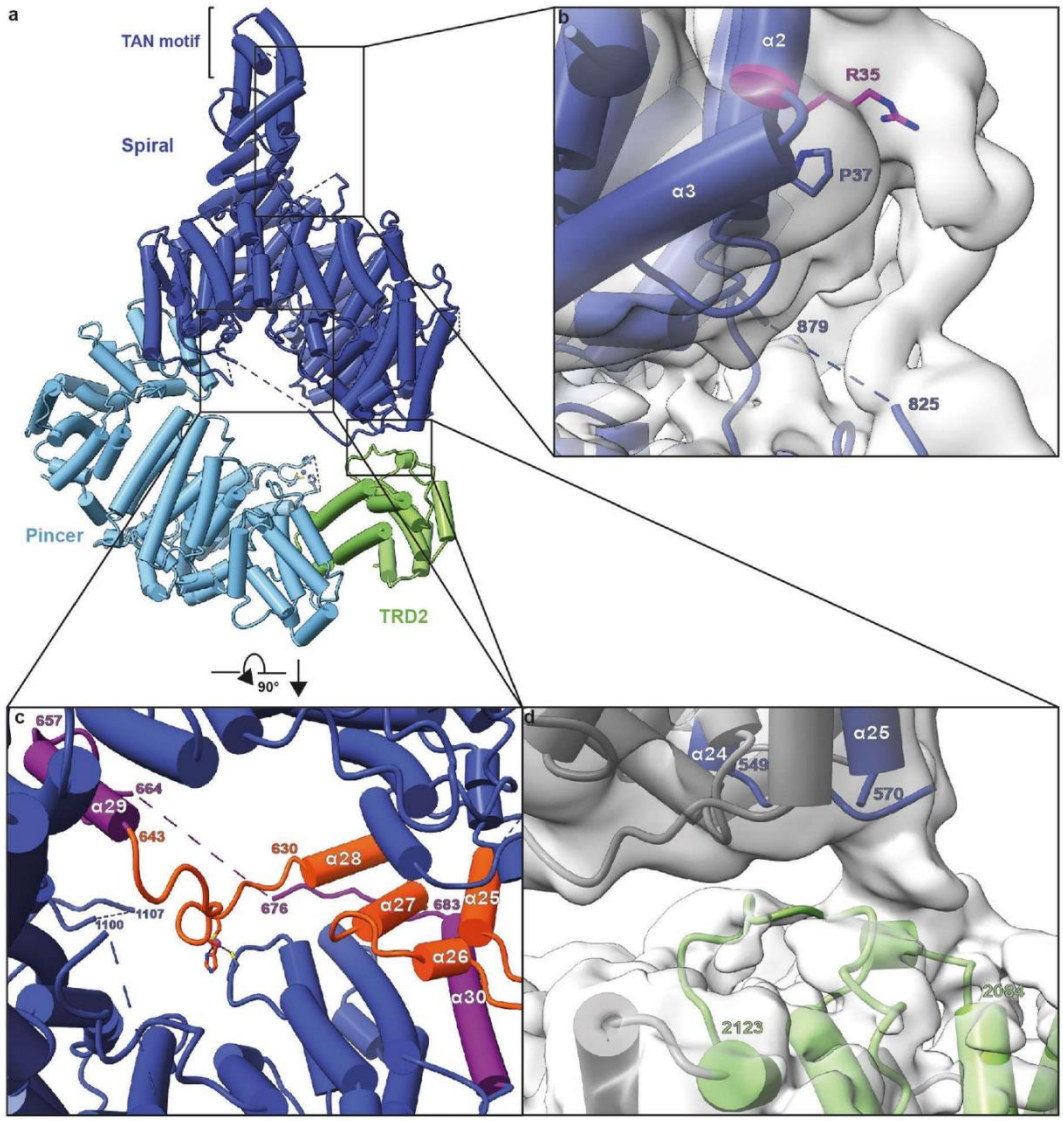

Extended Data Fig. 2 | N-terminal alpha-solenoid structure of human ATM. (**a**) Overview of organization of N-terminal spiral, pincer and TRD2 domains, helices depicted as cylinders. TAN motif labelled. (**b**) Interaction between unstructured loop 825–879 and R35 (helix 2). Density map contoured at 0.0034 and R35 colored in magenta. (**c**)Top view of spiral solenoid ring. Helices 25–28 and ring-crossing loop (630–643) colored in orange. Helices 29–30 and partially resolved loop (657–683) colored in purple. (**d**) Interaction between Spiral loop (549–570) joining helices 24 and 25 (blue), and TRD2 loops 2084–2092 and 2107–2123 (green). Density map contoured at 0.0032.

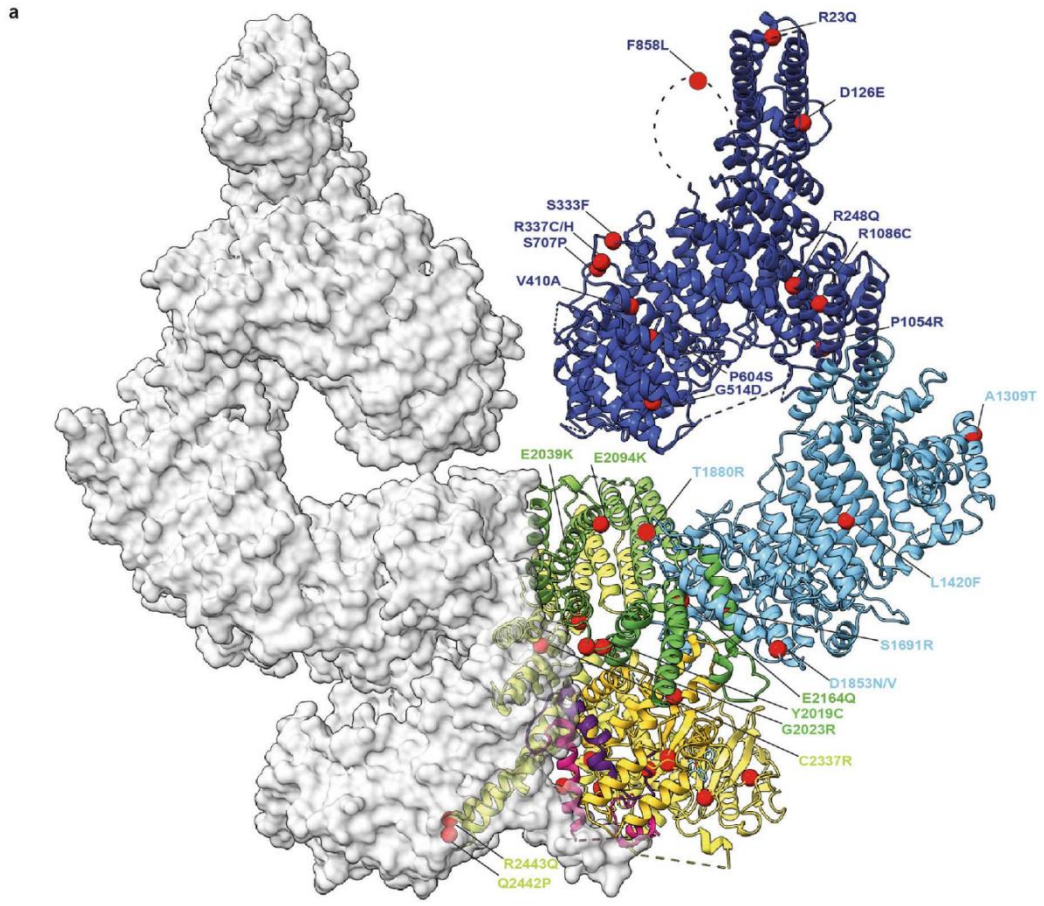

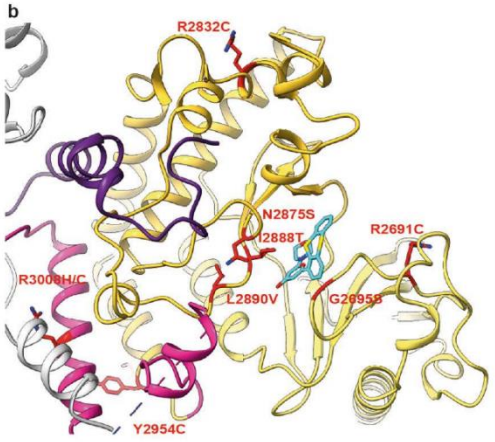

c

Domain	Mutations	Potential effects
Spiral	R23Q	Stabilisation of TAN motif
	D126E, R248Q, S333F, R337C/H, V410A, G514D, P604S, S707P, F858L, P1054R, R1086C	Stabilisation and charge distribution at Spiral interaction hub
Pincer	A1309T, L1420F, S1691R, D1853N/V, T1880R	Flexibility and folding of the N-terminus
FAT	Y2019C, G2023R, E2039K	Contact to kinase domain: might have an effect on a kinase activity
	E2094K, E2164Q	Folding of TRD2
	C2337R	Dimerisation
	Q2442P, R2443Q	Position of the PRD, kinase activity
	S2489F	HRD - kinase C-lobe connection
Kinase	R2691C, G2695S, N2875S, I2888T, L2890V	ATP binding
	R2832C	Kinase interaction with TRD1
	Y2954C	Kinase - PRD interaction, kinase regulation
	R3008H/C	PRD - TRD3 (opposite protomer) interaction

Extended Data Fig. 3 | Mapping of cancer-associated human ATM missense mutations. (**a**) Positions of commonly reported (count > 5) cancer mutations from COSMIC database depicted on to the ATM protomer. Approximate locations of F858L and T1880R mutations are shown based on unmodelled density. One ATM protomer coloured using domain colour-code, another-shown as a grey surface. Mutated residues are shown as red spheres with mutations indicated. (**b**) Model of KU-55933-bound ATM kinase with commonly (count > 5) mutated amino acid side chains coloured in red. Opposite protomer shown in grey. (**c**) Table summarising cancer-associated human ATM missense mutations. Mutations grouped based on their locations and coloured using domain colour-code.

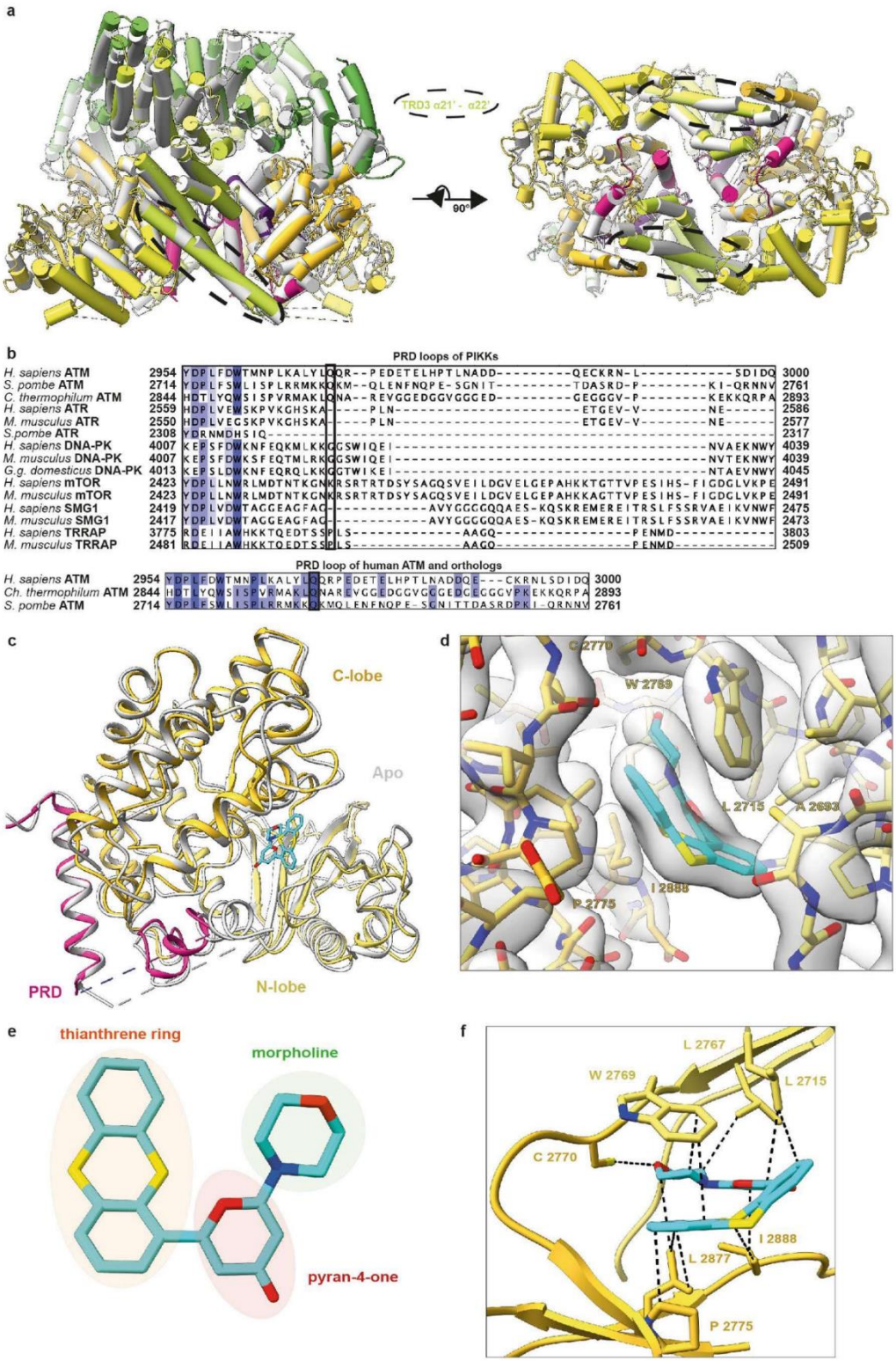

Extended Data Fig. 4 | See next page for caption.

Extended Data Fig. 4 | Conformation of KU-55933-bound human ATM. (**a**) Superimposition of KU-55933-bound human ATM dimer (color) and 'closed dimer' of human ATM (PDB ID: 5NP0; grey). Side and bottom views of C-terminal halves shown, helices depicted as cylinders. TRD3 α21-α22 indicated by black dotted line. (**b**) Sequence alignments of PRD loops from PIKKs from different organisms (top) and PRD loops of human ATM and its orthologs (bottom). PRD loops are colored by conservation and substrate-mimicking Q2971 of human PRD is highlighted. (**c**) Superimposition of kinase and PRD domains of inhibitor-bound (color) and apo human ATM (PDB ID: 6K9L; grey) models. (**d**) Cryo-EM density (grey, contoured at 0.0346) and model of the KU-55933 inhibited ATM active site. Clearly visible inhibitor proximal side chains labelled. (**e**) KU-55933 consists of three different ring systems: Thianthrene (orange), Pyran-4-one (red), Morpholine (green). (**f**) Detailed view of ATM active site with KU-55933. Van der Waals interactions indicated by dotted lines and interacting residues labelled.

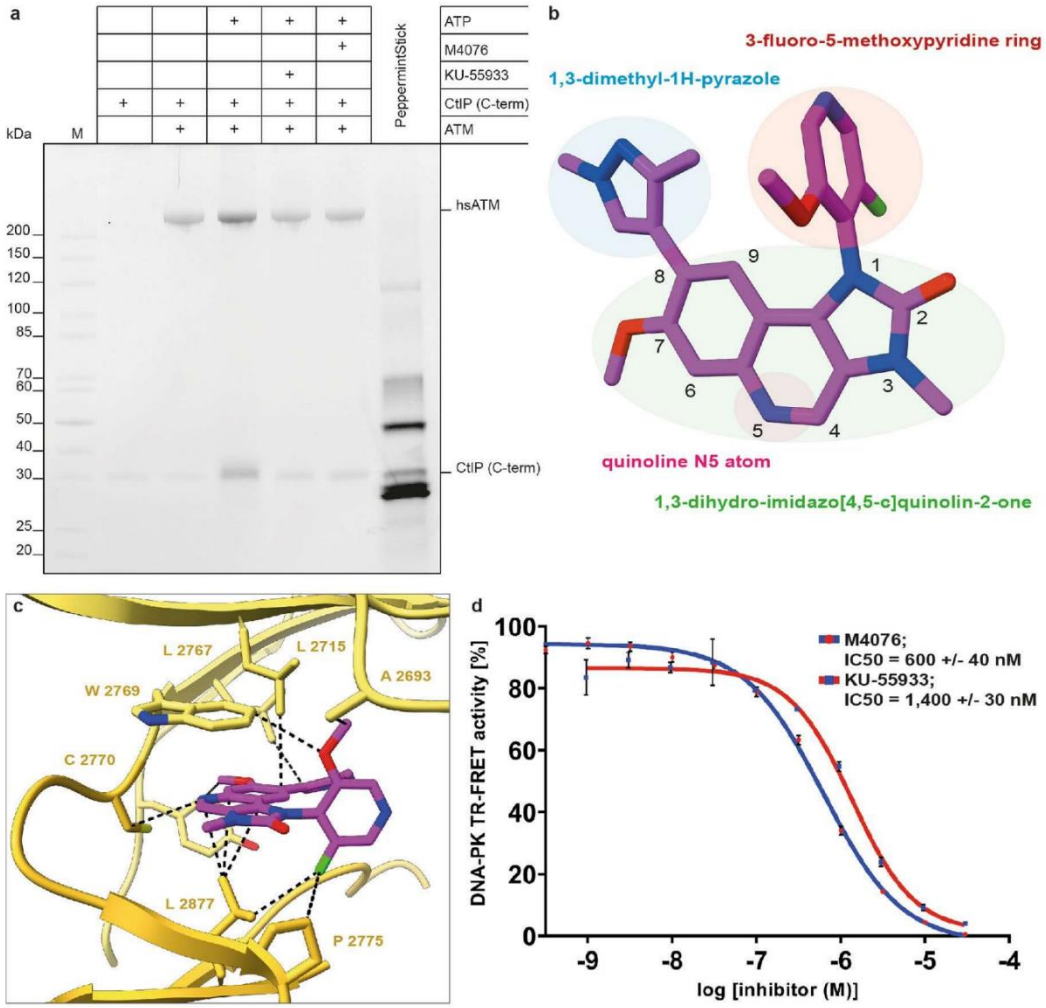

Extended Data Fig. 5 | Inhibition of ATM by M4076. (**a**) Inhibition of basal ATM kinase activity by M4076. Phosphorylation of CtIP C terminus (650–897, phosphomimetic mutation T847E) visualized by phosphoprotein SDS-PAGE staining, same gel as in Fig. 1a. The experiment was repeated twice with similar results. Uncropped gel image is presented in Source Data Fig. 1. (**b**) M4076 chemical structure and assignment of functional groups. (**c**) Detailed view of M4076 (magenta) bound ATM active site. Van der Waals interactions illustrated as black dotted lines and interacting residues labelled. (**d**) Dose-response curves of enzymatic DNA-PK kinase inhibition by M4076 and KU-55933. Data represent the mean ± s.e.m. from n = 16 independent experiments performed in duplicates for M4076 (IC50 = 600 ± 40 nM) and from one experiment performed in duplicates for KU-55933 (IC50 = 1,400 ± 30 nM). Data behind graph in panel d are available in Source Data Extended Data Fig. 5d.

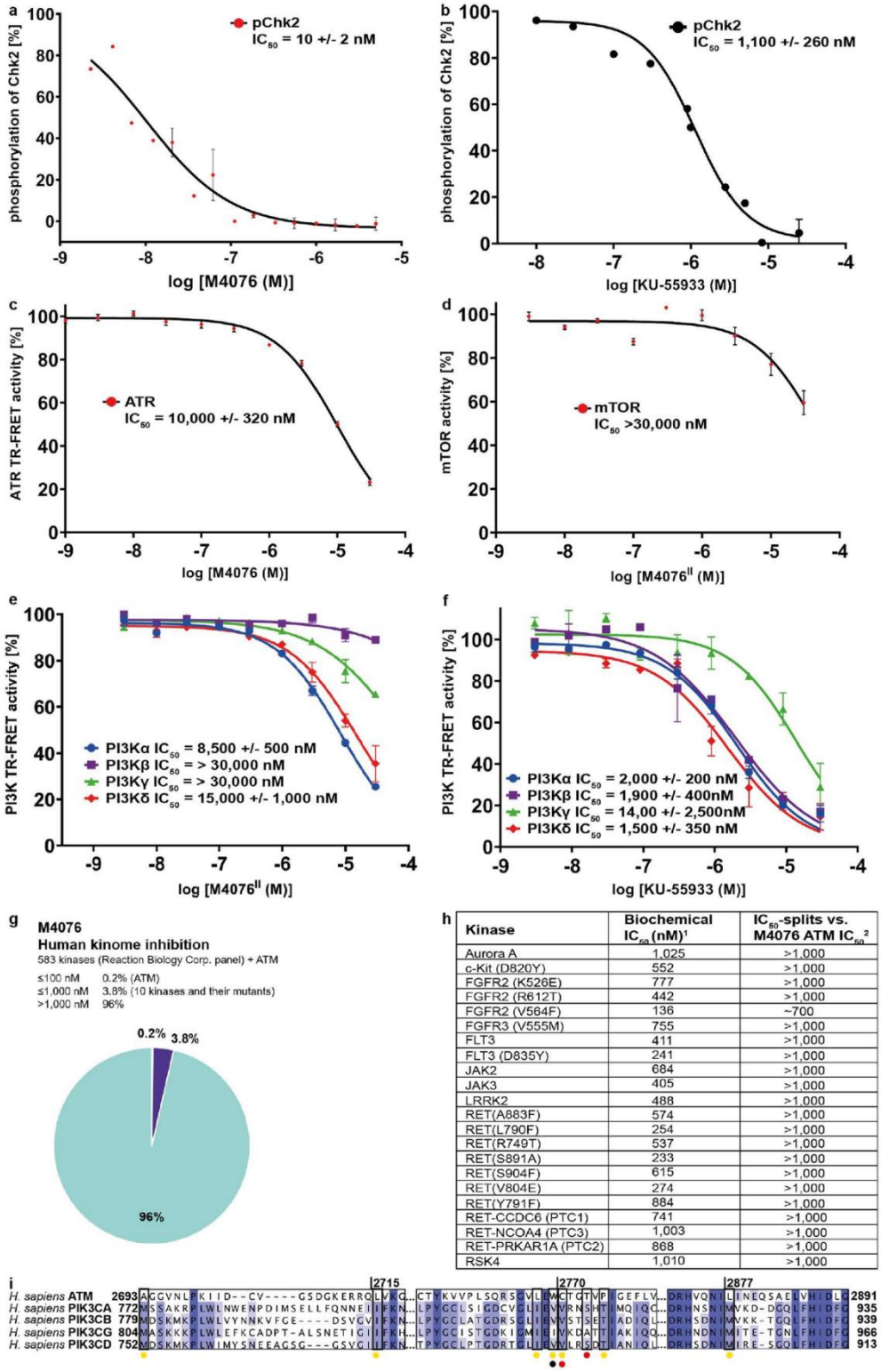

Kinase	Biochemical IC_{50} (nM)[1]	IC_{50}-splits vs. M4076 ATM IC_{50}[2]
Aurora A	1,025	>1,000
c-Kit (D820Y)	552	>1,000
FGFR2 (K526E)	777	>1,000
FGFR2 (R612T)	442	>1,000
FGFR2 (V564F)	136	~700
FGFR3 (V555M)	755	>1,000
FLT3	411	>1,000
FLT3 (D835Y)	241	>1,000
JAK2	684	>1,000
JAK3	405	>1,000
LRRK2	488	>1,000
RET(A883F)	574	>1,000
RET(L790F)	254	>1,000
RET(R749T)	537	>1,000
RET(S891A)	233	>1,000
RET(S904F)	615	>1,000
RET(V804E)	274	>1,000
RET(Y791F)	884	>1,000
RET-CCDC6 (PTC1)	741	>1,000
RET-NCOA4 (PTC3)	1,003	>1,000
RET-PRKAR1A (PTC2)	868	>1,000
RSK4	1,010	>1,000

Extended Data Fig. 6 | See next page for caption.

Extended Data Fig. 6 | Kinase specificity of KU-55933 and M4076 inhibitors. (**a**)In vitro cell-based IC50 for inhibition of 2 Gy-induced phosphorylation of CHK2 (pThr68) in the human colon carcinoma cell line HCT116 for M4076 (IC50 = 10 ± 2 nM) from a Luminex assay. Data represent the mean ± s.e.m. from n = 3 independent experiments performed in singlicates. (**b**) In vitro cell-based IC50 for inhibition of bleomycin-induced phosphorylation of CHK2 (pThr68) in the human colon carcinoma cell line HCT116 for KU-55933 (IC50 = 1,100 ± 260 nM) from an ELISA. Data represent the mean ± s.e.m. from n = 2 independent experiments performed in singlicates. (**c**) Dose-response curves of enzymatic ATR kinase inhibition by M4076. Data represent the mean ± s.e.m. from n = 7 independent experiments performed in duplicates for M4076 (IC50 = 10,000 ± 320 nM). (**d**) Dose-response curves of enzymatic mTOR kinase inhibition by the racemate of M4076. Data represent the mean ± s.e.m. from n = 1 experiment performed in duplicate for the racemate of M4076 (IC50 > 30,000 nM). (**e**)Dose-response curves of enzymatic inhibition of recombinant PIK3 kinases p110α/p85α, p110β/p85α, p120γ, and p110δ/p85α by the racemate of M4076. Data represent the mean ± s.e.m. from n = 1 experiment performed in duplicates for the racemate of M4076 (IC50 values above 8.5 μM). (**f**)Dose-response curves of enzymatic inhibition of recombinant PIK3 kinases p110α/p85α, p110β/p85α, p120γ, and p110δ/p85α by KU-55933. Data represent the mean ± s.e.m. from n = 1 experiment performed in duplicates (PIK3 isoforms α, β and δ: IC50 values ~2 μM; PI3Kγ: IC50 = 14 μM). (**g**) Reaction Biology Corporation (RBC) kinase selectivity profiles of 583 kinases for M4076 tested at 1 μM. Segment sizes of pie chart represent numbers of 583 kinases from RBC panel and ATM in addition with IC50 ranges (cyan: 96% of the tested 583 kinases showed kinase activity values above 50% corresponding to IC50 values above 1,000 nM; dark blue: 10 kinases and their mutants, 22 kinases in total (3.8% out of 583 kinases tested) showed kinase activity values below 50% corresponding to IC50 values between 100–1000 nM). ATM is the only kinase with an IC50 value below 100 nM (0.2%). (**h**) IC50 values of M4076 determined for 10 kinases and their mutants, which showed kinase activity values below 50% tested at 1 μM M4076 in the RBC kinase selectivity profile against 583 kinases (22 kinases in total, corresponding to the dark blue segment in the Reaction Biology kinase selectivity pie chart in Extended Data Fig. 6g). 1: M4076 was tested in duplicate in a 10-dose IC50 mode with 3-fold serial dilution starting at 10 μM. Reactions were carried out at Km ATP concentrations of individual kinases according to the RBC Km binning structure. 2: The biochemical ATM IC50 value of 0.2 nM for M4076 was used for IC50-split calculation of individual kinases. (**i**) Sequence alignment of human ATM and PIK3 kinases p110α/p85α, p110β/p85α, p120γ, and p110δ/p85α active sites, coloured by conservation. Glycine-rich, catalytic and activation loops labelled. ATM residues forming hydrogen interactions with the inhibitor are marked with red dots, van der Waals interactions - yellow dots, and π-stacking interactions - black dot. Data for panels a-h are available as Source Data (Source Data Extended Data Fig. 6a-h).

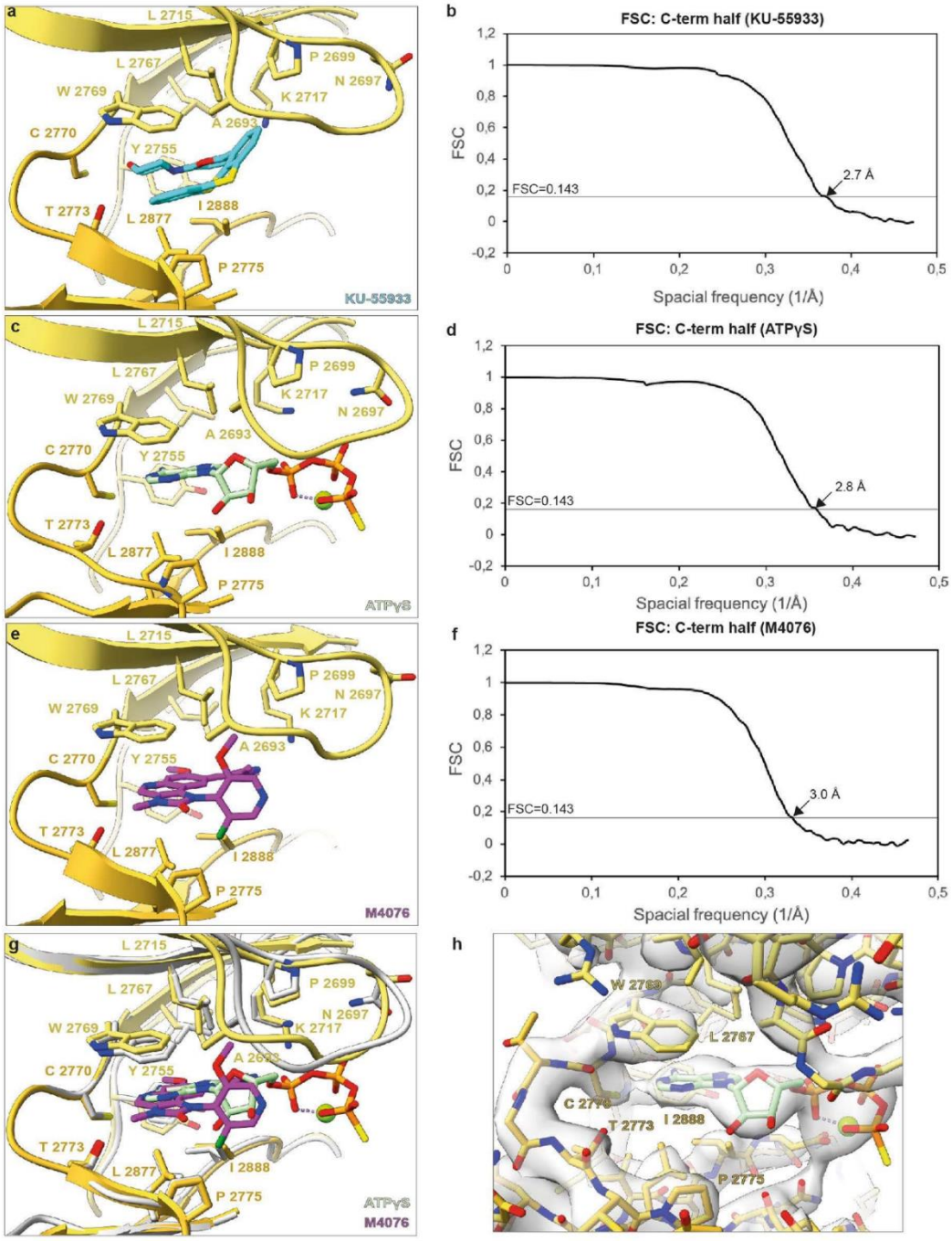

Extended Data Fig. 7 | Comparison of ATPγS-bound to KU-55933 and M4076 inhibited ATM kinase active sites. (**a**) Active site of KU-55933 (cyan) bound ATM (yellow) with highlighted surrounding residues. (**b**) Gold-standard Fourier shell correlation (FSC) curve from RELION-3.0 of the KU-55933 full ATM map. (**c**)Same as (A) with ATPγS (green, orange). (**d**) FSC curve from RELION-3.0 of the ATPγS bound ATM FATKIN map. (**e**)Same as (A) with M4076 (magenta). (**f**) FSC curve from CryoSPARC-2.14 of the M4076-bound ATM FATKIN map. (**g**) Superimposition of ATPγS (ATM in grey) and M4076 inhibitor (ATM in yellow) bound ATM active sites. (**h**) ATM active site density (grey, contoured at 0.0169) at 2.8 Å resolution with a fitted ATM model and ATPγS (orange, green).

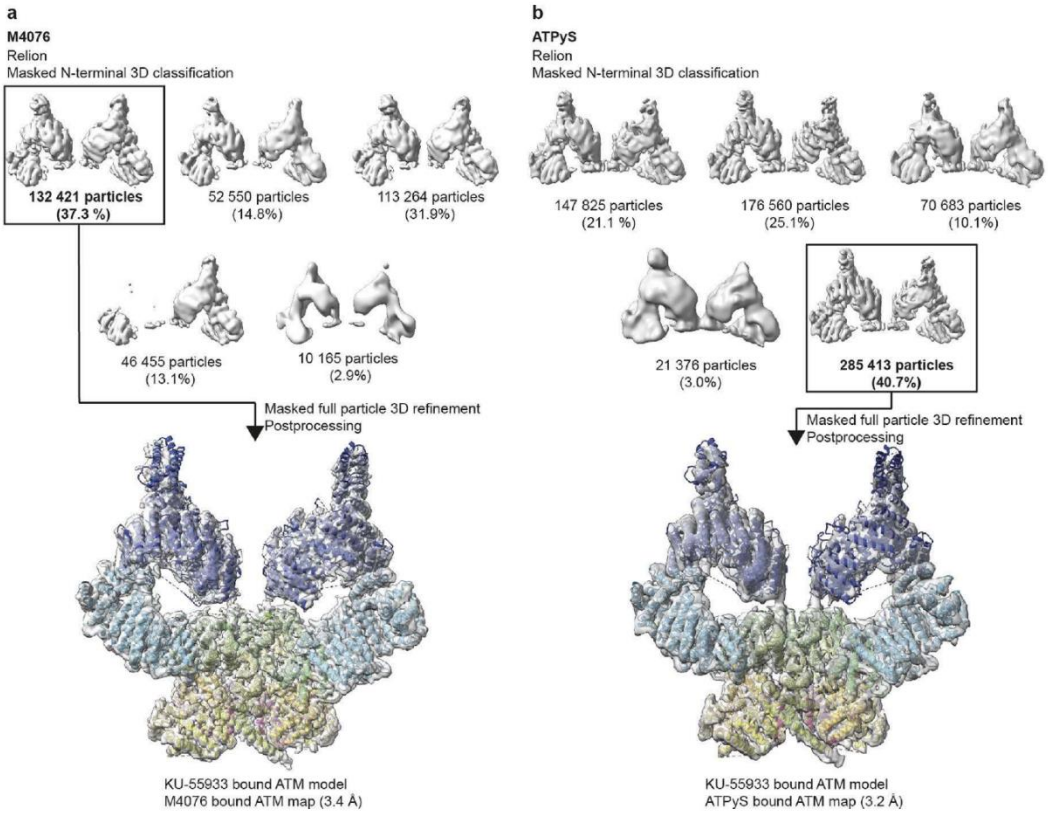

Extended Data Fig. 8 | N-terminal conformations of M4076 and ATPγS bound ATM. (**a**) Masked N-terminal 3D classification of M4076-bound ATM followed by further processing of dominant class and comparison to KU-55933 bound ATM conformation. (**b**) Masked N-terminal 3D classification of ATPγS bound ATM followed by further processing of dominant class and comparison to KU-55933 bound ATM conformation.

2.2 Structural mechanism of endonucleolytic processing of blocked DNA ends and hairpins by Mre11-Rad50

Fabian Gut*, Lisa Käshammer*, Katja Lammens, Joseph D. Bartho, Anna-Maria Boggusch, Erik van de Logt, Brigitte Kessler, Karl-Peter Hopfner, **Structural mechanism of endonucleolytic processing of blocked DNA ends and hairpins by Mre11-Rad50**, *Molecular Cell*, Volume 82, September 2022, Pages 3513-3522, https://doi.org/10.1016/j.molcel.2022.07.019

* These authors contributed equally.

Summary

In this manuscript we report the cryo-EM structures of the *E.coli* Mre11-Rad50 complex in its endonuclease and DNA hairpin-cleaving state. With these high-resolution structures and previous data from the exonuclease state, MR's DNA cleavage reaction can be summarized in a single, unified mechanism. MR in its ATP-bound state adopts an open Rad50 coiled-coil conformation with Mre11's nuclease domains blocked by the ATPase domain of Rad50. When the complex encounters DNA ends, the coiled-coils close while clamping the DNA in between. The two Mre11s translocate towards the side of the complex, positioning one active nuclease centre in close proximity to the DNA end backbone. This movement enables Mre11 to catalyse the hydrolysis reaction. Blocking the DNA ends with a bulky adduct such as Ku70/80, leads toward an inward movement of the Mre11 dimer to internal DNA regions. For hairpins, the Mre11 dimer moves in the same fashion towards the hairpin bubble.

Author contributions

I performed biochemical assays together with Fabian Gut, Lisa Käshammer and Anna-Maria Boggusch. Fabian Gut, Lisa Käshammer and Brigitte Kessler purified the proteins. Fabian Gut and Lisa Käshammer prepared cryo-EM grids, performed structure determination and modelling with the help of Katja Lammens and Joseph D. Bartho. Fabian Gut, Lisa Käshammer and Karl-Peter Hopfner analysed results. Karl-Peter Hopfner and Fabian Gut prepared the manuscript with contributions from all other authors.

Short article

Molecular Cell

Structural mechanism of endonucleolytic processing of blocked DNA ends and hairpins by Mre11-Rad50

Graphical abstract

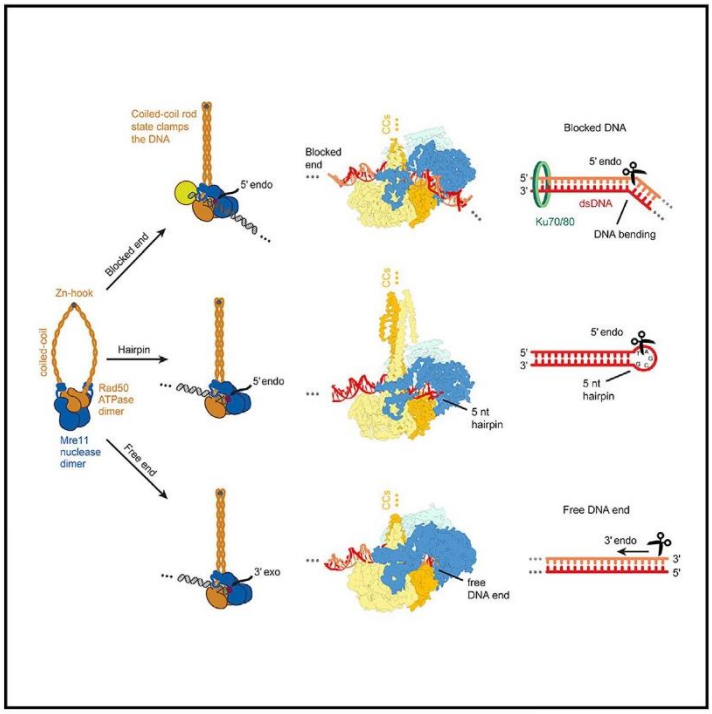

Highlights

- Cryo-EM structures of *Ec*Mre11-Rad50 bound to a protein-blocked DNA end and a hairpin
- A single structural framework unifying Mre11-Rad50's enigmatic nuclease diversity
- Mre11-Rad50 is loaded onto blocked DNA ends with Mre11 pointing away from the block
- Mre11-Rad50 strongly bends internal dsDNA for endonucleolytic cleavage

Authors

Fabian Gut, Lisa Käshammer, Katja Lammens, ..., Erik van de Logt, Brigitte Kessler, Karl-Peter Hopfner

Correspondence

hopfner@genzentrum.lmu.de

In brief

Gut et al. use cryoelectron microscopy and biochemical studies to reveal how the Mre11-Rad50 (MR) nuclease generates an endonucleolytic incision to remove protein blocks from a DNA double-strand break, providing also a unified mechanistic basis for MR's endonuclease, exonuclease, and hairpin-opening activities.

Gut et al., 2022, Molecular Cell *82*, 1–10
September 15, 2022
https://doi.org/10.1016/j.molcel.2022.07.019

CellPress

Please cite this article in press as: Gut et al., Structural mechanism of endonucleolytic processing of blocked DNA ends and hairpins by Mre11-Rad50, Molecular Cell (2022), https://doi.org/10.1016/j.molcel.2022.07.019

Molecular Cell

CellPress

Short article

Structural mechanism of endonucleolytic processing of blocked DNA ends and hairpins by Mre11-Rad50

Fabian Gut,[1,2,3] Lisa Käshammer,[1,2,3,4] Katja Lammens,[1,2] Joseph D. Bartho,[1,2] Anna-Maria Boggusch,[1,2] Erik van de Logt,[1,2] Brigitte Kessler,[1,2] and Karl-Peter Hopfner[1,2,5,*]

[1]Gene Center, Ludwig-Maximilians-Universität, 81377 Munich, Germany

[2]Department of Biochemistry, Ludwig-Maximilians-Universität, 81377 Munich, Germany

[3]These authors contributed equally

[4]Present address: MRC Laboratory of Molecular Biology, Structural Studies Division, Cambridge Biomedical Campus, Cambridge, UK

[5]Lead contact

*Correspondence: hopfner@genzentrum.lmu.de

https://doi.org/10.1016/j.molcel.2022.07.019

SUMMARY

DNA double-strand breaks (DSBs) threaten genome stability and are linked to tumorigenesis in humans. Repair of DSBs requires the removal of attached proteins and hairpins through a poorly understood but physiologically critical endonuclease activity by the Mre11-Rad50 complex. Here, we report cryoelectron microscopy (cryo-EM) structures of the bacterial Mre11-Rad50 homolog SbcCD bound to a protein-blocked DNA end and a DNA hairpin. The structures reveal that Mre11-Rad50 bends internal DNA for endonucleolytic cleavage and show how internal DNA, DNA ends, and hairpins are processed through a similar ATP-regulated conformational state. Furthermore, Mre11-Rad50 is loaded onto blocked DNA ends with Mre11 pointing away from the block, explaining the distinct biochemistries of 3′ → 5′ exonucleolytic and endonucleolytic incision through the way Mre11-Rad50 interacts with diverse DNA ends. In summary, our results unify Mre11-Rad50's enigmatic nuclease diversity within a single structural framework and reveal how blocked DNA ends and hairpins are processed.

INTRODUCTION

DNA double-strand breaks (DSBs) are a threat to genome integrity and cell viability and are linked to cancerogenesis in humans (Carbone et al., 2020). DSBs are repaired either by template-independent end-joining-type reactions (Chang et al., 2017; Della et al., 2004; Zhao et al., 2020) or by homology-directed repair (HDR) such as homologous recombination (Chen et al., 2018; Haber, 2018; Wright et al., 2018). Challenges for the repair of DSBs, which are formed by ionizing radiation, genotoxic chemicals, or various enzymatic processes, are obstructions in the form of chemical alterations, hairpins, or covalent protein adducts such as abortive topoisomerases (Johnson et al., 2021; Morimoto et al., 2019).

Obstructed DNA termini require processing by the Mre11-Rad50 (MR) complex, an ATP-dependent DSB sensor and nuclease that is found in all kingdoms of life (Hoa et al., 2016; Paull, 2018; Syed and Tainer, 2018). In eukaryotes, MR associates with Nbs1 to form the Mre11-Rad50-Nbs1 (MRN, MRX in yeast) complex (Carney et al., 1998), which is implicated in various DNA end reactions (Cejka and Symington, 2021; Delamarre et al., 2020; Kim et al., 2020; Marie and Symington, 2022), DNA damage signaling (Cassani et al., 2019; Hailemariam et al., 2019; Lee and Paull, 2005), and DNA tethering (Mojumdar et al., 2019; Seeber et al., 2016). The role of prokaryotic MR homologs (known as SbcCD in *Escherichia coli* [*E. coli*]) is less understood, but they are implicated in dealing with aberrant DNA structures formed by palindromes and over-replicated DNA (Eykelenboom et al., 2008; Wendel et al., 2018).

MR consists of two Rad50 ATP-binding cassette (ABC)-type ATPases and two Mre11 nucleases. Rad50 nucleotide binding domains (NBDs) together with Mre11 subunits assemble a DNA binding and processing "head" module (Hopfner et al., 2001). The 15–60 nm long Rad50 coiled-coil (CC) domains form long ring or rod structures, joined via an apical Zn-hook dimerization motif (Hopfner et al., 2002; Park et al., 2017). The ring shape is proposed to function as a topological gate to restrict nucleolytic cleavage to DSB and not intact genomic DNA. After DSB entry into the ring, the CCs switch to a rod and enable a cutting conformation of the head (Käshammer et al., 2019).

On clean DNA ends, MR/MRN possess 3′ → 5′ exonuclease activity (Paull and Gellert, 1998). Both MR and MRN can also open hairpin structures (Eykelenboom et al., 2008; Lobachev et al., 2002; Paull and Gellert, 1998). On blocked DNA ends, however, MR/MRN show 5′ endonuclease activity around 25–35 base pairs (bp) away from the block (Cannavo and Cejka, 2014; Deshpande et al., 2016). Furthermore, 3′ → 5′ back

Please cite this article in press as: Gut et al., Structural mechanism of endonucleolytic processing of blocked DNA ends and hairpins by Mre11-Rad50, Molecular Cell (2022), https://doi.org/10.1016/j.molcel.2022.07.019

resection from the 5′ nick toward the DNA end can generate short regions of ssDNA for the assembly of long-range resection machinery (Garcia et al., 2011; Mimitou and Symington, 2008), whereas repetitive endonuclease activity may lead to multiple incisions farther away from the block (Cannavo et al., 2019; Käshammer et al., 2019; Lim et al., 2015). *E. coli* MR (*Ec*MR) cleaves and possibly deprotects both 3′ and 5′ strands by generating a "clean" DSB (Connelly et al., 2003; Lim et al., 2015; Saathoff et al., 2018). A common basis for this broad and mechanistically confusing range of activities has not been established.

Recent work revealed how *Ec*MR binds a clean DNA end in 3′ exonuclease mode (Käshammer et al., 2019), but it remained unclear how physiologically more important endonuclease and hairpin-opening activities are carried out. Here, we use cryoelectron microscopy (cryo-EM) and biochemistry to investigate the *Ec*MR complex both in endonuclease and hairpin-opening states. Our results provide a structural basis for a unified nuclease mechanism of the Mre11-Rad50 complex through identification of a DNA cutting channel that can accommodate free DNA ends, hairpins, but—intriguingly—also bent internal sites of DNA. The mechanism can explain a broad range of prior biochemical data, for instance, the reversal of cleavage strands in 3′ exonuclease and 5′ endonuclease activities and the long cutting distances to the physical edge of the block.

RESULTS

Cryo-EM structure of *Ec*MR bound to a blocked DNA end in endonuclease mode

To reveal how Mre11-Rad50 detects obstructed DNA ends, we used cryo-EM and single-particle reconstruction on the *Ec*MR complex. We incubated 120 bp dsDNA with *Chaetomium thermophilum* Ku70/80 (Ku) to generate protein-blocked dsDNA ends (Figure 1A). Ku, a physiological block for eukaryotic MRN (Reginato et al., 2017; Wang et al., 2017), stimulates *Ec*MR's endonuclease similar to that of MRN (Käshammer et al., 2019). Compared with obstacles that are attached via a flexible linker to the 3′- or 5′-terminal base (e.g., DNA-biotin:streptavidin), DNA ends bound by the ring molecule Ku are cleaved farther inward, matching the DNA footprint of Ku (Käshammer et al., 2019). We incubated Ku-bound 120 bp DNA with the nuclease-deficient mutant *Ec*M^{H84Q}R (Figure S1A) and ATP prior to vitrification (Figure 1A), resulting in the three reconstructions: an *Ec*M^{H84Q}R endonucleolytic cutting state at 3.4 Å (Figures 1B, 1C, and S1; Tables 1 and S1), Ku bound to dsDNA at 3.5 Å (Figure S2), and a Ku-RM-MR-Ku state of two *Ec*M^{H84Q}R and Ku complexes bound to a single 120 bp dsDNA (Figure S2).

The 3.4 Å map showed a well-resolved *Ec*M^{H84Q}R catalytic head module bound to DNA. The overall architecture is similar to that in the exonuclease state (Käshammer et al., 2019, PDB: 6S85) (Figures 1B, 1C, and S3A). The Rad50^{NBDs} are dimerized and bind two Mg^{2+}-ADP. The CCs are in a rod configuration with a narrow opening for dsDNA next to the Rad50^{NBDs}. The Mre11 dimer is relocated from the autoinhibited state to one side of the Rad50^{NBD} dimer, forming a nuclease channel between one Mre11 (denoted "Mre11 (A)") and one Rad50 (denoted "Rad50 (A)") subunit. DNA binds along both Rad50^{NBDs} between the CCs and traverses the active site channel. In contrast to the exonuclease state, where the DNA ended at the nucleolytic di-metal center of *Ec*Mre11, we now see density for DNA that exits the channel on the other side (Figure 1B). A lower resolution reconstruction and LAFTER filtering resolved the extended path of DNA even further (Figure S1; Table 1), consistent with this configuration representing MR bound to internal DNA.

DNA in the endonuclease state forms more extensive contacts with Rad50 than the exonuclease state, since it also binds Rad50^{NBD} (B) at the exit of the nuclease channel. A symmetry-related site on Rad50^{NBD} (A) binds DNA on the distal site of the complex. Thus, only in the endonuclease all DNA binding sites on Rad50 are fully occupied (Figure S3A). DNA is well structured in the active site channel with a backbone phosphate contacting the di-metal moiety (likely Mn^{2+}). The metal coordination and active site geometry are very similar to that observed in the exonuclease state (Figures 1D and S3B), as well as in a high-resolution *Ec*Mre11 crystal structure in complex with Mn^{2+} in the absence of DNA (Liu et al., 2014; PDB: 4M0V). A water molecule, positionally inferred from the high-resolution crystal structure, would attack the DNA backbone in such a way as to cleave the 3′O–P bond, which is consistent with the biochemistry of the 5′ endonuclease and 3′ → 5′ exonuclease activities (Figures 1D and S3B) (Saathoff et al., 2018).

MR binds to free and blocked DNA ends with reversed polarity

It is yet unclear on which side of MR the block is located. To address this, we first biochemically assessed the binding of *Ec*M^{H84Q}R to the Ku-blocked dsDNA. Electrophoretic mobility shift assay (EMSA) showed efficient binding of *Ec*MR to both 2:1 and 1:1 Ku:DNA complexes with a saturating concentration of 40 nM *Ec*MR (Figure S3C). We also performed nuclease assays, which have shown that Ku efficiently stimulates the endonuclease activity of *Ec*MR, consistent with prior work (Käshammer et al., 2019). At a ratio of 2× Ku over DNA, we observe stimulation of endonuclease activity but also exonuclease products. Further, 4× Ku reduces exonuclease products and still leads to robust endonuclease, whereas 6× or higher Ku inhibits also endonuclease activity (Figure 1E). Likely, multiple Ku loading prevents *Ec*MR's DNA access (Bliss and Lane, 1997). The main endonuclease cleavage reactions are in the range of 30–45 bp (3′ 6-FAM label), which would correspond to a cleavage distance of 50–35 bp from the 5′ end. Please note that the endonuclease cleavage reactions around 45 bp might stem from 3′ endonuclease activities of *Ec*MR bound to the "other" end (Saathoff et al., 2018). Thus, Ku-bound DNA is an efficient endonuclease substrate for *Ec*MR.

To assess whether the block is situated at the Mre11 proximal or distal site, we made use of a subset of 2D classes that had two *Ec*MR complexes loaded onto a single DNA (Figure 1F). These particles led to an 8.2 Å reconstruction (Figure S2) that revealed the orientation of *Ec*MRs on the DNA and also showed density for Ku on both ends. We calculated a composite map combining the better-resolved individual reconstructions of Ku and *Ec*MR (Figures 1F, S1, and S2). Interestingly, both *Ec*MR complexes are oriented such that the Mre11 dimer points away from Ku, i.e., the Mre11 dimer is oriented on blocked DNA in

Please cite this article in press as: Gut et al., Structural mechanism of endonucleolytic processing of blocked DNA ends and hairpins by Mre11-Rad50, Molecular Cell (2022), https://doi.org/10.1016/j.molcel.2022.07.019

Molecular Cell
Short article

CellPress

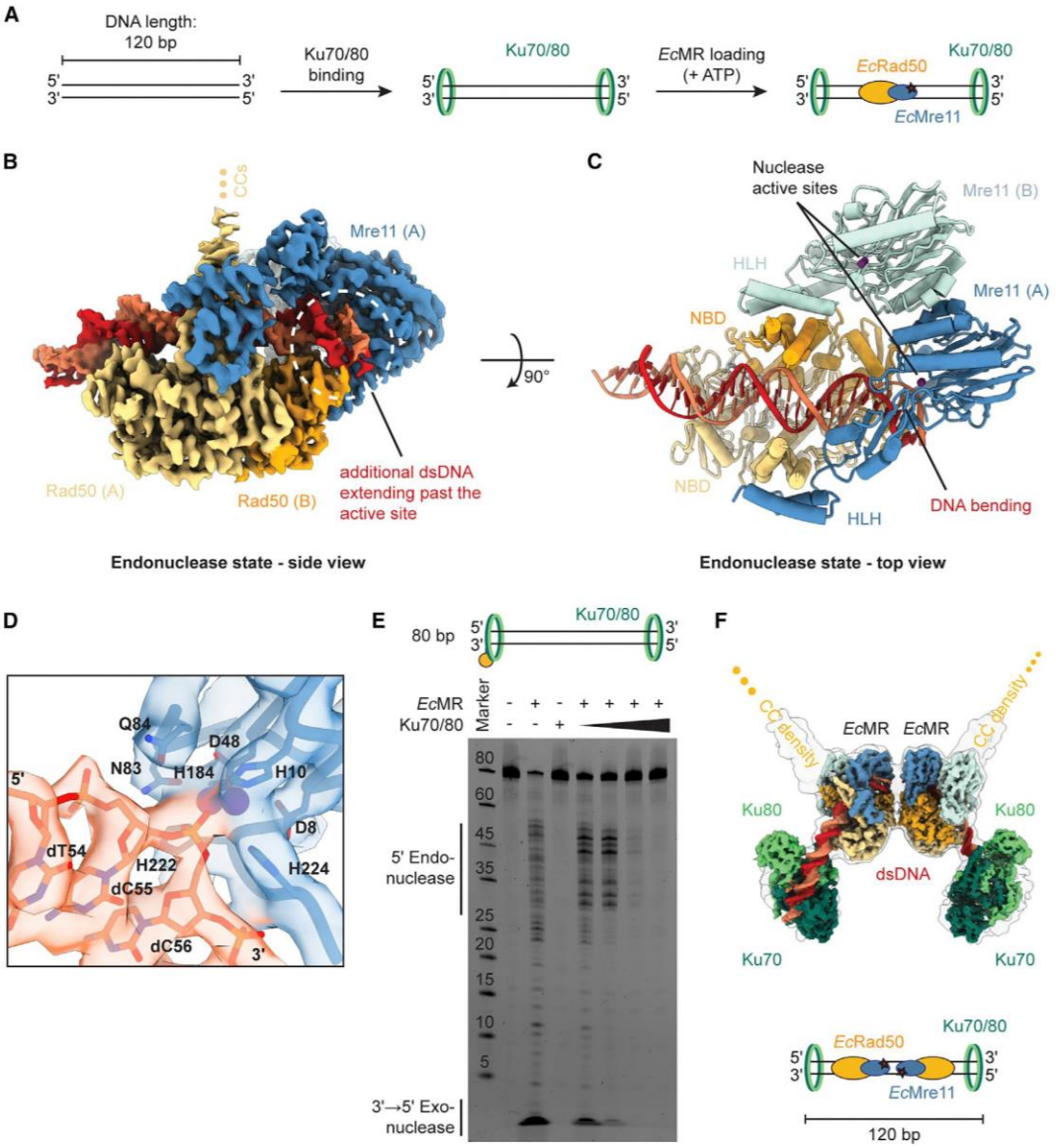

Figure 1. Structure and enzymatic activity of *Ec*Mre11-Rad50 in the endonuclease state

(A) Scheme of cryo-EM sample preparation to trap *Ec*MR in the endonuclease state.

(B) 3.4 Å density map of the *Ec*MR complex (Rad50 orange/yellow; Mre11 light/dark blue) bound to blocked DNA (red) in the endonuclease state. Rad50 and Mre11 dimers assemble a DNA channel that contains the nuclease active site. Extending coiled coils (CCs) are not resolved (dots).

(C) Atomic model of the endonuclease state.

(D) Nuclease active site of Mre11(A) in endonuclease state, (Mre11: blue; DNA: orange; Mn^{2+}: purple). Overlay: 3.4 Å cryo-EM map.

(E) Nuclease assay of *Ec*MR WT on an 80 bp 3′ 6-FAM-labeled, Ku-blocked DNA substrate with increasing excess of Ku over DNA (2×, 4×, 6×, and 10×), showing a strong reduction in endonuclease activity at higher Ku concentrations. Mild increase of Ku:DNA from 2× to 4× reduces unspecific nuclease products while the primary endonuclease activity remains intact.

(F) Composite map (top) and scheme (bottom) of the Ku-RM-MR-Ku assembly with two *Ec*MR complexes bound to one Ku-blocked 120 bp DNA. Semitransparent overlay: initial 8.2 Å cryo-EM map.

See also Figures S1 and S2, Table 1, and Video S1.

Please cite this article in press as: Gut et al., Structural mechanism of endonucleolytic processing of blocked DNA ends and hairpins by Mre11-Rad50, Molecular Cell (2022), https://doi.org/10.1016/j.molcel.2022.07.019

Table 1. Cryo-EM data collection, 3D reconstruction and model refinement statistics

	*Ec*MR endonuclease state (EMDB-14391) PDB: 7YZO	*Ec*MR endonuclease state with extended DNA (EMDB-14403) PDB: 7Z03	Ku-RM-MR-Ku state (EMDB-14392)	*Ec*MR hairpin-bound state (EMDB-14393) PDB: 7YZP	Ku70/80 DNA-bound state (EMDB-14394)
Data collection and processing					
Magnification	130,000	–	–	130,000	130,000
Voltage (kV)	300	–	–	300	300
Electron exposure (e-/Å^2)	44.68/44.90 45.27/37.92	–	–	46.60/47.01	44.68/44.90 45.27/37.92
Defocus range (μm)	−1.2 (−2.8)	–	–	−1.2 (−2.8)	−1.2 (−2.8)
Pixel size (Å)	1.059	–	–	1.059	1.059
Symmetry imposed	C1	–	–	C1	C1
Initial particle images (No.)	7,268,469	612,619	2,340,662	1,219,810	7,268,469
Final particle images (No.)	199,751	57,747	10,494	54,504	211,512
Map resolution (Å)	3.4	3.7	8.2	4.0	3.5
FSC threshold	0.143	0.143	0.143	0.143	0.143
Refinement					
Initial model (PDB code)	6S85	–	–	6S85/1DGO	–
Model resolution (Å)	3.5	–	–	4.1	–
FSC threshold	0.5	–	–	0.5	–
Map sharpening B factor (Å^2)	−119.2	–	–	−97.9	−96.9
Model composition					
Non-hydrogen atoms	13,072	13,072	–	14,101	–
Protein residues	1,497	1,497	–	1,633	–
Nucleic acid residues	62	78	–	59	–
Ligands					
Mn^{2+}	4	4	–	4	–
Mg^{2+}	2	2	–	2	–
ADP	2	2	–	2	–
dsDNA	1	1	–	1	–
RMSDs					
Bond lengths (Å)	0.004	–	–	0.002	–
Bond angles (°)	0.704	–	–	0.538	–
Validation					
MolProbity score	1.51	–	–	1.74	–
Clashscore	5.68	–	–	8.36	–
Poor rotamers (%)	0.08	–	–	0	–
Ramachandran plot					
Favored (%)	96.75	–	–	95.84	–
Allowed (%)	3.25	–	–	4.16	–
Disallowed (%)	0	–	–	0	–

endonuclease modes "inward" relative to the end. For comparison, it was oriented "outward" on a free DNA end (Figure S3D). *Ec*MR's active site is around ~55 nt from the 5′ end, which corresponds well to the ~50 nt incisions observed biochemically (Figure 1E), considering that there is still some space between Ku and *Ec*MR in these reconstructions.

The rather defined, central MR oligomer in the Ku-RM-MR-Ku assembly on the 120 bp DNA raises the question whether the RM:MR interaction is stable or merely a product of the molecular crowding on the short DNA. Using a 240 bp Ku-blocked dsDNA, we could not observe any 2D classes having multiple MR complexes. Thus, the interaction between adjacent *Ec*MR complexes is likely transient, if there is an interaction at all. We do not want to rule out other forms of oligomerization, for which there is at least evidence for eukaryotic MRN (Kissling et al., 2022; Moreno-Herrero et al., 2005).

A plausible explanation for the observed DNA Ku-RM-MR-Ku assembly is simultaneous loading of an MR complex from both

Please cite this article in press as: Gut et al., Structural mechanism of endonucleolytic processing of blocked DNA ends and hairpins by Mre11-Rad50, Molecular Cell (2022), https://doi.org/10.1016/j.molcel.2022.07.019

Molecular Cell
Short article

CellPress

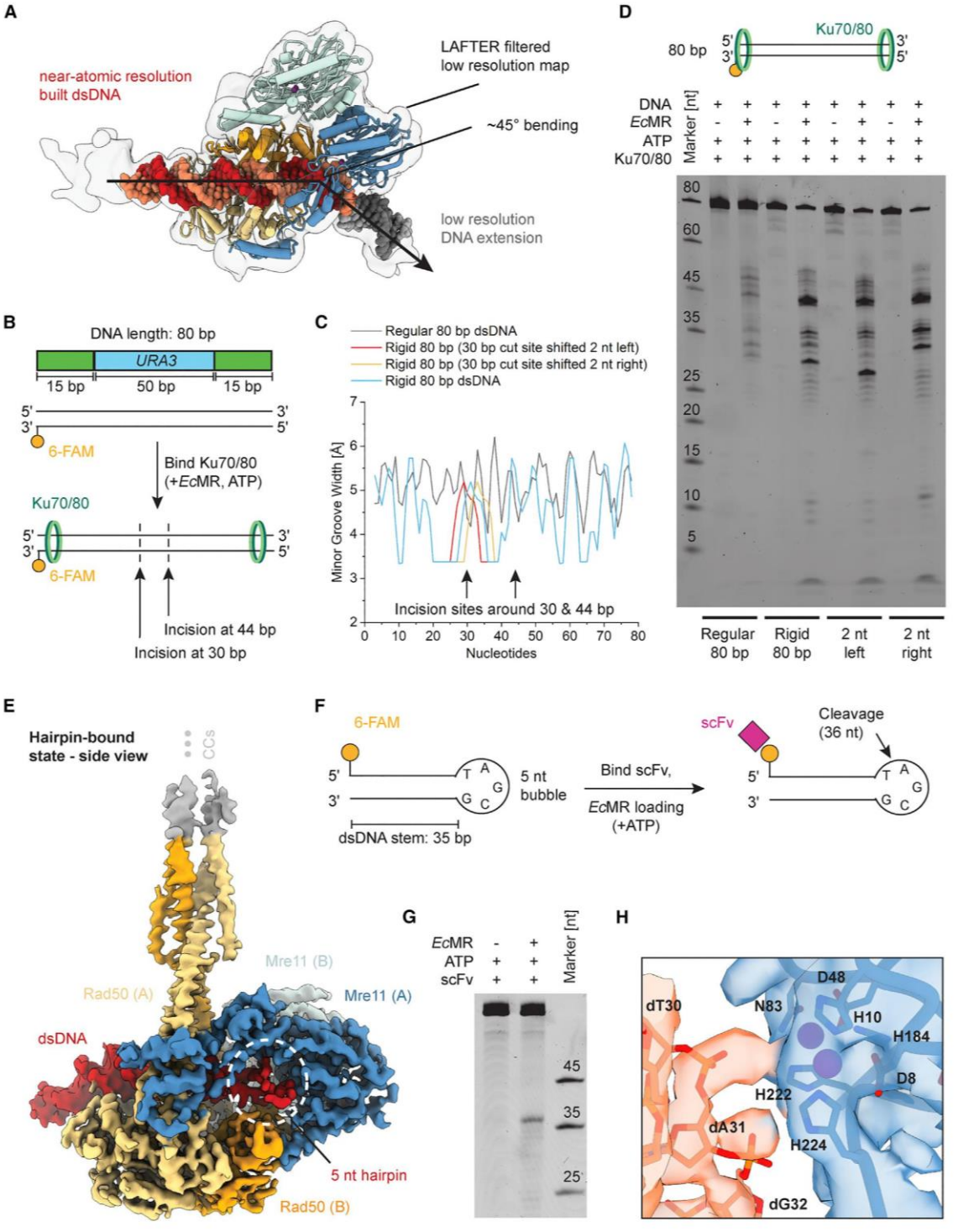

(legend on next page)

Please cite this article in press as: Gut et al., Structural mechanism of endonucleolytic processing of blocked DNA ends and hairpins by Mre11-Rad50, Molecular Cell (2022), https://doi.org/10.1016/j.molcel.2022.07.019

ends, resulting in the double-inward-facing RM:MR assembly. It should be noted that this is a result of the short two-ended DNA substrate; in a genomic context, *Ec*MR might only load unidirectionally and not form this RM-MR assembly. Nevertheless, the inward-facing configuration is consistent with and sufficient to explain a large body of biochemical data that showed differences between 3′ → 5′ exonuclease and 5′ endonuclease, such as cleavage site locations, cleavage chemistry, and strand preference. Thus, biochemical and topological differences between endonuclease and exonuclease are not caused by differences in the architecture of the underlying cutting states but by the polarity of how *Ec*MR binds at or near the DNA end.

MR bends DNA for endonucleolytic cutting

DNA passing through the active site channel is bent by ~45° (Figure 2A), which resolves our previous notation that linear continuation of DNA in the exonuclease structure would result in a clash with Mre11 (Käshammer et al., 2019). To interrogate the mechanistic relevance of DNA bending, we tested the effect of DNA mechanical properties through nuclease assays on rigid poly(dA·dT)-rich 80 bp dsDNA, based on the *URA3* promoter sequence (Rohs et al., 2009; Suter et al., 2000) (Figure 2B). The enhanced DNA rigidity is proposed to be a result of the reduced minor groove width of poly(dA·dT) (Figures 2C and S3E). *Ec*MR cleaves Ku-bound *URA3*-derived 80 bp dsDNA at two distinct positions, 30 and 44 nt from the labeled 3′ end (Figures 2B–2D), whereas a generic 80 bp dsDNA shows a broader cleavage pattern around 33 and 45 nt (Käshammer et al., 2019). The 30 and 44 nt sites in the *URA3*-derived dsDNA correspond to interspersed flexible regions within the poly(dA·dT) stretches, which have a predicted higher flexibility (Zhou et al., 2013) (Figures 2C and S3E). Intriguingly, shifting the predicted flexible region at 30 nt two nucleotides backward and forward resulted in respective 2 nt shifts of the preferential cleavage site at 30 nt, but not at 44 nt (Figures 2C, 2D, and S3E).

Cryo-EM structure of *Ec*MR bound to a hairpin

Besides free and protein-blocked DNA termini, a third, physiologically relevant, substrate for MR/MRN are hairpins (Connelly et al., 2003; Lim et al., 2015; Paull and Gellert, 1998; Trujillo and Sung, 2001). To determine the cryo-EM structure of the *Ec*MR complex bound to a dsDNA hairpin, we vitrified the *Ec*M^{H84Q}R mutant in the presence of ATP with a dsDNA hairpin, featuring a 35 bp stem and 5 nt loop (Figures 2E and S4). The 5′ 6-FAM-labeled hairpin substrate was incubated with a single-chain variable fragment (FAM-scFv) against fluorescein to block the other end (Figure 2F) (Pedrazzi et al., 1997). MR cleaves the hairpin with predominant incision in the loop, suggesting that *Ec*MR either preferentially loads directly onto the hairpin, or it is loaded onto the scFv-blocked end and slides (in inward conformation) a few bases to settle on the hairpin (Figures 2F, 2G, and S3F). The 4 Å reconstruction revealed again a structure that is very similar to endonuclease and exonuclease modes (Figures 2E and 2H). Density for DNA is well resolved at the nuclease active site. Compared with the exonuclease state, some additional density in the nuclease channel likely results from the hairpin loop (Figure S3G). At this stage, the map does not allow determination of the precise hairpin geometry, which might be flexible. However, the structural fitting is consistent with an incision occurring between the first two nucleotides of the hairpin loop, as determined by nuclease assays (Figures 2F–2H). As with the endonuclease state, clear density for both Mg^{2+}-ADP moieties in the Rad50^{NBDs} could be observed, indicating again a post-hydrolysis state.

After completion of exonuclease (Käshammer et al., 2019), endonuclease (this study), and hairpin (this study) states, we conclude that all of them involve a highly similar DNA-*Ec*MR geometry up to the DNA contacts at the di-metal center. Significant differences are only seen for the parts of DNA after the di-metal site, exiting the active site channel. The results show that MR's cutting channel can accommodate a wide range of DNA structures, while DNA cleavage is carried out by a highly similar MR conformation (Figure 3).

DISCUSSION

The Mre11-Rad50 complex detects and clears aberrant or blocked DNA termini to enable further repair and maintain genome integrity (Cejka and Symington, 2021; Paull, 2018; Syed and Tainer, 2018). To endonucleolytically cleave DNA at diverse termini, but not in intact genomic DNA, MR needs to topologically, but not chemically, recognize a particular block or DNA end. Such a topological recognition was indicated in a recent study, showing that DNA ends traverse a narrow channel formed by Mre11 and Rad50 to reach the nuclease site (Käshammer et al., 2019).

Here, we present structures of *Ec*MR bound to a blocked DNA end and a hairpin. MR's nuclease channel emerges as a versatile entity that can accommodate free ends, internal DNA, as well as hairpins, all recognized by a similar configuration of MR, consistent with the biochemically observed cleavage sites and chemistry (Saathoff et al., 2018). Thus, MR does not have different types of structurally distinct nuclease modes, rather the way MR is loaded onto DNA determines the mode of DNA cleavage. In

Figure 2. DNA bending in endonuclease state and structure of *Ec*MR in complex with a hairpin

(A) LAFTER-filtered map illustrates extended DNA and a 45° bending at the nuclease active site (map threshold of 0.0045).
(B) Schematic representation of the rigid poly(dA·dT) (T-tract) 80 bp dsDNA used to investigate DNA bending by *Ec*MRs.
(C) DNA shape predictions (Zhou et al., 2013), illustrating rigid and more flexible regions.
(D) Nuclease assay of *Ec*MR WT on different (regular and rigid) 3′ 6-FAM-labeled, Ku-blocked 80 bp DNA substrates (4:1 ratio Ku:DNA), showing predominant nuclease cleavage at sites consistent with more flexible regions, mapped in (C).
(E) 4 Å density map of the *Ec*MR complex bound to a DNA hairpin (red). Extending, but not resolved, CCs are depicted by the dots.
(F) Scheme illustrating the hairpin sample and experimental cleavage position.
(G) Nuclease assay of *Ec*MR WT on the 5′ 6-FAM-labeled, scFv-blocked DNA hairpin, showing predominant nuclease cleavage at 36 nt, as illustrated in (F).
(H) Nuclease active site of Mre11 (A) bound to a DNA hairpin (color code of Figure 1D). Overlay: 4 Å cryo-EM map.
See also Figures S1, S3, and S4, Table 1, and Video S1.

Please cite this article in press as: Gut et al., Structural mechanism of endonucleolytic processing of blocked DNA ends and hairpins by Mre11-Rad50, Molecular Cell (2022), https://doi.org/10.1016/j.molcel.2022.07.019

CellPress

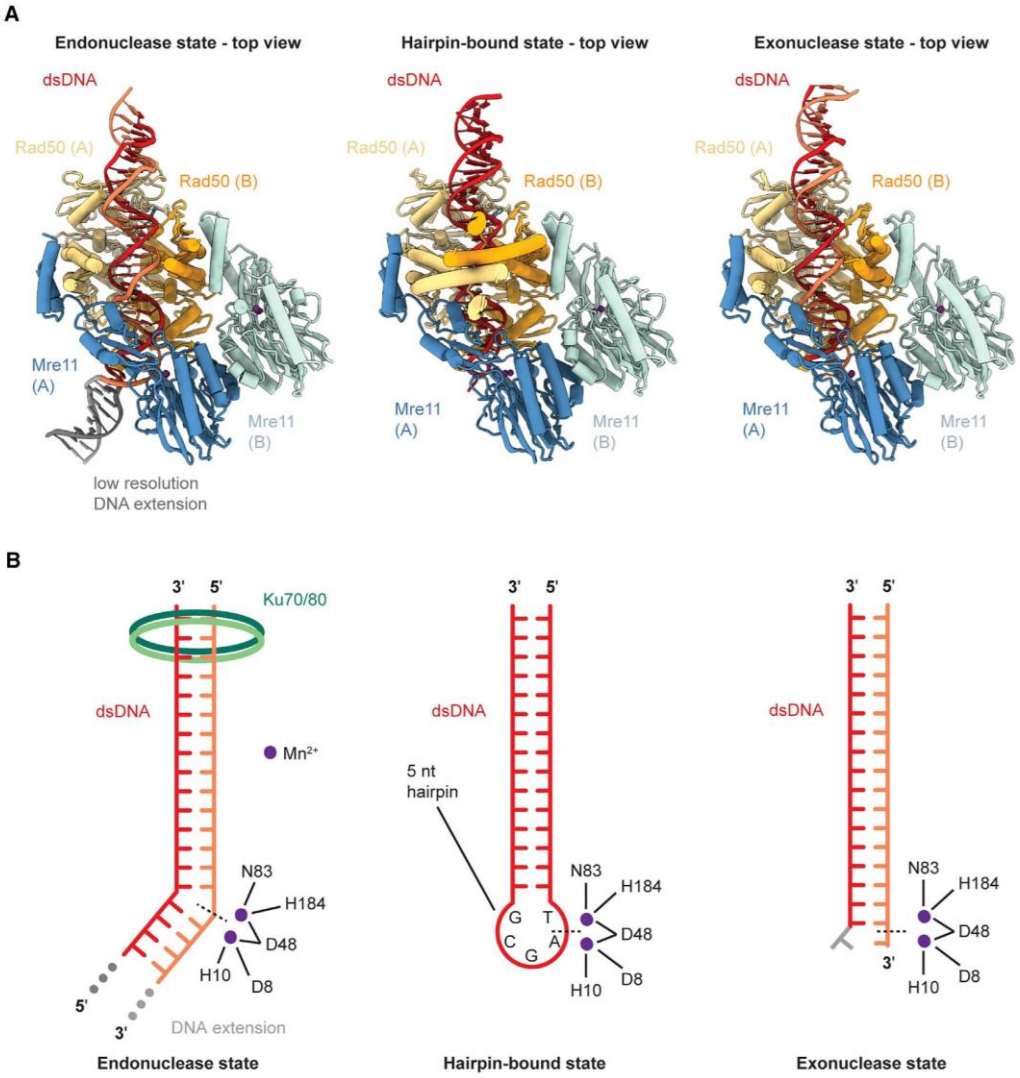

Figure 3. A unified nuclease mechanism as the basis for the processing of different DNA substrates

(A) Comparative view of all three nuclease active states of *Ec*MR shows a unified nuclease mechanism.

(B) Illustration of the nucleolytic cleavage positioning and active site residues on protein-blocked, hairpin, or free DNA termini.

See also Figure S3.

fact, our Ku-RM-MR-Ku structure points to an ATP-dependent loading reaction on Ku-bound DNA that leads to an inward-facing polarity where the Mre11 dimer is pointing away from the DSB. Based on the Ku-RM-MR-Ku structure (likely formed through symmetric loading of an inward-facing MR complex from either end), the inward-facing orientation of both *Ec*MRs positions the nuclease active site with ~55 nt from the 5′ end. Biochemically, we observe predominant 50 nt incisions, although they might be biased by local sequence/shape. Studies with MRX showed predominant cleavage at ~35 nt (Reginato et al., 2017; Wang et al., 2017), which one can achieve, based on our model, simply by sliding MR closer to Ku until the proteins almost touch.

The inward-facing configuration clarifies why in the endonuclease mode the 5′ strand is incised, whereas in the exonuclease mode (outward-facing configuration) it is the 3′ strand (Cannavo and Cejka, 2014; Deshpande et al., 2016). Furthermore, it explains the cleavage chemistry where in exonuclease mode, the phosphates are part of the leaving dNMPs, while in endonuclease mode, the phosphates remain attached to the newly formed DNA termini at the *Ec*MR-bound strand (Saathoff et al., 2018). Furthermore, the outward-facing orientation at the free end/hairpin may be a result of an inward-facing loading at the other end of the DNA oligos, followed by lateral sliding. So, it is possible that MR always loads with the same inward-facing polarity;

Please cite this article in press as: Gut et al., Structural mechanism of endonucleolytic processing of blocked DNA ends and hairpins by Mre11-Rad50, Molecular Cell (2022), https://doi.org/10.1016/j.molcel.2022.07.019

however, it may result in outward-facing polarity on the typical double-ended short DNA molecules used in biochemical assays. Structural alignments of human Rad50 and Mre11 AlphaFold2 models on the endonuclease-state structure further showed that the predicted human models are sterically able to adopt a very similar conformation than *Ec*MR (Figure S3H). Although details of the cutting state of eukaryotic MRN/X must await future experimental work, our proposed unified nuclease-cutting-state mechanism might be applicable to eukaryotic Mre11-Rad50 homologs.

An unexpected result was the DNA bending by MR in the endonuclease state. We estimate around 45°–50° in individual MR particles and Ku-MR-MR-Ku complexes, respectively. Several studies biochemically observed influence of DNA melting and unwinding in nuclease activities or DNA binding studies (Gobbini et al., 2018; Liu et al., 2016; Sharma et al., 2021; Zabolotnaya et al., 2020). We do not see evidence for active DNA melting in the endonuclease state, rather DNA is bent in a base-paired manner. However, as MR/MRN may form oligomers, DNA melting could take place in close vicinity or between complexes to compensate torsional stress forced onto the DNA. Internal bubbles or regions that are more easily meltable could also lead to preferential binding and cutting at these sites. Furthermore, the need for DNA bending could explain the promotion of endonuclease by a nick in the opposite strand (Deshpande et al., 2016). In any case, local DNA mechanical or shape properties, or the width of the minor groove, can apparently influence the position and effectivity of the DNA strand incision reaction. As these features can also be a function of local DNA sequence, an interesting area for future studies will be the physiological relevance of DNA mechanical properties or sequence in DSB processing by MRN/X. For instance, it could be linked to the recently observed local sequence-dependent cleavage of mitotic DSBs by MRX *in vivo* (Bazzano et al., 2021).

In summary, we reveal how MR structurally binds obstructed DNA termini and cuts them with endonuclease activity, unifying MR's distinct nuclease reactions in a common mechanistic framework.

Limitations of the study

We do not yet understand the precise mechanism of the ATP-dependent loading mechanism of Mre11-Rad50 onto DNA ends, why it cleaves near the DSB and does not slide inward, whether and how oligomerization is involved, and how MR additionally cleaves the 3′ strand opposing the 5′ incision with a different cleavage chemistry.

STAR★METHODS

Detailed methods are provided in the online version of this paper and include the following:

- KEY RESOURCES TABLE
- RESOURCE AVAILABILITY
  - Lead contact
  - Materials availability
  - Data and code availability
- EXPERIMENTAL MODEL AND SUBJECT DETAILS
  - Organisms as source for materials used in experiments
- METHOD DETAILS
  - Expression and purification of *Ec*MR
  - Expression and purification of Ku70/80
  - DNA substrates
  - Nuclease assay
  - Electrophoretic mobility shift assay (EMSA)
  - Grid preparation for cryo-electron microscopy
  - Electron microscopy data collection and processing
  - Model building
- QUANTIFICATION AND STATISTICAL ANALYSIS

SUPPLEMENTAL INFORMATION

Supplemental information can be found online at https://doi.org/10.1016/j.molcel.2022.07.019.

ACKNOWLEDGMENTS

EM data were collected at the Cryo-EM Core Facility of the Gene Center, Department of Biochemistry, LMU, Munich. We thank all members of the Hopfner lab for helpful discussions. K.-P.H. is supported by the Deutsche Forschungsgemeinschaft (CRC1361, HO2489/11-1) and the Gottfried-Wilhelm-Leibniz Prize. F.G. acknowledges the support from the Research Training Group 1721. L.K. acknowledges support from the International Max Planck Research School of Molecular and Cellular Life Sciences. K.L. is supported by the Deutsche Forschungsgemeinschaft (CRC1054, Project-ID 210592381) E.v.d.L. is supported by a PhD fellowship from Boehringer Ingelheim Fonds (BIF).

AUTHOR CONTRIBUTIONS

F.G. and L.K. prepared cryo-EM grids and performed structure determination and modeling. F.G., L.K., A.-M.B., and E.v.d.L. performed the biochemical analysis. F.G., L.K., and K.-P.H. analyzed results. F.G., L.K., and B.K. purified the proteins. K.L. and J.D.B. helped with data collection, structure determination, analysis, and modeling. K.-P.H. and F.G. wrote the paper with contributions from all other authors. K.-P.H. designed the overall study.

DECLARATION OF INTERESTS

The authors declare no competing interests.

Received: March 3, 2022
Revised: June 10, 2022
Accepted: July 23, 2022
Published: August 19, 2022

SUPPORTING CITATIONS

The following references appear in the supplemental information: Kashammer et al. (2019); Zhou et al. (2013); Tan et al. (2017); Evans et al., [https://doi.org/10.1101/2021.10.04].

REFERENCES

Afonine, P.V., Poon, B.K., Read, R.J., Sobolev, O.V., Terwilliger, T.C., Urzhumtsev, A., and Adams, P.D. (2018). Real-space refinement in PHENIX for cryo-EM and crystallography. Acta Crystallogr. D Struct. Biol. *74*, 531–544.

Asarnow, D., Palovcak, E., and Cheng, Y. (2019). UCSF pyem v0. 5. Zenodo. https://doi.org/10.5281/zenodo.3576630.

Bazzano, D., Lomonaco, S., and Wilson, T.E. (2021). Mapping yeast mitotic 5′ resection at base resolution reveals the sequence and positional dependence of nucleases in vivo. Nucleic Acids Res. *49*, 12607–12621.

Please cite this article in press as: Gut et al., Structural mechanism of endonucleolytic processing of blocked DNA ends and hairpins by Mre11-Rad50, Molecular Cell (2022), https://doi.org/10.1016/j.molcel.2022.07.019

Bepler, T., Morin, A., Rapp, M., Brasch, J., Shapiro, L., Noble, A.J., and Berger, B. (2019). Positive-unlabeled convolutional neural networks for particle picking in cryo-electron micrographs. Nat. Methods *16*, 1153–1160.

Bliss, T.M., and Lane, D.P. (1997). Ku selectively transfers between DNA molecules with homologous ends. J. Biol. Chem. *272*, 5765–5773.

Burnley, T., Palmer, C.M., and Winn, M. (2017). Recent developments in the CCP-EM software suite. Acta Crystallogr. D Struct. Biol. *73*, 469–477.

Cannavo, E., and Cejka, P. (2014). Sae2 promotes dsDNA endonuclease activity within Mre11-Rad50-Xrs2 to resect DNA breaks. Nature *514*, 122–125.

Cannavo, E., Reginato, G., and Cejka, P. (2019). Stepwise 5′ DNA end-specific resection of DNA breaks by the Mre11-Rad50-Xrs2 and Sae2 nuclease ensemble. Proc. Natl. Acad. Sci. USA *116*, 5505–5513.

Carbone, M., Arron, S.T., Beutler, B., Bononi, A., Cavenee, W., Cleaver, J.E., Croce, C.M., D'Andrea, A., Foulkes, W.D., Gaudino, G., et al. (2020). Tumour predisposition and cancer syndromes as models to study gene-environment interactions. Nat. Rev. Cancer *20*, 533–549.

Carney, J.P., Maser, R.S., Olivares, H., Davis, E.M., Le Beau, M., Yates, J.R., Hays, L., Morgan, W.F., and Petrini, J.H. (1998). The hMre11/hRad50 protein complex and Nijmegen breakage syndrome: linkage of double-strand break repair to the cellular DNA damage response. Cell *93*, 477–486.

Cassani, C., Vertemara, J., Bassani, M., Marsella, A., Tisi, R., Zampella, G., and Longhese, M.P. (2019). The ATP-bound conformation of the Mre11-Rad50 complex is essential for Tel1/ATM activation. Nucleic Acids Res. *47*, 3550–3567.

Cejka, P., and Symington, L.S. (2021). DNA end resection: mechanism and control. Annu. Rev. Genet. *55*, 285–307.

Chang, H.H.Y., Pannunzio, N.R., Adachi, N., and Lieber, M.R. (2017). Non-homologous DNA end joining and alternative pathways to double-strand break repair. Nat. Rev. Mol. Cell Biol. *18*, 495–506.

Chen, C.C., Feng, W., Lim, P.X., Kass, E.M., and Jasin, M. (2018). Homology-directed repair and the role of BRCA1, BRCA2, and related proteins in genome integrity and cancer. Annu. Rev. Cancer Biol. *2*, 313–336.

Connelly, J.C., de Leau, E.S., and Leach, D.R. (2003). Nucleolytic processing of a protein-bound DNA end by the E. coli SbcCD (MR) complex. DNA Repair (Amst) *2*, 795–807.

Croll, T.I. (2018). Isolde: a physically realistic environment for model building into low-resolution electron-density maps. Acta Crystallogr. D Struct. Biol. *74*, 519–530.

Delamarre, A., Barthe, A., de la Roche Saint-André, C., Luciano, P., Forey, R., Padioleau, I., Skrzypczak, M., Ginalski, K., Géli, V., Pasero, P., and Lengronne, A. (2020). MRX increases chromatin accessibility at stalled replication forks to promote nascent DNA resection and cohesin loading. Mol. Cell *77*, 395–410.e3.

Della, M., Palmbos, P.L., Tseng, H.M., Tonkin, L.M., Daley, J.M., Topper, L.M., Pitcher, R.S., Tomkinson, A.E., Wilson, T.E., and Doherty, A.J. (2004). Mycobacterial Ku and ligase proteins constitute a two-component NHEJ repair machine. Science *306*, 683–685.

Deshpande, R.A., Lee, J.H., Arora, S., and Paull, T.T. (2016). Nbs1 converts the human Mre11/Rad50 nuclease complex into an Endo/exonuclease machine specific for protein-DNA adducts. Mol. Cell *64*, 593–606.

Emsley, P., and Cowtan, K. (2004). Coot: model-building tools for molecular graphics. Acta Crystallogr. D Biol. Crystallogr. *60*, 2126–2132.

Evans, R., O'Neill, M., Pritzel, A., Antropova, N., Senior, A.W., Green, T., Žídek, A., Bates, R., Blackwell, S., and Yim, J. (2021). Protein complex prediction with AlphaFold-Multimer. BioRxiv.

Eykelenboom, J.K., Blackwood, J.K., Okely, E., and Leach, D.R. (2008). SbcCD causes a double-strand break at a DNA palindrome in the Escherichia coli chromosome. Mol. Cell *29*, 644–651.

Garcia, V., Phelps, S.E.L., Gray, S., and Neale, M.J. (2011). Bidirectional resection of DNA double-strand breaks by Mre11 and Exo1. Nature *479*, 241–244.

Ghosh, M., Vinay Kumar, N., Varshney, U., and Chary, K.V. (2000). Structural basis for uracil DNA glycosylase interaction with uracil: NMR study. Nucleic Acids Res. *28*, 1906–1912.

Gobbini, E., Vertemara, J., and Longhese, M.P. (2018). Local unwinding of double-strand DNA ends by the MRX complex promotes Exo1 processing activity. Mol. Cell. Oncol. *5*, e1511208.

Grant, T., Rohou, A., and Grigorieff, N. (2018). cisTEM, user-friendly software for single-particle image processing. eLife *7*, e35383.

Haber, J.E. (2018). DNA repair: the search for homology. BioEssays *40*, e1700229.

Hailemariam, S., Kumar, S., and Burgers, P.M. (2019). Activation of Tel11ATM kinase requires Rad50 ATPase and long nucleosome-free DNA but no DNA ends. J. Biol. Chem. *294*, 10120–10130.

Hoa, N.N., Shimizu, T., Zhou, Z.W., Wang, Z.Q., Deshpande, R.A., Paull, T.T., Akter, S., Tsuda, M., Furuta, R., Tsutsui, K., et al. (2016). Mre11 is essential for the removal of lethal topoisomerase 2 covalent cleavage complexes. Mol. Cell *64*, 1010.

Hopfner, K.P., Craig, L., Moncalian, G., Zinkel, R.A., Usui, T., Owen, B.A.L., Karcher, A., Henderson, B., Bodmer, J.L., McMurray, C.T., et al. (2002). The Rad50 zinc-hook is a structure joining Mre11 complexes in DNA recombination and repair. Nature *418*, 562–566.

Hopfner, K.P., Karcher, A., Craig, L., Woo, T.T., Carney, J.P., and Tainer, J.A. (2001). Structural biochemistry and interaction architecture of the DNA double-strand break repair Mre11 nuclease and Rad50-ATPase. Cell *105*, 473–485.

Johnson, D., Crawford, M., Cooper, T., Claeys Bouuaert, C., Keeney, S., Llorente, B., Garcia, V., and Neale, M.J. (2021). Concerted cutting by Spo11 illuminates meiotic DNA break mechanics. Nature *594*, 572–576.

Jumper, J., Evans, R., Pritzel, A., Green, T., Figurnov, M., Ronneberger, O., Tunyasuvunakool, K., Bates, R., Žídek, A., Potapenko, A., et al. (2021). Highly accurate protein structure prediction with AlphaFold. Nature *596*, 583–589.

Käshammer, L., Saathoff, J.H., Lammens, K., Gut, F., Bartho, J., Alt, A., Kessler, B., and Hopfner, K.P. (2019). Mechanism of DNA end sensing and processing by the Mre11-Rad50 complex. Mol. Cell *76*, 382–394.e6.

Kim, J.J., Lee, S.Y., Choi, J.H., Woo, H.G., Xhemalce, B., and Miller, K.M. (2020). PCAF-mediated histone acetylation promotes replication fork degradation by MRE11 and EXO1 in BRCA-deficient cells. Mol. Cell *80*, 327–344.e8.

Kissling, V.M., Reginato, G., Bianco, E., Kasaciunaite, K., Tilma, J., Cereghetti, G., Schindler, N., Lee, S.S., Guérois, R., Luke, B., et al. (2022). Mre11-Rad50 oligomerization promotes DNA double-strand break repair. Nat. Commun. *13*, 2374.

Lee, J.H., and Paull, T.T. (2005). ATM activation by DNA double-strand breaks through the Mre11-Rad50-Nbs1 complex. Science *308*, 551–554.

Liebschner, D., Afonine, P.V., Baker, M.L., Bunkóczi, G., Chen, V.B., Croll, T.I., Hintze, B., Hung, L.W., Jain, S., McCoy, A.J., et al. (2019). Macromolecular structure determination using X-rays, neutrons and electrons: recent developments in Phenix. Acta Crystallogr. D Struct. Biol. *75*, 861–877.

Lim, C.T., Lai, P.J., Leach, D.R., Maki, H., and Furukohri, A. (2015). A novel mode of nuclease action is revealed by the bacterial Mre11/Rad50 complex. Nucleic Acids Res. *43*, 9804–9816.

Liu, S., Tian, L.F., Liu, Y.P., An, X.M., Tang, Q., Yan, X.X., and Liang, D.C. (2014). Structural basis for DNA recognition and nuclease processing by the Mre11 homologue SbcD in double-strand breaks repair. Acta Crystallogr. D Biol. Crystallogr. *70*, 299–309.

Liu, Y., Sung, S., Kim, Y., Li, F., Gwon, G., Jo, A., Kim, A.K., Kim, T., Song, O.K., Lee, S.E., and Cho, Y. (2016). ATP-dependent DNA binding, unwinding, and resection by the Mre11/Rad50 complex. EMBO J. *35*, 743–758.

Lobachev, K.S., Gordenin, D.A., and Resnick, M.A. (2002). The Mre11 complex is required for repair of hairpin-capped double-strand breaks and prevention of chromosome rearrangements. Cell *108*, 183–193.

Marie, L., and Symington, L.S. (2022). Mechanism for inverted-repeat recombination induced by a replication fork barrier. Nat. Commun. *13*, 32.

Please cite this article in press as: Gut et al., Structural mechanism of endonucleolytic processing of blocked DNA ends and hairpins by Mre11-Rad50, Molecular Cell (2022), https://doi.org/10.1016/j.molcel.2022.07.019

Mimitou, E.P., and Symington, L.S. (2008). Sae2, Exo1 and Sgs1 collaborate in DNA double-strand break processing. Nature *455*, 770–774.

Mojumdar, A., Sorenson, K., Hohl, M., Toulouze, M., Lees-Miller, S.P., Dubrana, K., Petrini, J.H.J., and Cobb, J.A. (2019). Nej1 interacts with Mre11 to regulate tethering and Dna2 binding at DNA double-strand breaks. Cell Rep. *28*, 1564–1573.e3.

Moreno-Herrero, F., de Jager, M., Dekker, N.H., Kanaar, R., Wyman, C., and Dekker, C. (2005). Mesoscale conformational changes in the DNA-repair complex Rad50/Mre11/Nbs1 upon binding DNA. Nature *437*, 440–443.

Morimoto, S., Tsuda, M., Bunch, H., Sasanuma, H., Austin, C., and Takeda, S. (2019). Type II DNA topoisomerases cause spontaneous double-strand breaks in genomic DNA. Genes (Basel) *10*, 868.

Park, Y.B., Hohl, M., Padjasek, M., Jeong, E., Jin, K.S., Krężel, A., Petrini, J.H., and Cho, Y. (2017). Eukaryotic Rad50 functions as a rod-shaped dimer. Nat. Struct. Mol. Biol. *24*, 248–257.

Paull, T.T. (2018). 20 years of Mre11 biology: no end in sight. Mol. Cell *71*, 419–427.

Paull, T.T., and Gellert, M. (1998). The 3′ to 5′ exonuclease activity of Mre 11 facilitates repair of DNA double-strand breaks. Mol. Cell *1*, 969–979.

Pedrazzi, G., Schwesinger, F., Honegger, A., Krebber, C., and Plückthun, A. (1997). Affinity and folding properties both influence the selection of antibodies with the selectively infective phage (SIP) methodology. FEBS Lett. *415*, 289–293.

Pettersen, E.F., Goddard, T.D., Huang, C.C., Couch, G.S., Greenblatt, D.M., Meng, E.C., and Ferrin, T.E. (2004). UCSF Chimera–a visualization system for exploratory research and analysis. J. Comput. Chem. *25*, 1605–1612.

Pettersen, E.F., Goddard, T.D., Huang, C.C., Meng, E.C., Couch, G.S., Croll, T.I., Morris, J.H., and Ferrin, T.E. (2021). UCSF ChimeraX: structure visualization for researchers, educators, and developers. Protein Sci. *30*, 70–82.

Punjani, A., Rubinstein, J.L., Fleet, D.J., and Brubaker, M.A. (2017). cryoSPARC: algorithms for rapid unsupervised cryo-EM structure determination. Nat. Methods *14*, 290–296.

Punjani, A., Zhang, H., and Fleet, D.J. (2020). Non-uniform refinement: adaptive regularization improves single-particle cryo-EM reconstruction. Nat. Methods *17*, 1214–1221.

Ramlaul, K., Palmer, C.M., and Aylett, C.H.S. (2019). A local agreement filtering algorithm for transmission EM reconstructions. J. Struct. Biol. *205*, 30–40.

Reginato, G., Cannavo, E., and Cejka, P. (2017). Physiological protein blocks direct the Mre11-Rad50-Xrs2 and Sae2 nuclease complex to initiate DNA end resection. Genes Dev. *31*, 2325–2330.

Rohou, A., and Grigorieff, N. (2015). CTFFIND4: fast and accurate defocus estimation from electron micrographs. J. Struct. Biol. *192*, 216–221.

Rohs, R., West, S.M., Sosinsky, A., Liu, P., Mann, R.S., and Honig, B. (2009). The role of DNA shape in protein-DNA recognition. Nature *461*, 1248–1253.

Saathoff, J.H., Käshammer, L., Lammens, K., Byrne, R.T., and Hopfner, K.P. (2018). The bacterial Mre11-Rad50 homolog SbcCD cleaves opposing strands of DNA by two chemically distinct nuclease reactions. Nucleic Acids Res. *46*, 11303–11314.

Scheres, S.H. (2012). RELION: implementation of a Bayesian approach to cryo-EM structure determination. J. Struct. Biol. *180*, 519–530.

Seeber, A., Hegnauer, A.M., Hustedt, N., Deshpande, I., Poli, J., Eglinger, J., Pasero, P., Gut, H., Shinohara, M., Hopfner, K.P., et al. (2016). RPA mediates recruitment of MRX to forks and double-strand breaks to hold sister chromatids together. Mol. Cell *64*, 951–966.

Sharma, S., Anand, R., Zhang, X., Francia, S., Michelini, F., Galbiati, A., Williams, H., Ronato, D.A., Masson, J.Y., Rothenberg, E., et al. (2021). MRE11-RAD50-NBS1 complex is sufficient to promote transcription by RNA polymerase II at double-strand breaks by melting DNA ends. Cell Rep. *34*, 108565.

Suter, B., Schnappauf, G., and Thoma, F. (2000). Poly(dA.dT) sequences exist as rigid DNA structures in nucleosome-free yeast promoters in vivo. Nucleic Acids Res. *28*, 4083–4089.

Syed, A., and Tainer, J.A. (2018). The MRE11-RAD50-NBS1 complex conducts the orchestration of damage signaling and outcomes to stress in DNA replication and repair. Annu. Rev. Biochem. *87*, 263–294.

Tan, Y.Z., Baldwin, P.R., Davis, J.H., Williamson, J.R., Potter, C.S., Carragher, B., and Lyumkis, D. (2017). Addressing preferred specimen orientation in single-particle cryo-EM through tilting. Nat. Methods *14*, 793–796.

Trujillo, K.M., and Sung, P. (2001). DNA structure-specific nuclease activities in the Saccharomyces cerevisiae Rad50*Mre11 complex. J. Biol. Chem. *276*, 35458–35464.

Wang, W., Daley, J.M., Kwon, Y., Krasner, D.S., and Sung, P. (2017). Plasticity of the Mre11-Rad50-Xrs2-Sae2 nuclease ensemble in the processing of DNA-bound obstacles. Genes Dev. *31*, 2331–2336.

Wendel, B.M., Cole, J.M., Courcelle, C.T., and Courcelle, J. (2018). SbcC-SbcD and ExoI process convergent forks to complete chromosome replication. Proc. Natl. Acad. Sci. USA *115*, 349–354.

Wood, C., Burnley, T., Patwardhan, A., Scheres, S., Topf, M., Roseman, A., and Winn, M. (2015). Collaborative computational project for electron cryo-microscopy. Acta Crystallogr. D Biol. Crystallogr. *71*, 123–126.

Wright, W.D., Shah, S.S., and Heyer, W.D. (2018). Homologous recombination and the repair of DNA double-strand breaks. J. Biol. Chem. *293*, 10524–10535.

Zabolotnaya, E., Mela, I., Williamson, M.J., Bray, S.M., Yau, S.K., Papatziamou, D., Edwardson, J.M., Robinson, N.P., and Henderson, R.M. (2020). Modes of action of the archaeal Mre11/Rad50 DNA-repair complex revealed by fast-scan atomic force microscopy. Proc. Natl. Acad. Sci. USA *117*, 14936–14947.

Zhao, B., Rothenberg, E., Ramsden, D.A., and Lieber, M.R. (2020). The molecular basis and disease relevance of non-homologous DNA end joining. Nat. Rev. Mol. Cell Biol. *21*, 765–781.

Zheng, S.Q., Palovcak, E., Armache, J.P., Verba, K.A., Cheng, Y., and Agard, D.A. (2017). MotionCor2: anisotropic correction of beam-induced motion for improved cryo-electron microscopy. Nat. Methods *14*, 331–332.

Zhou, T., Yang, L., Lu, Y., Dror, I., Dantas Machado, A.C., Ghane, T., Di Felice, R., and Rohs, R. (2013). DNAshape: a method for the high-throughput prediction of DNA structural features on a genomic scale. Nucleic Acids Res. *41*, W56–W62.

Please cite this article in press as: Gut et al., Structural mechanism of endonucleolytic processing of blocked DNA ends and hairpins by Mre11-Rad50, Molecular Cell (2022), https://doi.org/10.1016/j.molcel.2022.07.019

STAR★METHODS

KEY RESOURCES TABLE

REAGENT or RESOURCE	SOURCE	IDENTIFIER
Chemicals, peptides, and recombinant proteins		
ATP	Sigma (Merck)	A3377
ATPγS	Sigma (Merck)	A1388
2-Mercaptoethanol	Carl-Roth	4227
DTT	Carl Roth	6908
Imidazole	Carl Roth	3899
β-Octylglycoside	Sigma (Merck)	O8001
BSA	New England bioLabs	B9000S
6-FAM scFv	Prof. Dr. Plückthun, University of Zürich (Pedrazzi et al., 1997)	N/A
Urea	Carl Roth	3941
EDTA	VWR International	6381-92-6
Ficoll 400	Carl Roth	CN90.3
Rotiphorese DNA sequencing system	Carl Roth	A431.1
$MgCl_2$	Merck	7791-18-6
$MnCl_2$	Sigma (Merck)	M3634
TCEP	Sigma (Merck)	646547
SIGMAFAST Protease Inhibitor Cocktail Tablet, EDTA free	Merck	S8830
Deposited data		
*Ec*MR coordinates (Endonuclease state)	This Paper	PDB: 7YZO
*Ec*MR head EM map (Endonuclease state)	This Paper	EMDB-14391
*Ec*MR head coordinates with extended DNA (Endonuclease state)	This Paper	PDB: 7Z03
*Ec*MR head EM map with extended DNA (Endonuclease state)	This Paper	EMDB-14403
Ku70/80 (bound to dsDNA) EM map	This Paper	EMDB-14394
Ku-RM-MR-Ku state EM map	This Paper	EMDB-14392
Ku-RM-MR-Ku state EM composite map	This Paper	EMDB-14392
*Ec*MR coordinates (Hairpin-bound)	This Paper	PDB: 7YZP
*Ec*MR head EM map (Hairpin-bound)	This Paper	EMDB-14393
Full Gel Images	This Paper	https://doi.org/10.17632/kdvrdjvz7d.1
Experimental models: Organisms/strains		
E. coli XL1 Blue	Expression System	N/A
E. coli Rosetta2	Expression System	N/A
E. coli BL21 (DE3)	Expression System	N/A
Spodoptera frugiperda sf21 cells	Expression System	N/A
Trichoplusia ni cells	Expression System	N/A
Oligonucleotides		
Oligonucleotides	Metabion	See Table S1
Primer	Metabion	See Table S1
Recombinant DNA		
pET21b-*Ec*Mre11	Saathoff et al., 2018	N/A
pET29-*Ec*Rad50	Saathoff et al., 2018	N/A

(*Continued on next page*)

Please cite this article in press as: Gut et al., Structural mechanism of endonucleolytic processing of blocked DNA ends and hairpins by Mre11-Rad50, Molecular Cell (2022), https://doi.org/10.1016/j.molcel.2022.07.019

Continued

REAGENT or RESOURCE	SOURCE	IDENTIFIER
pACEBac1-pIDK-*Ct*Ku70/80	Käshammer et al., 2019	N/A
Software and algorithms		
MotionCor2	Zheng et al., 2017	https://msg.ucsf.edu/em/software/motioncor2.html
CTFFIND4.1	Rohou and Grigorieff, 2015	http://grigoriefflab.janelia.org/ctffind4
Relion 3.0.8	Scheres, 2012	https://www3.mrc-lmb.cam.ac.uk/relion/index.php?title=Main_Page
Phenix	Afonine et al., 2018; Liebschner et al., 2019	https://www.phenix-online.org/
UCSF Chimera	Pettersen et al., 2004	https://www.cgl.ucsf.edu/chimera/
ChimeraX	Pettersen et al., 2021	https://www.rbvi.ucsf.edu/chimerax/
COOT	Emsley and Cowtan, 2004	https://www2.mrc-lmb.cam.ac.uk/Personal/pemsley/coot/
OriginPro	OriginLab	N/A
CryoSPARC v3.2.0	Punjani et al., 2017	https://cryosparc.com/
Topaz	Bepler et al., 2019	https://emgweb.nysbc.org/topaz.html
CisTEM v1.0.2	Grant et al., 2018	https://cistem.org/
High-throughput DNA Shape Prediction	Zhou et al., 2013	https://rohslab.usc.edu/DNAshape/index.html
AlphaFold v2.1.0	Jumper et al., 2021	https://colab.research.google.com/github/deepmind/alphafold/blob/main/notebooks/AlphaFold.ipynb
CCP-EM	Burnley et al., 2017	https://www.ccpem.ac.uk/
LAFTER v1.1	Ramlaul et al., 2019	https://github.com/StructuralBiology-ICLMedicine/lafter
pyEM v0.5	Asarnow et al., 2019	https://github.com/asarnow/pyem/tree/v0.5
ISOLDE	Croll, 2018	https://isolde.cimr.cam.ac.uk/static/isolde/doc/isolde.html
3DFSC	Tan et al., 2017	https://3dfsc.salk.edu/

RESOURCE AVAILABILITY

Lead contact

Further information and requests for resources and reagents should be directed to and will be fulfilled by the lead contact Karl-Peter Hopfner (hopfner@genzentrum.lmu.de).

Materials availability

This study did not generate new unique reagents.

Data and code availability

- The coordinate files generated during this study are available at the Protein Data Bank (https://www.rcsb.org/) with the accession codes PDB: 7YZO (Endonuclease state), PDB: 7Z03 (Endonuclease state with extended DNA) and PDB: 7YZP (Hairpin-bound state). The cryo-EM reconstructions generated during this study are available at the Electron Microscopy Data Bank (https://www.ebi.ac.uk/pdbe/emdb/) with the accession codes EMDB: EMD-14391 (Endonuclease state head complex at 3.4 Å), EMDB: EMD-14403 (LAFTER-filtered endonuclease state head complex with extended DNA), EMDB: EMD-14392 (Composite map and Ku-RM-MR-Ku state at 8.2 Å), EMDB: EMD-14394 (Ku70/80 bound to dsDNA at 3.5 Å) and EMDB: EMD-14393 (Hairpin-bound state head complex at 4 Å). Full gel images are deposited under the following https://doi.org/10.17632/kdvrdjvz7d.1.
- This paper does not report original code.
- Any additional information required to reanalyse the data reported in this paper is available from the lead contact upon request.

Please cite this article in press as: Gut et al., Structural mechanism of endonucleolytic processing of blocked DNA ends and hairpins by Mre11-Rad50, Molecular Cell (2022), https://doi.org/10.1016/j.molcel.2022.07.019

CellPress

EXPERIMENTAL MODEL AND SUBJECT DETAILS

Organisms as source for materials used in experiments

E. coli XL1 Blue cells were used for amplification of plasmid DNA.
E. coli BL21 (DE3) and *E. coli* Rosetta2 were used for recombinant protein expression.
Spodoptera frugiperda sf21 insect cells were used for virus production.
Trichoplusia ni insect cells were used for recombinant protein expression.

METHOD DETAILS

Expression and purification of *Ec*MR

Expression and purification of full-length *Ec*Mre11 (pET21b expression vector; C-terminal 6xHis-tag) and *Ec*Rad50 (pET29 expression vector) was performed as described in a previous publication (Käshammer et al., 2019). Both expression vectors were co-transfected into *E. coli* BL21 (DE3) or Rosetta2 bacterial cells for protein expression. Bacterial cultures were grown in LB media at 37°C to an OD_{600} of 0.6. Protein expression was induced using 0.5 mM IPTG and carried out at 18°C for 16 hours. Cells were harvested by centrifugation and resuspended in lysis buffer (25 mM Tris pH 7.5, 150 mM NaCl, 10 mM Imidazole, 5 mM β-Mercaptoethanol) before cell disruption by sonication. Cell lysate was cleared by centrifugation and the supernatant was applied onto 2.5 mL of pre-equilibrated Ni-NTA resin (QIAGEN). The protein immobilized on the resin was then washed with 20 mL lysis buffer and 25 mL wash buffer (25 mM Tris pH 7.5, 125 mM NaCl, 20 mM Imidazole and 5 mM β-Mercaptoethanol). Captured protein was eluted with 10 mL elution buffer (25 mM Tris pH 7.5, 100 mM NaCl, 200 mM Imidazole and 5 mM β-Mercaptoethanol) and loaded onto a 1 mL HiTrapQ column (GE). Elution from the anion exchange column was done by a step gradient with increasing salt concentration (Buffer A: 100 mM NaCl, 25 mM Tris pH 7.5, Buffer B: 1 M NaCl, 25 mM Tris pH 7.5). Ion exchange chromatography peak fractions were pooled, concentrated and purified via size-exclusion chromatography using a Superose 6 10/300 (GE Healthcare) column pre-equilibrated in size-exclusion buffer (125 mM NaCl, 20 mM Tris pH 7.5, 10% Glycerol). The protein fractions of interest were identified by SDS-PAGE, pooled, concentrated and stored at -80°C.

Expression and purification of Ku70/80

Expression and purification of full-length *Chaetomium thermophilum* Ku70/80 was performed as described in a previous publication (Käshammer et al., 2019). Codon-optimized synthetic DNA (Genscript, Piscataway, USA) encoding Ku70 (N-terminal human rhinovirus 3C-protease cleavable 6xHis-tag) and Ku80 was PCR amplified and cloned into pACEBac1 and pIDC respectively and expressed using the MultiBac technology. Recombination steps were carried out in *E. coli* XL1 Blue cells under addition of Cre recombinase (NEB). Baculovirus generation was done in *Spodoptera frugiperda* (sf21) insect cells (IPLB-Sf21AE). For protein expression, *Trichoplusia ni* High Five cells were co-infected using 1:5000 of baculovirus. Cells were cultured for 72 hours at 27°C and harvested by centrifugation. Cells were re-suspended in lysis buffer (50 mM HEPES pH 7.5, 1 M NaCl, 400 mM NH_4OAc, 5% glycerol, 0.5 mM TCEP supplemented with a SIGMAFAST Protease Inhibitor Cocktail Tablet, EDTA free (Merck)) and gently sonified for cell disruption. The lysate was incubated for 1 hour at 50°C and subsequently cleared by centrifugation at 34500 g and 4°C for 30 min. The cleared supernatant was applied onto 2 mL of pre-equilibrated Ni-NTA (QIAGEN) and the immobilized protein was then washed with 20 mL wash buffer (50 mM HEPES pH 7.5, 250 mM NaCl, 10 mM Imidazole and 0.5 mM TCEP). The protein was eluted in 10 mL elution buffer (50 mM HEPES pH 7.5, 250 mM NaCl, 500 mM Imidazole and 0.5 mM TCEP) before cleavage of the affinity tag by overnight incubation with human rhinovirus 3C-protease at 4°C during dialysis into low salt buffer (50 mM HEPES pH 7.5, 150 mM NaCl and 0.5 mM TCEP). The filtered protein was then loaded onto a 5 mL HiTrap Heparin HP column (GE Healthcare), equilibrated in dialysis buffer and eluted with an increasing salt gradient before purification via size-exclusion chromatography using a Superose 6 16/60 (GE Healthcare) column equilibrated in size-exclusion buffer (20 mM HEPES pH 7.5, 200 mM NaCl and 0.5 mM TCEP). Protein fractions of interest were identified by SDS-PAGE, pooled, concentrated and stored at -80°C.

DNA substrates

All oligonucleotides were purchased HPLC-purified from Metabion (Planegg, Germany) and additionally purified via PAGE if fluorescently labeled. For annealing, the complementary oligo mix was heated to 95°C and then slowly cooled down to 25°C with a gradual decrease of 0.1°C per second using a PCR cycler. Unlabeled oligos were mixed in a 1:1 ratio for annealing. If labeled oligos were used, a ratio of 1.1 to 1 of unlabeled to labeled was used. The used oligonucleotide sequences are listed in Table S1.

Nuclease assay

The nuclease reaction was carried out in assay buffer (25 mM Tris pH 7.5, 50 mM KCl, 5 mM $MgCl_2$, 2 mM $MnCl_2$, 0.2 mg/ml BSA,1 mM DTT, 1 mM ATP) with 250 nM *Ec*MR and 50 nM 6-FAM labeled 80 bp dsDNA or hairpin DNA substrate (Table S1). To investigate endonuclease activity of the *Ec*MR complex, the DNA termini of the 3′ 6-FAM labeled 80 bp dsDNA were blocked using 200 nM of Ku70/80 (4:1 ratio of Ku70/80:DNA), if not stated otherwise. Prior to the addition of *Ec*MR, the dsDNA was incubated with Ku70/80 for 30 min at 25°C. When using the 5′ 6-FAM labeled hairpin DNA, reactions were supplemented with a 15-fold excess of a single-chain variable fragment (scFv) against the 6-FAM label (Pedrazzi et al., 1997) to block the opposing dsDNA end. To ensure

Please cite this article in press as: Gut et al., Structural mechanism of endonucleolytic processing of blocked DNA ends and hairpins by Mre11-Rad50, Molecular Cell (2022), https://doi.org/10.1016/j.molcel.2022.07.019

binding of the scFv, the sample was incubated at 25°C for 15 to 30 min. The reaction was started by *Ec*MR addition and incubated at 37°C for 5 min. Reactions were terminated by mixing with an equal volume of loading buffer (8 M Urea, 20 mM EDTA, 6% Ficoll 400). Reaction products were resolved on 12% denaturing polyacrylamide gels (Rotiphorese DNAsequencing system) in 1x TBE buffer. Gels were run for 90 min at constant 32 W and scanned by a Typhoon fluorescence imager (GE healthcare) using a 473 nm Laser and 510 nm filter.

Electrophoretic mobility shift assay (EMSA)

For the EMSA of *Ec*MR (Mre11^{H84Q}, nuclease dead) with Ku70/80 end-blocked 120 bp dsDNA a 1:2 dilution series of *Ec*MR in assay buffer (50 mM KCl, 25 mM TRIS pH 7.5, 5 mM $MgCl_2$, 1 mM $MnCl_2$, 1 mM DTT, 0.2 mg/ml BSA, 5 mM ATP, 10% glycerol) was prepared ranging from 0 to 640 nM as final protein concentrations. The 5′ 6-FAM 120 bp dsDNA substrate was amplified by PCR from a pET21b expression vector using DNA primers (Table S1) purchased from Metabion (Planegg, Germany). For the 5′ 6-FAM labelled 120 bp dsDNA substrate a final concentration of 10 nM was used, incubated with a 2x molar excess of Ku70/80 to block the free DNA ends. The dsDNA:Ku70/80 mixture was incubated for 30 min at 25°C, before adding *Ec*MR. After addition of *Ec*MR, the reaction mix was incubated for additional 30 min at 25°C before loading onto a 4% non-denaturing acrylamide gel supplemented with 10 mM Mg-Acetate and 2 mM ATP. The acrylamide gels were run for 2 – 2.5 hours at 80V and 4°C using 0.5x TB running buffer supplemented with 10 mM Mg-Acetate.

Grid preparation for cryo-electron microscopy

Protein for grid preparation was purified as described with the exception that after ion exchange chromatography, the protein was pooled and snap-frozen in liquid nitrogen. Prior to grid preparation, the full length *Ec*MR was purified via size-exclusion chromatography using a S6 5/150 column (buffer: 50 mM KCl, 20 mM HEPES, pH 7.5). For the endonuclease samples, 10x Buffer (10 mM $MnCl_2$, 50 mM $MgCl_2$ and 10 mM ATP) was mixed with 120 bp dsDNA (Table S1) and Ku70/80 to final concentrations of 0.49 μM and 0.97 μM, respectively. To ensure binding of Ku to the DNA ends, the sample was incubated at 25°C for 15 to 30 min. The collected peak fraction of *Ec*MR was then added to a final concentration of 1.47 μM, resulting in a 1:2:3 molar ratio of DNA:Ku70/80:*Ec*MR. For the DNA hairpin samples, 10x Buffer (10 mM $MnCl_2$, 50 mM $MgCl_2$ and 10 mM ATP) was mixed with hairpin dsDNA (Table S1) and an anti–6-FAM scFv (Pedrazzi et al., 1997) to final concentrations of 0.41 μM and 4 μM, respectively. To ensure binding of the scFv to the 6-FAM labeled 5' DNA end, the sample was incubated at 25°C for 15 to 30 min. The collected peak fraction of *Ec*MR was added to a final concentration of 0.41 μM, resulting in a 1:10:1 molar ratio of DNA:scFv:*Ec*MR. For the hairpin sample, ß-OG was included as a detergent with a final concentration of 0.05% (w/v). After *Ec*MR addition, the samples were incubated for additional 15 min at 25°C and then kept on ice until grid preparation. We applied the protein solution to Quantifoil Cu 200 R2/1 or UltraAU R2/2 grids (tilted datasets, endonuclease state), previously glow discharged for 20 (endonuclease state) or 7 s (hairpin state) at 20 mA (GloQube, Quorum). Grids were prepared using a Leica EM GP plunge freezer (Leica) at 10°C and 95% humidity. For each prepared grid, 4.5 μl of sample was applied to the grids and blotted for 2.5 s before vitrification in liquid ethane.

Electron microscopy data collection and processing

Datasets were collected on a Titan Krios G3 transmission electron microscope (Thermo Fisher Scientific) operated at 300 kV with a K2 Summit direct electron detector (Gatan). All datasets were collected using the EPU software package (TFS) with an applied defocus range of -2.8 to -1.2 μM and a magnified pixel size of 1.059 Å. For the endonuclease state, we collected 2 untilted data subsets of 2,775 and 7,257 micrographs (10,032 micrographs in total; dataset 1) with respective total doses of 44.68 e^- Å^{-2} and 44.9 e^- Å^{-2}, as well as 2 tilted datasets of 2521 (dataset 2) and 2414 micrographs (dataset 3) with respective total doses of 45.27 e^- Å^{-2} and 37.92 e^- Å^{-2} and an applied stage tilt of -25°. Micrograph movies were motion-corrected and dose-weighted using MotionCor2 (Zheng et al., 2017) and CTF parameters were estimated using CTFFIND4 (Rohou and Grigorieff, 2015). For -25° tilt micrographs, additional patch CTF estimation was performed, using the patch CTF estimation job integrated in the cryoSPARC software framework (Punjani et al., 2017). The described micrographs were also used to process the cryo-EM reconstructions of the Ku-RM-MR-Ku and the DNA-bound Ku70/80 states. For the hairpin-bound state, we collected 2 untilted data sets of 6,768 and 10,098 micrographs (16,866 micrographs in total; datasets 4 and 5) with respective total doses of 46.6 e^- Å^{-2} and 47.01 e^- Å^{-2}. Micrograph movies were motion-corrected and dose-weighted using MotionCor2 (Zheng et al., 2017) and CTF parameters were estimated using CTFFIND4 (Rohou and Grigorieff, 2015). Unless stated otherwise, all cryo-EM data processing steps were conducted using cryoSPARC (v3.2.0 and former versions) and Relion v3.0.8 (Scheres, 2012), as illustrated in the processing schemes (Figures S1, S2, and S4). All reported resolutions are based on the gold standard FSC 0.143 criterion.

For the *Ec*MR endonuclease state structure, the micrographs of datasets 1-3 were processed. Extracted particle subsets were only merged into one particle set at later processing stages, after CTF refinement and particle polishing in RELION. For an initial round of particle picking, the cryoSPARC blob picker was used, followed by particle filtering via 2D classification using a 320-pixel box, yielding subsets of 124,161, 82,225 and 63,303 particles for the respective datasets. These particles were then separately used to train Topaz models (Bepler et al., 2019) for convolutional neural-network based particle picking and extraction, again using a 320-pixel box, yielding new particle subsets of 2,785,335, 628,444 and 607,004 particles for the respective datasets. Additional particle filtering via 2D classification was applied as described above, followed by 3D particle classification into 4 classes by cryoSPARC ab-initio reconstruction and heterogeneous refinement. Selection of the best classes after heterogeneous refinement led to particle

Please cite this article in press as: Gut et al., Structural mechanism of endonucleolytic processing of blocked DNA ends and hairpins by Mre11-Rad50, Molecular Cell (2022), https://doi.org/10.1016/j.molcel.2022.07.019

subsets of 102,929, 57,747 and 44,712 particles for the respective datasets 1, 2 and 3. The particle subsets were used to reconstruct initial cryo-EM electron densities for each data set and the initial densities were further refined in cryoSPARC, using homogeneous & non-uniform refinements (Punjani et al., 2020). At this stage, the three particle subsets were transferred to RELION, using the UCSF pyEM script (Asarnow et al., 2019), for CTF refinement and particle polishing. For particle subsets 2 and 3, an additional round of 2D classification was performed in RELION to sort-out junk particles, reducing the particle number to 55,301 and 41,521, respectively. The cryoSPARC densities were used as initial references (down sampled to 60 Å) for a first round of masked 3D refinements in RELION, followed by two iterative rounds of CTF refinement and particle polishing. Afterwards, the polished particle subsets were merged into a single subset of 199,751 particles, yielding a cryo-EM map of the *Ec*MR endonuclease state at 3.4 Å resolution (EMDB-14391), after an additional masked 3D refinement and solvent mask post-processing. The cryo-EM map was also post-processed by local filtering using the LAFTER software (Ramlaul et al., 2019), integrated into the CCP-EM software suite (Burnley et al., 2017; Wood et al., 2015), to better resolve flexible parts and loop regions within the map. The LAFTER-filtered map was used where indicated (see model building). Additionally, the refined cryoSPARC reconstruction from dataset 2 at 3.7 Å showed extended DNA density after the Mre11 nuclease active site (Figure S1E). Therefore, we applied local filtering using the LAFTER software (Ramlaul et al., 2019), yielding a cryo-EM map of the *Ec*MR endonuclease state with extended DNA (EMDB-14403).

Processing the Ku-RM-MR-Ku state structure, due to data quality reasons, only the micrographs of datasets 2 and 3 were included. Furthermore, processing was done solely using cryoSPARC. An initial round of particle picking using the blob picker and subsequent particle sorting by multiple rounds of 2D classification yielded in 3,043 good particles divided among 4 2D classes with an extraction box size of 320 pixel. This particle set was then used to train a Topaz model for convolutional neural-network based particle picking and extraction. Particle picking with the new Topaz model yielded in initial 286,192 particles, with a now increased extraction box size of 600-pixel, Fourier-cropped to 150 pixels. Again, particle sorting by multiple rounds of 2D classification were performed, leaving 18,803 good particles which could then be subjected to an ab-initio reconstruction with 2 classes, followed by heterogeneous refinement. Here, only the particles of the second class (64.4% of the original 18,803 particles) were further processed. The particle set was once more sorted by a 2D classification leaving a new particle set with 10,494 particles, which were re-extracted with a box size of 600-pixel without Fourier-crop. The particles were further refined using the cryoSPARC global and local CTF refinements and duplicate particles were removed within 100 Å (Punjani et al., 2017). A final refinement cycle using homogeneous and masked refinements (in use of the local refinement job implemented in cryoSPARC) yielded a final reconstruction at 8.2 Å (EMDB-14392). This cryo-EM map of the Ku-RM-MR-Ku state was then used to calculate a composite map using the better resolved maps of the *Ec*MR endonuclease state (EMDB-14391) and Ku70/80 bound to a DNA end (EMDB-14394). The composite map was calculated using the combine focused maps routine implemented in Phenix v1.17 (Liebschner et al., 2019).

For the Ku70/80 structure, the micrographs of datasets 1-3 described above were separately processed. Extracted particle subsets were only merged into one particle set at later processing stages, after CTF refinement and particle polishing in RELION v3.0.8. For an initial round of particle picking, blob picker implemented in cryoSPARC was used, followed by particle filtering in several rounds of 2D classification using a 320-pixel box, yielding subsets of 151,496, 83,893 and 89,088 particles for the respective datasets. These particles were then separately used to train Topaz models for convolutional neural-network based particle picking and extracted in a 320-pixel box. This led to new particle subsets of 2,989,830, 686,412 and 721,275 particles for the respective datasets. Afterwards, particle filtering via 2D classification was applied as described above, followed by 3D particle classification into 4 classes by cryoSPARC ab-initio reconstruction and heterogeneous refinement. Selection of the best classes after heterogeneous refinement led to new particle subsets of 173,314, 65,373 and 69,335 particles. The latter were used to reconstruct cryo-EM electron densities using cryoSPARC ab-initio reconstruction. These densities were further refined in cryoSPARC, using homogeneous & non-uniform refinements. At this stage, the three particle subsets were transferred to RELION, using the UCSF pyEM script, for movie refinement and particle polishing, followed by another polishing 2D classification and a 3D focused classification with 5 classes, after merging the polished subsets. Classes 2 to 5 were selected after the 3D focused classification, removing further low-quality particles. The resulting particle subset was subjected to a last round of polishing 2D classification. This then resulted in a final particle subset of 211,512 particles. After an intermediate masked 3D refinement run in CisTEM v1.0.2 (Grant et al., 2018), solvent mask post-processing in Relion resulted in a cryo-EM map of Ku70/80 bound to dsDNA at 3.5 Å resolution (EMDB-14394).

For the hairpin-bound structure, micrographs of datasets 4 and 5 were processed. Micrographs of datasets 4 and 5 were merged from the start. For an initial round of particle picking, again, the cryoSPARC blob picker was used. We performed initial particle sorting in several rounds of 2D classification using a 320-pixel box and by 3D ab initio reconstructions with several classes, yielding a total subset of 46,726 particles. These particles were used to train a Topaz model for convolutional neural-network based particle picking and extraction, again using a 320-pixel box, yielding a new subset with 1,299,536 particles. Those particles were sorted as described above, leading to a new particle subset of 61,845 particles. The particles were used to reconstruct an initial cryo-EM electron density, further refined using homogeneous & non-uniform refinements, which could then be used as an initial reference map. We transferred the particles to RELION, using the UCSF pyEM script, for masked 3D refinement, CTF refinement and particle polishing. The polished particle set was once more filtered by 2D classification, after two iterative polishing cycles, further reducing the particle number to 54,504. This final particle subset could then be used to reconstruct a cryo-EM map of the hairpin-bound state at 4.0 Å resolution (EMDB-14393), using masked 3D refinement and solvent mask post-processing. The cryo-EM map was also post-processed by local filtering using the LAFTER software to better resolve flexible parts and loop regions within the map. The LAFTER-filtered map was used where indicated (see model building).

Please cite this article in press as: Gut et al., Structural mechanism of endonucleolytic processing of blocked DNA ends and hairpins by Mre11-Rad50, Molecular Cell (2022), https://doi.org/10.1016/j.molcel.2022.07.019

Reconstructed cryo-EM maps were rendered using ChimeraX (Pettersen et al., 2021).

Model building

For the endonuclease state model (PDB: 7YZO), we performed rigid body fitting in UCSF Chimera (Pettersen et al., 2004) using the available cryo-EM structure of *Ec*MR in the exonuclease cutting state (PDB code: 6S85). Model building was performed manually in COOT (Emsley and Cowtan, 2004) using secondary structure restraints for protein and libg restraints for DNA, alternating with iterative rounds of real-space refinement in PHENIX 1.19 (Afonine et al., 2018; Liebschner et al., 2019) and molecular dynamics simulations in ISOLDE v1.3 (Croll, 2018). Since the registry of DNA binding could not be determined from the dsDNA densities, we used an arbitrary registry based on our experimental sequence.

For the model of the low-resolution endonuclease map with extended DNA (PDB: 7Z03), the further extending DNA after the Mre11 active site was manually built using the endonuclease state model as a starting point (PDB: 7YZO). We used the low-resolution cryoSPARC density (Figure S1, labeled with an asterisk) as well as the LAFTER-filtered cryo-EM densities. The extending dsDNA sequence was built as a separate B-DNA based on our experimental sequence. The created B-DNA stretch was connected to the 3.4 Å endonuclease model DNA and initially refined against the cryoSPARC 3.7 Å map (Figure S1E) using PHENIX 1.19 and libg DNA restraints. The extended dsDNA was further manually refined against the LAFTER-filtered map, whereas the protein was adapted from the 3.4 Å endonuclease state structure and not further edited.

For the DNA hairpin state (PDB: 7YZP), the dsDNA was built manually, using the hairpin DNA structure of 1DGO (Ghosh et al., 2000) as an initial template, which could be rigid-body docked into the template protein structure 6S85. An initial round of manual DNA refinement was performed in COOT and the DNA sequence was adjusted according to our experimental sequence. As for the endonuclease state, further model building was performed manually in COOT using secondary structure restraints for protein and libg restraints for DNA, alternating with iterative rounds of real-space refinement in PHENIX 1.19 and molecular dynamics simulations in ISOLDE v1.3. Furthermore, the *Ec*Rad50 CCs of the hairpin state could be extended by 34 and 39 amino acids on the n- and c-terminal parts, respectively, in comparison to the endo- and exonuclease states (PDB: 7YZO and 6S85). The stated residues were initially modelled using AlphaFold2 (Jumper et al., 2021), connecting the n- and c-terminal parts of the anti-parallel CCs by an artificial 6 amino acid PAS-Linker that was removed after rigid-body docking into the cryo-EM density. The protein main chains and the CC extensions were connected and included in a final round of refinement as described above.

For the DNA-bound Ku70/80 reconstruction, structural models were calculated using AlphaFold2 for both subunits (not deposited) and rigid-body docked into the density to structurally validate the Ku70/80 reconstruction. The derived models showed a good overall density fit except for the c-terminal parts of Ku70 and Ku80, which are not resolved by the map. The calculated Ku70/80 AlphaFold2 models were also used for the atomic model depicted in the supplementary movie (Video S1). Here, the atomic models were rigid-body docked into the composite map of the Ku-RM-MR-Ku state structure and the c-terminal portions not resolved by the cryo-EM reconstruction were truncated at residues A575 and E575, for Ku70 and 80, respectively. B-DNA was fitted into the clear dsDNA density of the Ku70/80 reconstruction first and refined using PHENIX 1.19 and manually in COOT using libg DNA restraints, before rigid-body docking into the composite map. The adapted dsDNA could then be connected to the DNA of the rigid-body docked *Ec*MR endonuclease model (PDB: 7YZO), completing the model used for the supplementary movie (Video S1). Due to clashes with the fitted dsDNA, the n-terminal parts of the Ku70 (residues 1-26) and Ku80 (residues 1-3) were truncated.

For the structural alignment of the *Ec*MR endonuclease state and the human Mre11-Rad50 homolog we calculated dimer models of each protein individually (*Hs*Rad50: amino acids 1-200 and 1133-1312 connected by a G_6 linker; *Hs*Mre11: amino acids 1-356) using a local installation of AlphaFold-Multimer (Evans et al., 2021)

Models were rendered using ChimeraX (Pettersen et al., 2021).

QUANTIFICATION AND STATISTICAL ANALYSIS

Directional Fourier shell correlation (FSC) determination was performed for the Endonuclease state head complex, the Ku70/80 bound to dsDNA and the Hairpin-bound state head complex, using the 3DFSC software (Tan et al., 2017) (Figures S1, S2, and S4).

OriginPro was used to plot the results of the high-throughput DNA shape prediction (Figures 2C and S3E).

Molecular Cell, Volume *82*

Supplemental information

Structural mechanism of endonucleolytic processing of blocked DNA ends and hairpins by Mre11-Rad50

Fabian Gut, Lisa Käshammer, Katja Lammens, Joseph D. Bartho, Anna-Maria Boggusch, Erik van de Logt, Brigitte Kessler, and Karl-Peter Hopfner

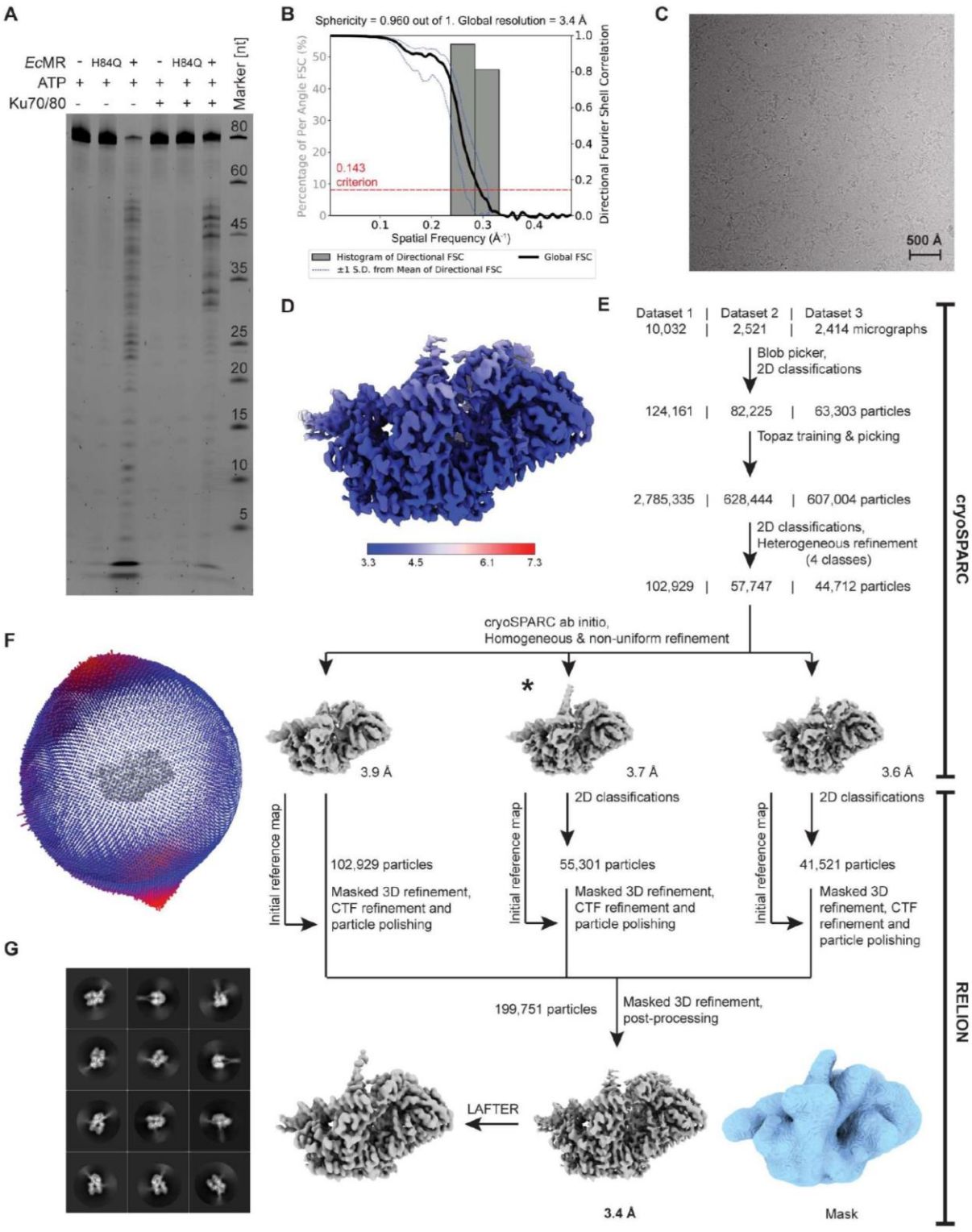

Figure S1 Related to Figure 1| Endonuclease State processing scheme

(A) Nuclease assay of *Ec*MR WT and H84Q nuclease dead on an 80 bp 3' 6-FAM labeled DNA substrate with free and Ku blocked ends (100 nM Ku, 2:1 Ku:DNA) which shows that the H84Q mutant is exo- and endonuclease nuclease deficient.

(B) Histogram and directional Fourier shell correlation (FSC) for the endonuclease state head complex. Directional FSC determination was performed with the 3DFSC software (Tan et al., 2017). A sphericity of 0.96 was determined indicating very isotropic angular distribution (a value of 1 stands

for completely isotropic angular distribution). The red line shows the 0.143 cut-off criterion which indicates a nominal resolution of 3.4 Å.

(C) Representative micrograph of the endonuclease sample containing *Ec*MR bound to Ku blocked 120 bp dsDNA in the presence of ATP.

(D) The local resolution of the endonuclease state head complex, calculated using ResMap and shown as color-coded surface representation.

(E) Flow chart showing the image-processing pipeline for the cryo-EM data analysis of the *Ec*MR endonuclease state. The asterisk marks the endonuclease state head complex reconstruction with extended DNA at 3.7 Å.

(F) Angular distribution of the particles used for the endonuclease state reconstruction.

(G) The twelve highest populated classes from the 2D classification of the *Ec*MR endonuclease state are shown.

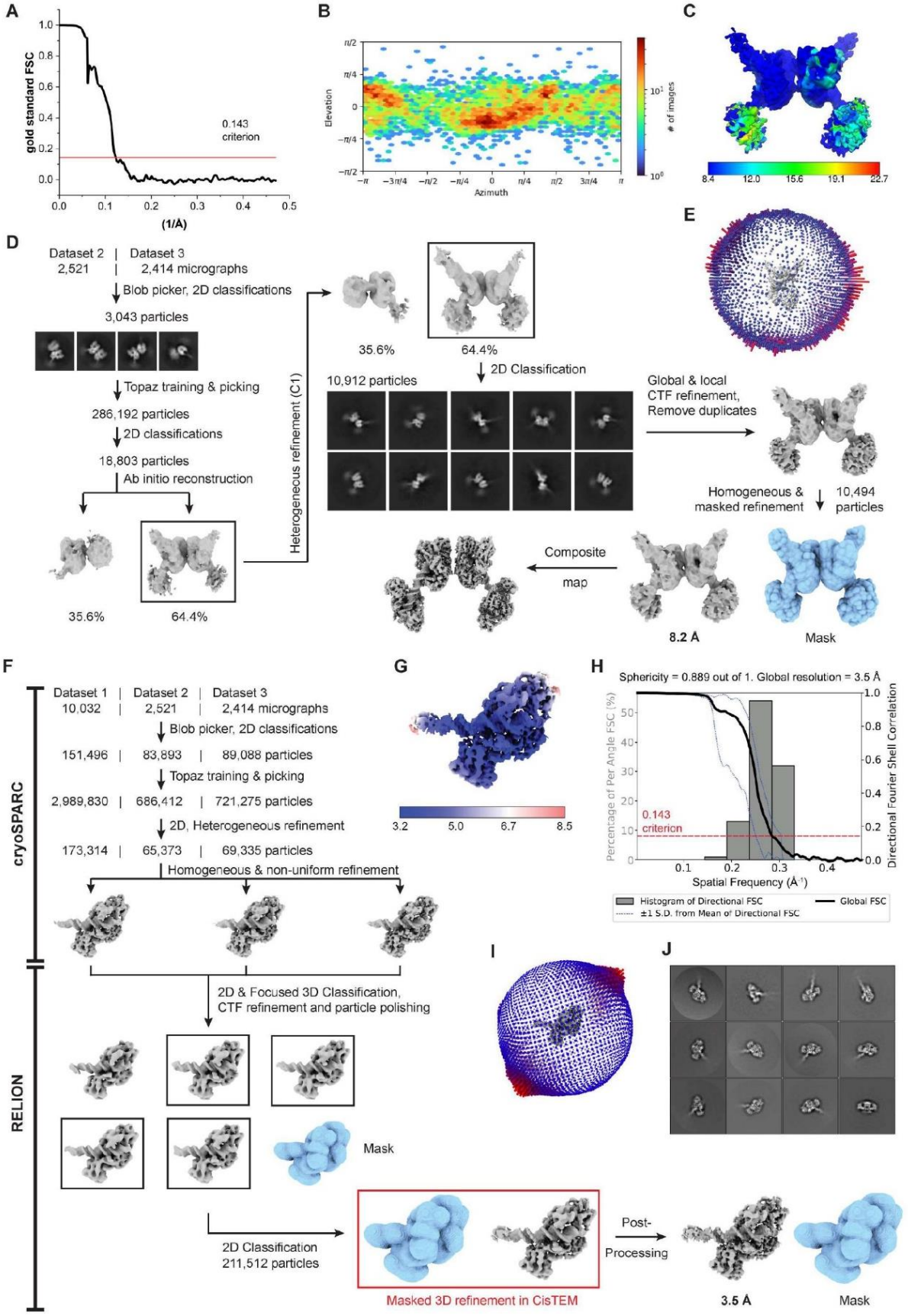
A
gold standard FSC
0.143
criterion
(1/Å)
B
Elevation
Azimuth
# of images
C
8.4
12.0
15.6
19.1
22.7
D
Dataset 2 | Dataset 3
2,521 | 2,414 micrographs
Blob picker, 2D classifications
3,043 particles
Topaz training & picking
286,192 particles
2D classifications
18,803 particles
Ab initio reconstruction
35.6%
64.4%
Heterogeneous refinement (C1)
2D Classification
10,912 particles
Global & local
CTF refinement,
Remove duplicates
Homogeneous &
masked refinement
10,494
particles
Composite
map
8.2 Å
Mask
E
F
cryoSPARC
RELION
Dataset 1 | Dataset 2 | Dataset 3
10,032 | 2,521 | 2,414 micrographs
Blob picker, 2D classifications
151,496 | 83,893 | 89,088 particles
Topaz training & picking
2,989,830 | 686,412 | 721,275 particles
2D, Heterogeneous refinement
173,314 | 65,373 | 69,335 particles
Homogeneous & non-uniform refinement
2D & Focused 3D Classification,
CTF refinement and particle polishing
Mask
2D Classification
211,512 particles
Masked 3D refinement in CisTEM
Post-
Processing
3.5 Å
Mask
G
3.2
5.0
6.7
8.5
H
Sphericity = 0.889 out of 1. Global resolution = 3.5 Å
Percentage of Per Angle FSC (%)
Directional Fourier Shell Correlation
0.143
criterion
Spatial Frequency (Å⁻¹)
Histogram of Directional FSC
±1 S.D. from Mean of Directional FSC
Global FSC
I
J

Figure S2 Related to Figure 1| Ku-RM-MR-Ku State and Ku70/80 processing schemes

(A) Gold-standard Fourier shell correlation (FSC) for the Ku-RM-MR-Ku complex. The red line shows the 0.143 cut-off criterion which indicates a nominal resolution of 8.2 Å.

(B) Angular distribution plot of the particles used for the Ku-RM-MR-Ku state 8.2 Å reconstruction.

(C) The local resolution of the Ku-RM-MR-Ku state, calculated with the cryoSPARC implementation and shown as color-coded surface representation.

(D) Flow chart showing the image-processing pipeline for the cryo-EM data analysis of the Ku-RM-MR-Ku state.

(E) Angular distribution of the particles used for the 8.2 Å reconstruction.

(F) Flow chart showing the image-processing pipeline for the cryo-EM data analysis of the Ku70/80 complex bound to DNA.

(G) The local resolution of the Ku70/80 complex, calculated using ResMap and shown as color-coded surface representation.

(H) Histogram and directional Fourier shell correlation (FSC) for the Ku70/80 DNA-bound state reconstruction. Directional FSC determination was performed with the 3DFSC software (Tan et al., 2017). A sphericity of 0.889 was determined indicating an isotropic angular distribution (a value of 1 stands for completely isotropic angular distribution). The red line shows the 0.143 cut-off criterion which indicates a nominal resolution of 3.5 Å.

(I) Angular distribution of the particles used for the Ku70/80 reconstruction.

(J) The twelve highest populated classes from the 2D classification of the Ku70/80 complex bound to DNA are shown.

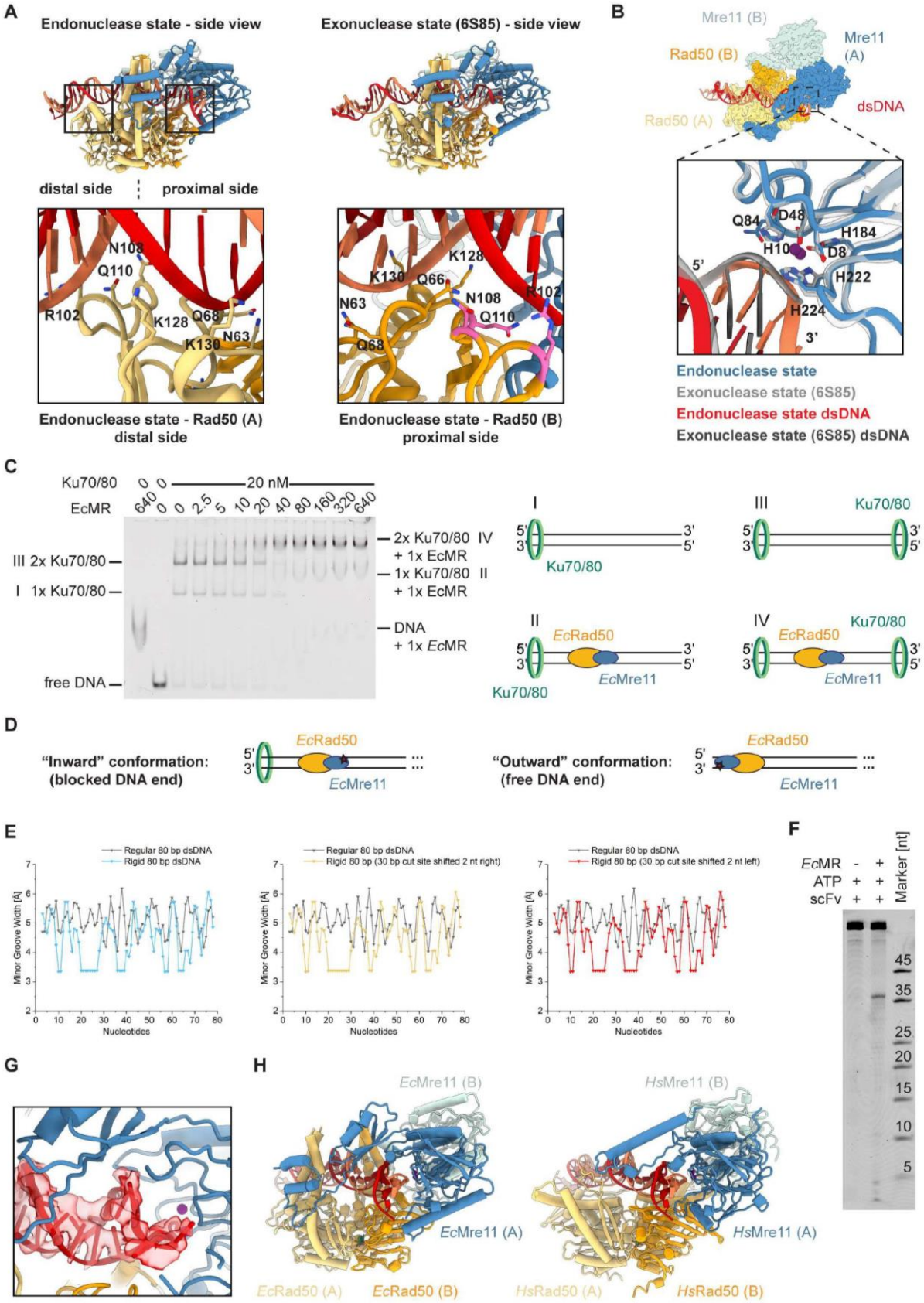
A
Endonuclease state - side view
Exonuclease state (6S85) - side view
distal side
proximal side
N108
Q110
R102
K128
Q68
K130
N63
K128
K130
Q66
N63
N108
Q110
R102
Q68
Endonuclease state - Rad50 (A)
distal side
Endonuclease state - Rad50 (B)
proximal side
B
Mre11 (B)
Mre11
(A)
Rad50 (B)
dsDNA
Rad50 (A)
Q84
D48
H184
H10
D8
5'
H222
H224
3'
Endonuclease state
Exonuclease state (6S85)
Endonuclease state dsDNA
Exonuclease state (6S85) dsDNA
C
Ku70/80
0 0 20 nM
EcMR
640 0 0 2.5 5 10 20 40 80 160 320 640
III 2x Ku70/80
I 1x Ku70/80
free DNA
2x Ku70/80 IV
+ 1x EcMR
1x Ku70/80 II
+ 1x EcMR
DNA
+ 1x EcMR
I
III
Ku70/80
II
EcRad50
EcMre11
IV
D
"Inward" conformation:
(blocked DNA end)
"Outward" conformation:
(free DNA end)
E
Regular 80 bp dsDNA
Rigid 80 bp dsDNA
Rigid 80 bp (30 bp cut site shifted 2 nt right)
Rigid 80 bp (30 bp cut site shifted 2 nt left)
Minor Groove Width [Å]
Nucleotides
F
EcMR - +
ATP + +
scFv + +
Marker [nt]
45
35
25
20
15
10
5
G
H
EcMre11 (B)
HsMre11 (B)
EcMre11 (A)
HsMre11 (A)
EcRad50 (A)
EcRad50 (B)
HsRad50 (A)
HsRad50 (B)

Figure S3 Related to Figure 1, 2 and 3| Structural and biochemical analysis of the Endonuclease and Hairpin-bound States

(A) The upper panel shows a comparison of endonuclease and exonuclease state (PDB: 6S85) models in side view. Subunits are illustrated using the same color code as in Figure 1 (Rad50 orange/yellow; Mre11 light/dark blue; DNA red). The lower panel shows interactions of Rad50 (A) and (B) with DNA in endonuclease state. DNA binding residues are depicted as sticks and residues involved in endonuclease state DNA binding, but not in exonuclease, are highlighted in pink.

(B) Nuclease active site comparison of Mre11(A) in endonuclease and exonuclease ((Kashammer et al., 2019); PDB: 6S85) state models. The Mre11(A) subunit is colored in dark blue (endonuclease) and light grey (exonuclease), the DNA in orange/red (endonuclease) and dark grey (exonuclease) and the Mn^{2+} ions in purple. DNA and enzymatically important residues are annotated and illustrated as sticks.

(C) Electrophoretic mobility shift assay of *Ec*M^{H84Q}R bound to Ku blocked 120 bp dsDNA. Illustration of the 4 different observed binding species.

(D) Illustration showing the different orientation of the *Ec*MR complex in the discussed "inward" and "outward" conformations, relative to the blocked or free DNA end.

(E) High-throughput DNA shape prediction (Zhou et al, 2013) of the regular and rigid 80 bp dsDNA, illustrating rigid and more flexible regions within the DNA oligos.

(F) Full gel image of the nuclease assay of *Ec*MR WT on the 5' 6-FAM labeled, scFv blocked DNA hairpin, showing predominant nuclease cleavage at 36 nt, illustrated in Figure 2F.

(G) Nuclease active site of Mre11 (A) bound to a DNA hairpin. Mre11 (A) is colored in dark blue, Rad50 (B) in orange and the hairpin DNA in red. The atomic model of the hairpin DNA is overlaid by the 4 Å cryo-EM density.

(H) Structural alignment of the *Ec*MR endonuclease state and human Rad50 (amino acids 1-200 and 1133-1312 connected by a G_6 linker) and Mre11 (amino acids 1-356) AlphaFold-Multimer (Evans et al., DOI:10.1101/2021.10.04.463034) predictions by rigid-body docking of the predicted models on the *Ec*MR endonuclease model. Rad50 is generally displayed in orange/yellow, Mre11 in light/dark blue and endonuclease state DNA in red. The Mn^{2+} ions of the endonuclease model are illustrated as purple spheres and the Mg^{2+}-ADP as green sticks and spheres, respectively. The predicted models support the concept that our proposed unified nuclease cutting state mechanism might also be applicable to eukaryotic Mre11-Rad50 homologs.

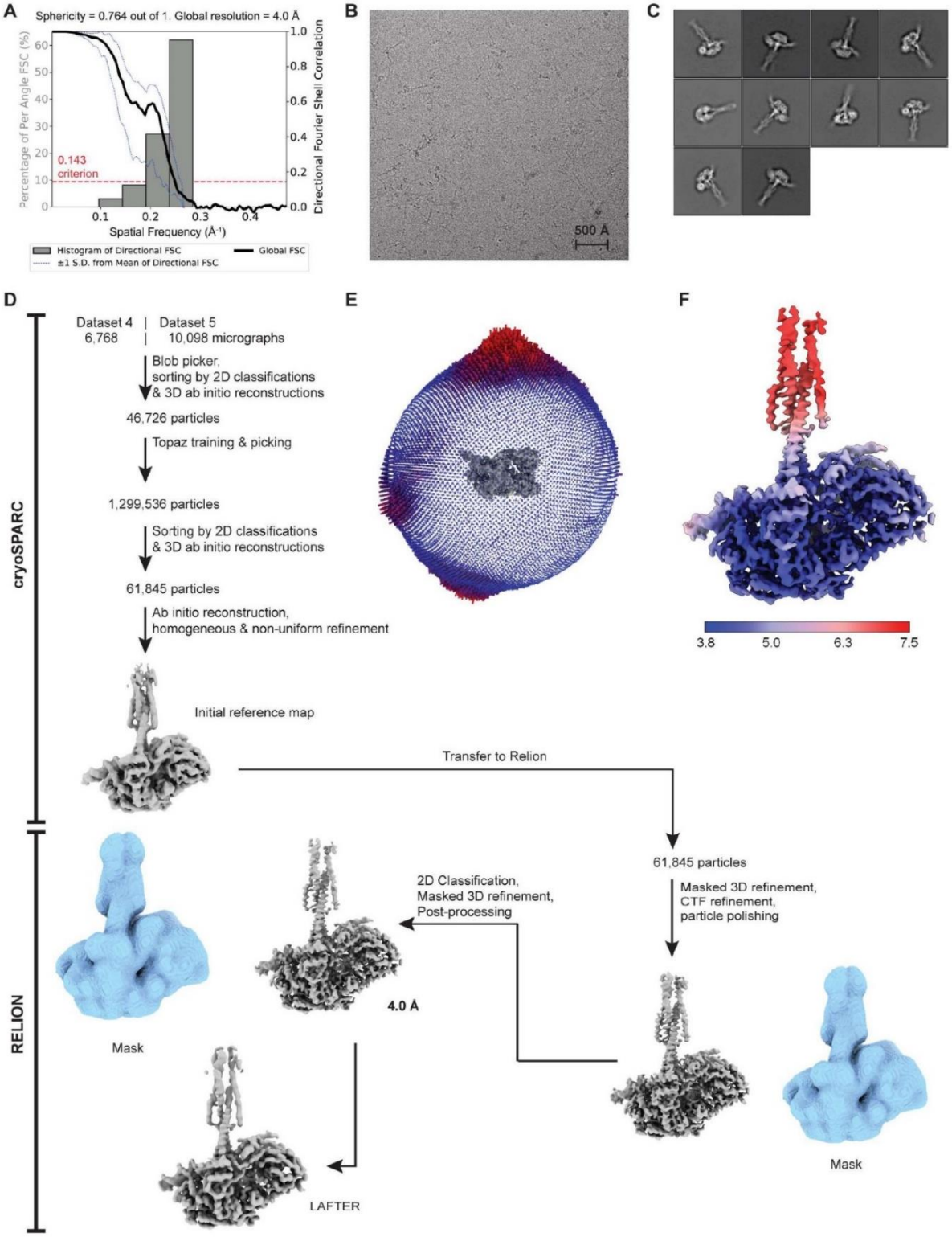

Figure S4 Related to Figure 2| Hairpin-bound State processing scheme

(A) Histogram and directional Fourier shell correlation (FSC) for the hairpin-bound state head complex. Directional FSC determination was performed with the 3DFSC software (Tan et al., 2017). A sphericity of 0.764 was determined indicating a mostly isotropic angular distribution (a value of 1

stands for completely isotropic angular distribution). The red line shows the 0.143 cut-off criterion which indicates a nominal resolution of 4 Å.

(B) Representative micrograph of the DNA hairpin sample containing *Ec*MR bound to the DNA hairpin in the presence of ATP.

(C) The ten highest populated classes from the 2D classification of the *Ec*MR hairpin-bound state are shown.

(D) Flow chart showing the image-processing pipeline for the cryo-EM data analysis of the *Ec*MR hairpin-bound state.

(E) Angular distribution of the particles used for the hairpin-bound state reconstruction.

(F) The local resolution of the *Ec*MR hairpin-bound state head complex, calculated using ResMap and shown as color-coded surface representation.

Table S1 Related to STAR Methods |PCR Primer and DNA oligomers used for cryo-EM samples and assays

Oligonucleotide	Sequence 5' to 3'
120 bp DNA for EM (fwd)	GCGTGGCACAACAACTGGCGGGCAAACAGTCGTTGCTGATTG GCGTTGCCACCTCCAGTCTGGCCCTGCACGCGCCGTCGCAAATT GTCGCGGCGATTAAATCTCGCGCCGATCAACTGG
120 bp DNA for EM (rev)	CCAGTTGATCGGCGCGAGATTTAATCGCCGCGACAATTTGCGA CGGCGCGTGCAGGGCCAGACTGGAGGTGGCAACGCCAATCAG CAACGACTGTTTGCCCGCCAGTTGTTGTGCCACGC
75 bp DNA hairpin for EM with 35 bp dsDNA stem and 5 nt bubble	6FAM-CGCTTTATCAGAAGCCAGACATTAACGCTTCTGGATAGC GTCCAGAAGCGTTAATGTCTGGCTTCTGATAAAGCG
80 bp DNA (fwd) for nuclease assays with Ku70/80	CGGGTAGTAGATGAGCGCAGGGACACCGAGGTCAAGTACATT ACCCTCTCATAGGAGGTGCGCTTTATCAGAAGCCAGAC
80 bp DNA (rev) for nuclease assays with Ku70/80	GTCTGGCTTCTGATAAAGCGCACCTCCTATGAGAGGGTAATGT ACTTGACCTCGGTGTCCCTGCGCTCATCTACTACCCG-6FAM
80 bp rigid DNA (fwd) for nuclease assays with Ku70/80	ACAGATGAACTTTAAAGAAAAAAAAAAAACAAGAAAAAAAACT AAGGCCAAAGAAACTTTAAAAAAACCTATCTTATAGT
80 bp rigid DNA (rev) for nuclease assays with Ku70/80	ACTATAAGATAGGTTTTTTTAAAGTTTCTTTGGCCTTAGTTTTTT TTCTTGTTTTTTTTTTTTCTTTAAAGTTCATCTGT-6FAM
80 bp rigid DNA (fwd) 2nt left for nuclease assays with Ku70/80	ACAGATGAACTTTAAAGAAAAAAAAAACAAGAAAAAAAAAACT AAGGCCAAAGAAACTTTAAAAAAACCTATCTTATAGT
80 bp rigid DNA (rev) 2nt left for nuclease assays with Ku70/80	ACTATAAGATAGGTTTTTTTAAAGTTTCTTTGGCCTTAGTTTTTT TTTTCTTGTTTTTTTTTTCTTTAAAGTTCATCTGT-6FAM
80 bp rigid DNA (fwd) 2nt right for nuclease assays with Ku70/80	ACAGATGAACTTTAAAGAAAAAAAAAAAAAACAAGAAAAAACT AAGGCCAAAGAAACTTTAAAAAAACCTATCTTATAGT
80 bp rigid DNA (rev) 2nt right for nuclease assays with Ku70/80	ACTATAAGATAGGTTTTTTTAAAGTTTCTTTGGCCTTAGTTTTTT CTTGTTTTTTTTTTTTTCTTTAAAGTTCATCTGT-6FAM
Primer (fwd) for 5'-6FAM 120 bp dsDNA (pET21b) for EMSA	6-FAM-GCGTGGCACAACAACTGGCGGG
Primer (rev) for 5'-6FAM 120 bp dsDNA (pET21b) for EMSA	CCAGTTGATCGGCGCGAGATTTAATCG
PCR product (fwd) 5'-6FAM 120 bp dsDNA (pET21b) for EMSA	GCGTGGCACAACAACTGGCGGGCAAACAGTCGTTGCTGATTG GCGTTGCCACCTCCAGTCTGGCCCTGCACGCGCCGTCGCAAATT GTCGCGGCGATTAAATCTCGCGCCGATCAACTGG
PCR product (rev) 5'-6FAM 120 bp dsDNA (pET21b) for EMSA	CCAGTTGATCGGCGCGAGATTTAATCGCCGCGACAATTTGCGA CGGCGCGTGCAGGGCCAGACTGGAGGTGGCAACGCCAATCAG CAACGACTGTTTGCCCGCCAGTTGTTGTGCCACGC

2.3 Cryo-EM structure of the Mre11-Rad50-Nbs1 complex reveals the molecular mechanism of scaffolding functions

Matthias Rotheneder*, Kristina Stakyte*, Erik van de Logt*, Joseph D. Bartho*, Katja Lammens, Yilan Fan, Aaron Alt, Brigitte Kessler, Christophe Jung, Wynand P. Roos, Barbara Steigenberger, Karl-Peter Hopfner, **Cryo-EM structure of the Mre11-Rad50-Nbs1 complex reveals the molecular mechanism of scaffolding functions**, *Molecular Cell*, Volume 83, January 2023, Pages 167-185, https://doi.org/10.1016/j.molcel.2022.12.003

* These authors contributed equally.

Summary

In this publication we present the first full-length cryo-EM structure of eukaryotic MRN. *Chaetomium thermophilum* MRN with ATPγS bound adopts an autoinhibited state, with closed coiled-coils and the Mre11 nuclease blocked by Rad50's ATPase domain. The asymmetric wrapping of a single Nbs1 around the Mre11 dimer clarifies the complex stoichiometry as $Mre11_2$:$Rad50_2$:$Nbs1_1$. The coiled-coils protrude from the globular head in a linear, rod-shape conformation with multiple interaction points in between. Using the protein structure prediction tool AlphaFold2 and X-ray crystallography, we were able to build the entire coiled-coils. At the apex of this domain, a zinc-hook dimerization motif enables MRN to form intercomplex multimers, an important function for DNA tethering in DSB repair pathways. Thereby, a newly characterized, eukaryote specific additional DNA binding site at the Mre11 C-terminus allows binding to internal DNA sites, whereas the canonical Rad50 DNA binding site strongly prefers DNA ends in an ATP-dependent manner.

Author contributions

I purified proteins with help from Matthias Rotheneder, Kristina Stakyte, Yilan Fan and Brigitte Kessler according to protocols established by Matthias Rotheneder, Kristina Stakyte, Aaron Alt and me. I performed *in vitro* assays and cloned constructs for *in vivo* studies together with Matthias Rotheneder, Kristina Stakyte and Yilan Fan. Together with Matthias Rotheneder, Kristina Stakyte and Joseph D. Bartho, I prepared cryo-EM grids and set up data collections. Joseph D. Bartho, Katja Lammens, Matthias Rotheneder, Kristina Stakyte and Karl-Peter Hopfner processed cryo-EM data and were involved in model building. Crystallisation was done by Brigitte Kessler, Matthias Rotheneder and Kristina Stakyte, X-ray data was interpreted by Katja Lammens, Matthias Rotheneder, Kristina Stakyte and Karl-Peter Hopfner. Christophe Jung measured and analysed fluorescence anisotropy experiments. Wynand P. Roos conducted and evaluated the *in vivo* assays. Barbara Steigenberger performed crosslinking mass spectrometry experiments. The manuscript was prepared by Karl-Peter Hopfner, Matthias Rotheneder, Kristina Stakyte, Joseph D. Bartho, Katja Lammens and me with the help from all other authors.

Molecular Cell

Article

Cryo-EM structure of the Mre11-Rad50-Nbs1 complex reveals the molecular mechanism of scaffolding functions

Graphical abstract

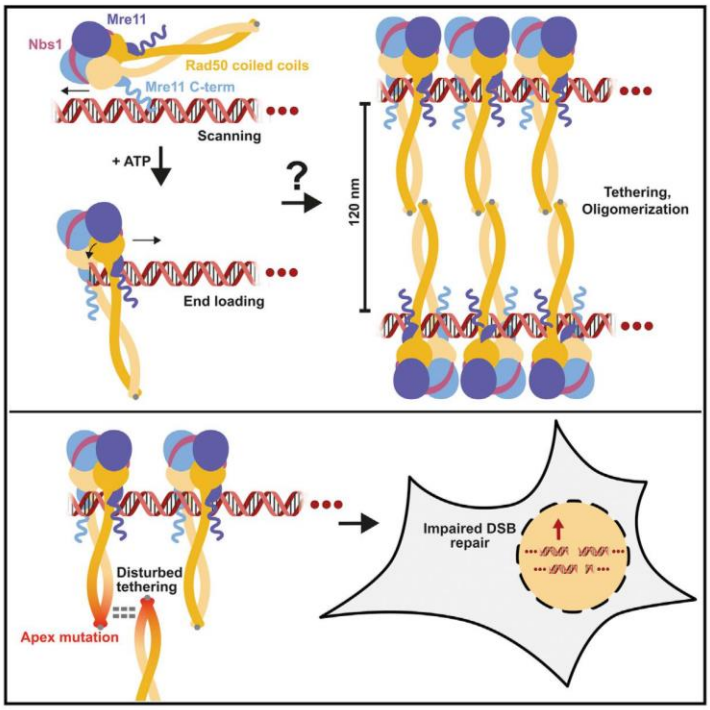

Authors

Matthias Rotheneder, Kristina Stakyte, Erik van de Logt, ..., Wynand P. Roos, Barbara Steigenberger, Karl-Peter Hopfner

Correspondence

hopfner@genzentrum.lmu.de

In brief

Rotheneder et al. determine the structure of eukaryotic Mre11-Rad50-Nbs1, reveal the basis for Nbs1 interaction with the Mre11 dimer, uncover ATP-dependent and -independent DNA-binding modes for DNA ends and internal DNA, and reveal that Rad50 coiled-coil apex tetramers form DNA-tethering structures in DNA double-strand break repair.

Highlights

- Cryo-EM structure of full-length, eukaryotic Mre11-Rad50-Nbs1 bound to ATPγS
- A single Nbs1 polypeptide wraps around and stabilizes the Mre11 dimer
- ATP-dependent and -independent binding modes for DNA ends and internal DNA
- Rad50 coiled-coil apex tetramerization forms MRN-MRN tethering structures

Rotheneder et al., 2023, Molecular Cell *83*, 1–19
January 19, 2023
https://doi.org/10.1016/j.molcel.2022.12.003

CellPress

Please cite this article in press as: Rotheneder et al., Cryo-EM structure of the Mre11-Rad50-Nbs1 complex reveals the molecular mechanism of scaffolding functions, Molecular Cell (2022), https://doi.org/10.1016/j.molcel.2022.12.003

Molecular Cell

CellPress

Article

Cryo-EM structure of the Mre11-Rad50-Nbs1 complex reveals the molecular mechanism of scaffolding functions

Matthias Rotheneder,[1,5] Kristina Stakyte,[1,5] Erik van de Logt,[1,5] Joseph D. Bartho,[1,5] Katja Lammens,[1] Yilan Fan,[1] Aaron Alt,[1,4] Brigitte Kessler,[1] Christophe Jung,[1] Wynand P. Roos,[2] Barbara Steigenberger,[3] and Karl-Peter Hopfner[1,6,*]

[1]Gene Center, Department of Biochemistry, Ludwig Maximilians Universität, Munich, Germany
[2]Institute for Toxicology, Johannes-Gutenberg-Universität, Mainz, Germany
[3]Mass Spectrometry Core Facility, Max-Planck-Institute of Biochemistry, Martinsried, Germany
[4]Present address: CureVac AG, Tübingen, Germany
[5]These authors contributed equally
[6]Lead contact
*Correspondence: hopfner@genzentrum.lmu.de
https://doi.org/10.1016/j.molcel.2022.12.003

SUMMARY

The DNA double-strand break repair complex Mre11-Rad50-Nbs1 (MRN) detects and nucleolytically processes DNA ends, activates the ATM kinase, and tethers DNA at break sites. How MRN can act both as nuclease and scaffold protein is not well understood. The cryo-EM structure of MRN from *Chaetomium thermophilum* reveals a 2:2:1 complex with a single Nbs1 wrapping around the autoinhibited Mre11 nuclease dimer. MRN has two DNA-binding modes, one ATP-dependent mode for loading onto DNA ends and one ATP-independent mode through Mre11's C terminus, suggesting how it may interact with DSBs and intact DNA. MRNs two 60-nm-long coiled-coil domains form a linear rod structure, the apex of which is assembled by the two joined zinc-hook motifs. Apices from two MRN complexes can further dimerize, forming 120-nm spanning MRN-MRN structures. Our results illustrate the architecture of MRN and suggest how it mechanistically integrates catalytic and tethering functions.

INTRODUCTION

DNA double-strand breaks (DSBs) can lead to cell death, gross chromosomal aberrations, aneuploidy, and tumorigenesis.[1] DSBs can be caused by ionizing radiation and genotoxic chemicals and frequently arise during DNA replication.[2] In addition, "programmed" DSBs are physiological intermediates in immunoglobulin gene rearrangements and meiotic chromosome recombination.[3,4] Cells have evolved two potent DSB sensing, signaling and repair branches. In end-joining reactions, such as non-homologous end joining (NHEJ), broken DNA ends are ligated without or with various amounts of limited processing, a procedure that can be potentially mutagenic.[5,6] In homologous recombination (HR), DNA ends are resected into long 3′ single strand overhangs, which pair with the homologous template for template-dependent DNA synthesis.[7–9] In eukaryotic cells, the usage of the different pathways is tightly regulated in the cell cycle.[10]

DSBs can feature chemical alterations, hairpins or covalently attached proteins.[3,11] Repair of diverse and obstructed DNA ends requires the Mre11-Rad50-Nbs1 (MRN, Mre11-Rad50-Xrs2 in yeast) complex,[12–14] which cuts the 5′ strand in the vicinity of the DNA end, followed by exonucleolytic back-resection in the 3′ to 5′ direction.[15,16] The resulting (single-stranded) ssDNA can act in strand annealing in end-joining reactions or can be further extended by 5′ to 3′ long-range resection in HR. MRN or bacterial MR homologs can also cleave the second strand, which will clip off the blocked DNA termini.[16–18] MR/MRN possesses two copies each of Mre11 and Rad50 and takes shape as a globular ATP-dependent DNA binding and nuclease module (head) with two protruding, up to 60-nm-long flexible coiled-coil (CC) domains.[19–22] The two Rad50 CC domains of an MR or MRN complex are apically linked together via a zinc-hook dimerization motif.[23–25] Recent structural data on *Escherichia coli* (*Ec*) MR (also denoted SbcCD) suggest that the linked CC domains act as gate and chemo-mechanical device via ring to rod transitions to promote ATP-dependent loading and cleavage of linear but not circular DNA.[26]

The third protein of eukaryotic MRN, Nbs1,[27] regulates MRs nuclease activity and acts as a protein interaction scaffold. MRE11, RAD50, or NBS1 are essential in mammals, while hypomorphic mutations lead to several genome instability syndromes, like Nijmegen breakage syndrome and ataxia-telangiectasia-like disorder, characterized by cancer predisposition,

Please cite this article in press as: Rotheneder et al., Cryo-EM structure of the Mre11-Rad50-Nbs1 complex reveals the molecular mechanism of scaffolding functions, Molecular Cell (2022), https://doi.org/10.1016/j.molcel.2022.12.003

neurodegeneration and/or immunological defects.[28–31] MRN has both enzymatic and structural functions in DSB repair. It is involved in HR and end-joining pathways, meiotic and replication-associated recombination, chromatin architecture, as well as telomere maintenance.[12,13,32] The various activities of MRN/X are tightly orchestrated and regulated by the cell-cycle state and additional factors, such as ataxia telangiectasia mutated (ATM)/Tel1, CtIP/Sae2, and Rif2.[33] CtIP/Sae2 functions as a DNA scaffold protein[34] and MRN/X coactivator[16,35–37] and is critical for DSB processing.[38,39] At *S. cerevisiae* telomeres, on the contrary, Sae2's coactivator function is counteracted by telomeric factor Rif2, which prevents endonucleolytic cleavage by MRX.[40–43]

MRN/X also recruits and activates the ATM kinase (Tel1 in yeast) at DSBs,[44–46] which phosphorylates a large number of target proteins and orchestrates the DNA-damage response.[47] An important but particularly poorly understood function of MRN/X is the tethering of DNA,[48–50] and more generally chromatin organization.[51–53] MRN/X forms large clusters *in vitro* and repair foci *in vivo*, both through head as well as CC domains.[23,54–56] Such clusters might also be involved in generating multiple cleavage events at DSBs as well.[57] The nature of these clusters and the mechanism how CC domains can act as gate in DSB sensing on one hand, or bridge MRN complexes in tethering functions on the other hand, remains puzzling.

Here, we report the cryoelectron microscopy (cryo-EM) structure of the *Chaetomium thermophilum* (*Ct*)MRN complex bound to ATPγS. Our structure not only clarifies the atomic architecture of eukaryotic MRN but also reveals several unexpected features that rationalize enzymatic and tethering functions in a single framework. A 3.8 Å reconstruction of MRN's catalytic head shows that 75 amino acids of Nbs1 wrap as an extended chain around both Mre11 subunits. This portion of Nbs1 agrees well with that of the minimal core of murine Nbs1 necessary to maintain embryonic viability,[28] suggesting that a key function of Nbs1 is to stabilize the Mre11 dimer. The Rad50 CC domains are in a rod configuration, stabilized by several points of interactions along their entire lengths. Unexpectedly, we not only observe zinc-hook mediated dimerization of the two CC domains in a rod configuration, but the apices of two MRN CC domains further dimerize to form joined MRN-MRN assemblies. Supported by cell-based and biochemical studies, the structure provides a molecular basis for the transient tethering of DNA ends and/or chromatids by MRN.

RESULTS

Cryo-EM structure of MRN

Recombinant *Ct*MRN forms a homogeneous complex with a 2:2:1 stoichiometry (Figure S1A). We vitrified the protein in the presence of ATPγS, which we found to stabilize the complex for cryo-EM. Since *Ct*MRN's ATPase is 10-fold stimulated by DNA (see below), similar to human (*Hs*)MRN and *Ec*MR,[58,59] the resulting ATPγS bound structure resembles an autoinhibited "resting" state of the complex between occasional ATP hydrolysis events.

In the micrographs, we observed single particles along large oligomers, entangled Rad50 CCs, and partially dissociated complexes (Figure S1B). We focused on isolated particles that typically showed a globular head module along with straight or curved protruding CCs. The highly elongated, flexible nature of the particles prevented us to obtain a cryo-EM map of the entire complex; however, we could reconstruct a structure covering the head and approximately 50% of the proximal CCs, and another covering 25% of the distal CCs around the zinc-hook.

Several rounds of automated particle picking, 2D classification, neural network-based particle picking, followed by extensive 3D classification, refinement, and polishing led to a 4.0 Å C1-reconstruction of the head (Figures 1A, S1C, S1D, and S2; Table 1). By further selecting for straight CCs and re-extracting the particles with bigger box sizes, we obtained a C2-symmetrical density with 4.8 Å overall resolution in which around 30 nm of the Rad50 CCs were resolved (Figures 1A, S2, and S3A–S3E). Different regions of the C1 map were improved by variability analysis, masking, as well as focused refinement and combined in a composite map (Figure S1D). We build an atomic model for the head and 30 nm of the Rad50 CCs, using various crystal structures and AlphaFold2 models as starting models (Figures 1A and S3F).

The catalytic head model consists of two Mre11, the two $Rad50^{NBD}$ (nucleotide binding domain) subunits, and an extended portion of Nbs1 that wraps around both Mre11 protomers (Figure 1A). The Mre11 nuclease domain assembles into the characteristic dimer, with its active sites blocked by both $Rad50^{NBD}$s to prevent unspecific DNA degradation. Following the nuclease domain, the helix-bundle Rad50-binding domain (RBD) attaches Mre11 to the Rad50 CCs. Overall, the architecture of the MRN head module is related to that of *Ec*MR bound to ATPγS, showing the autoinhibited "resting" state.[26]

*Ct*MRN-ATPγS segmented CCs are parallel and engaged as rod, in contrast to the *Ec*MR-ATPγS resting-state complex, where the CCs formed an open, flexible ring (Figure S4A). Both CCs interact with each other predominantly via contacts at the segment joints. In the presence of ATP, we observed a small fraction of particles that showed open CCs, similar to the structure observed in the *Ec*MR-ATPγS resting-state complex (Figure S4B).[26] This indicates that ATP, like in the bacterial complex, can induce CC opening. Additionally, the CCs are further held together by bridge elements formed by Mre11 that span the CCs in the vicinity of the $Rad50^{NBD}$s (Figures 1A and S4A). The structured bridge elements are mobile, and we observe subclasses with zero, one, or two bridge elements. The bridge element shows low sequence conservation and is absent in the prokaryotic MR complex. However, appropriate helical elements that may serve as a bridge are present in higher eukaryotes according to AlphaFold2 predictions (Figure S4C).

To validate the structural model and obtain additional architectural information, we performed lysine-specific chemical cross-linking followed by LC-MS/MS (CX-MS), which provides in-solution distance restraints of <30 Å between Cα atoms (Figures 1B and S4D). Out of 40 high-intensity crosslinks within MR mapped to our model, 35 fulfill the distance restraints. 5 (12.5%) fall outside the permitted distance constraints, indicating flexibility or perhaps a minor amount of aggregation. The permitted crosslinks especially validate the low-resolution parts of the map in the CCs and the fitting of the AlphaFold2 predicted CC segments (Figures 1A and S4D). The crosslinks also

Please cite this article in press as: Rotheneder et al., Cryo-EM structure of the Mre11-Rad50-Nbs1 complex reveals the molecular mechanism of scaffolding functions, Molecular Cell (2022), https://doi.org/10.1016/j.molcel.2022.12.003

CellPress

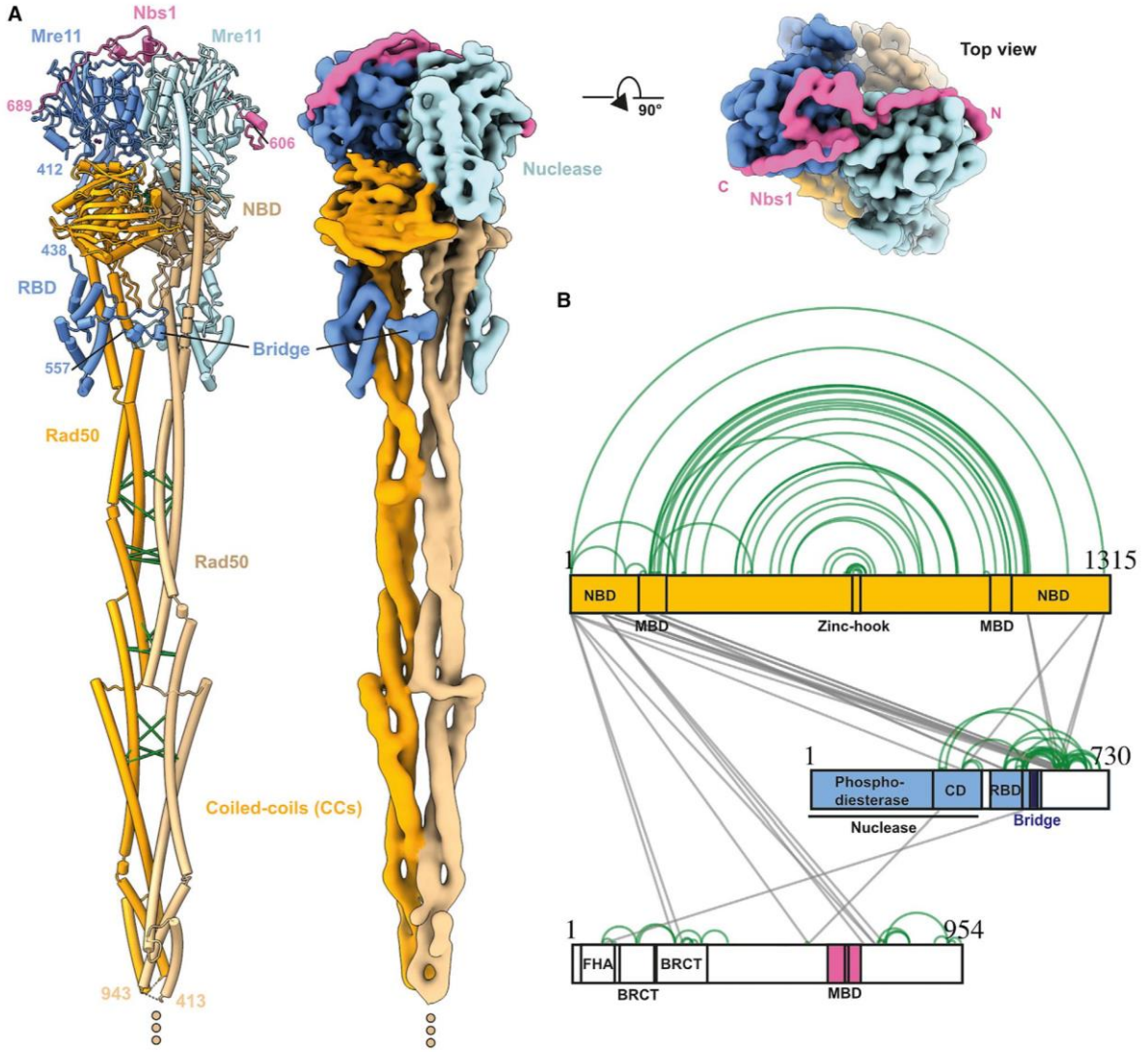

Figure 1. Structure of MRN in the resting state

(A) Cryo-EM structure and composite map of the *Ct*MRN complex with CCs in a closed conformation, created by combining focused higher resolution maps. The atomic model of the catalytic head domain and 30 nm of the Rad50 CCs region is shown (Mre11: blue; Rad50: orange; Nbs1 magenta). Crosslink restraints obtained by CX-MS are labeled green.

(B) Graphical overview of the lysine-specific chemical cross-linking mass spectrometry results (CX-MS). Colored portions indicate structurally characterized parts of each protein. CD, capping domain; NDB, nucleotide binding domain; MDB, Mre11 binding domain; RBD, Rad50 binding domain.

See also Figures S1–S4.

agree well with an extended conformation of the CCs and a lack of back-folding of the CCs as observed for structural maintenance of chromosomes (SMC) proteins.[60] Crosslinks with violated restraints are all located within the catalytic head and could be explained by flexibility (Video S1) or clustering head-head (see below). We observed several high-intensity crosslinks between the N-terminal part of Nbs1 (FHA-BRCT2 module) and the β sheets of Rad50 (Figure S4D) along with additional density at exactly this site, but it could not be assigned due to low resolution. Further, we found many crosslinks of the flexible Mre11 C terminus to various sites of the catalytic head, including the β sheets of Rad50 (Figure S4D).

A single Nbs1 wraps around the Mre11 dimer

A single Nbs1 polypeptide binds asymmetrically to both Mre11 phosphodiesterase domains (Figure 2A). Binding is centered

Please cite this article in press as: Rotheneder et al., Cryo-EM structure of the Mre11-Rad50-Nbs1 complex reveals the molecular mechanism of scaffolding functions, Molecular Cell (2022), https://doi.org/10.1016/j.molcel.2022.12.003

Table 1. Cryo-EM data collection, 3D reconstruction, and model refinement statistics

	*Ct*Composite (EMD-14881 PDB: 7ZR1)	*Ct*Head (EMD-14880)	*Ct*Long coiled coils (EMD-14878)	*Ct*Distant coiled coils (EMD-14879)	*Ct*RBD and bridge (EMD-14876)	*Ct*Nbs1 (EMD-14877)	*Ct*Zn hook (EMD-14882)	*Hs*M(H129N)N (EMD-15948 PDB: 8BAH)
Data collection and processing								
Magnification	130,000	–	–	–	–	–	–	130,000
Voltage (kV)	300	–	–	–	–	–	–	300
Electron exposure ($e^-/Å^2$)	44.68 44.90 45.27 37.92	–	–	–	–	–	–	47.72
Defocus range (μm)	−1.2 to −2.8	–	–	–	–	–	–	−1.2 to −2.8
Pixel size (Å)	1.059	–	–	–	–	–	–	1.059
Symmetry imposed	C1/C2	C1	C2	C2	C1	C1	C2	C1
Initial particle images (no.)	–	288,443	211,134	211,134	1,841,184	1,841,184	995,751	282,838
Final particle images (no.)	–	288,443	71,734	71,734	137,843	137,843	32,603	282,838
Map resolution (Å)	–	4.0	4.8	7.6	3.9	3.8	4.9	4.1
FSC threshold	–	0.143	0.143	0.143	0.143	0.143	0.143	0.143
Map resolution range (Å)	–	3.7–5.6	3.1–12.5	6.3–11.5	3.2–8.5	3.2–8.2	4.5–10.7	3.5–6.8
Refinement								
Initial model	4YKE, 5DA9, AlphaFold							AlphaFold, 3T1I
Model resolution (Å)[a]	6.0	4.2	8.4	10.0	7.7	4.0	–	4.3
FSC threshold	0.5	0.5	0.5	0.5	0.5	0.5	–	0.5
Map sharpening B factor ($Å^2$)	–	−140	0	0	−186	−171	–	−273
Model composition								
Non-hydrogen atoms	21,793	–	–	–	–	–	–	6,874
Protein residues	2,686	–	–	–	–	–	–	855
Ligand	4 Mn 2 Mg 2 ATPγS	–	–	–	–	–	–	4 Mn
B factors ($Å^2$)								
Protein	7.38/349.16/164.49[b]	–	–	–	–	–	–	34.73/214.30/121.86[b]
Ligand	107.84/252.96/178.22[b]	–	–	–	–	–	–	138.21/141.51/139.90[b]
RMSD								
Bond lengths (Å)	0.007	–	–	–	–	–	–	0.003
Bond angles (°)	1.161	–	–	–	–	–	–	0.537

(*Continued on next page*)

Table 1. *Continued*

	*Ct*Composite (EMD-14881 PDB: 7ZR1)	*Ct*Head (EMD-14880)	*Ct*Long coiled coils (EMD-14878)	*Ct*Distant coiled coils (EMD-14879)	*Ct*RBD and bridge (EMD-14876)	*Ct*Nbs1 (EMD-14877)	*Ct*Zn hook (EMD-14882)	*Hs*M(H129N)N (EMD-15948 PDB: 8BAH)
Validation								
MolProbity score	0.99	–	–	–	–	–	–	1.03
Clashscore	1.13	–	–	–	–	–	–	2.05
Poor rotamer (%)	0.59	–	–	–	–	–	–	0
Ramachandran plot								
Favored (%)	97.03	–	–	–	–	–	–	97.76
Allowed (%)	2.97	–	–	–	–	–	–	2.24
Disallowed (%)	0	–	–	–	–	–	–	0

[a]Model resolution refers only to the average resolution of region the of composite model refined within that map.
[b]min/max/mean *B* factors.

on the highly conserved KNFKxFxx motif (K659-F664), which binds right across the 2-fold symmetry axis of the M_2R_2 head in a pseudo-symmetric fashion (Figures 2A and S5A), similar to a previous partial crystal structure (Figure S5B).[61] However, the cryo-EM map, in conjunction with AlphaFold2 multimer analysis, enables us to trace the entire interaction region of Nbs1 (~75 residues) around the Mre11 dimer (Figures 1A, top view, and S3E).

A series of coordinated turns, N-terminal of the KNFKxFxx motif, form a small, compact central domain (Figure 2A), which appears to be a species-specific feature of Nbs1 homologs, and is missing in some species (Figure S5A). The N- and C-terminal chains of *Ct*Nbs1 turn and extend back past this central domain to wrap across the Mre11 phosphodiesterase dimer (Figure 2A, insets) and bind with reverse polarity to equivalent regions of the two Mre11 protomers. The asymmetry of Nbs1 binding to Mre11 correlates with asymmetric interactions between Mre11 and Rad50 (Figure S5C), suggesting the symmetry breaking of Nbs1 influences the behavior of the entire MRN complex. This may be driven by the Mre11 loop H213-L225, which alternately interacts with the N-terminal strand of Nbs1 (Figure S5C, left), or swings 15 Å to interact with Rad50 (Figure S5C, right). One Rad50 appears stabilized by this interaction, while the other shows a more flexible conformation, deviating up to 8 Å from the symmetry related position (Video S1).

Further 3D classification of the Mre11-Nbs1 interaction showed that particles could be divided into 5 classes: central domain with N-terminal chain bound (27%), central domain with C-terminal chain bound (27%), central domain with both chains bound (25%), central domain with neither chain bound (13%), and no Nbs1 bound (8%) (Figure S5D). This indicates that the interaction of Nbs1 with MR could be locally quite dynamic, perhaps to allow for conformational changes or response to interaction partners. Finally, we note that the 75-residue long Mre11 interaction region of Nbs1 more or less precisely corresponds to the minimal fragment of Nbs1 required to maintain embryonic viability, highlighting the importance of the asymmetric wrapping of the Mre11 dimer by Nbs1.[62]

In attempts to derive structures of human MRN, we obtained interpretable classes of *Hs*Mre11 bound to *Hs*Nbs1 (Rad50 apparently dissociated). In the resulting reconstruction to 4.1 Å, we observe the canonical Mre11 dimer, which is wrapped by a single Nbs1 polypeptide (Figures 2B and S6A–S6C). Consistently, *Hs*MRN purifies as a 2:2:1 complex (Figure S6F). Of note, the obtained Mre11 dimer, wrapped by Nbs1, is markedly different from the crystal structure of the *Hs*Mre11 nuclease domain, where a different dimer interface was formed at a disulfide bond, and in the absence of Nbs1.[63] We used AlphaFold2 multimer to predict the *Hs*$Mre11_2$:Nbs1 complex, and the obtained model can be rigid body docked with only a few minor adjustments into the map (Figure 2C). Again, Nbs1 binds in three sections to the Mre11 dimer, two lateral interactions, and the central KNFKxFxx motif across the dimer symmetry axis (Figure 2B). Interestingly, the directions of the KNFKxFxx motifs across the Mre11 dimers are reversed for human and Chaetomium proteins, showing quite significant species-specific adaptation in this interaction (Figures 2C and 2D). Both the Chaetomium as well as human KNFKxFxx motifs fit well to the

Please cite this article in press as: Rotheneder et al., Cryo-EM structure of the Mre11-Rad50-Nbs1 complex reveals the molecular mechanism of scaffolding functions, Molecular Cell (2022), https://doi.org/10.1016/j.molcel.2022.12.003

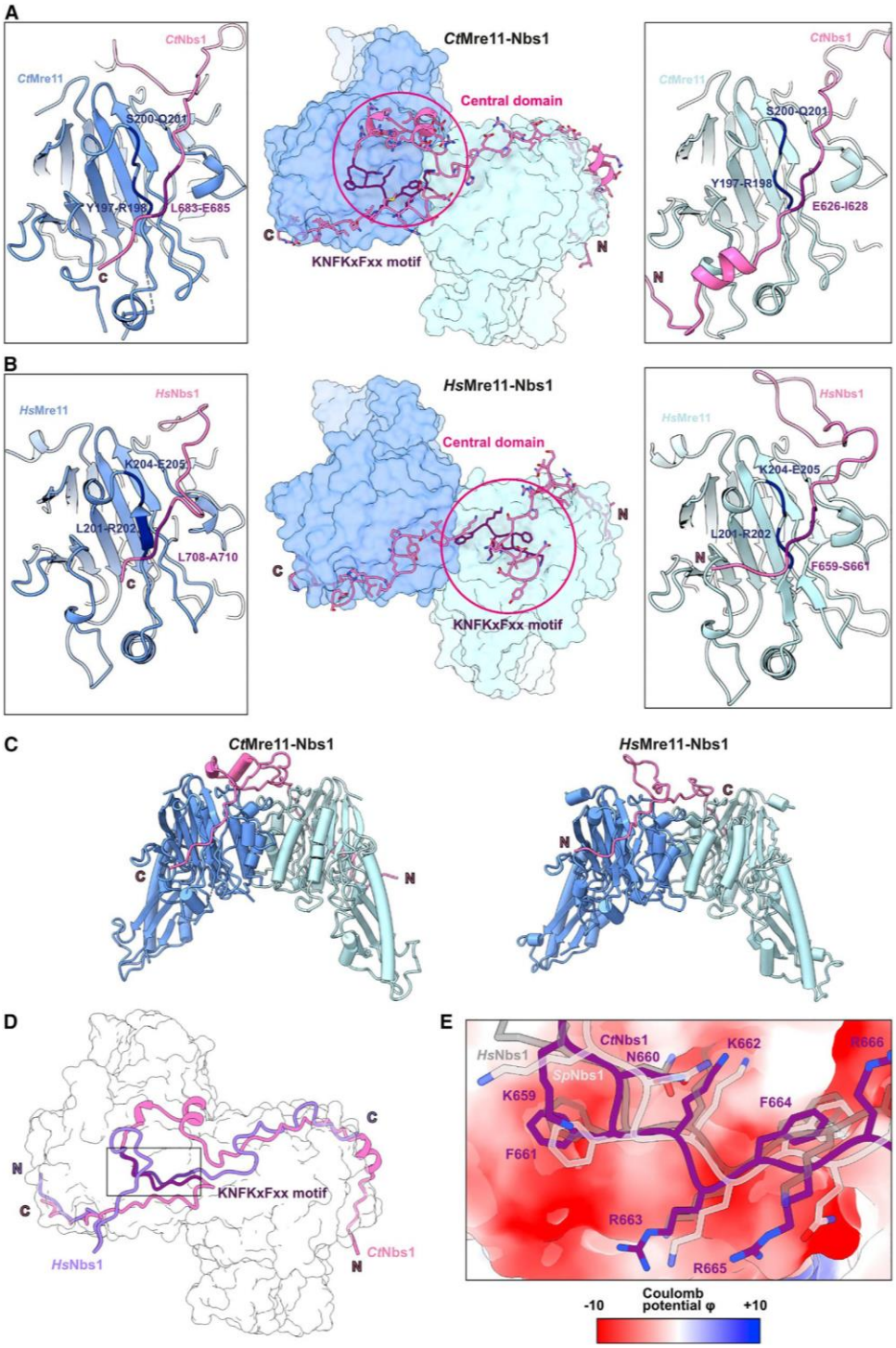

(legend on next page)

Please cite this article in press as: Rotheneder et al., Cryo-EM structure of the Mre11-Rad50-Nbs1 complex reveals the molecular mechanism of scaffolding functions, Molecular Cell (2022), https://doi.org/10.1016/j.molcel.2022.12.003

S. pombe crystal structure, with all species relying on a negatively charged Mre11 binding pocket (Figure 2E). Mutating the central KNFKxFxx and/or the flanking interaction elements reduced the ability of Nbs1 to complement an siRNA-mediated knockdown of Nbs1 in HR assay in U2OS cells (Figures S6D and S6E).

In summary, our structures reveal a conserved Mre11 dimer architecture and wrapping by a single Nbs1/Xrs2 polypeptide as an evolutionary conserved feature of MRN/X.

Rad50 is in a pre-engaged ATP state

The head module has one ATPγS moiety bound to each of the two Walker A motifs of the Rad50 dimer (Figures 3A and 3B). The signature motifs, a conserved motif characteristic for the ABC-type ATPase family, are approximately 10 Å away from the γ-(thio)phosphate of the ATPγS (Figure 3C), indicating that the observed state is not yet ATP-hydrolysis competent and may need an additional conformational change (perhaps through DNA binding) to trigger ATP hydrolysis. Comparing crystal structures of the isolated *Ct*Rad50^{NBD} bound to ATPγS and either DNA or the Mre11^{RBD},[64] which displayed signature motifs fully engaged with the *trans* γ-(thio) phosphates (Figure 3C), with the cryo-EM structure reveals an approximately 30° rotation of each of the two NBDs. Accompanying are corresponding movements of the CC domains (truncated in the crystal structures) (Video S2). Thus, in the full-length *Ct*MRN cryo-EM structure, the adhesion of the CC domains and possibly the Mre11 bridge, likely prevents the necessary rotation of the NBDs, which remain in a partially engaged state. Even in the presence of ATP, only a subset of particles showed an open CC conformation, altogether pointing to a tighter autoinhibition of MRN as compared with MR in the absence of DNA (Figure S4B). To evaluate, whether Nbs1 plays a structural role in stabilizing MR, we structurally analyzed *Ct*MR (lacking Nbs1). Interestingly, the catalytic head complexes became more unstable, as seen by movements of the Mre11 dimer relative to Rad50 in 2D classes (Figures S7C, S7F, and S7G). In addition, omitting Nbs1 also increased the number of classes and particles with open CCs in the presence of ATPγS, altogether suggesting that wrapping of the Mre11 dimer by Nbs1 is important for regulation and stability.

ATP-dependent and -independent DNA binding by MRN

The rod structure of the CCs raises the question of whether the canonical DNA-binding site on the Rad50^{NBD}s remains accessible to DNA (Figure 3C, crystal structure) and what role ATP plays in DNA binding. To assay ATP-dependent and -independent DNA binding, we used a fluorescence polarization anisotropy (FA)-based assay (STAR Methods). Wild-type *Ct*MRN complex binds to the 80-mer double-stranded (ds)DNA oligonucleotide with K_D's of 53 ± 5 and 30 ± 2 nM in the presence of ATP and ATPγS, respectively (Figure 4A). We attribute the higher K_D for ATP to hydrolysis-dependent turnover since DNA robustly stimulates ATP hydrolysis (see below). Surprisingly, MRN also binds DNA in absence of ATP with a somewhat higher K_D of 73 ± 7 nM (Figure 4A). DNA binding in the absence of ATP was also seen for human MRN,[65] which is in contrast to the strictly ATP-dependent DNA binding of prokaryotic MR.[21,66,67]

Interestingly, the binding curves converge to higher FA plateau values in presence of ATP and ATPγS (97 and 92 mP, respectively) compared with the curve with no nucleotides (57 mP) (Figure 4A). This approximately 2-fold FA increase in presence of ATP and ATPγS is a hint for the binding of a second DNA molecule, possibly through the eukaryote-specific Mre11 C-terminal extension.[68] We generated a mutant MRN complex (M$^{\Delta C}$RN), where this Mre11 extension (568–730) was removed (Figure 4B, top). The truncation still retains the bridge, as removal of the bridge resulted in an unstable complex that we were not able to characterize further. Our truncation site coincides with a recently described SPARTN (human Spartan) protease cleavage site in human Mre11 in certain cancers cells that reduced the affinity of *Hs*Mre11 to DNA.[69]

DNA-binding affinity of the Rad50^{NBD}s in the presence of ATP/ATPγS remained nearly unaltered (K_D = 51 ± 5 and 28 ± 2 nM, respectively). Moreover, the levels of the FA plateaus (56 mP, 27 mP, respectively) are consistent with FA increase caused by a single DNA oligomer, as seen above for the WT *Ct*MRN. In addition, sigmoidal DNA-binding curves for *Ct*MRN and *Ct*M$^{\Delta C}$RN with and without ATP with Hill coefficients >1 (ranging from 1.3 to 3.0, see STAR Methods) indicate cooperative binding modes possibly arising from protein oligomerization, similar to what was observed for *S. cerevisiae* MRX.[56]

In support for this interpretation, we noticed that DNA-bound *Ct*M$^{\Delta C}$RN complexes were significantly less prone to visual aggregation than *Ct*MRN (Figures S7A and S7B). Nevertheless, Hill coefficients are comparable between *Ct*MRN (no nucleotide: 3.0 ± 0.5; ATP: 1.5 ± 0.1; ATPγS: 2.2 ± 0.2) and *Ct*M$^{\Delta C}$RN (ATP: 1.5 ± 0.1; ATPγS: 2.2 ± 0.2), suggesting that the core MRN (without Mre11 C terminus) can also cooperatively interact with DNA, presumably through protein oligomerization (see also below).

To investigate the preference of *Ct*MRN and *Ct*M$^{\Delta C}$RN for DNA ends, we performed competition assays by adding

Figure 2. Structural comparison of *Ct*MN and *Hs*MN

(A) A single *Ct*Nbs1 polypeptide (magenta) binds asymmetrically across both *Ct*Mre11 (blue). The interfaces of the N- and C-terminal region, which bind with reverse polarity to equivalent regions on Mre11, as well as the central core binding region harboring the conserved KNFKxFxx motif, are shown.

(B) *Hs*MN shows a high similarity to *Ct*MN with respect to the Mre11 dimer. Due to higher flexibility, only a shorter *Hs*Nbs1 part could be resolved.

(C) A side-view comparison reveals a highly conserved Mre11 fold as well as Nbs1 path.

(D) Direct comparison of *Hs* and *Ct*Nbs1 paths across *Ct*Mre11 (contoured). Aligning both MN complexes emphasizes the reversed orientation of Nbs1 (magenta: *Ct*, purple: *Hs*).

(E) Overlay of the KNFKxFxx motifs for *S. pombe* (*Sp*, light gray, PDB: 4FBQ), *Hs* (gray), and *Ct* (purple) onto *Ct*Mre11. The electrostatic surface potential reveals a negatively charged binding pocket for this conserved motif.

See also Figures S5 and S6 and Video S1.

Please cite this article in press as: Rotheneder et al., Cryo-EM structure of the Mre11-Rad50-Nbs1 complex reveals the molecular mechanism of scaffolding functions, Molecular Cell (2022), https://doi.org/10.1016/j.molcel.2022.12.003

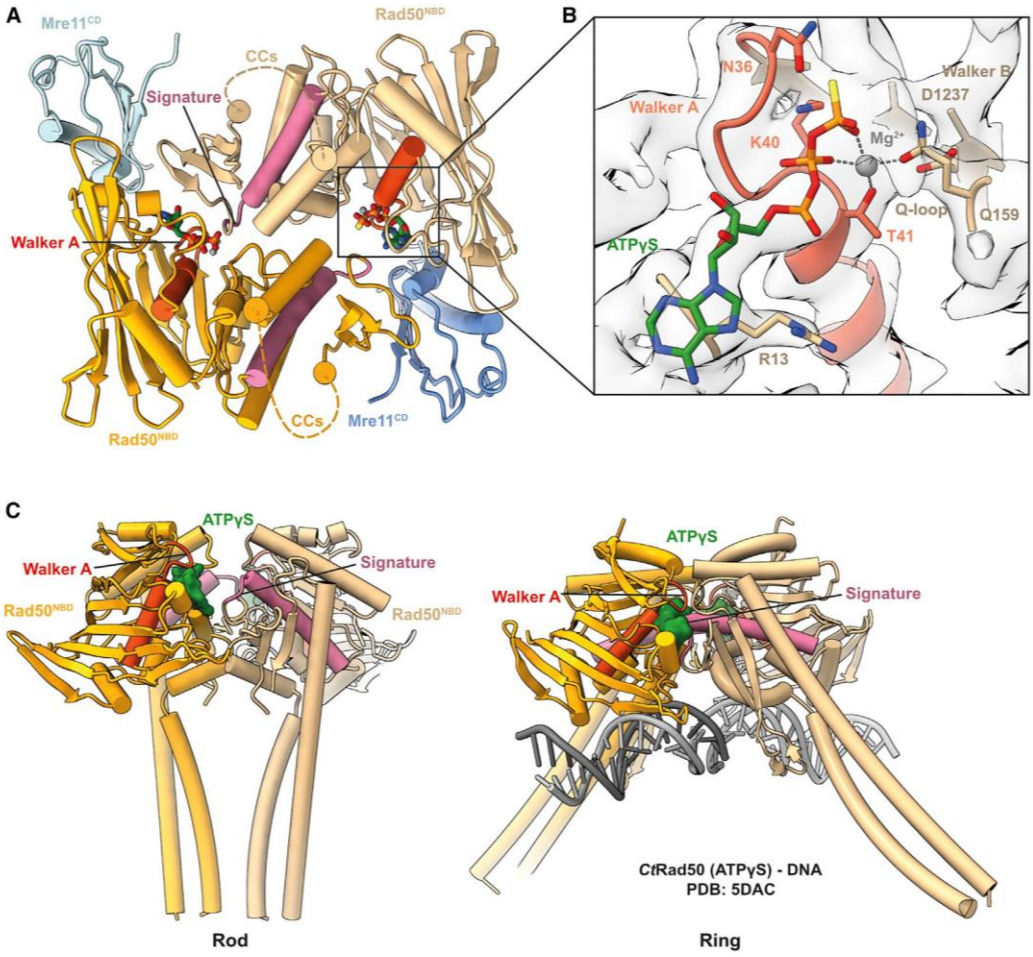

Figure 3. Rad50 in a pre-engaged ATP state

(A) Bottom view of Rad50^{NBD} with ATPγS bound. Enzymatically important elements are highlighted.

(B) Close-up view of the coordinated Mg^{2+} and ATPγS in the NBD of Rad50. The Mg^{2+} ion is depicted in gray and enzymatically important residues are annotated and illustrated as sticks. The atomic model is overlaid by the cryo-EM map.

(C) A comparison of the cryo-EM structure with the ATPγS bound Rad50 crystal structure (PDB: 5DAC) illustrates the differences in Rad50^{NBD} dimerization and the pre-engaged state of Rad50 in MRN.

See also Video S2.

increasing amounts of unlabeled circular or linearized plasmid DNA to the solution containing a fixed amount of protein and labeled 80-mer dsDNA. For *Ct*MRN, the linearized DNA competed approximately 3-fold better than the circular DNA, showing an only moderate preference for DNA ends (Figure 4C). However, for *Ct*M$^{\Delta C}$RN, linear DNA competed ~35-fold better than circular DNA (Figure 4D).

We tested the effect of DNA-stimulated ATP hydrolysis on DNA-binding properties by ATPase assays. Similar to *Hs*MRN, we find that linear DNA stimulated *Ct*MRNs ATPase approximately 10-fold, whereas circular DNA stimulated MRN only 2-fold (Figure 4E).[58] ATPase rates of *Ct*M$^{\Delta C}$RN were generally reduced to 2/3 of WT MRN's ATPase levels but showed a similar 10-fold (linear) and 2-fold (circular) stimulation by DNA (Figure 4F). The lower ATPase rate might be caused by a less stable protein. However, the strong increase of M$^{\Delta C}$RN's preference for ATP-dependent binding of linear vs. circular DNA is unlikely caused by the moderate reduction in ATPase activity, especially because the same increase in preference for linear over circular DNA is observed in the presence of ATPγS.

We also tested *Ct*MR alone for the interdependence of nucleotide and DNA binding (Figure S7D). *Ct*MR binds DNA in a nucleotide dependent fashion and has lost the ability to interact with DNA in the absence of ATP/ATPγS. This might be due to the decreased stability of the head (as seen in the cryo-EM data in

Please cite this article in press as: Rotheneder et al., Cryo-EM structure of the Mre11-Rad50-Nbs1 complex reveals the molecular mechanism of scaffolding functions, Molecular Cell (2022), https://doi.org/10.1016/j.molcel.2022.12.003

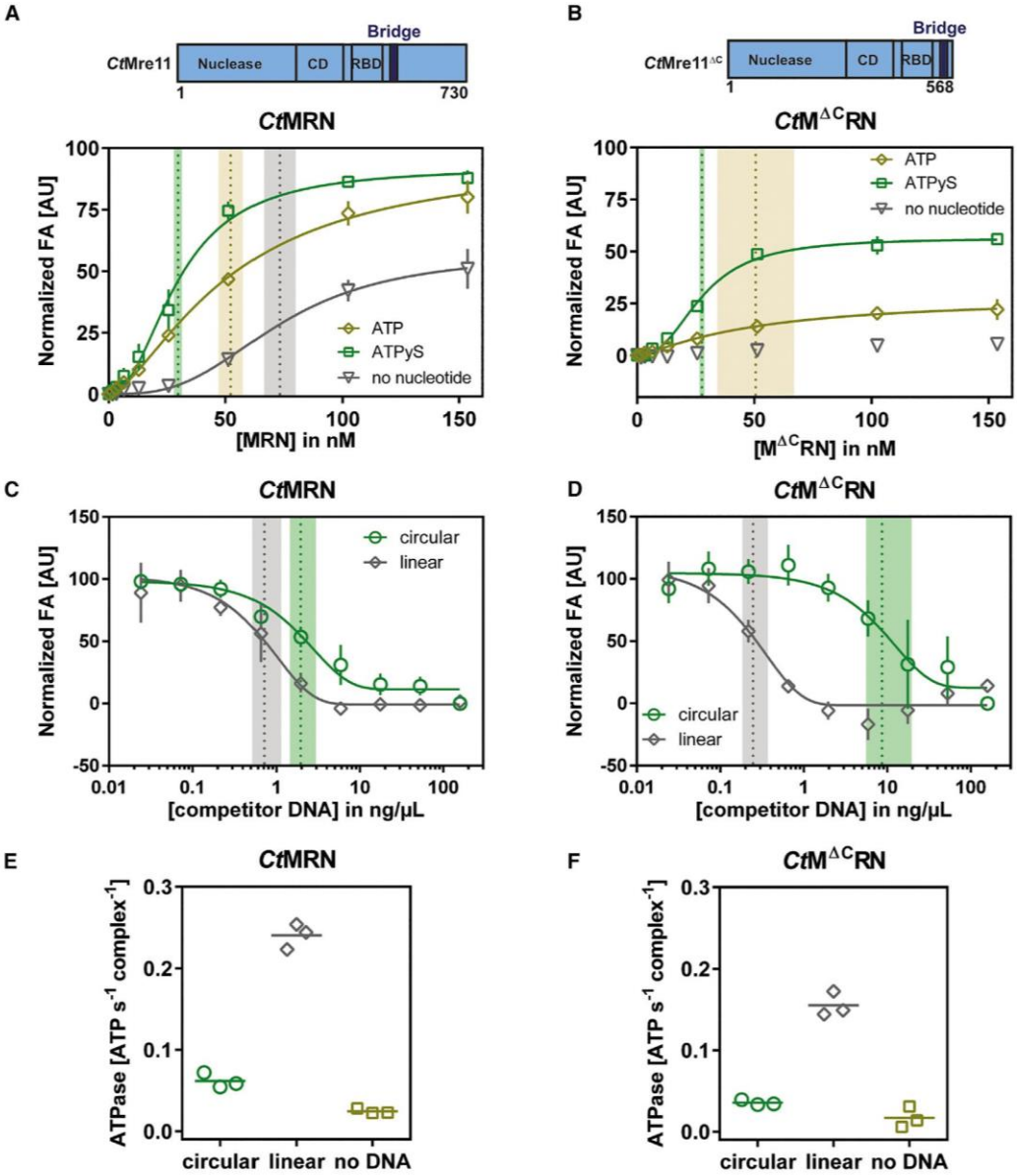

Figure 4. ATP-dependent and -independent DNA binding by MRN

(A) Top, depiction of full-length *Ct*Mre11 construct used in the DNA binding and ATPase assays. Fluorescence anisotropy-based assay documenting the effect of ATP and ATPγS on *Ct*MRN binding toward 80-mer dsDNA. The wild-type complex binds cooperatively to dsDNA also in the absence of ATP. For (A)–(D), data are presented as mean ± SD, n = 3.

(B) Depiction of *Ct*Mre11$^{\Delta C}$ construct used in the DNA binding and ATPase assays. Similar fluorescence anisotropy assay as in (A) using the C-terminal truncated *Ct*M$^{\Delta C}$RN complex. *Ct*M$^{\Delta C}$RN binding to DNA was nearly abolished in the absence of ATP/ATPγS, while it retained DNA binding in the presence of ATP or ATPγS.

(C) DNA-binding competition assay utilizing the FA-based experiment as in (A) and (B) and adding increasing amounts of unlabeled circular or linearized plasmid DNA to the experiment. The results reveal that *Ct*MRN binds linear and circular DNA with a similar affinity.

(D) DNA-binding competition assay as in (C) showing that *Ct*M$^{\Delta C}$RN complex has a strong preference for linear DNA.

(E) ATPase assays of *Ct*MRN showing the stimulation of the ATP hydrolysis rate by the addition of linearized DNA.

(F) ATPase assays of *Ct*M$^{\Delta C}$RN showing the stimulation of the ATP hydrolysis rate by the addition of linearized DNA, as for *Ct*MRN.

Please cite this article in press as: Rotheneder et al., Cryo-EM structure of the Mre11-Rad50-Nbs1 complex reveals the molecular mechanism of scaffolding functions, Molecular Cell (2022), https://doi.org/10.1016/j.molcel.2022.12.003

the presence of ATPγS), which might further disintegrate in the absence of ATP/ATPγS. However, DNA-stimulated ATPase behaves similar to WT and is only robustly seen in the presence of linear DNA (Figure S7E).

We conclude that MRN possesses two DNA-binding components. The first binds preferentially DNA ends in an ATP-dependent manner, much like bacterial MR. The second mode is ATP independent with contributions by the *Ct*Mre11 C-terminal tail and Nbs1 (Figure S7D). These additional interactions increase binding of internal DNA elements.

MRN-MRN tethering via zinc-hook tetramerization

During cryo-EM data processing, we noted 2D classes that resembled Rad50 zinc-hook dimers in the "closed" rod configuration (Figure S1C). We denote the tips of the dimerized CCs of a single MRN complex as CC apex. 2D class averages did not show single apices but depicted apex dimers: two Rad50 zinc-hooks, joined via Zn^{2+} coordination to form the canonical apex in rod configuration, further dimerize in an antiparallel fashion to tether two MRN complexes. We could reconstruct a cryo-EM map at an overall resolution of 4.9 Å, which resolved another 14 nm of the total CCs (Figures 5A and S8; Table 1). To obtain a higher resolution and independently verify this apex-apex interaction, we crystallized and determined the structure of the CC region around the zinc-hook (*Ct*Rad50$^{589–782}$) (Figure 5B; Table 2).[70] The asymmetric unit of the crystal consists of a dimer of zinc-hook dimers, i.e., two tethered apices, in the same arrangement as observed by cryo-EM (Figure 5B).

The apex of a single $M_2R_2N_1$ is formed by joint coordination of a Zn^{2+} ion through the zinc-hook motifs, as observed in crystal structures of archaeal and human Rad50 zinc-hook regions[23,24,71] (Figure 5C). In both cryo-EM and crystal structure, the two CCs are arranged in the same rod configuration, which apparently enables an antiparallel interaction of two apices through formation of a new interface (Figure 5D).[23] Hereby, F688 of one Rad50 dimer binds into a hydrophobic pocket (I651 and L654) at the last CC segment joint of the other Rad50 dimer, and vice versa. This hydrophobic interaction is flanked with salt bridges between R684 and E655, R687 and E658, and K686 and D736. Due to the dimeric nature of the CC rods, the tethering interactions can form on both sides of a given apex, thus leading to formation of two-dimensional sheets of antiparallel tethered apices in the crystal lattice (Figure S8D). Interestingly, we observe apex multimers in cryo-EM, supporting the idea of higher-order apex interactions (Figure S8E). Due to the low number of particles, we could not obtain higher resolved 3D maps at this stage.

Since the *Ct*Rad50 zinc-hook shows structural conservation to the previously published crystal structure of the *Hs*Rad50 zinc-hook,[24] we inspected the underlying crystal lattice (PDB: 5GOX). Intriguingly, the *Hs*Rad50 apices adopt related, compared with *Ct*Rad50, longitudinally shifted and somewhat distinct, tethered structures within the crystal lattice (Figure 6A). Similar to that in *Ct*Rad50, the same region at the tip of the CC helix mediates this interaction with the neighboring apex. The overall mode of antiparallel interactions of both human and *C. thermophilum* CC apices suggest that apex-apex interactions might be a conserved feature to tether two or more MRN complexes.

Zinc-hook tetramerization is required for efficient DNA repair in human cells

To assess the functional significance of MRN-MRN tethering on recombinational DNA-damage repair in living cells, we mutated the *Hs*Rad50 apex tethering element (DENQS675-679AAAAA; Rad50^{apex}). Purified *Hs*MR^{apex}N complex maintains $M_2R_2N_1$ stoichiometry, a thermal stability profile similar to WT *Hs*MRN (Figures S6F and S6I), ATP/ATPγS stimulated DNA binding, and linear dsDNA stimulated ATPase (Figures S6G and S6H). Thus, the apex loop mutation does not disrupt the general fold of Rad50 and preserves its DNA-stimulated ATPase properties. A slightly reduced DNA-binding activity might indicate some defects in this area, which, however, may stem from a reduced clustering propensity.

We analyzed the capability of *Hs*MR^{apex}N to repair reactive oxygen species (ROS)-mediated DNA damage through Comet assays in U2OS cells. Endogenous Rad50 was knocked down via siRNAs and the cells were transfected with WT or mutated Rad50, along with WT Mre11 and WT Nbs1 to have all components expressed at the same level. Knockdown of endogenous Rad50 without supplementing plasmid expressed MRN caused impaired DNA repair upon ROS-induced stress (Figure 6B). Residual repair capacity may be attributed to remaining levels of endogenous Rad50 after siRNA knockdown. Transfection with WT MRN fully rescued the repair deficiency (Figure 6B). Transfection with MR^{apex}N only led to a partial rescue, despite robust overexpression of the proteins (Figure S6J). The rescue level is slightly better than in the absence of MRN transfection, indicating that the mutant has a residual but substantially affected repair capacity. We also employed a direct repeat GFP (DR-GFP) HR assay (Figure 6C). While expression of a plasmid containing WT Rad50 robustly rescued the recombination defects of an siRNA knockdown of Rad50, the Rad50^{apex} plasmid was about halfway between WT and empty control. Nevertheless, the apex mutations appear to have less of an impact in the DR-GFP assay than in the Comet assay.

Interestingly, during the course of our analysis with *Ct*MR (lacking Nbs1), we occasionally observed the formation of semi-regular clusters, where rows of oligomerized head modules are connected via many tethered CCs, generating regular 120–140 Å wide molecular Velcros (Figure 6D). This shows that CC-CC clustering via the apex and head-head clustering can cooperate to form large assemblies.

Taken together, these data suggest that the apex tethering element mutation compromises MRN function in DSB repair and that the structurally observed tethering interaction is an important feature of MRN in human cells.

DISCUSSION

The MRN complex is a multifunctional DSB repair factor that senses and processes DSBs.[12–14] MRN also has functions in ATM activation, DNA tethering, telomere maintenance and chromatin organization.[16,20,35,43,45,46,51,72,73] Using cryo-EM analysis and crystallography, we determined the structure of MRN in a

Please cite this article in press as: Rotheneder et al., Cryo-EM structure of the Mre11-Rad50-Nbs1 complex reveals the molecular mechanism of scaffolding functions, Molecular Cell (2022), https://doi.org/10.1016/j.molcel.2022.12.003

CellPress

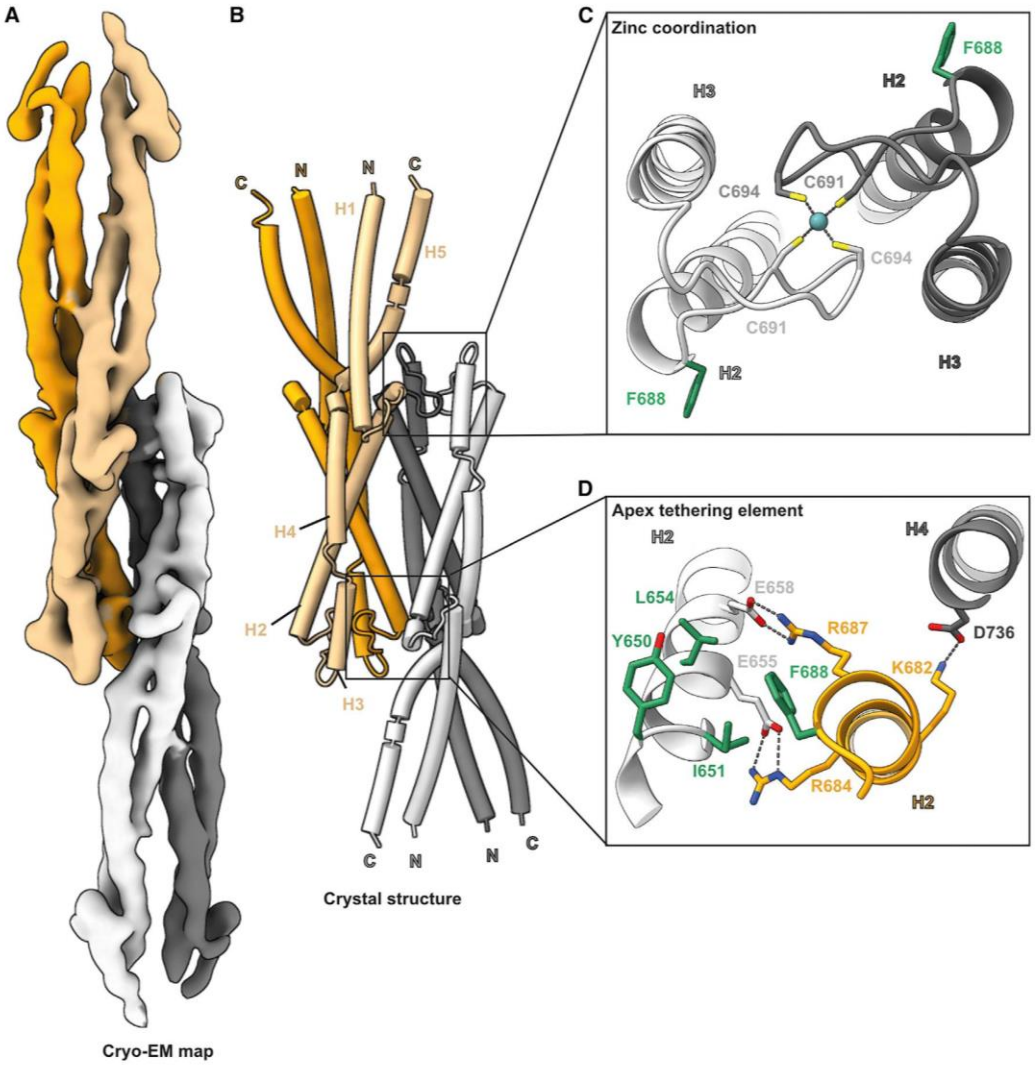

Figure 5. Structure of the *Ct*Rad50 zinc-hook tetramer

(A) Cryo-EM map of zinc-hook tetramer at 4.9 Å resolution, where each Rad50 monomer belonging to one MRN complex is depicted in related color.

(B) Atomic model of the zinc-hook tetramer crystal structure shown in comparison with the cryo-EM map.

(C) Close-up view of the Zn^{2+}-binding site.

(D) Rad50 apex tethering element with the residues involved in the interaction are shown in stick representation.

See also Figure S8.

resting state, providing an architectural framework and mechanism for the unresolved question of how MRN combines catalytic and structural tethering functions.

The structure clarifies the complex stoichiometry as $M_2R_2N_1$. Parts of Nbs1 wrap as an elongated chain around the Mre11 nuclease domain dimer, arguing that an essential function of Nbs1 is to stabilize the Mre11 dimer and head architecture, which might be critical for ATM activation and other functions of the complex. For instance, the *S. cerevisiae* Nbs1/Xrs2 provides nuclear localization and is required for ATM/Tel1 recruitment and canonical end-joining activities, while it is dispensable for nuclease-associated functions of MRN/X.[74] In mice, Nbs1 deletions cause embryonic lethality; however, a minimal Mre11-binding fragment that more or less precisely correlates with the portion of Nbs1 that we visualize here was shown to restore viability and enable ATM activation.[62] These data indicate that the observed wrapping of the Mre11 dimer by Nbs1 would be particularly important for roles in DNA tethering and Tel1 activation. Work on the bacterial MR complex suggests that the Mre11 dimer might need to transiently open up during

Please cite this article in press as: Rotheneder et al., Cryo-EM structure of the Mre11-Rad50-Nbs1 complex reveals the molecular mechanism of scaffolding functions, Molecular Cell (2022), https://doi.org/10.1016/j.molcel.2022.12.003

Table 2. Data collection and refinement statistics (molecular replacement)

	Zinc-hook (PDB: 7ZQY)
Data collection	
Space group	P1
Cell dimensions	
a, b, c (Å)	43.49, 53.97, 110.42
α, β, γ (°)	75.847, 78.742, 89.996
Resolution (Å)	2.5[a]
R_{sym} or R_{merge}	7.8 (67.4)
$I/\sigma I$	7.86 (1.72)
Completeness (%)	97.4 (91.3)
Redundancy	3.55
Refinement	
Resolution (Å)	2.5
No. Reflections	63.401
R_{work}/R_{free}	26.42/28.30
No. Atoms	
Protein	5,801
Ligand/ion	2 Zn^{2+}
Water	3
B factors (Å^2)	
Protein	81
Ligand/ion	79.5
Water	75.55
RMSD	
Bond lengths (Å)	0.012
Bond angles (°)	1.779

Values in parentheses are for highest-resolution shell.
[a]Final data were collected on a single crystal.

relocation from the resting to the cutting state.[26] In eukaryotes, Nbs1 would need to transiently dissociate at least from one of the Mre11 protomers upon formation of a putative cutting state structure. This is plausible because we do observe some classes of MRN where one or the other lateral section of Nbs1 has dissociated from the Mre11 nuclease dimer.

An unexpected observation was that the *Ct*MRN-ATPγS CCs adopt a closed rod state, rather than the open, flexible ring structure that was observed for the *Ec*MR-ATPγS complex.[26] We attributed the open state to loading onto DNA ends, especially those that carry a proteinaceous block. It is difficult to envision how a blocked DNA end could enter between the CCs in this closed rod configuration. Further functional clarification must await structures of DNA complexes of MRN. Eukaryotic MRN could be more autoinhibited than bacterial MR, which makes sense considering the much more complex functional spectrum and the perhaps greater cytotoxic threat that unregulated DNA cleavage by MRN might pose on eukaryotic genomes. However, the CCs might also be more dynamic as seen in atomic force microscopy.[54,75,76] We also observe a subpopulation of open CC domains exclusively in the presence of ATP, in line with the idea that ATP binding is needed to open the CCs.[77] Comparison with the crystal structures of *Ct*Rad50^{NBD} in complex with ATPγS reveals that a full engagement of the NBDs with the signature motif binding to the γ-phosphate of ATP needs an approximately 60° rotation of NBDs with respect to the other, a movement that would pry the CCs open (Figure 3C; Video S2).[64] A switch between a semi-engaged NBD (this study) and engaged NBD (Rad50^{NBD} crystal structures) would be consistent with studies that show partially open and closed conformations of NBDs on archaeal MR.[78] It is likely that cooperative ATP and DNA binding may help to stabilize the open CC conformation with fully engaged NBDs since linear DNA triggers ATP hydrolysis approximately 10-fold in both *C. thermophilum* (Figure 4F) and human MRN (Figure S6G).[58] Thus, it is reasonable to assume that DNA interacts with MRN after ATP dependent loading on DSBs such that DNA is bound at Rad50's NBDs between the CC, consistent with a prior crystallographic analysis of *Ct*Rad50 and crystal as well as cryo-EM structures of prokaryotic MR in complex with DNA.[26,64,79]

The spectrum of DNA-binding activities by MRN is more complex than for bacterial MR, which only displayed DNA-binding activities that were highly specific for DNA ends and fully dependent on ATP.[59] We identify the C-terminal extension of eukaryotic Mre11 as responsible for the additional nucleotide independent DNA binding activity, as well as the increased capacity to bind circular compared with linear DNA, separating DNA-binding modes into one that involves the core head complex and is highly specific for DNA ends and ATP, and another that is ATP independent and extends DNA binding also to undamaged DNA regions. The C terminus could directly bind DNA or could help modulate DNA-binding properties of the Mre11 catalytic core to bind DNA in a nucleotide independent fashion.[80] A DNA binding site in the C terminus of *S. cerevisiae* Mre11 has been identified early on.[81] The *Sc*Mre11-5 mutation (deletion of C terminus of Mre11) did not lead to MMS sensitivity in yeast,[68,81] consistent with the ability of *Ct*M$^{\Delta C}$RN to efficiently bind and process DNA ends *in vitro* in an ATP dependent fashion. However, Mre11-5 specifically abolished formation (but not processing) of meiotic breaks, and diminished meiotic chromatin association, which hint toward defects in association with intact DNA.[82] We envision that MRN, similar to bacterial MR, is loaded onto DBSs in a configuration where the DNA end passes through the CCs, while internal DNA is recognized in a more peripheral fashion via Mre11's C terminus (Figure 6E).

The presence of two DNA-binding modes fits very well with the DNA-binding dynamics observed in single-molecule DNA curtain experiments.[18] The canonical, ATP-dependent Rad50 DNA-binding site seems to be responsible for binding to DNA ends, where *Hs*MRN was observed to cleave Ku and itself off in a process that requires ATP. However, before DNA end recognition, MRN was observed to diffuse along linear DNA in an ATP-independent fashion. Furthermore, the *Hs*Mre11 C terminus was found to be cleaved by the SPRTN protease in human cancer cells and attributed to loss of DNA binding.[69] From our results, DSB-sensing and -processing capacity might still be intact in these tumor cells, while MRNs poorly understood role in chromosome organization or transcription might be affected, a role that could require specifically interaction with intact DNA.[51,52]

Perhaps the most important result of our work is the apex dimerization, which integrates catalytic and tethering functions.

Please cite this article in press as: Rotheneder et al., Cryo-EM structure of the Mre11-Rad50-Nbs1 complex reveals the molecular mechanism of scaffolding functions, Molecular Cell (2022), https://doi.org/10.1016/j.molcel.2022.12.003

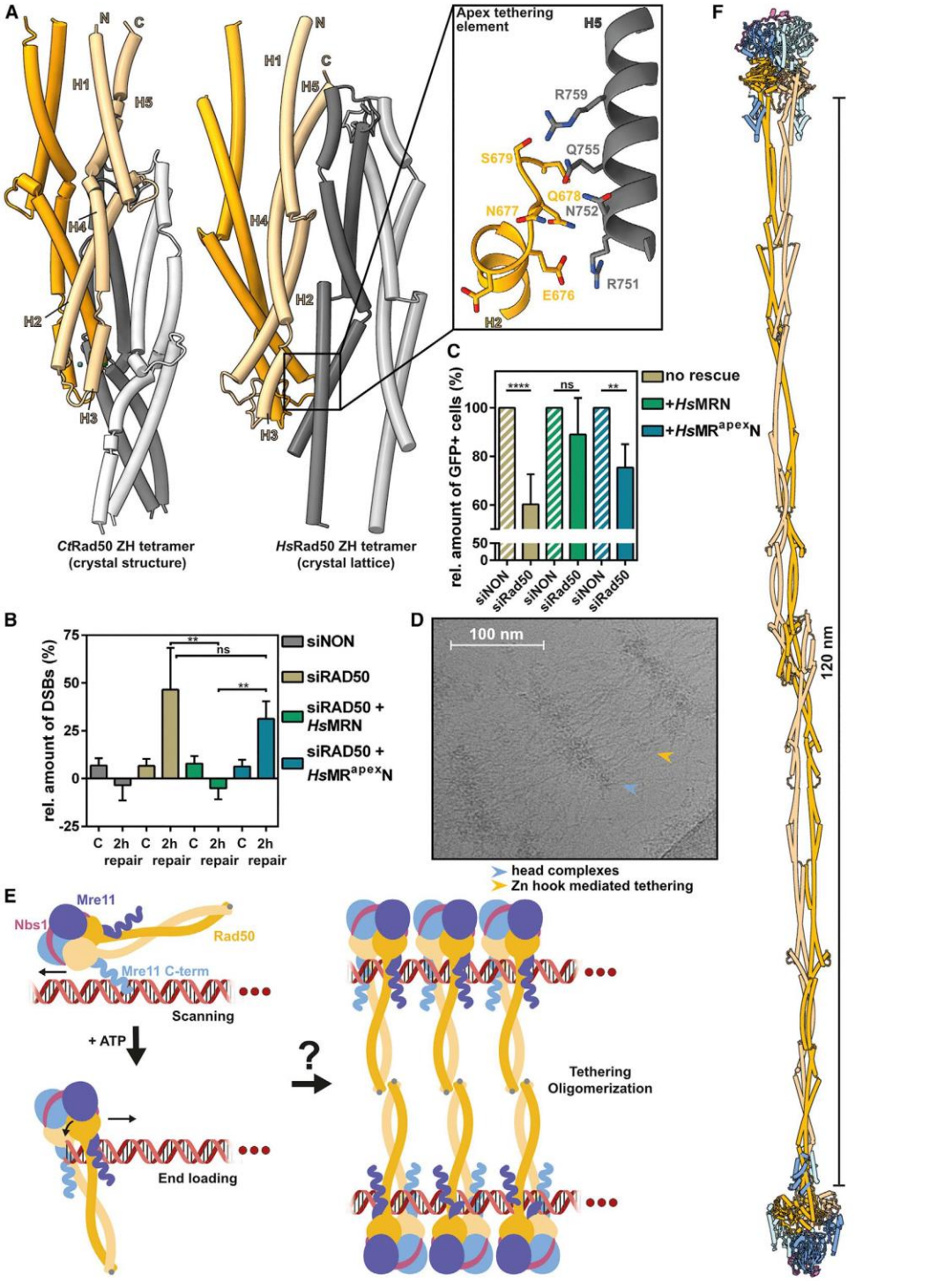

(legend on next page)

Please cite this article in press as: Rotheneder et al., Cryo-EM structure of the Mre11-Rad50-Nbs1 complex reveals the molecular mechanism of scaffolding functions, Molecular Cell (2022), https://doi.org/10.1016/j.molcel.2022.12.003

Early negative-stain electron microscopy, AFM and cell-based studies show that CC apices from different MR/MRN complexes can associate and that MRN has functions in tethering of different DNA elements.[20,23–25,49,54,56,76,83] Based on structural work on the zinc-hook regions,[23,24,71] it was assumed that the dimerization of two zinc-hooks can occur between the CCs of a single MRN complex (intra-complex) or between the CCs from different MRN complexes (inter-complex). However, the emerging role of the CC domains as a critical chemo-mechanical gate, rather than a mere linker element, made it unlikely that zinc-hooks switch from intra- to inter-complex interaction modes. Rather they act as stably associated hinges that can switch between ring and rod states of the CCs of a single MRN complex.

Our cryo-EM data now resolve this prevailing conundrum, showing that two apex regions in the rod configuration can further dimerize to join two MRN-MRN complexes (Figure 6F), which clarifies the mode how MRN-MRN dimers are tethered generating large structures spanning up to approximately 120 nm (Figure 6F). The small hydrophobic anchor surrounded by salt bridges might be quite transient, but clustering through additional head-head interactions[56] could form a stable molecular Velcro through multivalent interactions[20,54] (Figure 6E). The observed head-head distances are well suited to tether DSBs, chromatids, or perhaps even meiotic chromosomes at synaptonemal complexes.[49]

The type of interface with small hydrophobic parts and ion pairs is characteristic of the types of interactions found in liquid-liquid phase-separated condensates.[84] Inspection of the crystal lattice of *Ct*Rad50^{apex} shows that 1D-lattice-like interactions between multiple apices might form. It is therefore possible that DNA tethering by MRN proceeds via multivalent interactions much like those proposed for phase-separated condensates.

The *Hs*Rad50^{hook} crystal lattice revealed a similar tetrameric arrangement (Figure 6A).[24] Mutating the apex tethering interface impaired the repair of ROS-mediated DNA damage in human cells, showing its functional significance. However, we do not find a strong impact of the apex mutants in the DR-GFP assay, which monitors HR on a clean break. It is therefore possible that these interactions are important in a different functional context, roles that have to be addressed in future studies. Part of the apex-apex interface is a loop insertion element in the CC that carries an SQ-motif (S635, Q636). This site has been noticed and studied before, and it was found to be phosphorylated by both ATM and ATR.[85,86] Mutations in S635 affected DSB repair, checkpoint activation, and survival, as well as cohesin loading at sites of replication restart.[85,86] These phenotypes were not caused by defects in the nuclease activity, since *Hs*MRN^{S635G} had unaltered nuclease activity *in vitro*[85] and indicate that tethering may be subject to regulation by ATM and ATR in human cells. From a structural point of view, phosphorylation could increase the stability of the tethering through interactions with nearby basic amino acids on the opposing apex protomer, but it could also alter the geometry of the apex and reduce tethering through geometric issues. We note that the apex-apex interfaces are not well conserved in evolution and the functional importance of MRN-MRN tethering and its regulation may differ in different species. Replacing the zinc-hook region with the hinge domain of the bacterial SMC protein MukB did not result in increased camptothecin and hydroxyurea sensitivity in *S. pombe*.[75] Further studies are needed to generalize apex tethering to other organisms, and the geometric interplay between apex tethering (CCs need closed rod state) and DNA loading (might require CC ring state). Latter opens an intriguing window into a potential regulation of catalytic and structural functions of MRN through apex interactions and dynamics.

In summary, we provide the framework for the molecular architecture of MRN. We reveal an unexpected, closed conformation of MRN CCs that enables topology-sensitive binding of DNA ends as well as DNA end tethering.

Limitations of the study

We do not yet understand the precise mechanisms how eukaryotic MRN interacts with intact DNA and DSBs using both DNA-binding elements and head module clustering. Furthermore, the precise biological contexts where apex-apex interactions play critical functions, and which DNA elements are bridged, need to be addressed using a broader spectrum of cell-based functional assays.

STAR★METHODS

Detailed methods are provided in the online version of this paper and include the following:

Figure 6. Zinc-hook-mediated MRN-MRN tethering

(A) Comparison of *Ct*Rad50 and *Hs*Rad50 zinc-hook tetramers. Crystal structure of *Ct*Rad50 zinc-hook tetramer and crystal lattice of *Hs*Rad50 zinc-hook (PDB: 5GOX) tetramer indicates conserved zinc-hook tethering mechanism. Inset illustrates the apex tethering element and its interactions.

(B) DNA comet assay shows the relative amount of DNA double-strand breaks (DSBs) after 2 h following the treatment (or control without the treatment) of U2OS cells with tert-butyl hydroperoxide. Cells treated with siRAD50 show high levels of DNA damage. Transfection with wild-type human MRN decreases DNA damage to control levels, while transfection with MR^{apex}N does not (n = 3, **p < 0.01, ns = not significant, by t test; mean ± SD).

(C) Mutation of apex tethering element in human MRN impairs DNA repair *in cellulo*. DR-GFP assay shows the relative number of cells expressing DR-GFP after 48 h following the I-SceI cut in U2OS cells (n = 5, ****p < 0.0001 **p < 0.01, ns = not significant, by t test; mean ± SD).

(D) Representative micrograph containing *Ct*MR condensates. Arrows indicate the main features: the globular head domains oligomerize via head-to-head interactions and are linked to another stripe of oligomerized head complexes via apex-apex interactions. The contrast is enhanced for better visualization. Scale bars, 100 nm.

(E) Model of DNA scanning, end detection, and DNA tethering by MRN. MRN complex scans DNA via the C terminus of Mre11. Upon DNA end detection, MRN loads onto DNA in an ATP-dependent mechanism and binds DNA via the canonical Rad50-binding site. Further oligomerization may occur via Rad50^{NBD}s and zinc-hook leading to DNA end tethering.

(F) Model of MRN-MRN tethered dimers, spanning 120 nm.

See also Figure S6.

Please cite this article in press as: Rotheneder et al., Cryo-EM structure of the Mre11-Rad50-Nbs1 complex reveals the molecular mechanism of scaffolding functions, Molecular Cell (2022), https://doi.org/10.1016/j.molcel.2022.12.003

CellPress

SUPPLEMENTAL INFORMATION

Supplemental information can be found online at https://doi.org/10.1016/j.molcel.2022.12.003.

ACKNOWLEDGMENTS

EM data were collected at the Cryo-EM Core Facility of the Gene Center, Department of Biochemistry, LMU, Munich. We are grateful for the support by Gregor Witte for help in the collection of X-ray diffraction data. We gratefully thank Stephan Woike for providing his experience in rendering of structural movies. Funding was provided by the Deutsche Forschungsgemeinschaft (CRC1361, Gottfried Wilhelm Leibniz-Prize, HO2489/11-1and GRK1721 to K.-P.H., CRC1054 to K.L.) and a PhD fellowship from Boehringer Ingelheim Fonds (BIF) to E.v.d.L.

AUTHOR CONTRIBUTIONS

M.R., K.S., E.v.d.L., A.A., B.K., and Y.F. were involved in protein production, crystallization, and *in vitro* assays. M.R., K.S., E.v.d.L., K.L., J.D.B., A.A., and K.-P.H. carried out structural studies. C.J. performed fluorescence anisotropy measurements and segmentation of protein-DNA aggregates. W.P.R. contributed the *in cellulo* Comet and DR-GFP assays to quantify the DNA repair efficiency. B.S. processed crosslinked complexes and performed mass spectrometry analysis. K.-P.H. designed overall research and provided funding. All authors were involved in the interpretation of data, final manuscript preparation, and approval.

DECLARATION OF INTERESTS

The authors declare no competing interests.

Received: May 3, 2022
Revised: October 14, 2022
Accepted: December 3, 2022
Published: December 27, 2022

REFERENCES

1. Carbone, M., Arron, S.T., Beutler, B., Bononi, A., Cavenee, W., Cleaver, J.E., Croce, C.M., D'Andrea, A., Foulkes, W.D., Gaudino, G., et al. (2020). Tumour predisposition and cancer syndromes as models to study gene-environment interactions. Nat. Rev. Cancer *20*, 533–549. https://doi.org/10.1038/s41568-020-0265-y.
2. Tubbs, A., and Nussenzweig, A. (2017). Endogenous DNA damage as a source of genomic instability in cancer. Cell *168*, 644–656. https://doi.org/10.1016/j.cell.2017.01.002.
3. Johnson, D., Crawford, M., Cooper, T., Claeys Bouuaert, C., Keeney, S., Llorente, B., Garcia, V., and Neale, M.J. (2021). Concerted cutting by Spo11 illuminates meiotic DNA break mechanics. Nature *594*, 572–576. https://doi.org/10.1038/s41586-021-03389-3.
4. Zhang, Y., Zhang, X., Dai, H.Q., Hu, H., and Alt, F.W. (2022). The role of chromatin loop extrusion in antibody diversification. Nat. Rev. Immunol. *22*, 550–566. https://doi.org/10.1038/s41577-022-00679-3.
5. Chaplin, A.K., Hardwick, S.W., Liang, S., Kefala Stavridi, A., Hnizda, A., Cooper, L.R., De Oliveira, T.M., Chirgadze, D.Y., and Blundell, T.L. (2021). Dimers of DNA-PK create a stage for DNA double-strand break repair. Nat. Struct. Mol. Biol. *28*, 13–19. https://doi.org/10.1038/s41594-020-00517-x.
6. Zhao, B., Rothenberg, E., Ramsden, D.A., and Lieber, M.R. (2020). The molecular basis and disease relevance of non-homologous DNA end joining. Nat. Rev. Mol. Cell Biol. *21*, 765–781. https://doi.org/10.1038/s41580-020-00297-8.
7. Wright, W.D., Shah, S.S., and Heyer, W.D. (2018). Homologous recombination and the repair of DNA double-strand breaks. J. Biol. Chem. *293*, 10524–10535. https://doi.org/10.1074/jbc.TM118.000372.
8. Haber, J.E. (2018). DNA repair: the search for homology. Bioessays *40*. e1700229. https://doi.org/10.1002/bies.201700229.
9. Chen, C.C., Feng, W., Lim, P.X., Kass, E.M., and Jasin, M. (2018). Homology-directed repair and the role of BRCA1, BRCA2, and related proteins in genome integrity and cancer. Annu. Rev. Cancer Biol. *2*, 313–336. https://doi.org/10.1146/annurev-cancerbio-030617-050502.
10. Scully, R., Panday, A., Elango, R., and Willis, N.A. (2019). DNA double-strand break repair-pathway choice in somatic mammalian cells. Nat. Rev. Mol. Cell Biol. *20*, 698–714. https://doi.org/10.1038/s41580-019-0152-0.
11. Morimoto, S., Tsuda, M., Bunch, H., Sasanuma, H., Austin, C., and Takeda, S. (2019). Type II DNA topoisomerases cause spontaneous double-strand breaks in genomic DNA. Genes (Basel) *10*. https://doi.org/10.3390/genes10110868.
12. Syed, A., and Tainer, J.A. (2018). The MRE11-RAD50-NBS1 complex conducts the orchestration of damage signaling and outcomes to stress in DNA replication and repair. Annu. Rev. Biochem. *87*, 263–294. https://doi.org/10.1146/annurev-biochem-062917-012415.
13. Paull, T.T. (2018). 20 years of Mre11 biology: no end in sight. Mol. Cell *71*, 419–427. https://doi.org/10.1016/j.molcel.2018.06.033.
14. Cejka, P. (2015). DNA end resection: nucleases team up with the right partners to initiate homologous recombination. J. Biol. Chem. *290*, 22931–22938. https://doi.org/10.1074/jbc.R115.675942.
15. Garcia, V., Phelps, S.E.L., Gray, S., and Neale, M.J. (2011). Bidirectional resection of DNA double-strand breaks by Mre11 and Exo1. Nature *479*, 241–244.

16. Deshpande, R.A., Lee, J.H., Arora, S., and Paull, T.T. (2016). Nbs1 converts the human Mre11/Rad50 nuclease complex into an Endo/exonuclease machine specific for protein-DNA adducts. Mol. Cell *64*, 593–606. https://doi.org/10.1016/j.molcel.2016.10.010.

17. Connelly, J.C., de Leau, E.S., and Leach, D.R. (2003). Nucleolytic processing of a protein-bound DNA end by the E. coli SbcCD (MR) complex. DNA Repair (Amst) *2*, 795–807.

18. Myler, L.R., Gallardo, I.F., Soniat, M.M., Deshpande, R.A., Gonzalez, X.B., Kim, Y., Paull, T.T., and Finkelstein, I.J. (2017). Single-molecule imaging reveals how Mre11-Rad50-Nbs1 initiates DNA break repair. Mol. Cell *67*, 891–898.e4. https://doi.org/10.1016/j.molcel.2017.08.002.

19. Hopfner, K.P., Karcher, A., Craig, L., Woo, T.T., Carney, J.P., and Tainer, J.A. (2001). Structural biochemistry and interaction architecture of the DNA double-strand break repair Mre11 nuclease and Rad50-ATPase. Cell *105*, 473–485.

20. de Jager, M., van Noort, J., van Gent, D.C., Dekker, C., Kanaar, R., and Wyman, C. (2001). Human Rad50/Mre11 is a flexible complex that can tether DNA ends. Mol. Cell *8*, 1129–1135. https://doi.org/10.1016/s1097-2765(01)00381-1.

21. Lammens, K., Bemeleit, D.J., Möckel, C., Clausing, E., Schele, A., Hartung, S., Schiller, C.B., Lucas, M., Angermüller, C., Söding, J., et al. (2011). The Mre11:Rad50 structure shows an ATP-dependent molecular clamp in DNA double-strand break repair. Cell *145*, 54–66. https://doi.org/10.1016/j.cell.2011.02.038.

22. Lim, H.S., Kim, J.S., Park, Y.B., Gwon, G.H., and Cho, Y. (2011). Crystal structure of the Mre11-Rad50-ATPgammaS complex: understanding the interplay between Mre11 and Rad50. Genes Dev. *25*, 1091–1104. https://doi.org/10.1101/gad.2037811.

23. Hopfner, K.P., Craig, L., Moncalian, G., Zinkel, R.A., Usui, T., Owen, B.A., Karcher, A., Henderson, B., Bodmer, J.L., McMurray, C.T., et al. (2002). The Rad50 zinc-hook is a structure joining Mre11 complexes in DNA recombination and repair. Nature *418*, 562–566. https://doi.org/10.1038/nature00922.

24. Park, Y.B., Hohl, M., Padjasek, M., Jeong, E., Jin, K.S., Krężel, A., Petrini, J.H., and Cho, Y. (2017). Eukaryotic Rad50 functions as a rod-shaped dimer. Nat. Struct. Mol. Biol. *24*, 248–257. https://doi.org/10.1038/nsmb.3369.

25. Hohl, M., Kochańczyk, T., Tous, C., Aguilera, A., Krężel, A., and Petrini, J.H. (2015). Interdependence of the rad50 hook and globular domain functions. Mol. Cell *57*, 479–491. https://doi.org/10.1016/j.molcel.2014.12.018.

26. Käshammer, L., Saathoff, J.H., Lammens, K., Gut, F., Bartho, J., Alt, A., Kessler, B., and Hopfner, K.P. (2019). Mechanism of DNA end sensing and processing by the Mre11-Rad50 complex. Mol. Cell *76*, 382–394.e6. https://doi.org/10.1016/j.molcel.2019.07.035.

27. Carney, J.P., Maser, R.S., Olivares, H., Davis, E.M., Le Beau, M., Yates, J.R., 3rd, Hays, L., Morgan, W.F., and Petrini, J.H. (1998). The hMre11/hRad50 protein complex and Nijmegen breakage syndrome: linkage of double-strand break repair to the cellular DNA damage response. Cell *93*, 477–486. https://doi.org/10.1016/s0092-8674(00)81175-7.

28. Bian, L., Meng, Y., Zhang, M., and Li, D. (2019). MRE11-RAD50-NBS1 complex alterations and DNA damage response: implications for cancer treatment. Mol. Cancer *18*, 169. https://doi.org/10.1186/s12943-019-1100-5.

29. Buis, J., Wu, Y., Deng, Y., Leddon, J., Westfield, G., Eckersdorff, M., Sekiguchi, J.M., Chang, S., and Ferguson, D.O. (2008). Mre11 nuclease activity has essential roles in DNA repair and genomic stability distinct from ATM activation. Cell *135*, 85–96. https://doi.org/10.1016/j.cell.2008.08.015.

30. Luo, G., Yao, M.S., Bender, C.F., Mills, M., Bladl, A.R., Bradley, A., and Petrini, J.H. (1999). Disruption of *mRad50* causes embryonic stem cell lethality, abnormal embryonic development, and sensitivity to ionizing radiation. Proc. Natl. Acad. Sci. USA *96*, 7376–7381.

31. Zhu, J., Petersen, S., Tessarollo, L., and Nussenzweig, A. (2001). Targeted disruption of the Nijmegen breakage syndrome gene NBS1 leads to early embryonic lethality in mice. Curr. Biol. *11*, 105–109.

32. Marie, L., and Symington, L.S. (2022). Mechanism for inverted-repeat recombination induced by a replication fork barrier. Nat. Commun. *13*, 32. https://doi.org/10.1038/s41467-021-27443-w.

33. Cejka, P., and Symington, L.S. (2021). DNA end resection: mechanism and control. Annu. Rev. Genet. *55*, 285–307. https://doi.org/10.1146/annurev-genet-071719-020312.

34. Andres, S.N., Li, Z.M., Erie, D.A., and Williams, R.S. (2019). Ctp1 protein-DNA filaments promote DNA bridging and DNA double-strand break repair. J. Biol. Chem. *294*, 3312–3320. https://doi.org/10.1074/jbc.RA118.006759.

35. Cannavo, E., and Cejka, P. (2014). Sae2 promotes dsDNA endonuclease activity within Mre11-Rad50-Xrs2 to resect DNA breaks. Nature *514*, 122–125. https://doi.org/10.1038/nature13771.

36. Reginato, G., Cannavo, E., and Cejka, P. (2017). Physiological protein blocks direct the Mre11-Rad50-Xrs2 and Sae2 nuclease complex to initiate DNA end resection. Genes Dev. *31*, 2325–2330. https://doi.org/10.1101/gad.308254.117.

37. Wang, W., Daley, J.M., Kwon, Y., Krasner, D.S., and Sung, P. (2017). Plasticity of the Mre11-Rad50-Xrs2-Sae2 nuclease ensemble in the processing of DNA-bound obstacles. Genes Dev. *31*, 2331–2336. https://doi.org/10.1101/gad.307900.117.

38. Sartori, A.A., Lukas, C., Coates, J., Mistrik, M., Fu, S., Bartek, J., Baer, R., Lukas, J., and Jackson, S.P. (2007). Human CtIP promotes DNA end resection. Nature *450*, 509–514. https://doi.org/10.1038/nature06337.

39. Mimitou, E.P., and Symington, L.S. (2008). Sae2, Exo1 and Sgs1 collaborate in DNA double-strand break processing. Nature *455*, 770–774. https://doi.org/10.1038/nature07312.

40. Roisné-Hamelin, F., Pobiega, S., Jézéquel, K., Miron, S., Dépagne, J., Veaute, X., Busso, D., Du, M.L., Callebaut, I., Charbonnier, J.B., et al. (2021). Mechanism of MRX inhibition by Rif2 at telomeres. Nat. Commun. *12*, 2763. https://doi.org/10.1038/s41467-021-23035-w.

41. McGee, J.S., Phillips, J.A., Chan, A., Sabourin, M., Paeschke, K., and Zakian, V.A. (2010). Reduced Rif2 and lack of Mec1 target short telomeres for elongation rather than double-strand break repair. Nat. Struct. Mol. Biol. *17*, 1438–1445. https://doi.org/10.1038/nsmb.1947.

42. Martina, M., Clerici, M., Baldo, V., Bonetti, D., Lucchini, G., and Longhese, M.P. (2012). A balance between Tel1 and Rif2 activities regulates nucleolytic processing and elongation at telomeres. Mol. Cell. Biol. *32*, 1604–1617. https://doi.org/10.1128/MCB.06547-11.

43. Khayat, F., Cannavo, E., Alshmery, M., Foster, W.R., Chahwan, C., Maddalena, M., Smith, C., Oliver, A.W., Watson, A.T., Carr, A.M., et al. (2021). Inhibition of MRN activity by a telomere protein motif. Nat. Commun. *12*, 3856. https://doi.org/10.1038/s41467-021-24047-2.

44. Cassani, C., Vertemara, J., Bassani, M., Marsella, A., Tisi, R., Zampella, G., and Longhese, M.P. (2019). The ATP-bound conformation of the Mre11-Rad50 complex is essential for Tel1/ATM activation. Nucleic Acids Res. *47*, 3550–3567. https://doi.org/10.1093/nar/gkz038.

45. You, Z., Chahwan, C., Bailis, J., Hunter, T., and Russell, P. (2005). ATM activation and its recruitment to damaged DNA require binding to the C terminus of Nbs1. Mol. Cell. Biol. *25*, 5363–5379. https://doi.org/10.1128/MCB.25.13.5363-5379.2005.

46. Lee, J.H., and Paull, T.T. (2005). ATM activation by DNA double-strand breaks through the Mre11-Rad50-Nbs1 complex. Science *308*, 551–554. https://doi.org/10.1126/science.1108297.

47. Lee, J.H., and Paull, T.T. (2021). Cellular functions of the protein kinase ATM and their relevance to human disease. Nat. Rev. Mol. Cell Biol. *22*, 796–814. https://doi.org/10.1038/s41580-021-00394-2.

48. Mojumdar, A., Sorenson, K., Hohl, M., Toulouze, M., Lees-Miller, S.P., Dubrana, K., Petrini, J.H.J., and Cobb, J.A. (2019). Nej1 interacts with Mre11 to regulate tethering and Dna2 binding at DNA double-strand

breaks. Cell Rep. *28*, 1564–1573.e3. https://doi.org/10.1016/j.celrep.2019.07.018.

49. Seeber, A., Hegnauer, A.M., Hustedt, N., Deshpande, I., Poli, J., Eglinger, J., Pasero, P., Gut, H., Shinohara, M., Hopfner, K.P., et al. (2016). RPA mediates recruitment of MRX to forks and double-strand breaks to hold sister chromatids together. Mol. Cell *64*, 951–966. https://doi.org/10.1016/j.molcel.2016.10.032.
50. Cassani, C., Gobbini, E., Vertemara, J., Wang, W., Marsella, A., Sung, P., Tisi, R., Zampella, G., and Longhese, M.P. (2018). Structurally distinct Mre11 domains mediate MRX functions in resection, end-tethering and DNA damage resistance. Nucleic Acids Res. *46*, 2990–3008. https://doi.org/10.1093/nar/gky086.
51. Salifou, K., Burnard, C., Basavarajaiah, P., Grasso, G., Helsmoortel, M., Mac, V., Depierre, D., Franckhauser, C., Beyne, E., Contreras, X., et al. (2021). Chromatin-associated MRN complex protects highly transcribing genes from genomic instability. Sci. Adv. *7*. eabb2947. https://doi.org/10.1126/sciadv.abb2947.
52. Forey, R., Barthe, A., Tittel-Elmer, M., Wery, M., Barrault, M.B., Ducrot, C., Seeber, A., Krietenstein, N., Szachnowski, U., Skrzypczak, M., et al. (2021). A role for the Mre11-Rad50-Xrs2 complex in gene expression and chromosome organization. Mol. Cell *81*, 183–197.e6. https://doi.org/10.1016/j.molcel.2020.11.010.
53. Delamarre, A., Barthe, A., de la Roche Saint-André, C., Luciano, P., Forey, R., Padioleau, I., Skrzypczak, M., Ginalski, K., Géli, V., Pasero, P., and Lengronne, A. (2020). MRX increases chromatin accessibility at stalled replication forks to promote nascent DNA resection and cohesin loading. Mol. Cell *77*, 395–410.e3. https://doi.org/10.1016/j.molcel.2019.10.029.
54. Zabolotnaya, E., Mela, I., Williamson, M.J., Bray, S.M., Yau, S.K., Papatziamou, D., Edwardson, J.M., Robinson, N.P., and Henderson, R.M. (2020). Modes of action of the archaeal Mre11/Rad50 DNA-repair complex revealed by fast-scan atomic force microscopy. Proc. Natl. Acad. Sci. USA *117*, 14936–14947.
55. Frame, F.M., Rogoff, H.A., Pickering, M.T., Cress, W.D., and Kowalik, T.F. (2006). E2F1 induces MRN foci formation and a cell cycle checkpoint response in human fibroblasts. Oncogene *25*, 3258–3266. https://doi.org/10.1038/sj.onc.1209352.
56. Kissling, V.M., Reginato, G., Bianco, E., Kasaciunaite, K., Tilma, J., Cereghetti, G., Schindler, N., Lee, S.S., Guérois, R., Luke, B., et al. (2022). Mre11-Rad50 oligomerization promotes DNA double-strand break repair. Nat. Commun. *13*, 2374. https://doi.org/10.1038/s41467-022-29841-0.
57. Cannavo, E., Reginato, G., and Cejka, P. (2019). Stepwise 5′ DNA end-specific resection of DNA breaks by the Mre11-Rad50-Xrs2 and Sae2 nuclease ensemble. Proc. Natl. Acad. Sci. USA *116*, 5505–5513. https://doi.org/10.1073/pnas.1820157116.
58. Deshpande, R.A., Lee, J.H., and Paull, T.T. (2017). Rad50 ATPase activity is regulated by DNA ends and requires coordination of both active sites. Nucleic Acids Res. *45*, 5255–5268. https://doi.org/10.1093/nar/gkx173.
59. Saathoff, J.H., Käshammer, L., Lammens, K., Byrne, R.T., and Hopfner, K.P. (2018). The bacterial Mre11-Rad50 homolog SbcCD cleaves opposing strands of DNA by two chemically distinct nuclease reactions. Nucleic Acids Res. *46*, 11303–11314. https://doi.org/10.1093/nar/gky878.
60. Bürmann, F., Lee, B.G., Than, T., Sinn, L., O'Reilly, F.J., Yatskevich, S., Rappsilber, J., Hu, B., Nasmyth, K., and Löwe, J. (2019). A folded conformation of MukBEF and cohesin. Nat. Struct. Mol. Biol. *26*, 227–236. https://doi.org/10.1038/s41594-019-0196-z.
61. Schiller, C.B., Lammens, K., Guerini, I., Coordes, B., Feldmann, H., Schlauderer, F., Möckel, C., Schele, A., Strässer, K., Jackson, S.P., et al. (2012). Structure of Mre11-Nbs1 complex yields insights into Ataxia-telangiectasia-like disease mutations and DNA damage signaling. Nat. Struct. Mol. Biol. *19*, 693–700. https://doi.org/10.1038/nsmb.2323.
62. Kim, J.H., Grosbart, M., Anand, R., Wyman, C., Cejka, P., and Petrini, J.H.J. (2017). The Mre11-Nbs1 interface is essential for viability and tumor suppression. Cell Rep. *18*, 496–507. https://doi.org/10.1016/j.celrep.2016.12.035.
63. Park, Y.B., Chae, J., Kim, Y.C., and Cho, Y. (2011). Crystal structure of human Mre11: understanding tumorigenic mutations. Structure *19*, 1591–1602. https://doi.org/10.1016/j.str.2011.09.010.
64. Seifert, F.U., Lammens, K., Stoehr, G., Kessler, B., and Hopfner, K.P. (2016). Structural mechanism of ATP-dependent DNA binding and DNA end bridging by eukaryotic Rad50. EMBO J. *35*, 759–772. https://doi.org/10.15252/embj.201592934.
65. Paull, T.T., and Gellert, M. (1999). Nbs1 potentiates ATP-driven DNA unwinding and endonuclease cleavage by the Mre11/Rad50 complex. Genes Dev. *13*, 1276–1288.
66. Hopfner, K.P., Karcher, A., Shin, D.S., Craig, L., Arthur, L.M., Carney, J.P., and Tainer, J.A. (2000). Structural biology of Rad50 ATPase: ATP-driven conformational control in DNA double-strand break repair and the ABC-ATPase superfamily. Cell *101*, 789–800.
67. Rojowska, A., Lammens, K., Seifert, F.U., Direnberger, C., Feldmann, H., and Hopfner, K.P. (2014). Structure of the Rad50 DNA double-strand break repair protein in complex with DNA. EMBO J. *33*, 2847–2859. https://doi.org/10.15252/embj.201488889.
68. Usui, T., Ohta, T., Oshiumi, H., Tomizawa, J., Ogawa, H., and Ogawa, T. (1998). Complex formation and functional versatility of Mre11 of budding yeast in recombination. Cell *95*, 705–716.
69. Na, J., Newman, J.A., Then, C.K., Syed, J., Vendrell, I., Torrecilla, I., Ellermann, S., Ramadan, K., Fischer, R., and Kiltie, A.E. (2021). SPRTN protease-cleaved MRE11 decreases DNA repair and radiosensitises cancer cells. Cell Death Dis. *12*, 165. https://doi.org/10.1038/s41419-021-03437-w.
70. Jumper, J., Evans, R., Pritzel, A., Green, T., Figurnov, M., Ronneberger, O., Tunyasuvunakool, K., Bates, R., Žídek, A., Potapenko, A., et al. (2021). Highly accurate protein structure prediction with AlphaFold. Nature *596*, 583–589. https://doi.org/10.1038/s41586-021-03819-2.
71. Soh, Y.M., Basquin, J., and Gruber, S. (2021). A rod conformation of the Pyrococcus furiosus Rad50 coiled coil. Proteins *89*, 251–255. https://doi.org/10.1002/prot.26005.
72. Lee, J., and Dunphy, W.G. (2013). The Mre11-Rad50-Nbs1 (MRN) complex has a specific role in the activation of Chk1 in response to stalled replication forks. Mol. Biol. Cell *24*, 1343–1353. https://doi.org/10.1091/mbc.E13-01-0025.
73. Lamarche, B.J., Orazio, N.I., and Weitzman, M.D. (2010). The MRN complex in double-strand break repair and telomere maintenance. FEBS Lett. *584*, 3682–3695. https://doi.org/10.1016/j.febslet.2010.07.029.
74. Oh, J., Al-Zain, A., Cannavo, E., Cejka, P., and Symington, L.S. (2016). Xrs2 dependent and independent functions of the Mre11-Rad50 complex. Mol. Cell *64*, 405–415. https://doi.org/10.1016/j.molcel.2016.09.011.
75. Tatebe, H., Lim, C.T., Konno, H., Shiozaki, K., Shinohara, A., Uchihashi, T., and Furukohri, A. (2020). Rad50 zinc hook functions as a constitutive dimerization module interchangeable with SMC hinge. Nat. Commun. *11*, 370. https://doi.org/10.1038/s41467-019-14025-0.
76. Moreno-Herrero, F., de Jager, M., Dekker, N.H., Kanaar, R., Wyman, C., and Dekker, C. (2005). Mesoscale conformational changes in the DNA-repair complex Rad50/Mre11/Nbs1 upon binding DNA. Nature *437*, 440–443. https://doi.org/10.1038/nature03927.
77. Lee, J.H., Mand, M.R., Deshpande, R.A., Kinoshita, E., Yang, S.H., Wyman, C., and Paull, T.T. (2013). Ataxia telangiectasia-mutated (ATM) kinase activity is regulated by ATP-driven conformational changes in the Mre11/Rad50/Nbs1 (MRN) complex. J. Biol. Chem. *288*, 12840–12851. https://doi.org/10.1074/jbc.M113.460378.
78. Canny, M.D., and Latham, M.P. (2022). LRET-derived HADDOCK structural models describe the conformational heterogeneity required for DNA cleavage by the Mre11-Rad50 DNA damage repair complex. eLife *11*, e69579. https://doi.org/10.7554/eLife.69579.

79. Liu, Y., Sung, S., Kim, Y., Li, F., Gwon, G., Jo, A., Kim, A.K., Kim, T., Song, O.K., Lee, S.E., and Cho, Y. (2016). ATP-dependent DNA binding, unwinding, and resection by the Mre11/Rad50 complex. EMBO J. *35*, 743–758. https://doi.org/10.15252/embj.201592462.

80. Williams, R.S., Moncalian, G., Williams, J.S., Yamada, Y., Limbo, O., Shin, D.S., Groocock, L.M., Cahill, D., Hitomi, C., Guenther, G., et al. (2008). Mre11 dimers coordinate DNA end bridging and nuclease processing in double-strand-break repair. Cell *135*, 97–109. https://doi.org/10.1016/j.cell.2008.08.017.

81. Furuse, M., Nagase, Y., Tsubouchi, H., Murakami-Murofushi, K., Shibata, T., and Ohta, K. (1998). Distinct roles of two separable in vitro activities of yeast Mre11 in mitotic and meiotic recombination. EMBO J. *17*, 6412–6425. https://doi.org/10.1093/emboj/17.21.6412.

82. Borde, V., Lin, W., Novikov, E., Petrini, J.H., Lichten, M., and Nicolas, A. (2004). Association of Mre11p with double-strand break sites during yeast meiosis. Mol. Cell *13*, 389–401.

83. He, J., Shi, L.Z., Truong, L.N., Lu, C.S., Razavian, N., Li, Y., Negrete, A., Shiloach, J., Berns, M.W., and Wu, X. (2012). Rad50 zinc hook is important for the Mre11 complex to bind chromosomal DNA double-stranded breaks and initiate various DNA damage responses. J. Biol. Chem. *287*, 31747–31756. https://doi.org/10.1074/jbc.M112.384750.

84. Banani, S.F., Lee, H.O., Hyman, A.A., and Rosen, M.K. (2017). Biomolecular condensates: organizers of cellular biochemistry. Nat. Rev. Mol. Cell Biol. *18*, 285–298. https://doi.org/10.1038/nrm.2017.7.

85. Gatei, M., Jakob, B., Chen, P., Kijas, A.W., Becherel, O.J., Gueven, N., Birrell, G., Lee, J.H., Paull, T.T., Lerenthal, Y., et al. (2011). ATM protein-dependent phosphorylation of Rad50 protein regulates DNA repair and cell cycle control. J. Biol. Chem. *286*, 31542–31556. https://doi.org/10.1074/jbc.M111.258152.

86. Gatei, M., Kijas, A.W., Biard, D., Dörk, T., and Lavin, M.F. (2014). RAD50 phosphorylation promotes ATR downstream signaling and DNA restart following replication stress. Hum. Mol. Genet. *23*, 4232–4248. https://doi.org/10.1093/hmg/ddu141.

87. Zheng, S.Q., Palovcak, E., Armache, J.P., Verba, K.A., Cheng, Y., and Agard, D.A. (2017). MotionCor2: anisotropic correction of beam-induced motion for improved cryo-electron microscopy. Nat. Methods *14*, 331–332. https://doi.org/10.1038/nmeth.4193.

88. Rohou, A., and Grigorieff, N. (2015). CTFFIND4: fast and accurate defocus estimation from electron micrographs. J. Struct. Biol. *192*, 216–221. https://doi.org/10.1016/j.jsb.2015.08.008.

89. Zivanov, J., Nakane, T., Forsberg, B.O., Kimanius, D., Hagen, W.J., Lindahl, E., and Scheres, S.H. (2018). New tools for automated high-resolution cryo-EM structure determination in RELION-3. eLife *7*, e42166. https://doi.org/10.7554/eLife.42166.

90. Liebschner, D., Afonine, P.V., Baker, M.L., Bunkóczi, G., Chen, V.B., Croll, T.I., Hintze, B., Hung, L.W., Jain, S., McCoy, A.J., et al. (2019). Macromolecular structure determination using X-rays, neutrons and electrons: recent developments in Phenix. Acta Crystallogr. D Struct. Biol. *75*, 861–877. https://doi.org/10.1107/S2059798319011471.

91. Pettersen, E.F., Goddard, T.D., Huang, C.C., Couch, G.S., Greenblatt, D.M., Meng, E.C., and Ferrin, T.E. (2004). UCSF Chimera–a visualization system for exploratory research and analysis. J. Comput. Chem. *25*, 1605–1612. https://doi.org/10.1002/jcc.20084.

92. Goddard, T.D., Huang, C.C., Meng, E.C., Pettersen, E.F., Couch, G.S., Morris, J.H., and Ferrin, T.E. (2018). UCSF ChimeraX: meeting modern challenges in visualization and analysis. Protein Sci. *27*, 14–25. https://doi.org/10.1002/pro.3235.

93. Emsley, P., Lohkamp, B., Scott, W.G., and Cowtan, K. (2010). Features and development of coot. Acta Crystallogr. D Biol. Crystallogr. *66*, 486–501. https://doi.org/10.1107/S0907444910007493.

94. Klykov, O., Steigenberger, B., Pektaş, S., Fasci, D., Heck, A.J.R., and Scheltema, R.A. (2018). Efficient and robust proteome-wide approaches for cross-linking mass spectrometry. Nat. Protoc. *13*, 2964–2990. https://doi.org/10.1038/s41596-018-0074-x.

95. Punjani, A., Rubinstein, J.L., Fleet, D.J., and Brubaker, M.A. (2017). cryoSPARC: algorithms for rapid unsupervised cryo-EM structure determination. Nat. Methods *14*, 290–296. https://doi.org/10.1038/nmeth.4169.

96. Bepler, T., Kelley, K., Noble, A.J., and Berger, B. (2020). Topaz-denoise: general deep denoising models for cryoEM and cryoET. Nat. Commun. *11*, 5208. https://doi.org/10.1038/s41467-020-18952-1.

97. Burnley, T., Palmer, C.M., and Winn, M. (2017). Recent developments in the CCP-EM software suite. Acta Crystallogr. D Struct. Biol. *73*, 469–477. https://doi.org/10.1107/S2059798317007859.

98. Ramlaul, K., Palmer, C.M., and Aylett, C.H.S. (2019). A local agreement filtering algorithm for transmission EM reconstructions. J. Struct. Biol. *205*, 30–40. https://doi.org/10.1016/j.jsb.2018.11.011.

99. Asarnow, D., Palovcak, E., and Cheng, Y. (2019). UCSF pyem v0.5. Zenodo. https://doi.org/10.5281/zenodo.3576630.

100. Croll, T.I. (2018 Jun 1). ISOLDE: a physically realistic environment for model building into low-resolution electron-density maps. Acta Crystallogr D Struct Biol *74* (Pt 6), 519–530. Epub 2018 Apr 11. PMID: 29872003; PMCID: PMC6096486. https://doi.org/10.1107/S2059798318002425.

101. Berger, I., Fitzgerald, D.J., and Richmond, T.J. (2004). Baculovirus expression system for heterologous multiprotein complexes. Nat. Biotechnol. *22*, 1583–1587. https://doi.org/10.1038/nbt1036.

102. Stakyte, K., Rotheneder, M., Lammens, K., Bartho, J.D., Grädler, U., Fuchß, T., Pehl, U., Alt, A., van de Logt, E., and Hopfner, K.P. (2021). Molecular basis of human ATM kinase inhibition. Nat. Struct. Mol. Biol. *28*, 789–798. https://doi.org/10.1038/s41594-021-00654-x.

103. Scheltema, R.A., Hauschild, J.P., Lange, O., Hornburg, D., Denisov, E., Damoc, E., Kuehn, A., Makarov, A., and Mann, M. (2014). The Q Exactive HF, a benchtop mass spectrometer with a pre-filter, high-performance quadrupole and an ultra-high-field Orbitrap analyzer. Mol. Cell. Proteomics *13*, 3698–3708. https://doi.org/10.1074/mcp.M114.043489.

104. Grimm, M., Zimniak, T., Kahraman, A., and Herzog, F. (2015). xVis: a web server for the schematic visualization and interpretation of crosslink-derived spatial restraints. Nucleic Acids Res. *43*, W362–W369. https://doi.org/10.1093/nar/gkv463.

105. Kosinski, J., von Appen, A., Ori, A., Karius, K., Müller, C.W., and Beck, M. (2015). Xlink Analyzer: software for analysis and visualization of cross-linking data in the context of three-dimensional structures. J. Struct. Biol. *189*, 177–183. https://doi.org/10.1016/j.jsb.2015.01.014.

106. Seifert, F.U., Lammens, K., and Hopfner, K.P. (2015). Structure of the catalytic domain of Mre11 from Chaetomium thermophilum. Acta Crystallogr. F Struct. Biol. Commun. *71*, 752–757. https://doi.org/10.1107/S2053230X15007566.

107. Jung, C., Bandilla, P., von Reutern, M., Schnepf, M., Rieder, S., Unnerstall, U., and Gaul, U. (2018). True equilibrium measurement of transcription factor-DNA binding affinities using automated polarization microscopy. Nat. Commun. *9*, 1605. https://doi.org/10.1038/s41467-018-03977-4.

108. Jung, C., Schnepf, M., Bandilla, P., Unnerstall, U., and Gaul, U. (2019). High sensitivity measurement of transcription factor-DNA binding affinities by competitive titration using fluorescence microscopy. J. Vis. Exp. https://doi.org/10.3791/58763.

109. Kabsch, W. (2010). Xds. Acta Crystallogr. D Biol. Crystallogr. *66*, 125–132. https://doi.org/10.1107/S0907444909047337.

110. McCoy, A.J., Grosse-Kunstleve, R.W., Adams, P.D., Winn, M.D., Storoni, L.C., and Read, R.J. (2007). Phaser crystallographic software. J. Appl. Crystallogr. *40*, 658–674. https://doi.org/10.1107/S0021889807021206.

111. Bradford, M.M. (1976). A rapid and sensitive method for the quantitation of microgram quantities of protein utilizing the principle of protein-dye

Please cite this article in press as: Rotheneder et al., Cryo-EM structure of the Mre11-Rad50-Nbs1 complex reveals the molecular mechanism of scaffolding functions, Molecular Cell (2022), https://doi.org/10.1016/j.molcel.2022.12.003

binding. Anal. Biochem. *72*, 248–254. https://doi.org/10.1006/abio.1976.9999.

112. Nikolova, T., Marini, F., and Kaina, B. (2017). Genotoxicity testing: comparison of the gammaH2AX focus assay with the alkaline and neutral comet assays. Mutat. Res. Genet. Toxicol. Environ. Mutagen. *822*, 10–18. https://doi.org/10.1016/j.mrgentox.2017.07.004.

113. Lu, Y., Liu, Y., and Yang, C. (2017). Evaluating in vitro DNA damage using comet assay. J. Vis. Exp. https://doi.org/10.3791/56450.

114. Pierce, A.J., Johnson, R.D., Thompson, L.H., and Jasin, M. (1999). XRCC3 promotes homology-directed repair of DNA damage in mammalian cells. Genes Dev. *13*, 2633–2638. https://doi.org/10.1101/gad.13.20.2633.

115. Krumm, A., and Roos, W.P. (2017). Assessing the effect of Class I histone deacetylase activity on DNA double-strand break repair by homologous recombination. Methods Mol. Biol. *1510*, 115–123. https://doi.org/10.1007/978-1-4939-6527-4_9.

116. Richardson, C., Moynahan, M.E., and Jasin, M. (1998). Double-strand break repair by interchromosomal recombination: suppression of chromosomal translocations. Genes Dev. *12*, 3831–3842. https://doi.org/10.1101/gad.12.24.3831.

Please cite this article in press as: Rotheneder et al., Cryo-EM structure of the Mre11-Rad50-Nbs1 complex reveals the molecular mechanism of scaffolding functions, Molecular Cell (2022), https://doi.org/10.1016/j.molcel.2022.12.003

STAR★METHODS

KEY RESOURCES TABLE

REAGENT or RESOURCE	SOURCE	IDENTIFIER
Antibodies		
anti-Rad50	Cell Signalling	Cat# #3427; RRID: AB_2176936
anti-Nbs1	Abcam	Cat# ab175800; RRID: AB_2927495
anti-Vinculin	Santa Cruz	Cat# sc-73614
anti-beta-Actin	Santa Cruz	Cat# sc-47778
anti-rabbit	Li-COR Bioscience	Cat# 926–32213
Chemicals, peptides, and recombinant proteins		
ATP	Sigma (Merck)	A3377
ATPγS	Sigma (Merck)	A1388
2-Mercaptoethanol	Carl-Roth	4227
Imidazole	Carl Roth	3899
β-Octylglycoside	Sigma (Merck)	O8001
BSA	New England BioLabs	B9000S
BS3	Thermo-Fisher Scientific	21580
DTT	Carl Roth	6908
Cellulose phosphate fine mesh resin	Merck	C2258
2-chloroacetamide	Merck	C0267
1-ethyl-3-carbodiimide hydrochloride	Thermo-Fisher Scientific	22980
EDTA	VWR International	6381-92-6
FLAG M2 affinity resin	Sigma (Merck)	A2220
3x FLAG peptide	Neo Biotech	NB-45-00069
HRV3C protease	Cytiva	27084301
LysC	Promega	VA1170
Lipofectamine RNAiMAX	Invitrogen	13778100
Trypsin	Promega	VA9000
$MgCl_2$	Merck	7791-18-6
$MnCl_2$	Sigma (Merck)	M3634
NADH	Carl Roth	AE12.1
PEP	Panreac AppliChem	A2271
PK/LDH	Merck	P0294
Polyethylenimine Hydrochloride	Polysciences	#24765
Puromycin	Carl Roth	0240.3
PvuII-HF	New England BioLabs	R3151S
TCEP	Sigma (Merck)	646547
SIGMAFAST Protease Inhibitor Cocktail Tablet, EDTA free	Merck	S8830
Small Volume LoBase SensoPlate	Greiner	788892
TURBO DNase	Thermo-Fisher Scientific	AM2238
TURBO broth medium	Molecular Dimensions	MD12-104-1
Trifluoroacetic acid	Merck	91707
Urea	Carl Roth	3941

(*Continued on next page*)

Please cite this article in press as: Rotheneder et al., Cryo-EM structure of the Mre11-Rad50-Nbs1 complex reveals the molecular mechanism of scaffolding functions, Molecular Cell (2022), https://doi.org/10.1016/j.molcel.2022.12.003

Continued

REAGENT or RESOURCE	SOURCE	IDENTIFIER
Deposited data		
Map: CtMRN head with coils, RBD and bridge	This paper	EMDB: EMD-14876
Map: CtMRN focus map of Nbs1-Mre11 interaction	This paper	EMDB: EMD-14877
Map: CtMRN long coiled coils map	This paper	EMDB: EMD-14878
Map: CtMRN coiled coils focus map	This paper	EMDB: EMD-14879
Map: CtMRN catalytic head focus map	This paper	EMDB: EMD-14880
Map: CtMRN composite map	This paper	EMDB: EMD-14881
Map: CtRad50 Zn hook map	This paper	EMDB: EMD-14882
Map: HsMN	This paper	EMDB: EMD-15948
CtMRN model of composite map	This paper	PDB: 7ZR1
CtRad50 Zn Hook crystal structure	This paper	PDB: 7ZQY
HsMN model	This paper	PDB: 8BAH
Biochemical raw data	This paper	Mendeley Data: https://doi.org/10.17632/v93tby2spy.1
Experimental models: Cell lines		
Homo sapiens U2OS	Comet and DR-GFP assay	RRID:CVCL_0042
Homo sapiens HEK293T	Expression System	ATCC: CRL-3216
Experimental models: Organisms/strains		
E. coli XL1 Blue	Cloning System	N/A
E. coli BL21 Rosetta	Expression System	N/A
Spodoptera frugiperda sf21 cells	Expression System	N/A
Trichoplusia ni cells	Expression System	N/A
Oligonucleotides		
Oligonucleotides	Metabion	See Table S1
Primers	Metabion	See Table S1
Recombinant DNA		
pACEBac1-plDK-*ct*MRN	This paper	N/A
pACEBac1-*ct*MR	This paper	N/A
pUC19	New England BioLabs	N3041S
pET47b-*ct*Rad50_598-782	This paper	N/A
pDRGFP	Addgene	26475
pCBAScel	Addgene	26477
pACEMam1-pMDC-*hs*MRN	This paper	N/A
pACEMam1-pMDC-*hs*MR^{apex}N	This paper	N/A
pACEMam1-pMDC-*hs*M(H129N)RN	This paper	N/A
pACEMam1-*hs*Nbs1	This paper	N/A
pACEMam1-*hs*Nbs1^{central}	This paper	N/A
pACEMam1-*hs*Nbs1^{flank}	This paper	N/A
pACEMam1-*hs*Nbs1$^{central+flank}$	This paper	N/A
Software and algorithms		
MotionCor2	Zheng et al.[87]	https://msg.ucsf.edu/em/software/motioncor2.html
CTFFIND4.1	Rohou and Grigorieff[88]	http://grigoriefflab.janelia.org/ctffind4
Relion 3.0.8	Scheres et al.[89]	https://www3.mrc-lmb.cam.ac.uk/relion/index.php?title=Main_Page
Phenix	Liebschner et al.[90]	https://www.phenix-online.org/

(*Continued on next page*)

Please cite this article in press as: Rotheneder et al., Cryo-EM structure of the Mre11-Rad50-Nbs1 complex reveals the molecular mechanism of scaffolding functions, Molecular Cell (2022), https://doi.org/10.1016/j.molcel.2022.12.003

Continued

REAGENT or RESOURCE	SOURCE	IDENTIFIER
UCSF Chimera	Pettersen et al.[91]	https://www.cgl.ucsf.edu/chimera/
ChimeraX	Goddard et al.[92]	https://www.rbvi.ucsf.edu/chimerax/
COOT	Emsley et al.[93]	https://www2.mrc-lmb.cam.ac.uk/Personal/pemsley/coot/
Prism	GraphPad	N/A
Proteome Discoverer (version 2.4.0.305)	Thermo Fisher	https://www.thermofisher.com/order/catalog/product/OPTON-31040?SID=srch-srp-OPTON-31040
XlinkX node for Proteome Discoverer, incl. PD node	Klykov et al.[94]; Thermo Fisher	https://www.thermofisher.com/order/catalog/product/OPTON-31047?SID=srch-srp-OPTON-31047 https://www.hecklab.com/software/xlinkx/
Comet IV	Perceptive Instruments Ltd	N/A
Labview 9.0	National Instruments	https://www.ni.com/de-de/support/downloads/software-products/download.labview.html#
Custom-written script for FA analysis	This paper	https://zenodo.org/record/7353848#Y38qNnaZNnI
OriginPro	OriginLab	N/A
CryoSPARC v3.2.0	Punjani et al.[95]	https://cryosparc.com/
Topaz	Bepler et al.[96]	https://emgweb.nysbc.org/topaz.html
AlphaFold v2.1.0	Jumper et al.[70]	https://colab.research.google.com/github/deepmind/alphafold/blob/main/notebooks/AlphaFold.ipynb
CCP-EM	Burnley et al.[97]	https://www.ccpem.ac.uk/
LAFTER v1.1	Ramlaul et al.[98]	https://github.com/StructuralBiology-ICLMedicine/lafter
pyEM v0.5	Asarnow et al., 2019[99]	https://doi.org/10.5281/zenodo.3576630
ISOLDE	Croll, 2018[100]	https://isolde.cimr.cam.ac.uk/static/isolde/doc/isolde.html

RESOURCE AVAILABILITY

Lead contact

Further information and requests for resources and reagents should be directed to and will be fulfilled by the lead contact, Karl-Peter Hopfner (hopfner@genzentrum.lmu.de).

Materials availability

Plasmids generated in this study are available on request through the lead contact (hopfner@genzentrum.lmu.de).

Data and code availability

- The coordinate files generated during this study are available at the Protein Data Bank (https://www.rcsb.org/) with the accession codes PDB: 7ZR1 (*Ct*MRN head & coiled coils), PDB: 7ZQY (*Ct*Rad50 zinc-hook tetramer) and PDB: 8BAH (*Hs*M(H129N)N). The cryo-EM reconstructions generated during this study are available at the Electron Microscopy Data Bank (https://www.ebi.ac.uk/pdbe/emdb/) with the accession codes EMDB: EMD-14881 (Composite map of *Ct*MRN head & coiled coils), EMDB: EMD-14880 (*Ct*MRN catalytic head), EMDB: EMD-14876 (*Ct*MRN RBD & bridge), EMDB: EMD-14877 (*Ct*MRN catalytic head & Nbs1), EMDB: EMD-14878 (*Ct*MRN long coiled coils), EMDB: EMD-14879 (*Ct*MRN distant coiled coils), EMDB: EMD-14882 (*Ct*Rad50 zinc-hook tetramer), EMDB: EMD-15948 (*Hs*M(H129N)N). Raw gel images, blots, representative Micrographs, fluorescence anisotropy images and XL-MS results are made available (https://doi.org/10.17632/v93tby2spy.1).
- Custom-written script for fluorescence anisotropy analysis is made available (https://zenodo.org/record/7353848#Y38qNnaZNnI).
- Any additional information required to reanalyse the data reported in this paper is available from the lead contact upon request.

Please cite this article in press as: Rotheneder et al., Cryo-EM structure of the Mre11-Rad50-Nbs1 complex reveals the molecular mechanism of scaffolding functions, Molecular Cell (2022), https://doi.org/10.1016/j.molcel.2022.12.003

CellPress

EXPERIMENTAL MODEL AND SUBJECT DETAILS

Organisms as source for materials used in experiments

E. coli XL1 Blue cells were used for amplification of plasmid DNA.

Spodoptera frugiperda SF21 insect cells were used for virus production.

E. coli Rosetta2, *Trichoplusia ni* insect cells and *Homo sapiens* HEK293T were used for recombinant protein expression.

Homo sapiens U2OS cells were used for Comet and DR-GFP assays.

METHOD DETAILS

Expression and purification of the *Ct*MRN complex

Codon-optimised synthetic genes (Genscript, Piscataway, USA) encoding *Ct*Mre11, *Ct*Rad50, *Ct*Nbs1 were PCR amplified and cloned into pACEBac1 (*Ct*Mre11, *Ct*Mre11$^{\Delta C}$, *Ct*Rad50) and pIDK (*Ct*Nbs1) plasmids using MultiBac expression system.[101] The C-terminal truncation of *Ct*Mre11 was introduced via Around-the-horn PCR. Recombination steps were carried out in *Escherichia coli* XL1Blue cells (Stratagene) under the addition of Cre-recombinase (NEB). Baculoviruses containing *Ct*MRN, *Ct*M$^{\Delta C}$RN or *Ct*MR were generated in *Spodoptera frugiperda* (SF21) insect cells (IPLB-Sf21AE) and virus titers were determined by small-scale test expression. 1 L of *Trichoplusia ni* High Five cells (Invitrogen), seeded to 1 mio/mL, were infected with 1:1000 of respective baculovirus and cultured for 72 h at 27°C. Cells were harvested by centrifugation.

The fresh cell pellet was resuspended in 50 mL of Lysis buffer (50 mM HEPES pH 7.0, 250 mM NaCl, 10% glycerol, 0.5 mM TCEP, 5 μL TURBO DNase (Thermo Fisher Scientific), supplemented with a SIGMAFAST Protease Inhibitor Cocktail Tablet, EDTA free (Merck) on ice. All further purification steps were performed on ice or in an 8°C cold room. The cells were lysed using a Dounce homogenizer followed by sonication for 1 min (50% duty cycle, 5 output control). The lysate was cleared by centrifugation at 17000 rpm for at least 1 h using an SS-34 rotor. The soluble supernatant was prefiltered with a Millex fiber-glass filter (Roth) and filtered using 0.45 μm PVDF membrane filters (Merck Millipore).

The lysate was applied onto a 5 mL HiTrap Heparin HP column (GE Healthcare) attached to an AKTA Pure system (GE Healthcare) and equilibrated in Buffer A (50 mM HEPES pH 7.0, 250 mM NaCl, 10% glycerol, 0.5 mM TCEP). The column was washed with 5 CV Buffer A, 5 CV of 7% Buffer B (50 mM HEPES pH 7.0, 1 M NaCl, 10% glycerol, 0.5 mM TCEP). Protein was eluted with 33% Buffer B, pooled, and dialyzed for 8 h in SEC buffer (20 mM HEPES 7.0, 200 mM NaCl, 10% Glycerol, 0.5 mM TCEP). 1 g (dry mass) cellulose phosphate (CP) fine mesh resin (Merck) was prepared according to protocol and equilibrated in SEC buffer. The dialyzed protein was applied to CP resin, which was washed until no DNA eluted anymore. Protein was eluted by the addition of CP elution buffer (20 mM HEPES 7.0, 400 mM NaCl, 10% glycerol, 0.5 mM TCEP) to a total of 10 CV. The CP eluate was concentrated and applied to size exclusion chromatography (SEC; Superose 6, 10/300, GE Healthcare) in SEC buffer (No glycerol was added for cryo-EM grid preparation). Stoichiometric *Ct*MRN complex eluted at 0.4 CV.

Expression and purification of the *Hs*MRN complex

Codon-optimised synthetic genes (Genscript, Piscataway, USA) encoding *Hs*Mre11, *Hs*Rad50, *Hs*Nbs1 were PCR amplified and cloned into pACEMam1 (*Hs*Rad50, *Hs*Nbs1) and pMDC (*Hs*Mre11) plasmids using the MultiMam expression system.[101] The C-terminus of Mre11 continues with an HRV 3C cleavage site and a Twin-FLAG tag (DYKDDDDK). The nuclease dead mutant *Hs*Mre11 H129N was introduced via QuickChange PCR, the Rad50^{apex} mutant via Gibson assembly. Recombination steps were carried out in *Escherichia coli* XL1Blue cells (Stratagene) under the addition of Cre-recombinase (NEB). For MRN wild-type and MRN mutant expression, the plasmids pACEMam1_pMDC_*Hs*MRN, pACEMam1_pMDC_*Hs*MR^{apex}N and pACEMam1_pMDC_*Hs*M(H129N)RN were transfected into 1 L HEK293T cells, following the protocol as described.[102] Cells were cultured for 72 h at 37 °C and then harvested by centrifugation.

Cell lysis was performed as described for *Ct*MRN with a lysis buffer consisting of 50 mM HEPES pH 8.0, 250 mM NaCl, 10% glycerol, 0.1 mM DTT, 0.5 mM $MnCl_2$, 5 μL TURBO DNase (Thermo Fisher Scientific), supplemented with a SIGMAFAST Protease Inhibitor Cocktail Tablet, EDTA free (Merck).

The lysate was applied onto 3 mL FLAG M2 affinity resin (Sigma), equilibrated in Buffer A (50 mM HEPES pH 8.0, 250 mM NaCl, 10% glycerol, 0.1 mM DTT, 0.5 mM $MnCl_2$) and incubated for 2 h rolling. The column was washed with 10 CV Buffer A, 20 CV Buffer HS (50 mM HEPES pH 8.0, 1 M NaCl, 10% glycerol, 0.1 mM DTT, 0.5 mM $MnCl_2$) and re-equilibrated in Buffer A afterwards. Protein was eluted with 200 μg/mL 3x FLAG-peptide (NeoBiotech) in Buffer A to a total volume of 5 CV. The eluate was concentrated and applied to size exclusion chromatography (Superose 6, 10/300, GE Healthcare) in SEC buffer (20 mM HEPES pH 8.0, 150 mM NaCl, 0.5 mM TCEP, 1 mM MnCl2). Stoichiometric *Hs*MRN complex eluted at 0.5 CV.

Thermal shift assay

Freshly purified *Hs*MRN at 0.5 μM was subjected to a Tycho NT.6 system (NanoTemper) to measure changes in the intrinsic fluorescence (at 330 nm and 350 nm) with respect to increasing temperature. The measurements were performed in standard capillaries (NanoTemper).

Please cite this article in press as: Rotheneder et al., Cryo-EM structure of the Mre11-Rad50-Nbs1 complex reveals the molecular mechanism of scaffolding functions, Molecular Cell (2022), https://doi.org/10.1016/j.molcel.2022.12.003

Crosslinking mass spectrometry

Freshly purified *Ct*MRN complex was diluted in compensation buffer to obtain a protein concentration of 0.25 mg/mL in 20 mM HEPES (pH 7.0), 200 mM NaCl, 5 mM $MgCl_2$, 1 mM $MnCl_2$, 0.2 mM TCEP, 1 mM ATPγS. The complex was incubated for 15 min at 21°C, then a 6.2 mM solution of bis sulfosuccinimidyl suberate (BS3), dissolved in 20 mM HEPES (pH 8.5) buffer, was added to obtain a final concentration of 31.1 μM BS3. The protein was crosslinked for 30 min @ 35°C before it was quenched by the addition of 1 M Tris-HCl (pH 8.0) to a final concentration of 62 mM.

To the crosslinked proteins, 4 M Urea and 50 mM Tris (pH 8.0) were added. The mixture was sonicated using a Bioruptor Plus sonication system (Diogenode) for 10x 30 s at high intensity. Thereafter, 40 mM 2-chloroacetamide (CAA, Sigma-Aldrich) and 10 mM tris(2-carboxyethyl) phosphine (TCEP; Thermo Fisher Scientific) were added for the reduction and alkylation of disulfide bonds. After incubation for 20 min at 37°C, the samples were diluted 1:2 with MS grade water (VWR). Crosslinked proteins were digested overnight at 37°C by addition of 0.5 μg of LysC and 1 μg of trypsin (Promega). Afterward, the mixture was acidified with 10% trifluoroacetic acid (TFA; Merck) in water to a final concentration of 1%, followed by desalting of the peptides using Sep-Pak C18 1cc vacuum cartridges (Waters). Desalted peptides were vacuum-dried.

Vacuum-dried peptides were dissolved in buffer A (0.1% formic acid). For nano-LC separation of the peptides at a flow rate of 250 nL/min, the Thermo Easy-nLC 1000 (Thermo Fisher Scientific) equipped with a 30-cm analytical column (inner diameter: 75 microns; packed in-house with ReproSil-Pur C18-AQ 1.9-micron beads, Dr. Maisch GmbH) was used. Through the nanoelectrospray interface, eluting peptides were sprayed into the benchtop Orbitrap Q Exactive HF (Thermo Fisher Scientific).[103] As gradient, the following steps were programmed with increasing addition of buffer B (80% acetonitrile, 0.1% formic acid): linear increase from 8 to 30% over 60 minutes, followed by a linear increase to 60% over 5 minutes, a linear increase to 95% over the next 5 minutes, and finally maintenance at 95% for another 5 minutes. The mass spectrometer was operated in data-dependent mode with survey scans from m/z 300 to 1650 Th (resolution of 60k at m/z = 200 Th), and up to 15 of the most abundant precursors were selected and fragmented using stepped Higher-energy collisional Dissociation (HCD with a normalized collision energy of value of 19, 27, 35). The MS2 spectra were recorded with a dynamic m/z range (resolution of 30k at m/z = 200 Th). AGC targets for MS1 and MS2 scans were set to 3 x 10^6 and 10^5, respectively, within a maximum injection time of 100 and 60 ms for the MS1 and MS2 scans, respectively. Charge state 2 was excluded from fragmentation to enrich the fragmentation scans for cross-linked peptide precursors.

The acquired raw data were processed using Proteome Discoverer (version 2.5.0.400) with the XlinkX/PD nodes integrated.[94] To identify the crosslinked peptide pairs, a database search was performed against a FASTA containing the sequences of the proteins under investigation as well as a contaminant database. DSS was set as a crosslinkers. Cysteine carbamidomethylation was set as fixed modification and methionine oxidation and protein N-term acetylation were set as dynamic modifications. Trypsin/P was specified as protease and up to two missed cleavages were allowed. Furthermore, identifications were only accepted with a minimum score of 40 and a minimal delta score of 4. Otherwise, standard settings were applied. Filtering at a 1% false discovery rate (FDR) at peptide level was applied through the XlinkX Validator node with setting simple.

The crosslinks were analyzed and visualized using the xVis Crosslink Analyzer Webserver and the Xlink Analyser software for UCSF Chimera.[91,104,105]

Cryo-EM grid preparation

Freshly purified full length *Ct*MRN or *Ct*MR complexes were diluted in compensation buffer to obtain a protein concentration of 0.27 mg/mL in 20 mM HEPES (pH 7.6), 200 mM NaCl (125 mM NaCl to obtain condensates), 5 mM $MgCl_2$, 1 mM $MnCl_2$, 20 μM $ZnCl_2$, 0.2 mM TCEP, 2 mM ATPγS. Freshly purified full length *Hs*M(H129N)RN complex was diluted in compensation buffer to obtain a protein concentration of 0.29 mg/mL in 20 mM HEPES (pH 7.0), 140 mM NaCl, 5 mM $MgCl_2$, 1 mM $MnCl_2$, 20 μM $ZnCl_2$, 0.2 mM TCEP, 2 mM ATPγS. The complexes were incubated for at least 10 min at 21°C to bind ions and nucleotide. Just before plunging, Octyl β-D-glucopyranoside (β-OG) was added to a final concentration of 0.05%. Grids were prepared using a Leica EM GP plunge freezer (Leica). β-OG containing samples (4.5 μl) were deposited onto plasma cleaned (GloQube, Quorum) copper grid (Cu 200, R2/1, Quantifoil). The samples were applied to the grids at 15°C and 95% humidity and blotted for 2.5 s before plunge-freezing the grid in liquid ethane.

Cryo-EM data acquisition

Six datasets of *Ct*MRN-ATPγS (a total of 29349 micrographs), three datasets of *Hs*M(H129N)RN (a total of 11325 micrographs) and one dataset of *Ct*MR (14730 micrographs) were acquired on a Titan Krios transmission electron microscope (Thermo Fisher Scientific) operated at 300 kV, with a K2 summit direct electron detector (Gatan) operated in counting mode and energy filter (Gatan). Data acquisition was automated with the EPU (Thermo Fisher Scientific) software package. Images were recorded at a nominal magnification of 130,000x (1.059 Å/pix) with a defocus range of 1.0 μm to 2.8 μm, and a total dose of 45 $e^-/Å^2$ over 40 frames.

Cryo-EM image processing

Motion correction with MotionCor2 and CTF estimation with CTFFind4 were performed on the fly for all datasets using an in-house developed pipeline.[87,88] Further processing was performed using Relion v3.0[89] and CryoSPARC v3.2.0,[95] and older versions. Initially,

Please cite this article in press as: Rotheneder et al., Cryo-EM structure of the Mre11-Rad50-Nbs1 complex reveals the molecular mechanism of scaffolding functions, Molecular Cell (2022), https://doi.org/10.1016/j.molcel.2022.12.003

particles were picked in CryoSPARC using the implemented blob picker. After 2D classification, selected particles were used to train the TOPAZ deep picker.[96] TOPAZ was trained iteratively until no further increase in particle numbers and particles were extracted using box sizes of 768 pix (Ct Long CC map), 352 pix (*Ct* Catalytic head map), 352 pix (*Ct* Zinc hook tetramer), 180 pix (*Hs*MN).

For *Ct*MRN, initial models were generated using CryoSPARC *ab-initio* reconstruction. The particles for the catalytic head map were transferred to Relion, further sorted by 2D classification and subjected to focused 3D refinement by masking the catalytic head. This resulted in the C1 map of the catalytic head at 4.0 Å. Further, focused 3D classification resulted in five different classes that showed different degrees of Nbs1 binding to the catalytic head. Non-uniform (NU) refinement of the Long CC particles in CryoSPARC led to a C2 map with 4.8 Å overall resolution. Further local refinements of the C2 maps led to two maps of the CCs with 6.8 Å and 7.6 Å, respectively. Maps were LAFTER filtered[98] in the CCP-EM software suite.[97]

The full complement of picked particles were additionally processed independently in CryoSPARC. Particles were initially sorted by rounds of 2D classification and heterogeneous refinement. 3D variability was used to divide the particles by Rad50 orientation. The classes corresponding to the extremes of Rad50 motion were used for heterogeneous refinement. The most stable class further processed by non-uniform refinement producing a map of the catalytic head with extended Rad50 coiled coils and the Mre11 bridge at an overall resolution of 3.92 Å. Local refinement with a mask for Nbs1 and the Mre11 phosphodiesterase domains produced a map of Nbs1 interactions at 3.75 Å.

The Zinc hook (ZH) particles were processed in CryoSPARC. An *ab-initio* reconstruction was created from the particles picked in TOPAZ. Particles were repicked and sorted via heterogeneous refinement with 5 references from a ZH tetramer, ZH octamer, Mre11, MRN catalytic head, and a part of the CCs. The ZH particles were pooled and sorted via iterative rounds of 2D classification. From NU refinement, followed by local refinement a 4.9 Å C2 map of the ZH was calculated. To avoid over-refining, the map was eventually filtered to 7 Å.

For *Hs*M(H129N)RN, initial analysis was performed on dataset 1 (8589 micrographs). In CryoSPARC particles were picked using blob picking, followed by 2D classification, selection of the Mre11-dimer classes, *ab-initio*, and homogeneous refinement. The map was then used to generate templates for template picking on all 3 datasets. After 2D classification, Mre11-dimer classes were used for two rounds of TOPAZ training, 2D classification, and selection of Mre11-dimer classes, resulting in 282838 particles. Non-uniform refinement was performed using the *ab-initio* from dataset 1 as a template. Local refinement resulted in a final map of *Hs*M(H129N)N with a resolution of 4.1 Å.

Model building

The *Ct*MRN head and coiled coils model was prepared using a combination of crystal structure templates, AlphaFold2 predictions, and *de novo* building. Initial models were rigid body fitted in UCSF Chimera[91] using 4YKE[106] for the Mre11 phosphodiesterase and capping domains, and 5DA9[64] for the Mre11^{RBD}s and Rad50 nuclease domains and coiled coils until residues 214 and 1107. Alphafold2 predictions were used as templates for Nbs1 (606 to 689) bound to the Mre11 phosphodiesterase dimer, Rad50 DNA binding site loops (1176 to 1187) and coiled coils (215 to 1106), and Mre11 bridge (523 to 557) (Figure S3F).[70] Further model building and refinement was performed in Coot 0.9.[93] Initial models were morphed into EM density by real space refinement with local restrains, then further refined with optional restraints based on local resolution. Regions not matching the initial models, in particular the non-symmetric loops, were manually built. The model was refined against several focused maps, and LAFTER filtered maps were used for poorly resolved and partially flexible regions. The Mre11-Rad50 head module was refined against EMD-14880. Nbs1 and interacting residues of Mre11 were refined against EMD-14877. Mre11^{RBD} and bridge, and the neighboring Rad50 coiled coils and loops were refined against EMD-14876. The remaining Rad50 coiled coils were refined against EMD-14878 and EMD-14879. Real space refinement and validation were performed in Phenix 1.20.1.[90]

The *Hs*M(H129N)N structure was prepared by docking AlphaFold2 predictions using UCSF Chimera,[91] which were further refined into the density using Coot 0.9.[93] Refinement was conducted with comparison to the *Hs*Mre11 crystal structure (3T1I), from which individual chains docked to match the dimerization interface observed in the EM density.[63] Sharpened and LAFTER filtered maps were used for refinement in Coot. Real space refinement and validation were performed in Phenix.[90]

DNA stimulated ATPase assays

We used an NADH-coupled assay to monitor the rate of ATP hydrolysis by MRN. The ATPase rate was assayed in reaction buffers containing 250 nM MRN complex, 20 mM HEPES pH 7.0, 80 mM NaCl; 5 mM MgCl2, 1 mM MnCl2, 0.1 mg/mL BSA, 0.2 mM TCEP, 0.25 mM NADH, 20 U/ml PK, 30 U/ml LDH, 2 mM Phosphoenolpyruvate (PEP), the reaction was started by addition of 1 mM ATP and 52 ng/μL DNA (Table S1). The measurements were started immediately after ATP addition for 2 h at 37 °C. The oxidation rate of NADH was assayed fluorometrically by measuring the fluorescence at 460 nm (excitation 340 nm) on a Tecan microplate reader (Infinite M1000).

Direct fluorescence polarization anisotropy (nucleotide dependence)

Fluorescence polarization anisotropy was used to monitor MRN binding to 80 bp dsDNA. 5 nM of 3' 6-FAM-labeled DNA was incubated with increasing amounts of MRN in ATP (20 mM HEPES pH 7.0, 100 mM NaCl, 5 mM $MgCl_2$, 0.2 mg/ml BSA, 1 mM ATP, 0.5 mM TCEP), ATPγS (20 mM HEPES pH 7.0, 100 mM NaCl, 5 mM $MgCl_2$, 0.2 mg/ml BSA, 1 mM ATPγS, 0.5 mM TCEP) and no nucleotide (20 mM HEPES pH 7.0, 100 mM NaCl, 5 mM $MgCl_2$, 0.2 mg/ml BSA, 0.5 mM TCEP) assay

Please cite this article in press as: Rotheneder et al., Cryo-EM structure of the Mre11-Rad50-Nbs1 complex reveals the molecular mechanism of scaffolding functions, Molecular Cell (2022), https://doi.org/10.1016/j.molcel.2022.12.003

buffers. All DNA binding reactions were done without the addition of $MnCl_2$ to avoid DNA degradation. After 15 min incubation at 37 °C, the fluorescence anisotropy was measured at an excitation wavelength of 488 nm and an emission wavelength of 520 nm using an automated polarization microscope.[107,108] Each sample was measured at twelve different z-planes to reduce the effect of potential fluorescing protein-DNA aggregates that could lead to erroneous FA values, these measurements were repeated three times for each of the 3-4 replicates. The FA values were calculated for each image using the following formula, requiring the parallel ($I^{=}$) and perpendicular (I^{+}) fluorescence intensities and the instrumental G-factor (G = 1.15 for our setup, as determined by measuring free dye in solution). Regions of interest (ROI) were defined as equal-sized regions around the maxima in the respective channels.

$$FA(z,t) = \frac{I^{=}(z,t) - GI^{+}(z,t)}{I^{=}(z,t) + 2I^{+}(z,t)}$$

Finally, we calculated for each sample the median FA value of all images acquired from a given well to reduce variability, namely the contribution to FA of images containing potential protein-DNA aggregates.

Competitive fluorescence polarization anisotropy (topology dependence)

Fluorescence polarization anisotropy was used to monitor *Ct*MRN and *Ct*M$^{\Delta C}$RN binding to linear and circular DNA. 5 nM of 3' 6-FAM-labeled 80 bp dsDNA was incubated with 45 nM MRN in ATPγS containing assay buffer (20 mM HEPES pH 7.0, 100 mM NaCl, 5 mM $MgCl_2$, 0.2 mg/ml BSA, 1 mM ATP, 0.5 mM TCEP). After 10 min incubation, increasing amount of either circular or linear (obtained by digesting of circular DNA with PvuII-HF NEB) pUC19 plasmid DNA was added. After 15 min incubation at 37 °C, the fluorescence anisotropy was measured using the same setup as described above.

Fluorescence imaging and segmentation of protein-DNA aggregates

To characterize the relative amount of aggregates between samples, we acquired for each sample z-stacks of widefield fluorescence images. Image segmentation of the aggregates was performed using a custom-written Definiens XD 2.0 script (Munich, Germany). The image analysis procedure was the following. The individual aggregates appear in bright, relatively round objects within a heterogeneous background arising from the inhomogeneous widefield illumination. To facilitate the detection of the contour of the objects, we applied a 3D-Gaussian filter with a kernel size of 5 × 5 × 3 pixels, followed by a second 3D-Gaussian filter with the same kernel size. We then subtracted the latter image from the previous one. This procedure resulted in a background-subtracted image. Then, we applied a global threshold and carried out segmentation using an algorithm implemented in the Definiens XD 2.0 software platform. Briefly, the Multi-Threshold Segmentation algorithm splits the image domain and classifies the resulting image objects based on a defined pixel value threshold. This results in segmented patterns classified as "aggregates" or "background". We then extracted for each frame the total number of aggregate particles, their size (in a 2D projection within our optical resolution of about approx. 0.5 μm), and their average fluorescence intensity. The latest parameter can be assumed to be proportional to the number of protein-DNA aggregating in a single particle.

Crystallization and structure determination of the *Ct*Rad50 Zn-hook domain

Codon-optimized synthetic DNA (Genscript, Piscataway, USA) encoding *Ct*Rad50$^{598\text{-}782}$ was PCR amplified and cloned into pET47b (6xHis-HRV3C-*Ct*Rad50$^{598\text{-}782}$). The construct was expressed in *Escherichia coli* BL21 Rosetta cells (Novagen). 0.5 L of *E. coli* culture were grown in TURBO Broth™ medium (Molecular Dimensions) containing Kanamycin (50 μg/mL) and Chloramphenicol (34 μg/mL) at 37°C to an OD_{600} of 2.0 before induction with 0.4 mM IPTG. Upon induction, further cultivation was performed at 18°C, until the cells reached an OD_{600} of 7.0.

The cells were harvested via centrifugation (10 min, 3000 g, 4°C) and resuspended in 150 mL lysis buffer (50 mM HEPES 7.5, 250 mM NaCl, 10 % Glycerol, 5 mM β-Mercaptoethanol, 2 μL TURBO DNase (Thermo-Fisher Scientific), supplemented with a SIGMAFAST Protease Inhibitor Cocktail Tablet, EDTA free (Merck). The cells were lysed via sonication for 3x 3 min (50% duty cycle, 5 output control), and cleared lysate was prepared by centrifugation at 17 000 rpm for 1 h using an SS-34 rotor.

5 mL Ni-NTA beads (Macherey-Nagel) were equilibrated in Buffer A (50 mM HEPES 7.5, 250 mM NaCl, 10 % Glycerol, 5 mM β-mercaptoethanol) and incubated with cleared lysate for 1 h at 8°C on a rolling incubator. The beads were washed with 3 CV of Buffer A, 3 CV Buffer A and 20 mM Imidazole, followed by 3 CV Buffer A. 5 mL of Buffer A containing 50 μL HRV3C protease (Cytiva) were added, and the beads were incubated over night at 8°C on a rolling incubator. On the next day the eluate was applied to a fresh 5 mL of Ni-NTA, equilibrated in Buffer A and the flow-through was collected. EDTA was added to a final concentration of 1 mM and the protein was concentrated to 30 mg/ml. A Superose 200 16/60 HiLoad column (Cytiva) was equilibrated in SEC buffer (20 mM HEPES 7.5, 150 mM NaCl, 1 mM EDTA, 5% Glycerol, 0.5 mM TCEP) and 3 mL of the concentrated protein sample was injected. The eluate was fractionated and analyzed on SDS PAGE.

Crystals of *Ct*Rad50$^{598\text{-}782}$ were grown in hanging drops by mixing 1.5 μl protein at 4.5 mg/mL and 1.5 μl reservoir solution (0.1 M MES pH 6.8, 0.6 M NaCl, 18% PEG4000). The crystals were soaked in a reservoir solution supplemented with 10% 1,4-butanediol and frozen in liquid Nitrogen. X-ray data to a resolution of 2.5 Å were collected at EMBL Hamburg P14 beamline at PETRA III storage ring (DESY Hamburg) at 100K. Data were indexed, integrated and scaled with XDS/XSCALE[109] in space group P1. The structure was solved by molecular replacement with the program Phaser[110] using a Rad50 Zn-hook search model calculated by AlphaFold2. Model

Please cite this article in press as: Rotheneder et al., Cryo-EM structure of the Mre11-Rad50-Nbs1 complex reveals the molecular mechanism of scaffolding functions, Molecular Cell (2022), https://doi.org/10.1016/j.molcel.2022.12.003

building was done in Coot and refinement was performed with Phenix. Prior to model building and refinement, we randomly omitted 10% of the reflections for monitoring the free R value. Data collection and model statistics are stated in Table 2. All figures were prepared using UCSF Chimera or UCSF ChimeraX.[92]

Cells and culture conditions

The human osteosarcoma cell line U2OS (RRID:CVCL 0042) was cultivated in DMEM containing 10% fetal bovine serum (FBS) and penicillin/streptomycin at 37°C in a humidified 5% CO_2 atmosphere.

Protein extracts and Western blot analysis

Whole-cell protein extracts were prepared by disrupting cell pellets in Lysis Buffer (20 mM Tris pH 8.5, 1 mM EDTA, 1 mM β-mercaptoethanol, 5% glycerol) supplemented with various protease and phosphatase inhibitors (0.02 M β-glycerophosphate, 1 mM Na_3VO_4, 0.1 mM Phenylmethylsulfonyl fluoride, 0.01 mM MG-132, 0.01 M dithiothreitol, 0.01 M NaF and cOmplete™) using sonification. The protein concentration was determined using the Bradford method as described.[111] 30 μg of protein were separated by sodium dodecyl sulfate-polyacrylamide gel electrophoresis (SDS-PAGE) and transferred overnight at 100 mA in blotting buffer (0.025 M tris, 0.192 M glycine, 20% methanol) onto a nitrocellulose membrane. All primary antibodies were used at 1:1000 dilution in 5% BSA in Tris buffered saline (TBS) containing 0.1% Tween and 1% Na-Azide. The antibodies used were anti-Rad50 (Cell Signalling, #3427), anti-Nbs1 (Abcam, ab175800), anti-beta-Actin (Santa Cruz, SC-47778) and anti-Vinculin (Santa Cruz, sc-73614). The secondary antibodies (Li-COR Bioscience) were diluted (1:10000) in TBS containing 0.1% Tween and the proteins were visualized using the Odyssey® Infrared Imaging System (LI-COR Biotechnology).

Transfections

For RAD50 and NBS1 knockdown, U2OS cells were transfected with siRNA targeting RAD50 (s792, Silencer®Select, ThermoFisher Scientific), NBS1 (s536526, Silencer®Select, ThermoFisher Scientific) and negative control siRNA (#AM4611; Life Technologies) using Lipofectamine RNAiMAX (Invitrogen), according to the manufacturer's instructions. The siRNA-mediated knockdown of RAD50 was confirmed at the protein level using Western blot analysis.

For RAD50 and NBS1 wild-type and mutant expression, the plasmids pACEMam1_pMDC_*Hs*MRN, pACEMam1_pMDC_*Hs*MR^{apex}N, pACEMam1_*Hs*Nbs1, pACEMam1_*Hs*Nbs1^{central}, pACEMam1_*Hs*Nbs1^{flank}, pACEMam1_*Hs*Nbs1$^{central+flank}$ were transfected into U2OS cells using Polyethylenimine Hydrochloride (PEI) (#24765; Polysciences). 1 μg plasmid DNA was mixed with 3 μg PEI in 200 μl serum and antibiotic-free DMEM medium, 45 min later the DNA/PEI complex was added to the cells dropwise. The RAD50 and NBS1 expression was confirmed by Western blot analysis.

Neutral and comet assay

DSBs and their repair was monitored by single-cell gel electrophoresis under neutral conditions. RAD50 was knocked down in U2OS cells, 8 hours later the cells were transfected with the respective expression plasmids. 16 h later the knockdown and transfected cells were reseeded into three Petri dishes, designated untreated, tert-Butyl hydroperoxide (t-BuOOH) treated, and t-BuOOH treated with 2 h repair. The next day, the cells were exposed to 150 μM t-BuOOH for 1 h. The comet assays were performed, as described.[112] Shortly, cells were embedded in 0.5% low melting point agarose in PBS and spread onto glass slides coated with 1.2% agarose. All following steps were performed at 4°C unless stated otherwise. Cells were lysed in lysing solution (2.5 M NaCl, 100 mM EDTA, 10 mM Tris, 1% Na-Laurylsarcosinate, 1% Triton X-100) at a pH of 7.5. Slides were electrophoresed for 25 min in electrophoresis buffer (90 mM Tris pH 7.5, 90 mM boric acid, 2 mM EDTA) at 7.4 V/cm, fixed in 100% methanol, and then dried. All following steps were performed at room temperature. DNA was stained using propidium iodide (50 μg/ml) and 50 cells per slide were evaluated using a fluorescence microscope and the Comet IV software (Perceptive Imaging, Liverpool, UK). Data are expressed as tail intensity, which denotes the percentage of DNA in the tail multiplied by the length between the center of the head and tail.[113]

DR-GFP reporter assay

For determining the influence of RAD50 and NBS1 wild-type and mutant proteins on homology-directed repair the DR-GFP reporter assay was used.[114] U2OS cells were generated that contain a stabile genomic integrated DR-GFP reporter construct, and the assay was performed as described.[115] Shortly, the pDRGFP (Addgene plasmid 26475) plasmid was transfected into U2OS cells by mixing 1 μg plasmid DNA with 3 μg PEI in 200 μl serum and antibiotic antibiotic-free DMEM medium. 45 min later the DNA/PEI complex was added to the cells dropwise. Following selection with Puromycin (0240.3, Carl Roth GmbH) and expansion the cells were designated U2OS DR-GFP. RAD50 or NBS1 was knocked down, as described, and the influence of wild-type and mutant RAD50 or NBS1 on homologous recombination was determined by co-transfection with the appropriate plasmid (RAD50 or NBS1) along with a plasmid that expresses the rare cutting endonuclease I-SceI, namely pCBASceI (Addgene plasmid 26477),[116] as described. The GFP signal, showing homologous recombination repair activity, was quantified by flow cytometry (FacsCantoII, BD Bioscience).

Please cite this article in press as: Rotheneder et al., Cryo-EM structure of the Mre11-Rad50-Nbs1 complex reveals the molecular mechanism of scaffolding functions, Molecular Cell (2022), https://doi.org/10.1016/j.molcel.2022.12.003

QUANTIFICATION AND STATISTICAL ANALYSIS

For ATPase assay, the linear decrease in fluorescence between 200 s and 800 s was fitted to a linear regression in GraphPad Prism and the slope was used to calculate the ATPase rate using the following formula (Figures 3E and 3F). The NADH slope was calculated using a calibration curve which was recorded by titrating ADP to a constant NADH solution in a reaction buffer without MRN/DNA.

$$ATPase\ rate\left[ATP\ complex^{-1}s^{-1}\right] = \frac{slope[FU\ s^{-1}]}{NADH\ slope\left[-\ 587.9\frac{FU}{\mu M\ ATP}c_{MRN}[\mu M\ complex]\right]}$$

Direct fluorescence anisotropy data were analyzed using Prism (GraphPad) and K_D values derived by fitting the anisotropy data to a Specific binding with Hill slope model, using the following formula (Figures 3A and 3B):

$$FU = \frac{B_{max}[MRN\ in\ nM]^h}{K_D{}^h[MRN\ in\ nM]^h}$$

Competitive fluorescence anisotropy data were analyzed using Prism (GraphPad) by fitting the anisotropy data to a One phase decay model, using the following formula, K_D was calculated as ln(2)/K (Figures 3C and 3D).

$$FU = (FU_{max} - FU_{min})e^{-K\left[DNA\ in\ ng/\mu l\right]} + FU_{min}$$

Data of fluorescence imaging and segmentation of protein-DNA aggregates were plotted using Prism (GraphPad) (Figure S7B).

Neutral comet assay data are expressed as tail intensity, which denotes the percentage of DNA in the tail multiplied by the length between the center of the head and tail and plotted using GraphPad Prism (Figure 5B).

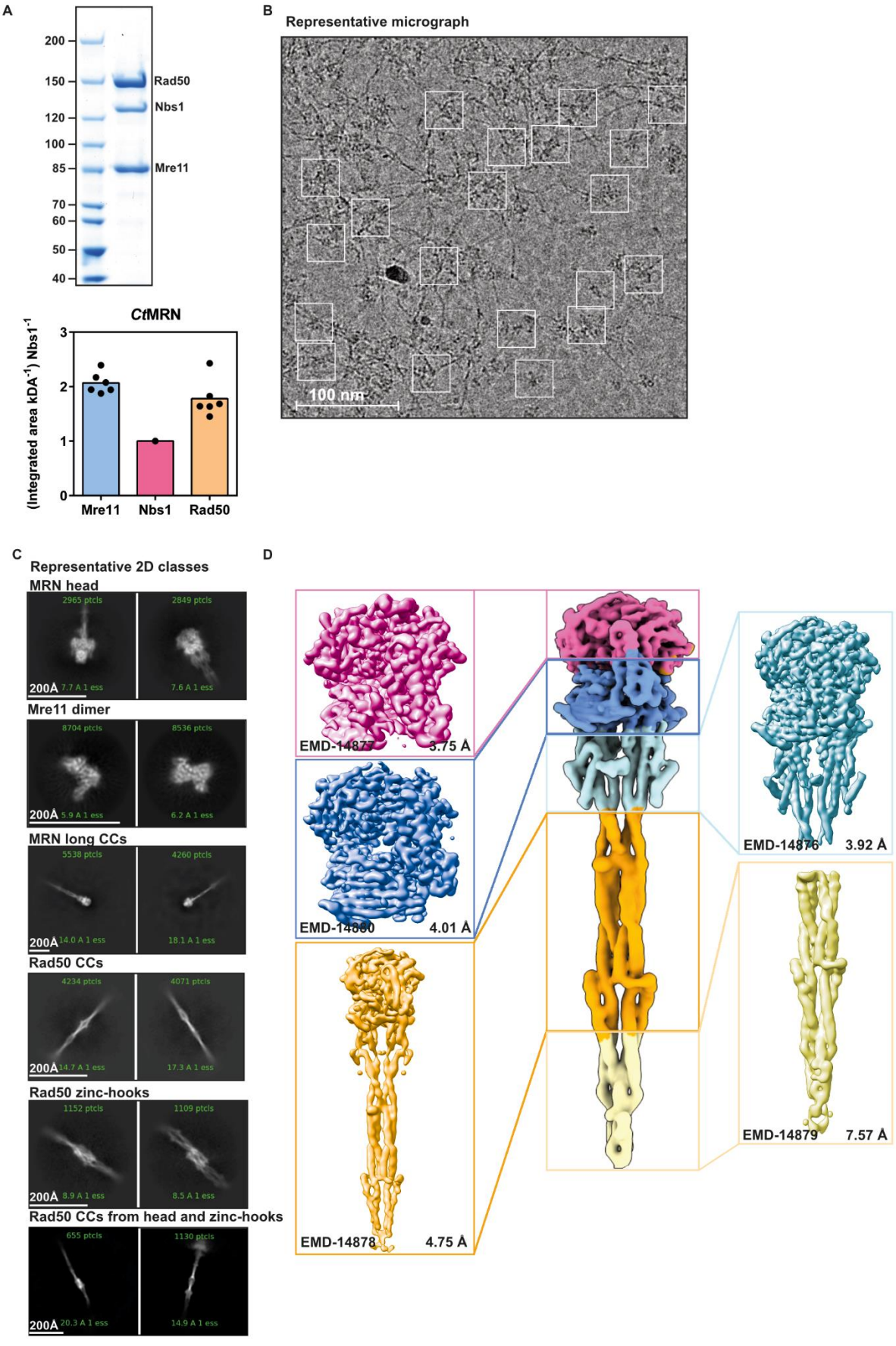
A
200
150
120
100
85
70
60
50
40
Rad50
Nbs1
Mre11
CtMRN
(Integrated area kDA-1) Nbs1-1
3
2
1
0
Mre11
Nbs1
Rad50
B
Representative micrograph
100 nm
C
Representative 2D classes
MRN head
2965 ptcls
2849 ptcls
200Å 7.7 A 1 ess
7.6 A 1 ess
Mre11 dimer
8704 ptcls
8536 ptcls
200Å 5.9 A 1 ess
6.2 A 1 ess
MRN long CCs
5538 ptcls
4260 ptcls
200Å 14.0 A 1 ess
18.1 A 1 ess
Rad50 CCs
4234 ptcls
4071 ptcls
200Å 14.7 A 1 ess
17.3 A 1 ess
Rad50 zinc-hooks
1152 ptcls
1109 ptcls
200Å 8.9 A 1 ess
8.5 A 1 ess
Rad50 CCs from head and zinc-hooks
655 ptcls
1130 ptcls
200Å 20.3 A 1 ess
14.9 A 1 ess
D
EMD-14877 3.75 Å
EMD-14880 4.01 Å
EMD-14878 4.75 Å
EMD-14876 3.92 Å
EMD-14879 7.57 Å

Figure S1: *Ct*MRN complex cryo-EM preparation. Related to Figure 1.

(A) Representative SDS-PAGE of purified *Ct*MRN complex and gel quantification (n = 6).

(B) Representative Micrograph of *Ct*MRN-ATPγS. Representative MRN particles are boxed. Scale bar 100 nm.

(C) Representative 2D classes of particles picked within the *Ct*MRN-ATPγS datasets. Scale bars 200 Å. Box sizes are 352 pix for MRN head, 220 pix for Mre11 dimer, 1000 pix for MRN long CCs, 352 pix for Rad50 CCs, 352 pix for Rad50 zinc-hooks and 600 pix for Rad50 CCs from head and zinc-hooks.

(D) Composite map colored according to the individual maps used. The highest resolved areas from the depicted LAFTER filtered maps were used to generate a composite map.

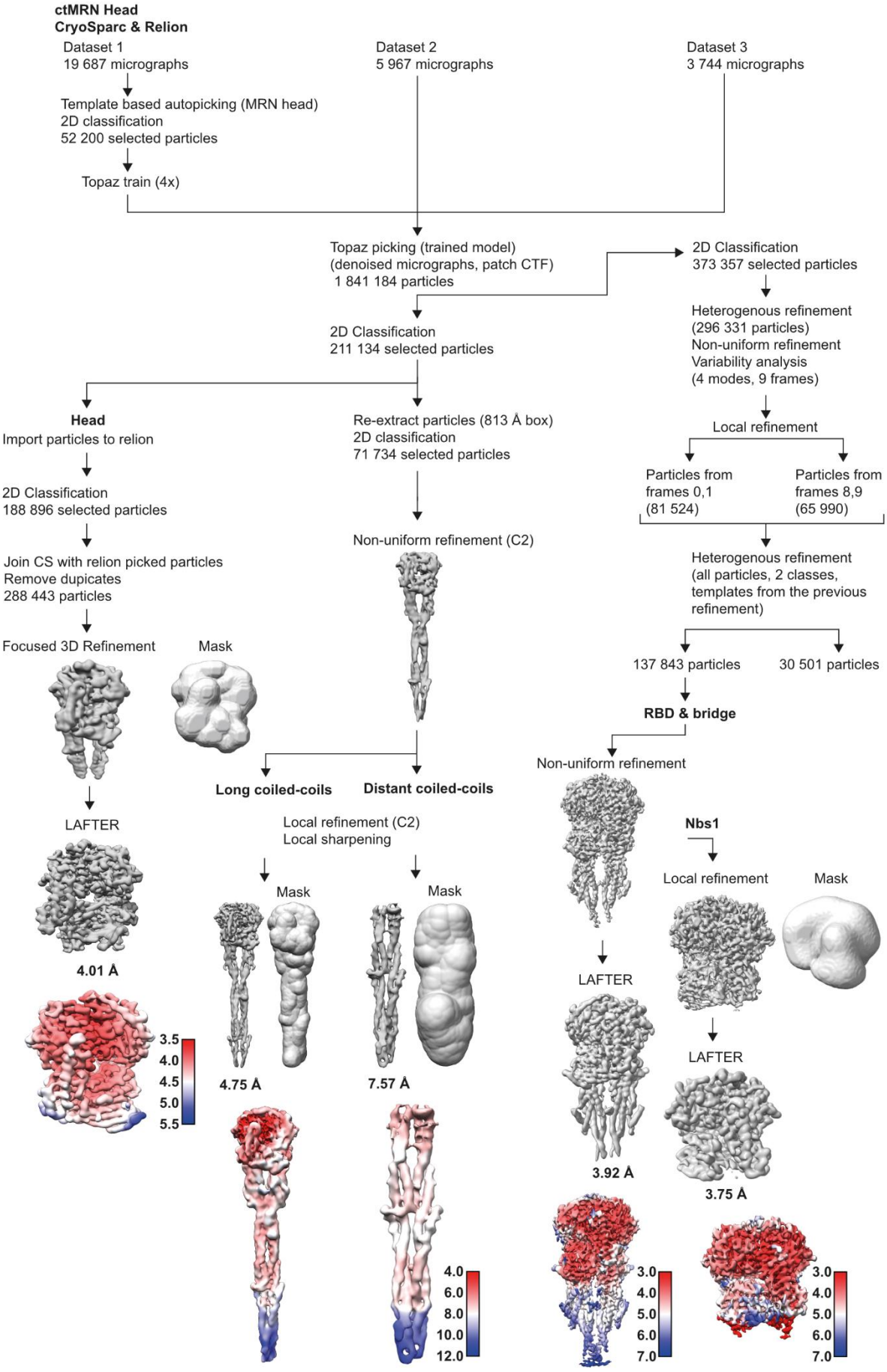
ctMRN Head
CryoSparc & Relion
Dataset 1
19 687 micrographs
Dataset 2
5 967 micrographs
Dataset 3
3 744 micrographs
Template based autopicking (MRN head)
2D classification
52 200 selected particles
Topaz train (4x)
Topaz picking (trained model)
(denoised micrographs, patch CTF)
1 841 184 particles
2D Classification
373 357 selected particles
Heterogenous refinement
(296 331 particles)
Non-uniform refinement
Variability analysis
(4 modes, 9 frames)
2D Classification
211 134 selected particles
Local refinement
Particles from
frames 0,1
(81 524)
Particles from
frames 8,9
(65 990)
Head
Import particles to relion
Re-extract particles (813 Å box)
2D classification
71 734 selected particles
2D Classification
188 896 selected particles
Non-uniform refinement (C2)
Heterogenous refinement
(all particles, 2 classes,
templates from the previous
refinement)
Join CS with relion picked particles
Remove dupicates
288 443 particles
137 843 particles
30 501 particles
Focused 3D Refinement
Mask
RBD & bridge
Non-uniform refinement
Long coiled-coils
Distant coiled-coils
LAFTER
Local refinement (C2)
Local sharpening
Nbs1
Mask
Mask
Local refinement
Mask
4.01 Å
3.5
4.0
4.5
5.0
5.5
4.75 Å
7.57 Å
LAFTER
LAFTER
3.92 Å
3.75 Å
4.0
6.0
8.0
10.0
12.0
3.0
4.0
5.0
6.0
7.0
3.0
4.0
5.0
6.0
7.0

Figure S2: Processing schemes for the *Ct*MRN catalytic head and CC maps. Related to Figure 1, 2.
Processing schemes of *Ct*MRN-ATPγS head, long coiled-coils, distant coiled-coils and RBD & bridge with local resolution estimates at the end of each processing branch.

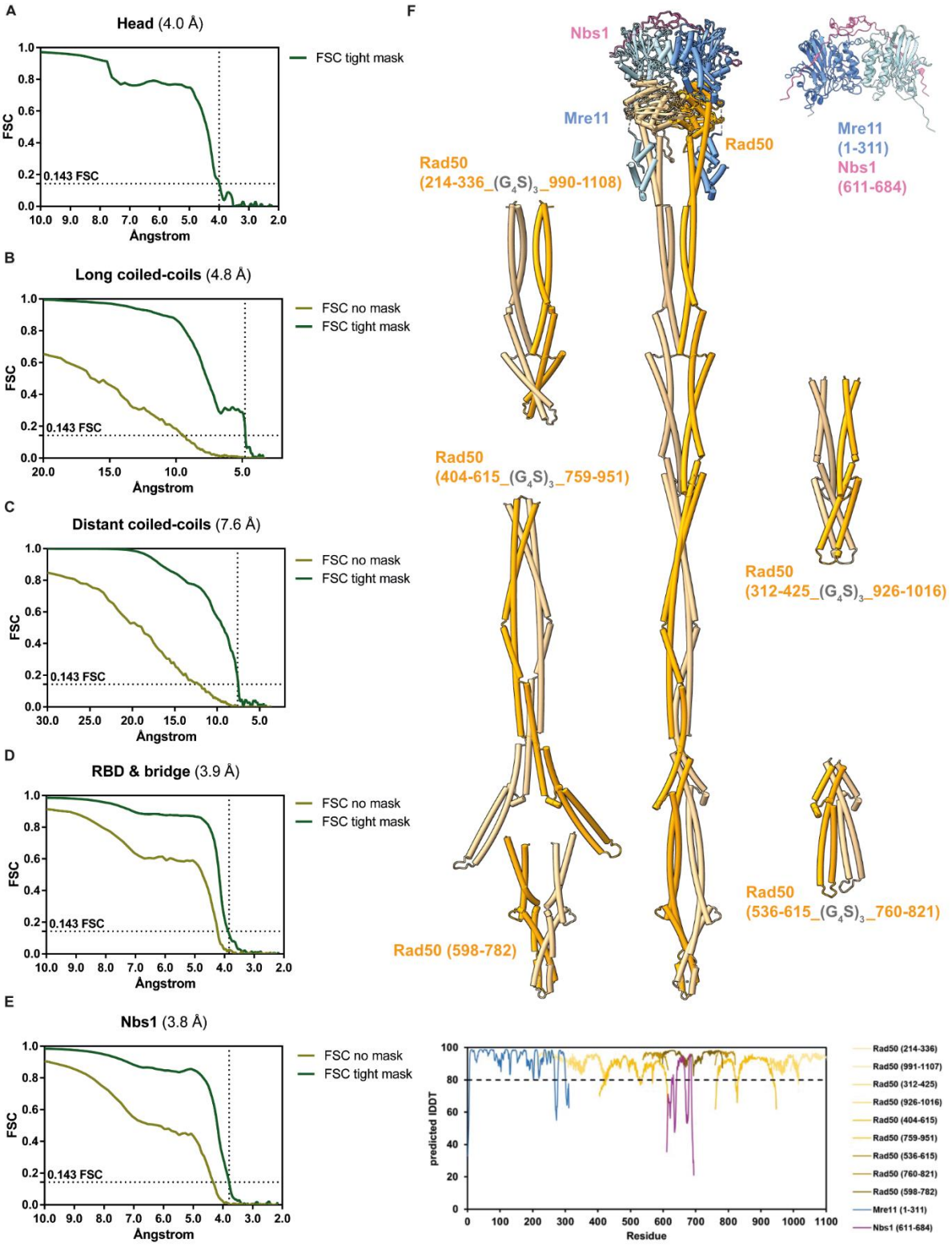

Figure S3: FSC curves and AlphaFold2 models. Related to Figure 1, 2, 6.

A) FSC curves of the Head map (Relion v3.0).

B) FSC curves of the long coiled coils map (CryoSPARC v3.2.0).

C) FSC curves of the distant coiled coils map (CryoSPARC v3.2.0).

D) FSC curves of the RBD & bridge map (CryoSPARC v3.2.0).

E) FSC curves of the Nbs1 map (CryoSPARC v3.2.0).

F) AlphaFold2 models used to build a full-length MRN model and the predicted IDDT scores (>80 indicates high confidence models).

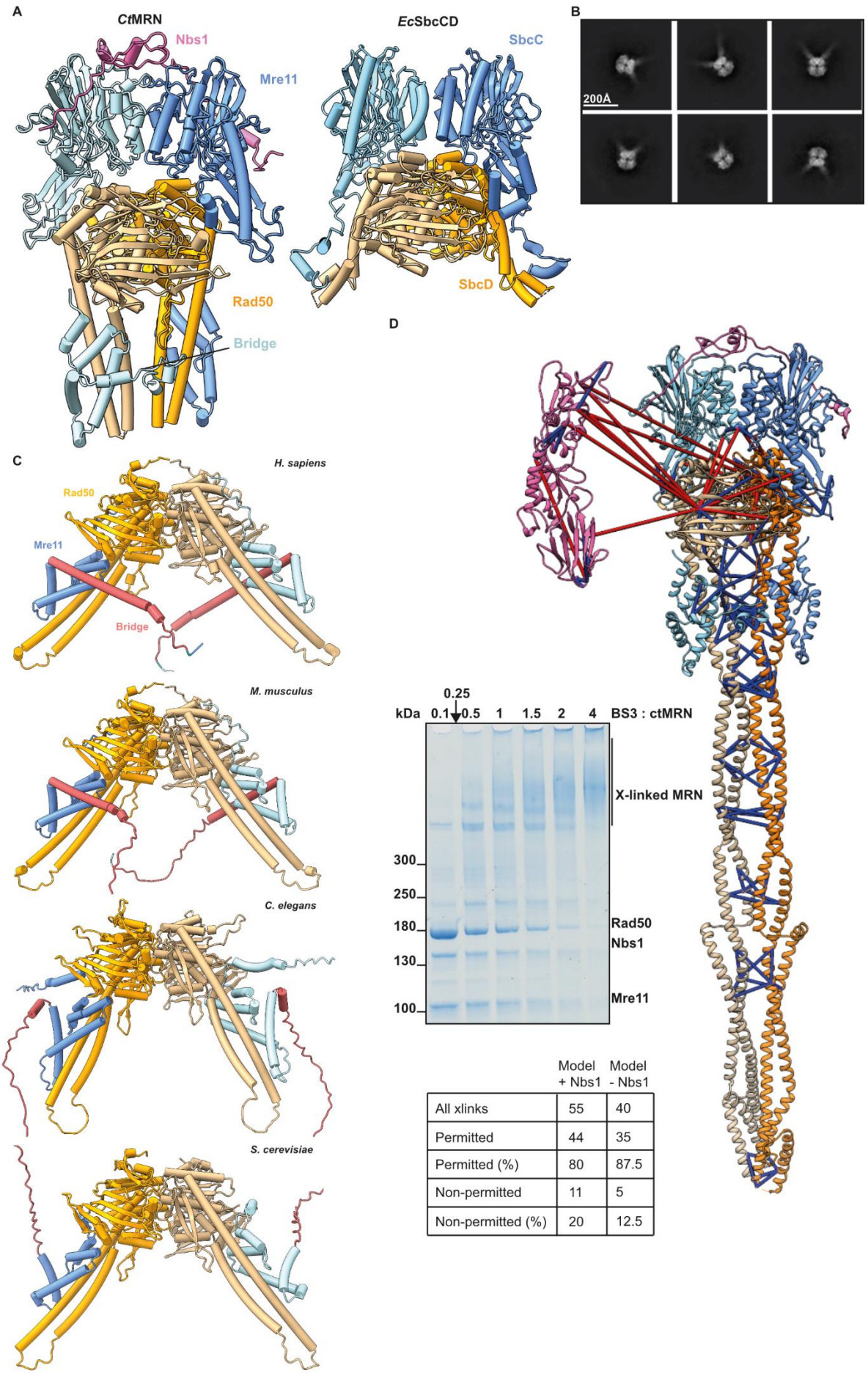

	Model + Nbs1	Model - Nbs1
All xlinks	55	40
Permitted	44	35
Permitted (%)	80	87.5
Non-permitted	11	5
Non-permitted (%)	20	12.5

Figure S4: Conformations of Rad50 CCs and crosslinking MS statistics. Related to Figure 1, 3.

A) Comparison of the cryo-EM structures of the eukaryotic *Ct*MRN complex and the prokaryotic *Ec*MR/SbcCD complex bound to ATPγS. Mre11/SbcD colored in blue, Rad50/SbcC colored orange, Nbs1 colored pink.

B) 2D classes of *Ct*MRN particles bound to ATP showing open coiled coils. Scale bar 200 Å.

C) AlphaFold2 predicted structures of *H. sapiens*, *M. musculus*, *C. elegans* and *S. cerevisiae* $Rad50^{NBD}$ and interacting Mre11 portion with bridge element.

D) Gel of CX-MS sample preparation, our *Ct*MRN model and AlphaFold2 predicted *Ct*Nbs1 N-terminus with crosslinks mapped, and summary table of mapped crosslinks.

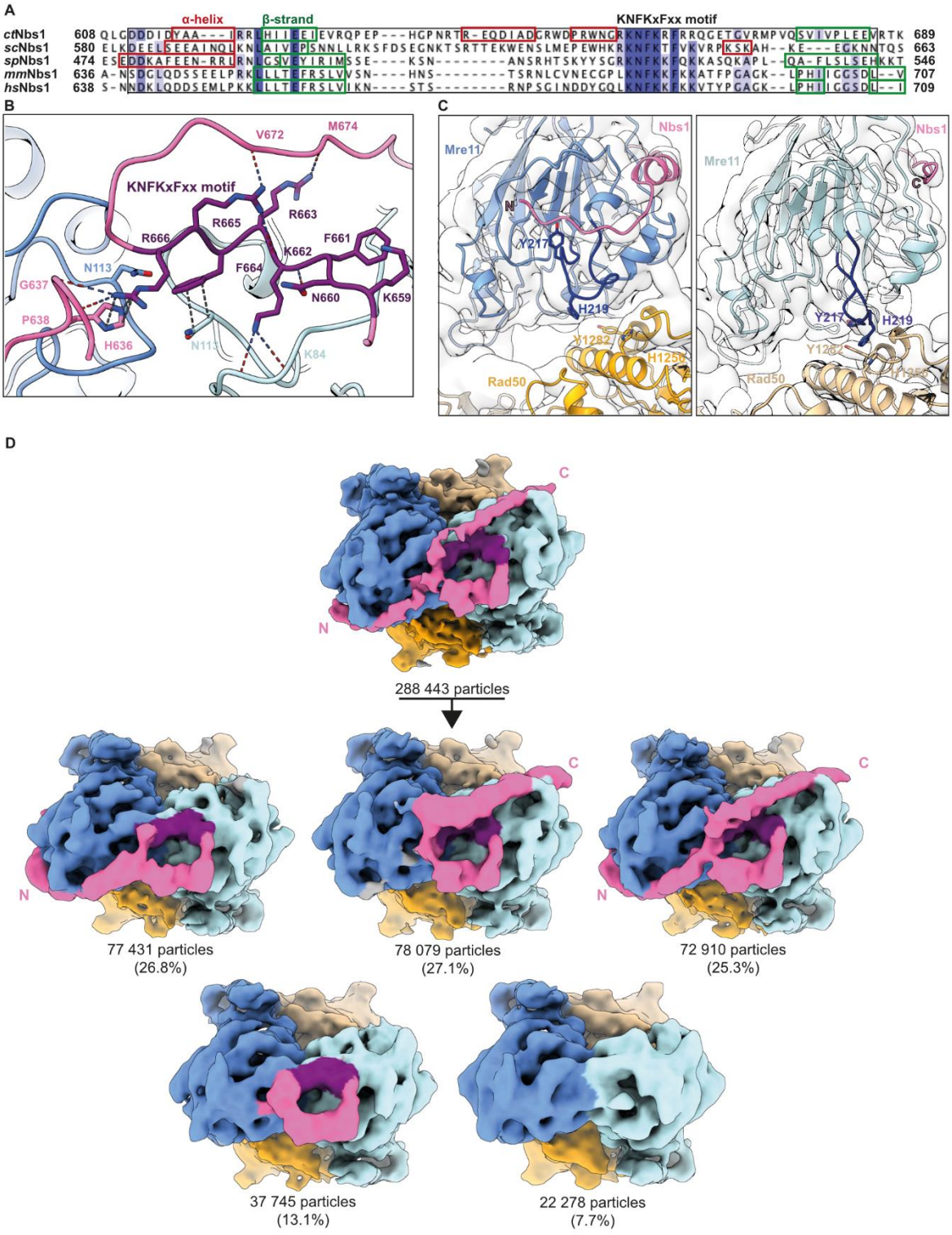

Figure S5: Structural characterization of Nbs1. Related to Figure 2.

(A) Sequence alignment of Nbs1 from different species. Conserved residues were highlighted in shades of blue, predicted α-helices were framed in red and predicted β-strands were framed in green. Alignments were calculated with ClustalΩ, secondary structure predictions with JPred4.

(B) Side view of the *Ct* KNFKxFxx motif (purple) interactions with *Ct*Mre11 (shades of blue).

(C) Side-by-side comparison of N- and C-termini of resolved Nbs1 peptide interacting with Mre11. Longer N-terminus of Nbs1 interacts with Mre11 loop containing Y217 and H219 residues affecting Mre11-Rad50 interaction at this site.

(D) Heterogeneity of Nbs1-Mre11/Rad50 interactions. 3D classification revealed full interaction (25.3%), CD/N-terminal interaction (26.8%), CD/C-terminal interaction (27.1%), CD interaction (13%), no Nbs1 present (7.7%). Rad50 highlighted in shades of orange, Mre11 in shades of blue, Nbs1 in pink, KNFKxFxx motif in purple.

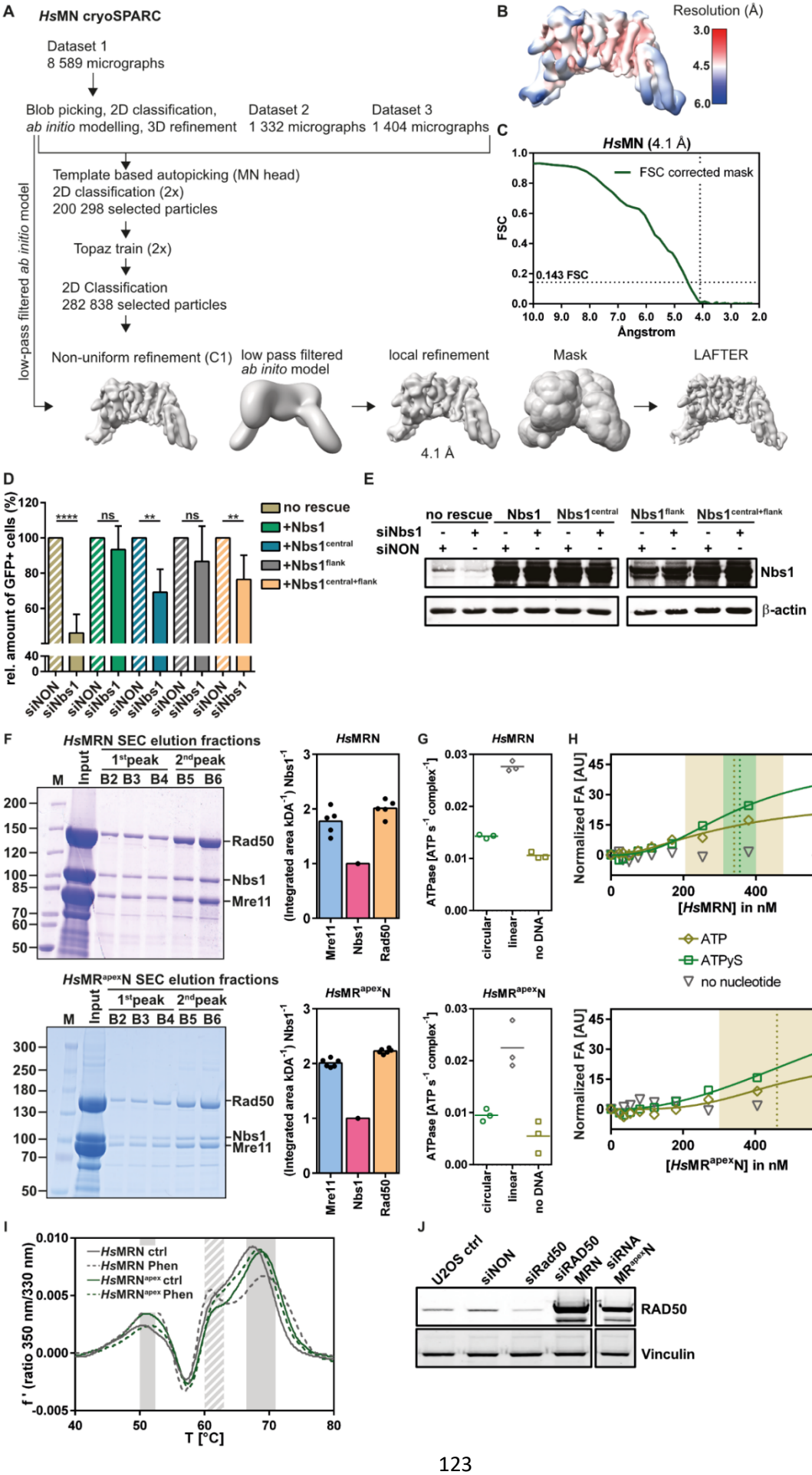
A
HsMN cryoSPARC
Dataset 1
8 589 micrographs
Blob picking, 2D classification,
ab initio modelling, 3D refinement
Dataset 2
1 332 micrographs
Dataset 3
1 404 micrographs
Template based autopicking (MN head)
2D classification (2x)
200 298 selected particles
Topaz train (2x)
2D Classification
282 838 selected particles
low-pass filtered ab initio model
Non-uniform refinement (C1)
low pass filtered ab initio model
local refinement
Mask
LAFTER
4.1 Å
B
Resolution (Å)
3.0
4.5
6.0
C
HsMN (4.1 Å)
FSC corrected mask
FSC
0.143 FSC
Ångstrom
D
rel. amount of GFP+ cells (%)
no rescue
+Nbs1
+Nbs1central
+Nbs1flank
+Nbs1central+flank
siNON
siNbs1
E
no rescue
Nbs1
Nbs1central
Nbs1flank
Nbs1central+flank
siNbs1
siNON
Nbs1
β-actin
F
HsMRN SEC elution fractions
Input
1stpeak
2ndpeak
B2 B3 B4 B5 B6
Rad50
Nbs1
Mre11
HsMRN
(Integrated area kDA-1) Nbs1-1
HsMRapexN SEC elution fractions
HsMRapexN
G
HsMRN
ATPase [ATP s-1 complex-1]
circular
linear
no DNA
HsMRapexN
H
Normalized FA [AU]
[HsMRN] in nM
ATP
ATPγS
no nucleotide
[HsMRapexN] in nM
I
HsMRN ctrl
HsMRN Phen
HsMRNapex ctrl
HsMRNapex Phen
f' (ratio 350 nm/330 nm)
T [°C]
J
U2OS ctrl
siNON
siRad50
siRAD50
MRN
siRNA
MRapexN
RAD50
Vinculin

Figure S6: Structural and functional analysis of *Hs*MRN. Related to Figure 2, 4, 6.

(A) Cryo-EM processing scheme for *Hs*MN in CryoSPARC v3.3.2.

(B) Local resolution estimation of the *Hs*MN cryo-EM map.

(C) FSC curve of the *Hs*MN cryo-EM map (CryoSPARC v3.3.2).

(D) DR-GFP assay with a siRNA targeting Nbs1. For each rescue setup, the respective siNON control is represented striped in the same color and used for normalization (n = 6, ****P < 0.0001 **P < 0.01, ns = not significant, by t-test; mean ± SD).

(E) Knock-down of Nbs1 and overexpression of wild-type and mutated *Hs*Nbs1 protein. Western blot stained with anti-Nbs1 antibody and β-actin loading control. siNON: non-targeting siRNA; siNbs1: siRNA targeting Nbs1. Irrelevant lanes were digitally removed.

(F) Representative SDS-PAGE of purified *Hs*MRN and *Hs*MR^{apex}N complexes with normalized gel quantifications of complex stoichiometry (n = 5).

(G) *Hs*MRN and *Hs*MR^{apex}N ATPase rates show a similar stimulation of the ATP hydrolysis rate by the addition of linearized DNA as observed for *Ct*MRN. The overall ATPase rates are one-fold lower as compared to *Ct*MRN. Mutation of the Rad50^{apex} leaves the ATP hydrolysis rates unaltered.

(H) Fluorescence anisotropy-based assay assessing the effect of ATP and ATPγS on *Hs*MRN and *Hs*MR^{apex}N binding towards 80-mer dsDNA reveal a weaker DNA binding compared to *Ct*MRN but are unaffected by mutations in the Rad50^{apex}. K_D values with their respective errors are indicated with dotted lines and the shaded area. The K_D value calculation failed for *Hs*MR^{apex}N ATPγS (n = 3, mean ± SD).

(I) Microscale thermophoresis thermal shift assay with purified *Hs*MRN and *Hs*MR^{apex}N complexes. 5 mM Phenanthrolin (Phen) was added as indicated. Main melting regions are shown in grey, minor in striped grey. No apparent changes could be observed.

(J) Knock-down of Rad50 and overexpression of wild-type and mutated *Hs*MRN complex. Western blot stained with anti-Rad50 antibody and Vinculin loading control. U2OS ctrl: untreated cells, siNON: non-targeting siRNA; siRad50: siRNA targeting Rad50; siRad50 *Hs*MRN: siRNA targeting Rad50, transfection with codon-optimized wt MRN genes; siRad50 *Hs*MR^{apex}N: siRNA targeting Rad50, transfection with codon-optimized mutant MRN genes. Irrelevant lanes were digitally removed.

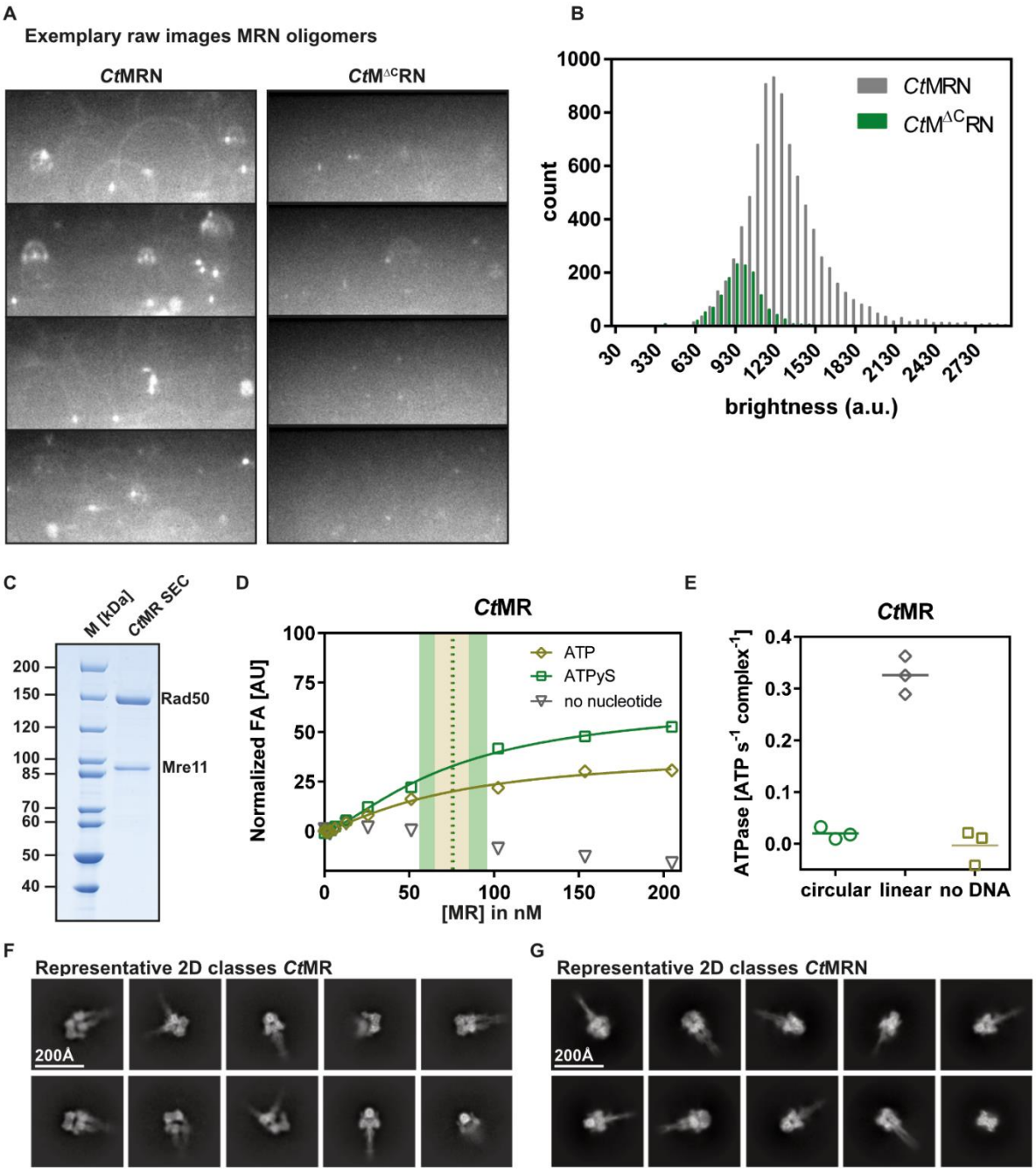

Figure S7: Quantification of *Ct*MRN clustering and role of *Ct*Nbs1. Related to Figure 4, 6.

(A) Exemplary fluorescence images of *Ct*MRN/ *Ct*M$^{\Delta C}$RN with FAM-labeled DNA.

(B) Histogram of *Ct*MRN-DNA and *Ct*M$^{\Delta C}$RN-DNA cluster formation. Fluorescence images were collected and clusters grouped based on their size.

(C) Representative SDS-PAGE of purified *Ct*MR complex.

(D) Fluorescence anisotropy-based assay assessing the effect of ATP and ATPγS on *Ct*MR binding towards 80-mer dsDNA. K_D values with their respective errors are indicated with dotted lines and the shaded area (n = 3, mean ± SD).

(E) *Ct*MR ATPase rates show a similar stimulation of the ATP hydrolysis rate by the addition of linearized DNA as observed for *Ct*MRN.

(F) Representative 2D classes obtained for *Ct*MR head complexes with ATPγS. The complex displays a higher heterogeneity and flexibility with open and closed coiled coil domains, as well as asymmetrically bound Mre11 dimers. Scale bar 200 Å, box size 352 pix.

(G) Representative 2D classes obtained for *Ct*MRN head complexes with ATPγS, Rad50 coiled-coils are closed and the complex appears rigid and symmetrically. Scale bar 200 Å, box size 352 pix.

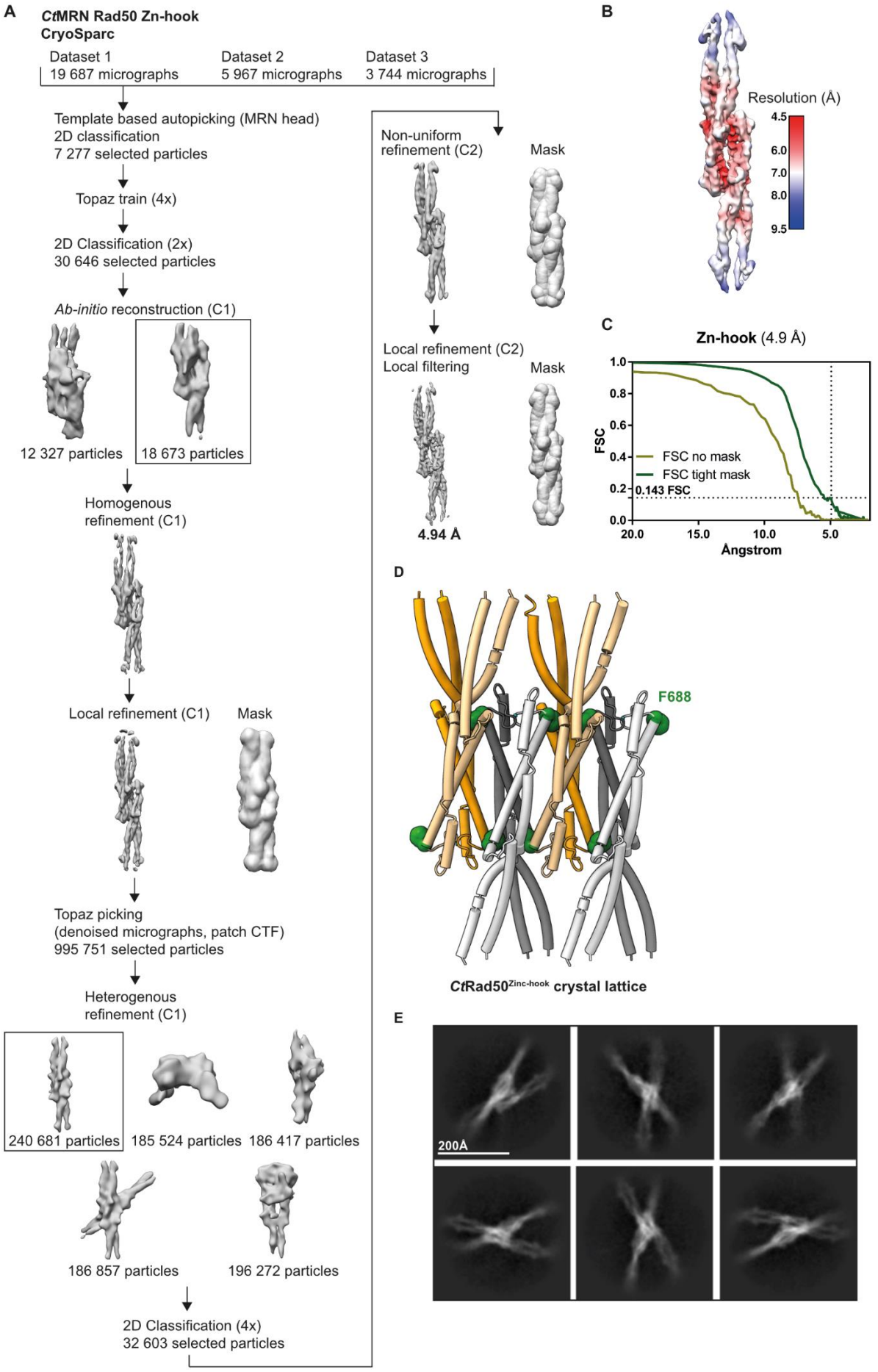
A
CtMRN Rad50 Zn-hook
CryoSparc
Dataset 1
19 687 micrographs
Dataset 2
5 967 micrographs
Dataset 3
3 744 micrographs
Template based autopicking (MRN head)
2D classification
7 277 selected particles
Topaz train (4x)
2D Classification (2x)
30 646 selected particles
Ab-initio reconstruction (C1)
12 327 particles
18 673 particles
Homogenous refinement (C1)
Local refinement (C1)
Mask
Topaz picking
(denoised micrographs, patch CTF)
995 751 selected particles
Heterogenous refinement (C1)
240 681 particles
185 524 particles
186 417 particles
186 857 particles
196 272 particles
2D Classification (4x)
32 603 selected particles
Non-uniform refinement (C2)
Mask
Local refinement (C2)
Local filtering
Mask
4.94 Å
B
Resolution (Å)
4.5
6.0
7.0
8.0
9.5
C
Zn-hook (4.9 Å)
FSC
1.0
0.8
0.6
0.4
0.2
0.0
FSC no mask
FSC tight mask
0.143 FSC
20.0
15.0
10.0
5.0
Ångstrom
D
F688
CtRad50Zinc-hook crystal lattice
E
200Å

Figure S8: Processing schemes for the *Ct*MRN Zinc-hook map and higher order structures. Related to Figure 5, 6.

(A) Cryo-EM processing scheme for the *Ct*Rad50 Zn-hook in CryoSPARC v3.2.0.

(B) Local resolution estimation of the *Ct*Rad50 Zn-hook cryo-EM map.

(C) FSC curve of the cryo-EM Zn-hook map (CryoSPARC v3.2.0).

(D) Crystal lattice of *Ct*Rad50$^{zinc\text{-}hook}$ with F688 residue hidden in the lattice arrangement.

(E) 2D classes of *Ct*Rad50 zinc-hook octamers. Scale bar 100 Å.

Table S1: Oligonucleotides used in this study.

Primers				
Oligo ID[1]	**type**	**source**	**description**	**Sequence (5' – 3')**
219_M(N521).rev	ATH PCR[2]	MB[3]	Truncated *Ct*Mre11(1-521)	AAGAAAATTCTTTTCCATGACCTTTCTGAAGT
220_M(N568).rev	ATH PCR	MB	Truncated *Ct*Mre11(1-568)	TTCTTTCGCGGGCTCGG
175_MR88_lin_for	ATH PCR	MB	Together with 219/220 respectively	AGCGGAGGTTCTCTTGAAGTCC
229_CtR50(782).fw	QC PCR	MB	QC primer to insert stop codon	GATCAGGACCTGGCCTAAATTCTGTACAGGC
230_ CtR50(782).rv	QC PCR	MB	QC primer to insert stop codon	GCCTGTACAGAATTTAGGCCAGGTCCTGATC
211_ctR_Zn.for	Cloning	MB	Cloning *Ct*Rad50(598-782)	TCCTCTTTCAGGGACCCGCCACACAACAGGAACTCAAG
212_ctR_Zn.rev	Cloning	MB	Cloning *Ct*Rad50(598-782)	AGGCCTGTACAGAATTCGGGCCAGGTCCTGATCCTC
63_hsM_H129N.fw	QC PCR	MB	Cloning *Hs*Mre11(H129N)	CATCCACGGAAACAACGACGACCCAAC
64_hsM_H129N.fw	QC PRC	MB	Cloning *Hs*Mre11(H129N)	GTTGGGTCGTCGTTGTTTCCGTGGATG
221_AAA_I.for	Gibson	MB	with 222, Gibson Insert to generate *Hs*Rad50(DENQS675-679AAAA)	GACAGGGCAGCAAGCAGCGGCAGCTGCGGTCAGTTGAGTGATGAACTGAGAGTAGACAGCGGT
222_AAA_I.rev	Gibson	MB	with 221, Gibson Insert to generate *Hs*Rad50(DENQS675-679AAAA)	ACTCAACTGACCGCAGCTGCCGCTGCTTGCTGCCCTGTCTGCCAGCGCGAGTTCCAGACCGAAG
223_linMR68.for	Gibson	MB	Vector for Gibson Assembly, *Hs*Rad50(DENQS675-679AAAA)	GAGAGTAGACAGCGGTGGC
224_linMR68.rev	Gibson	MB	Vector for Gibson Assembly, *Hs*Rad50(DENQS675-679AAAA)	TCCAGACCGAAGCTGAGC
Oligonucleotides for assays				
Oligo ID[1]	**type**	**source**	**description**	**Sequence and modifications[4] (5' – 3')**
9m	Nuclease	MB	Annealed with 10m to obtain 70 bp DNA substrate used in assays	GTAAGTGCCGCGGTGCGGGTGCCAGGGCGTGCCCTTGGGCTCCCCGGGCGCGTACTCCACCTCATGCATC-6-FAM
10m	Nuclease	MB	Annealed with 9m to obtain 70 bp DNA substrate used in assays	GATGCATGAGGTGGAGTACGCGCCCGGGGAGCCCAAGGGCACGCCCTGGCACCCGCACCGCGGCACTTAC
14m	DNA binding,	MB	Annealed with 15m to obtain 80 bp DNA	CGGGTAGTAGATGAGCGCAGGGACACCGAGGTCAAGTACATTACCC

	ATPase		substrate used in assays	TCTCATAGGAGGTGCGCTTTATCAGAA*G*C*C*A*G*A*C
15m	DNA binding, ATPase	MB	Annealed with 14m to obtain 80 bp DNA substrate used in assays	GTCTGGCTTCTGATAAAGCGCACCTCCTATGAGAGGGTAATGTACTTGACCTCGGTGTCCCTGCGCTCATCTACTACCCG-6-FAM
pUC19	DNA binding, ATPase	NEB	Used in assays, either circular or linearized (PvuII-HF, NEB)	Addgene catalog number #50005

[1] Oligo ID: an index number to identify oligos used in the study. A full list of oligos used by the authors can by obtained from the corresponding author.

[2] ATH PCR: Around the horn PCR, performed as described by NEB Inc. (https://international.neb.com/applications/cloning-and-synthetic-biology/site-directed-mutagenesis)

[3] MB: Primers were ordered from Metabion international AG and shipped as lyophilized powder. Primers longer than 50 bp and modified oligonucleotides were purified via HPLC.

[4] Modifications: * symbolizes phosphorothioates to protect against degradation; 6-FAM: 6-Carboxyfluorescein label

3. Discussion

3.1 Structural analysis of MRN

The MRN complex plays a central role in DSB repair as it senses breaks, tethers DNA ends, recruits downstream DDR factors and ultimately initiates end resection to determine the pathway choice towards HR. Apart from the essential roles in DNA repair, MRN acts in telomere maintenance and chromatin organization. Using a combination of cryo-EM, X-ray crystallography, XL-MS and biochemical analysis, we solved the structure of *Ct*MRN in an autoinhibited state and provide a mechanism for the unsolved question of how MRN combines catalytic and structural tethering tasks.

3.1.1 Nbs1 asymmetrically wraps around the Mre11 dimer

To fulfil the multitude of functions, MRN needs to be assembled correctly and folded in a distinct manner. Over a long period, the complex stoichiometry was considered to resemble a 2:2:2 ratio, thereby forming a symmetric complex. In contrast, our purifications of the human and *Chaetomium thermophilum* complex solely yielded a 2:2:1 stoichiometry with one Nbs1 per complex. Thereby, different purification strategies and expression systems were tested (Tag-free from insect cells for *Ct*MRN, FLAG-tagged on Mre11 and Nbs1, expressed in insect or human cells for *Hs*MRN) with the same results. The overexpression of *Hs*MRN in human cells as the natural expression system is a strong argument for the 2:2:1 stoichiometry as most publications use insect cells as non-native expression system. Nevertheless, different labs reported various purifications of human and yeast MRN/X from insect cells that resemble a 2:2:1 complex ratio as well[210-214].

While a previous *S.pombe* crystal structure left the possibility of two Nbs1 subunits binding to the Mre11 catalytic core, both more physiological cryo-EM structures of *Ct*MRN and *Hs*MN display one Nbs1 wrapped around the Mre11 dimer[92]. Nonetheless, the general path of Nbs1 binding is very similar in the crystal structure: two Nbs1 sequences bind at the phosphodiesterase domain sites, one Nbs1 subunit bridges the dimer interface via its conserved KNFKxFxK motif. In both cryo-EM data sets, a single, elongated Nbs1 chain binds all three interaction sites previously observed in X-ray crystallography. Thereby, Nbs1 binds the two phosphodiesterase domain sites in reverse polarity. The KNFKxFxx motifs reside in a negatively charged Mre11-binding pocket, as observed in the crystal structure. N-terminal of the KNFKxFxx motif, a small, compact central domain (CD) appears to be a species-specific feature of *Ct*Nbs1 homologs, which misses in humans. When the human and the thermophilic fungi structures are aligned, the reversed direction of the KNFKxFxx motifs across the Mre11 dimers represents yet another species-specific feature.

Interestingly, the observed *Hs*Mre11 dimer differs from a recent crystal structure of the *Hs*Mre11 catalytic core with an interface formed over a disulfide bond, and in the absence of Nbs1 (**Figure 13A**)[103]. Analogous to ROS-activated ATM, this state could be a transiently oxidized Mre11 dimer in response to oxidative stress with yet unknown implications for MRN function. In the autoinhibited conformation, obtained by aligning *Hs*Mre11 on *Ct*MRN, the X-ray structure would clash with the Rad50 globular head, potentially pointing towards a role of the rotated, covalently linked Mre11 dimer in an active MRN form (**Figure 13B**). However, in the reducing milieu of the nucleus, the presence of a constitutive covalent dimer seems unlikely and this *Hs*Mre11 X-ray structure might as well be a mere crystallisation artefact.

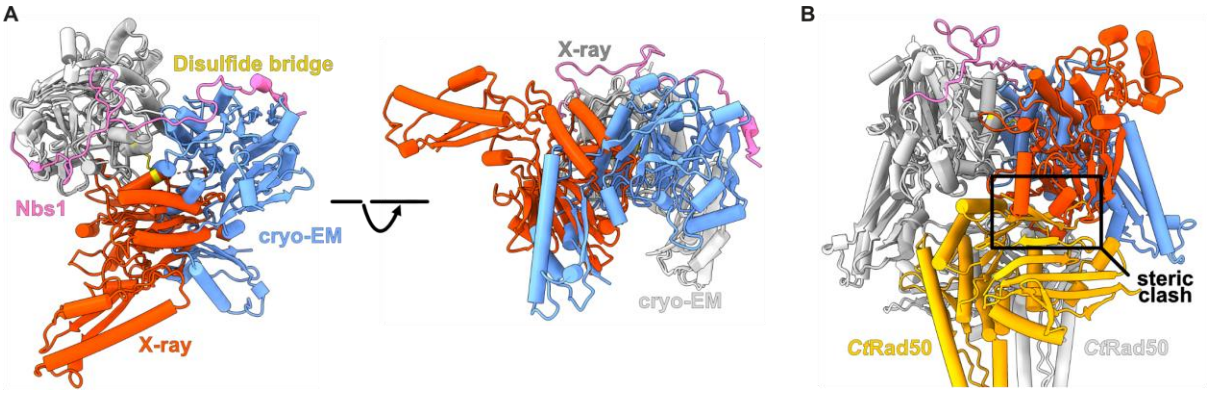

Figure 13: Comparison of the *Hs*MN cryo-EM structure (this work) with a previous *Hs*Mre11 crystal structure (PDB: 3T1I). **A**: Both structures aligned on one Mre11 (light grey: cryo-EM, grey: X-ray). The other protomer is coloured blue (cryo-EM) or orange-red (X-ray), Nbs1 in pink and the disulfide bridge highlighted in yellow. **B**: The human structures aligned on the autoinhibited state of *Ct*MRN (*Ct*Mre11 and *Ct*Nbs1 not shown, Rad50 coloured in yellow and grey). The *Hs*MN cryo-EM structure would adopt a very similar position as the *Ct*Mre11 dimer whereas the crystal structure clashes with Rad50.

The conserved KNFKxFxx motif and its flanking regions were shown to be important for Nbs1 function in DSB repair, as mutants in these sequences could not fully rescue a Nbs1 knockdown. Disrupting the Mre11 binding sequence leads to a reduced or omitted Nbs1 binding to the MR core complex, most likely resulting in an impaired nuclear import, regulation and eventually activity. In line with our *in cellulo* data, the roughly 75 amino acid long Mre11-interacting Nbs1 sequence was observed to be the minimal fragment in mice to restore embryonic viability in an Nbs1 knockout[128]. Interestingly, the binding of Nbs1 to Mre11 turned out to be quite heterogenous, only a quarter of total particles displayed full interaction, the other half CD/C-terminal or CD/N-terminal interactions, 13 % only CD interaction and roughly 8 % had no Nbs1 present. This heterogeneity points towards a possibly rather dynamic Nbs1-Mre11 interaction to facilitate conformational changes during DNA binding and processing and to integrate signals from interaction partners such as CtIP. While Nbs1 stabilizes the Mre11 dimer and overall head architecture, data from prokaryotic MR proposes a transient opening of the Mre11 dimer to relocate from its autoinhibited position to the cutting state. This model would require the dissociation of Nbs1 CD and one binding site at the phosphodiesterase site, which is conceivable in the face of a pronounced Nbs1-Mre11 binding dynamic. In summary, Nbs1 binding is essential for a proper MRN complex stability and function whilst multiple binding modes allow for the required conformational flexibility.

3.1.2 XL-MS extends cryo-EM data

The structured N-terminal domain of Nbs1 that contains the phosphopeptide binding domains FHA and BRCT1/2 is flexibly linked with the Mre11 binding region at the C-terminus. This flexible linkage disallowed to visualize the relatively small N-terminus (ca. 40 kDa) during cryo-EM studies. Therefore, XL-MS studies were performed to analyse the *Ct*MRN complex as whole in solution.

In general, results from XL-MS confirm the observed MRN structure with the closed, linearly extended CCs conformation. In this low-resolution part, Alphafold2 predictions were used to build the entire coiled-coil domain and validated by different crosslinks. Further, XL-MS results indicate a lack of CCs back-folding as observed for SMC proteins, together with the apex-apex dimerization an important feature to promote long-range DNA tethering (covered in 3.1.5). The catalytic head complex contains

a few crosslinks with violated distance restraints, a possible consequence of intrinsic flexibility or head-head oligomerization (covered in 3.1.5). Interestingly, the FHA and BRCT1/2 domains of Nbs1 crosslink to several positions on the β-sheets of Rad50, an interface as well crosslinking to the flexible C-terminus of Mre11. Moreover, additional electron density was observed near this site that could not be assigned due to missing resolution. Therefore, this density might be originating from the flexible Mre11 C-terminus or Nbs1 N-terminal part.

3.1.3 Rad50 autoinhibits Mre11

The obtained full-length *Ct*MRN-ATPγS structure represents an autoinhibited state of the complex, analogous to the published *E.coli* MR-ATPγS structure[98]. Both structures show Mre11's active site blocked by the Rad50 NBDs. As a major difference, the eukaryotic CCs domain forms a rod-like conformation, whereas the *Ec*MR complex has open CCs. With the open coils, *Ec*MR may slide along the DNA, able to pass protein-DNA complexes to scan for DSBs. In the eukaryotic system, the closed coils prevent the loading of blocked DNA ends into the complex while MRN can still bind linear DNA (covered in 3.1.4). Thus, the eukaryotic MRN complex might be tighter autoinhibited than the bacterial counterpart. This could reflect the more complex functional spectrum and the more severe detrimental effects of unregulated DNA cleavage by MRN on eukaryotic genomes.

Interestingly, 2D classes of open CCs could be observed in a dataset with ATP. ATP and ATPγS greatly vary in their hydrolysis rate, with ATPγS being hydrolysed much slower. This might suggest that the open CCs conformation is a state after ATP hydrolysis, with ADP or no nucleotide bound. Another possibility could be that the ATP binding step shortly opens the CCs. Due to a lacking hydrolysis activity with ATPγS, the nucleotide exchange rate is expected to be far lower and such a state would be less likely observable. Thereby, Nbs1 influences the coiled-coil dynamics as well. In the cryo-EM dataset with *Ct*MR, a certain number of particles displayed an open state, while Nbs1 showed no effect on the ATPase rate. Hence, Nbs1 probably affects coiled-coils dynamics by an overall complex stabilizing function and not by shifting the ATPase behaviour. With a lack of Nbs1, the complex has a higher degree of flexibility which could lead to a higher mobility of the coils, uncoupled from the nucleotide state. Further structural studies in different nucleotide states or by altering the ATPase domain should be performed to clarify coiled-coil dynamics in eukaryotic MRN.

The asymmetry of Nbs1 binding to Mre11 further induces asymmetric interactions between Mre11 and Rad50. Thereby, the Mre11 loop H213-L225, alternately interacting with the N-terminal strand of Nbs1 or with Rad50 possibly stabilizes one Rad50 while the other becomes more flexible. By breaking the symmetry in the catalytic core, Nbs1 influences MRN's entire properties including Rad50 NBDs. In the observed structure, the Rad50 NBDs reside in a pre-engaged state as the signature motifs are approximately 10 Å away from the ATPγS γ-(thio)phosphate. Hence, this conformation precludes ATP hydrolysis. Comparing the pre-engaged state with the crystal structures of *Ct*Rad50^{NBD}-ATPγS in the fully engaged state, possessing truncated, but open coiled-coils, indicates that the NBDs in the cryo-EM structure need to rotate roughly 60° with respect to the other for full engagement[109]. This movement could pry the CCs open. The switch between a pre-engaged and engaged NBD would be consistent with studies that show partially open and closed conformations of NBDs on archaeal MR[215].

Interestingly, linear DNA greatly increases MRNs ATP hydrolysis rate, possibly pointing towards a cooperative ATP and DNA binding to stabilize the open CC conformation. Thereby, DNA most likely is bound in between the CC and the Rad50^{NBD}s after ATP-dependent loading close to DSBs, as observed in previous X-ray structures of *Ct*Rad50 and bacterial MR[98,109].

3.1.4 Mre11's C-terminus adds an ATP-independent DNA-binding mode

Next to the canonical ATP-dependent DNA binding site at Rad50, we identified a second region of MRN to be able to attach to DNA in an ATP-independent manner: The C-terminus of Mre11. This region is unique to eukaryotes, prokaryotes lacking this sequence display a solely ATP-dependent DNA-end binding. Intriguingly, a recent study suggested the Mre11 C-terminus to be cleaved off by the DPC-dependent protease SPARTN, thereby reducing the affinity of *Hs*Mre11 to DNA[96]. Mutational studies with the truncated *Ct*M$^{\Delta C}$RN construct revealed that this construct cannot bind DNA without a nucleotide, whereas the K_D values are similar to WT MRN in the presence of ATP or ATPγS. In addition, the WT showed roughly 2-fold higher fluorescence anisotropy values, possibly by binding of two DNA substrates to one MRN complex at the respective sites. On top, sigmoidal binding curves and analysis of visual aggregation indicate a cooperative binding mode originating from protein oligomerization (covered in 3.1.5). Truncating Mre11 resulted in reduced aggregation, but still similar Hill-coefficients. Therefore, the MRN core possesses protein oligomerization capabilities as well.

After characterizing the DNA binding parameters of Mre11's C-terminus, the role of this newly identified region was still puzzling. We proposed a potential involvement in recognizing internal DNA sequences, not DSBs, to eventually aid in fulfilling the other tasks of MRN besides DSB repair. While the core of MRN and its functions in DSB repair are highly conserved, the unique Mre11 C-terminus might support the eukaryote-specific roles of telomere maintenance or chromatin organisation. To prove the theory, anisotropy assays were performed with linear or circular DNA as competitors to short linear DNA strands. Here, the lack of Mre11's C-terminus greatly decreased the affinity to circular DNA, supporting the model of Mre11's tail attaching to internal regions. These data are in accordance to single-molecule experiments with DNA curtains[123]. In this setup, MRN was able to bind and process DNA ends in an ATP-dependent manner, whereas before end recognition MRN diffused along linear DNA ATP-independently[123]. Hence, the eukaryote-specific Mre11 C-terminus could as well be important for MRN to scan the genome for breaks and requires further functional characterization in cellular assays.

Analysing the DNA binding properties of the *Ct*MR construct, very similar observations to the *Ct*M$^{\Delta C}$RN were made. Without nucleotide, no DNA binding was visible. This points towards a combined role of the Mre11 C-terminus and Nbs1 in binding to internal DNA sequences. As both factors are quite flexibly attached to the MRN core complex, structural visualization of a potential interaction proved impossible. Further, XL-MS data do not indicate crosslinks between the C-terminus of Mre11 and Nbs1. However, such an interaction might form only in the presence of DNA or is based on indirect contacts. Another possible explanation for the lack of DNA-binding in MR without nucleotide could be that the increased flexibility of MR in absence of Nbs1 and nucleotide destabilized the complex to an extend preventing DNA-binding of Mre11's C-terminal tail. Yet, the flexible nature of the C-terminal tail should still allow DNA binding in a disintegrated complex. Further, the observed ATP-hydrolysis rates similar to the WT do not indicate a very extensive destabilization.

3.1.5 MRN oligomerization

One of the most intriguing findings in the cryo-EM datasets were the extremely long, linear CCs that in 2D classification additionally showed the formation of joined zinc-hooks. To resolve this interaction to a better resolution, an X-ray structure was determined of the zinc-hook region. Consistent with the first hints observed in cryo-EM, the crystal structure features two dimeric CC apices in an antiparallel manner to enable the tethering of a tetrameric MRN-MRN assembly. Hereby, the very tip of the

protruding CCs is formed by coordination of the Zn^{2+} ion by a Rad50 dimer originating from a single MRN complex. Similar observations were made in structures from archaeal and human Rad50[106,216]. The *Chaetomium thermophilum* CCs additionally interact antiparallel over a newly identified interface consisting of F688 of one Rad50 dimer binding into a hydrophobic pocket, and a multitude of ionic interactions. Comparing this structure with the previous *Hs*Rad50 crystal structure, an analogous interface consisting of antiparallel CCs can be detected in the crystal lattice[216]. Hence, the mode of long-range tethering mediated over antiparallel assembly of the CCs seems to be an evolutionary conserved feature of MRN. The dimeric nature of the CC rods thereby allows the interactions to form on both sides to form two-dimensional sheets, as seen in the crystal lattices and possibly in the cryo-EM analysis of *Ct*MR. Hereby, semi-regular 120-140 Å wide molecular Velcros, consisting of oligomerized head modules connected over several tethered CCs, appeared. Surprisingly, these assemblies formed without the addition of DNA which is thought be an oligomerization nucleus for MRN. However, residual DNA from the protein purification, a common issue working with the *Ct*MRN complex, could still be present. Increasing the salt concentration to a non-physiological value (200 mM) dissolved these oligomers, hence it is reasonable to assume that this assembly is mediated to great extent by ionic interactions. These types of interactions are not only seen in the zinc-hook region, but also head-head clustering over Rad50 β-sheets possibly depends on them (**Figure 14**). This interaction is in principle not relying on DNA binding as the interface is as well accessible in the autoinhibited state. Still, binding of multiple MRN complexes to a single DNA strand might enhance these interactions as the MRN complexes are then confined to diffuse laterally instead of three-dimensional as in solution, therefor having a higher chance of encountering each other. Future studies will be needed to investigate the formation of molecular Velcros with the full MRN complex, to characterize the involved residues and the role of DNA.

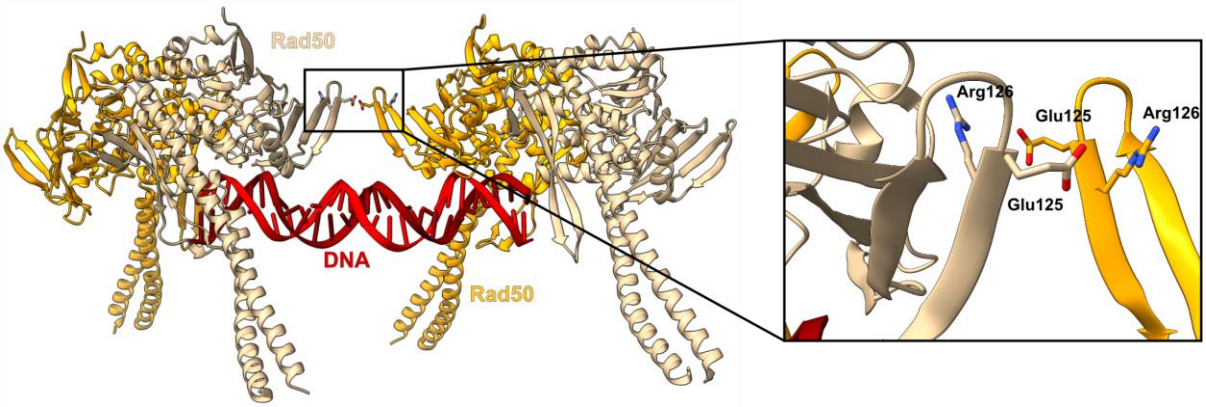

Figure 14: Model of head-head oligomerization. Two *Ct*Rad50-DNA crystal structures (PDB: 5DAC) were aligned on the DNA, the interface in the Rad50 β-sheets, involving Glu125 and Arg126 is highlighted. Due to the dimeric nature, this interaction can occur on both sides to eventually form a beads-on-a-string like assembly.

Earlier studies suggested a switch of the zinc-hook between an intra-complex and an inter-complex state to transition from structurally linking the Rad50 CCs towards tethering of distant DNA (**Figure 15**)[120,121]. This model would require an opening of the hook to form MRN-MRN assemblies. In contrast, our structural data strongly favours a model without the need for energetically unfavourable zinc-hook opening, instead the hooks remain in an intra-complex state and tethering is mediated by apex-apex interactions. We appreciate the zinc-hooks as stably associated hinges, able to switch between a ring (covered in **Figure 8**) and rod (this study) state of the CCs in one MRN complex. Hence, the CCs emerge as a chemo-mechanical gate, and not as a sole linker element as previously perceived. The switch from intra- to inter-complex tethering thereby seems unlikely.

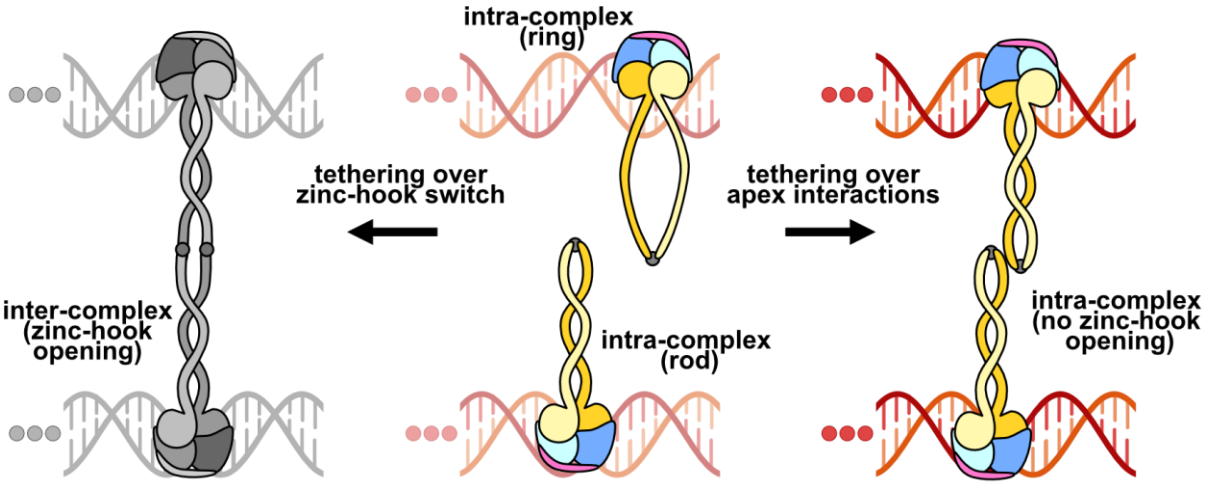

Figure 15: Model for zinc-hook mediated DNA tethering. The CCs reside in a ring or rod shape, depending on the nucleotide and DNA-binding state (middle), the zinc-hook is formed by intra-complex interactions. To tether DNA, previous publications suggested an opening of the intra-complex zinc-hooks to form an inter-complex assembly (left side, greyed out)[120,121]. The presented structural data favours a model of tethering mediated over CC apex-apex interactions, without the requirement of zinc-hook opening. Hence, the zinc-hooks remain in the intra-complex state (right side).

With the multitude of possible interaction points between MRN complexes, one could envision that MRN is able to undergo liquid-liquid phase-separation (LLPS) to form large condensates. Proteins forming LLPS condensates often display small hydrophobic surfaces and potential ion pairs, similar to MRN. These assemblies might enable efficient DNA tethering and serve as a recruiting-hub for downstream factors. In support of this theory, we observed MRN-DNA clusters during fluorescence anisotropy measurement. However, further experiments are needed to distinguish if the observed clusters were aggregates or LLPS condensates. The MRN interacting protein, MRNIP, was shown to form LLPS droplets, and incorporates MRN in these condensates to possibly promote MRN phase-separation and eventually contribute to efficient DNA repair[160].

In the cellular context, mutating the apex tethering interface significantly reduced the repair of ROS-mediated, chemically unclean DSBs in a Comet-assay setup. This type of experiment measures general DSB repair, independent of the underlying pathway. Surprisingly, no strong impact of the tethering mutant on HR-mediated repair of clean DSBs, induced by restriction enzymes in the DR-GFP assay, was observable. However, the DR-GFP assay setup relies on a very long repair period (>48 h), requires just a single repair event per cell and the essentiality of Rad50 precludes a gene knock-out, so a knock-down of the WT gene was performed. These prerequisites possibly lead to a repair mainly mediated by the still remaining, low-abundant endogenous MRN complex, therefor the effects of the apex mutant might be masked. Nevertheless, MRN-MRN tethering via the zinc-hook regions is especially important for chemically heterogenous DNA breaks, and not only involved in HR, but most likely in other DSB repair pathways as well. Further studies addressing the role of MRN-MRN tethering in NHEJ, A-EJ and chromatin organization will shed light on the broader tasks of MRN.

To regulate the tethering function, the apex interface contains an ATM/ATR phosphorylation site, the SQ-motif at S635 and Q636 in human Rad50[217]. Mutating the serine influenced DSB repair, checkpoint activation, cell survival, and cohesin loading at sites of replication restart while the nuclease activity is unaltered[218]. Phosphorylation at this site might increase the tethering stability due to additional

interactions with positively charged amino acids from the other protomer in the vicinity. Contrary, the altered geometry in the apex could as well reduce the tethering capabilities through geometric issues.

3.1.6 A possible MRN activation mechanism

The presented full-length *Ct*MRN structure clarifies the architecture of eukaryotic MRN, indicates how MRN integrates scaffolding and enzymatic functions and explains Nbs1s roles in regulating the core complex. Nevertheless, the solved ATPγS bound, autoinhibited state gives only hints on how MRN might transition from the inactive conformation towards an active, DNA bound state. Further studies are required to reconstitute DNA with MRN in its cutting state. Until then, with the help of Alphafold2, the underlying structures and structural comparisons, a first model can be proposed.

CtIP was early on shown to activate the MRN nuclease by direct binding to the complex in a phosphorylation-dependent context[63]. Thereby, the conserved C-terminus of CtIP plays a central role, a minimal peptide was sufficient to stimulate MRN's endonuclease[84]. Modelling dimeric *Ct*Rad50 in complex with the monomeric *Ct*CtIP C-terminus displayed the NBDs in the fully engaged state, with CtIP binding to the Rad50 β-sheets (**Figure 16A**). Interestingly, the S634 residue of *Ct*CtIP, corresponding to T847 in *Hs*CtIP, directly points towards an arginine residue of the β-sheets. Thus, this known CDK phosphorylation site could, upon phosphorylation, cell-cycle dependently mediate a specific interaction with Rad50. The N-terminal, partly positively charged part of the predicted CtIP fragment is predicted to take a path along the upper interface of the Rad50 NBDs, a negatively charged region, hence possibly a second binding site (**Figure 16B**). However, no really close interaction is calculated in this partly disordered and with low confidence predicted region. Further N-terminal of this site, not included in the shown CtIP prediction, a patch of multiple positively charged amino acids (RTRKGPTNDTPTRSR) might as well bind to the Rad50 interface, with the predicted CtIP N-terminal sequence then serving as a flexible linker. A prediction of Mre11 and CtIP did not return an interaction.

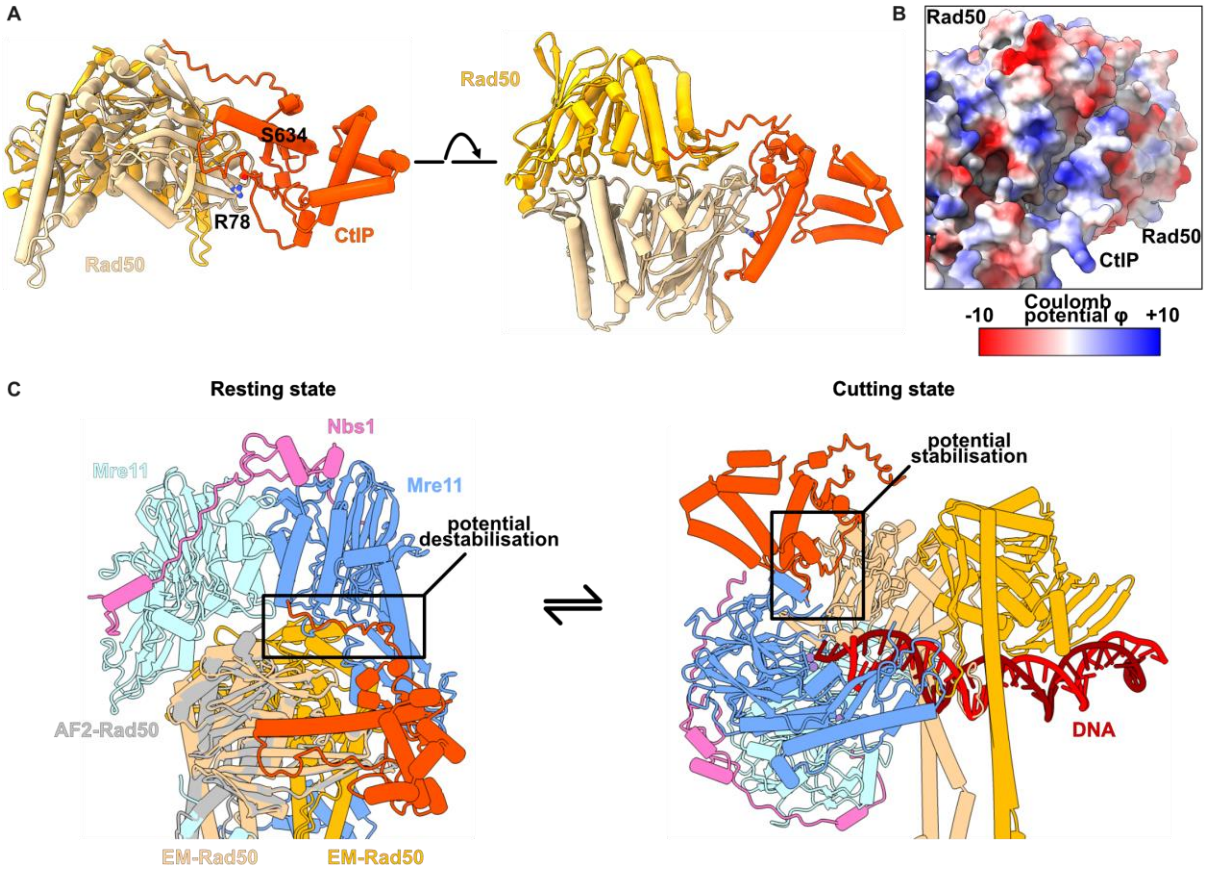

Figure 16: A CtIP-Rad50 Alphafold2 model provides first hints at the activation mechanism of MRN. **A**: Predicting the *Ct*Rad50^{NBD} dimer (beige and yellow, coiled-coil domain substituted with a poly-glycine linker) in complex with a single *Ct*CtIP$^{491-685}$ C-terminal fragment (orange-red) suggests a binding towards the Rad50 β-sheets in a phosphorylation dependent manner of S634 (T847 in *Hs*CtIP). **B**: The N-terminal sequence of the predicted CtIP fragment associates with the negatively charged upper Rad50 dimer interface. **C**: Scenarios for CtIP-mediated MRN activation. Left side: CtIP acting on the resting state by partly destabilizing the Mre11-Rad50 interface through insertion of the N-terminal region (Alphafold2 model aligned to the *Ct*MRN cryo-EM structure). Right side: CtIP acting on the cutting state by potentially stabilizing the gap in the Mre11-Rad50 interface (Alphafold2 model aligned the exo-state of *Ec*MR (PDB: 6S85), then the *Ct*Mre11-Nbs1 and Rad50 parts were docked onto the *Ec*Mre11 structure respectively. For better visualization, the predicted Rad50 structure and the *Ec*MR parts are not shown).

To support the transition from the autoinhibited to the active conformation, two structure- and prediction-based scenarios are conceivable (**Figure 16C**). By aligning the inactive *Ct*MRN structure with the Rad50-CtIP prediction, the N-terminal sequence of the CtIP fragment would clash with the Mre11 dimer. This clash could destabilize the upper interface of Mre11-Rad50, inducing a more mobile Mre11 state to eventually result in relocation to the active conformation.

The second possibility can be visualized by aligning the predicted Rad50-CtIP structure to the active conformation of bacterial Rad50. Then, the *Ct*MN structure is super-positioned with the bacterial Mre11 dimer to resemble a possible cutting state of *Ct*MRN-CtIP. In this theoretical structure, CtIP might stabilize the Mre11 dimer in the active conformation by bridging a gap between the Rad50 β-sheets and Mre11, to mediate an indirect interaction.

Both scenarios are not excluding the other one, a combination of them would lead to a first destabilization of the inactive state, in the context of the highly regulated MRN complex a likely

requirement, and then the stabilization of the active conformation to facilitate effective DNA end processing.

3.2. A unified cleavage mechanism for prokaryotic MR

Studying the, at the core, evolutionary conserved bacterial MR complex has several practical advantages over the eukaryotic system. Prokaryotes have no posttranslational modification and a decreased number of involved factors in HR, leading to a less complex regulatory network influencing DSB repair. Further, proteins can be easily expressed in *E.coli* and purified in high amounts, specific for MR, the bacterial complex can be stored over a long period without suffering from degradation and aggregation. On cryo-EM grids, MR is simpler to handle and reconstitutions with different DNA substrates were possible.

A previous study already solved structures of *Ec*MR in its resting, ATP-bound state and as well in the cutting, ADP- and DNA-bound state. This study focussed on the less physiological exonuclease cut at DNA ends, but set the basis for further understanding. More physiologically, MR first needs to introduce an endonucleolytic incision upstream of a DSB and then further digests the strand towards the break to leave short overhangs. In biochemical assays, this activity is promoted by blocked DNA ends, for example by the NHEJ factor Ku70/80. A reconstitution with double-sided Ku-blocked DNA and *Ec*MR reveals a very similar cutting state for the endonucleolytic incision compared to the exonuclease state. Thereby, the autoinhibited Mre11 dimer in the resting state relocates towards the DNA end (exo) or inwards onto an internal DNA sequence (endo) and positions one active centre poised for hydrophilic attack on the sugar-phosphate backbone. In the case of DNA hairpins, another substrate of MR, the Mre11 dimer accommodates the hairpin bubble at the active site in a similar manner. Hence, the nuclease channel represents an adaptable structure element, able to accommodate free DNA ends, internal sequences, and hairpins. All three DNA substrates are recognized by a similar configuration of MR, which is consistent with the biochemically observed cleavage sites and chemistry. As a result, MR possesses one nuclease conformation, MR loading onto DNA determines the mode of DNA cleavage. MR(N)s versatility allows cells to generalize the initial steps of HR-mediated repair with only one complex, the MR(N) complex, being involved in end processing and for eukaryotic cells signalling to ATM. In the context of oligomerization, the usage of a single, mostly C2-symmetric complex enables multiple interactions sites between the same complexes on a linear DNA strand and through zinc-hook tethering. If more than one type of complex would be used by cells to process the different DNA end substrates, additional factors or more complex interfaces would be needed to result in similar, biologically important assemblies.

3.2.1 MR loading reaction

To process diverse DNA termini, MR needs to topologically, and not chemically, recognize DSBs. DNA breaks are characterized by a relaxed, bendable state, which lacks in supercoiled, intact genomic DNA[119]. Hence, MR binding to DNA requires a roughly 45°-50° degree bending for the endonuclease state to harbour the internal DNA sequence. Previous biochemical studies and the effect of rigid DNA support this theory for a chemo-mechanical trigger of the physiological endonuclease cut[98,100]. In accordance, a nicked DNA substrate with a higher degree of flexibility promotes the endonucleolytic incision[212]. For oligomerized MR(N), the DNA bending might as well induce melting to compensate for increased torsional stress, an event observed in several other studies[219-221].

Prior to DNA bending, MR first needs to load onto DNA. The Ku-RM-MR-Ku structure suggests an ATP-dependent loading reaction on blocked DNA with an inward-facing polarity of the Mre11 dimer pointing away from the DNA end. The inward-facing configuration explains the endonucleolytic 5' strand incision, while in the exonuclease state (outward-facing configuration) the 3' strand is cut. This leads to a distinct cleavage chemistry, where an exonucleolytic cut results in dNMPs with attached phosphates leaving, while the newly formed DNA termini on the *Ec*MR-bound strand retain the phosphates during endonuclease activity. Interestingly, the outward-facing orientation at free ends could be a result of an inward-facing loading at the opposite end of a DNA oligo, which is followed by lateral sliding. This would imply that MR loads in an unified mechanism as well, while the outward-facing configuration on the rather artificial double-ended short DNA molecules used in biochemical and structural analysis might be an *in vitro* artefact.

The ring-conformation of the long Rad50 CCs thereby allows loading over free and blocked DNA ends onto internal DNA sequences. For a larger block, extending the ring-cavity, either the zinc-hook or the head complex would need to transiently open up to channel the internal DNA through (**Figure 17**). Both options were observed in AFM studies[122]. However, it is unclear if such large blocks exist under physiological conditions. In the case of head opening, the Rad50^{NBD} domains would need to detach, and additionally the Mre11 dimer relocate to either one single Rad50 or disengage as well.

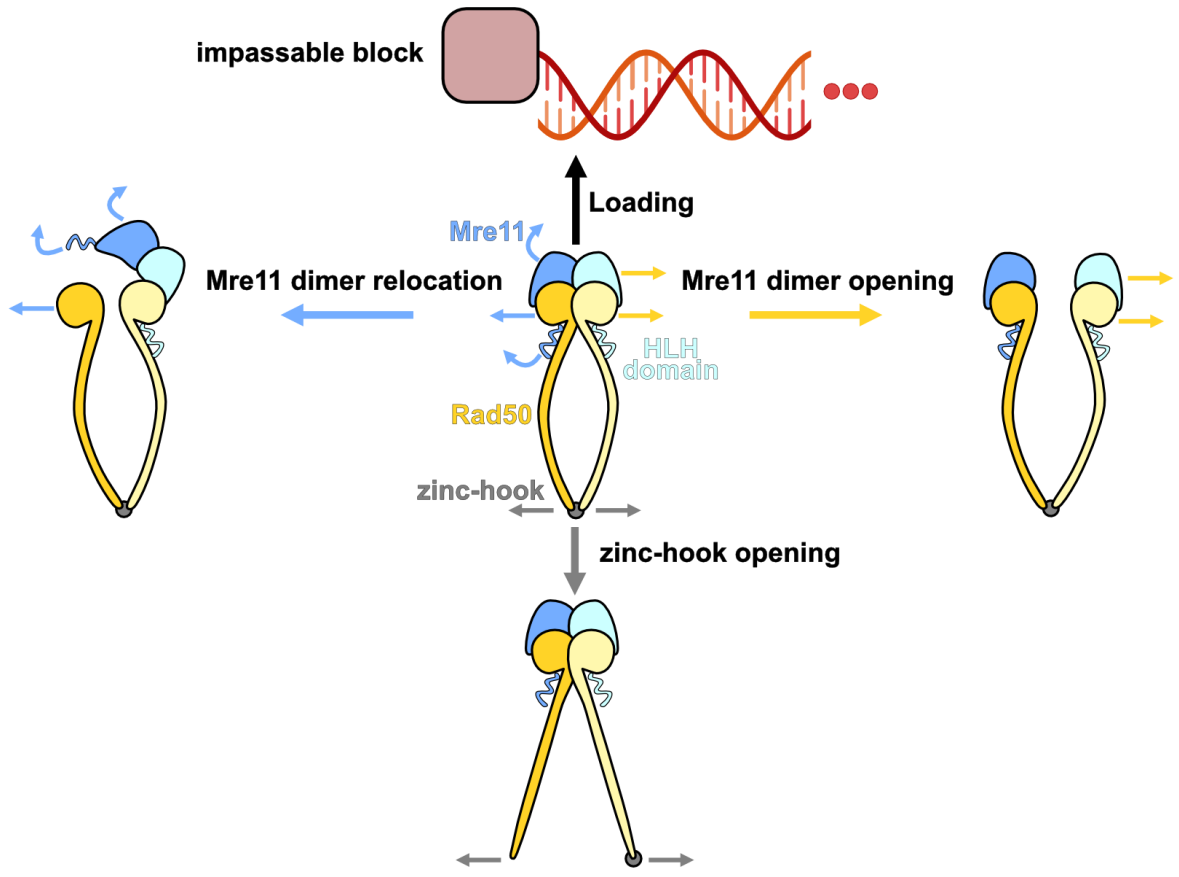

Figure 17: Loading of MR onto an impassably blocked DNA. The arrow colours indicate the different opening possibilities (blue: Mre11 dimer relocation, yellow: Mre11 dimer opening, grey: zinc-hook opening).

The loading reaction represents a challenging study subject, as this state is most likely highly transient and therefor difficult to capture structurally. AFM studies can only describe a coarse mechanism due to restricted resolution. Therefore, biochemical investigations with constructs altered in certain

complex movements, e.g. Mre11-dimer relocation, Rad50^{NBD} opening or disengaged Mre11 might suggest first hints.

3.3 Structure of *Hs*ATM

As a central player of the DDR, the ATM kinase has been extensively studied. Recruited and activated by MRN, ATM phosphorylates a pleiotropy of targets to steer the DSB repair, arrest the cell cycle and possibly initiate apoptosis. Thus, this important kinase has become the focus of attention for novel cancer therapies. Several research groups reported cryo-EM structures of the fission yeast, *Chaetomium thermophilum* as well as human ATM, however the resolution was in large parts limited and thus insufficient to build a near-complete atomic model of human ATM to serve as a basis for structure-based drug design[166,222,223].

In this work, we solved *Hs*ATM bound to ATPγS and the inhibitors KU-55933 and M4076 to resolutions reaching below 3 Å respectively. The inhibitors reduced the overall flexibility; thus, a near-complete atomic model could be obtained. A few flexible loops, e.g. around the cancer-associated mutation F858L could not be resolved. However, these intrinsically mobile regions could require a certain degree of freedom to accommodate a variety of interaction partners which only then induce a specific fold. Two novel zinc-binding motifs in the spiral and pincer domains were identified. The role of these motifs is rather a structural than a catalytic, as mutations decreased thermal stability but left the kinase activity unaltered. Further, they might serve as interaction motifs to bind other proteins or DNA. Related motifs are found in other PIKK family members, for example a zinc-finger motif in the N-terminal HEAT domain of yeast Mec1/ATR stabilizes the interface with the Ddc2/ATRIP protein[224].

While the kinase domain appears very rigid, the N-terminal solenoid domain can adopt multiple conformations. The majority of particles displayed a symmetric dimer with a small gap between the two opposing spiral domains, roughly a third showed a symmetrically related dimer with the spiral domains interacting with each other. A small subset of particles is asymmetric with one flexibly detached spiral domain. The spiral-spiral contact is a novel feature not observed in previous *Hs*ATM structures which dimerize solely over the FAT domains[223]. Therefore, the inhibitor-bound ATM structure might resemble an even more stable dimeric state, with the result that inhibition not only blocks the active site but also precludes monomerization.

3.3.1 ATM activation mechanisms

In the presented structures, the inhibitor shuts down ATMs phosphorylation ability, while the active site still seems to be in a catalytical competent conformation with Q2971 mimicing the SQ/TQ substrate. The PRD further blocks the access to the active site and is hold in position by contacts with the TRD3 CCs of the other protomer, a feature observed in all dimeric ATM structures. Upon monomerization, the interaction with the TRD3 region would vanish, thereby enabling a movement of the PRD to free the access to the active site (**Figure 18C**). A reported monomeric *Hs*ATM structure indeed supports this mechanism, however the underlying resolution is quite low and no other structural reports in this direction were published yet[225]. In the context of the fairly large hydrophobic patch between the dimeric TRD2s, the biochemically described dimer-to-monomer transition would require large structural rearrangements or binding of certain shielding interaction partners to prevent the hydrophobic residues from energetically unfavoured exposition[168]. For other PIKK family members, activating factors ATRIP (ATR), Ku70/80 (DNA-PKcs) and RHEB (mTOR) binding to the

N-terminal HEAT-repeats induce conformational changes reaching the active site to promote activity[226-228]. Contrary, a short Nbs1-peptide binding to ATM did not alter the overall dimeric fold[130]. It is well conceivable that this region alone was too short and the full MRN complex together with DNA binding at the N-terminal region is required for a robust conformational rearrangement in ATM.

Next to the in the field intensively discussed dimer-to-monomer transition theory, MRN-activated ATM might as well reside as an active dimer. This theory would bypass the need for an extensive TRD2 hydrophobic patch shielding and is more compatible with the model of a ROS-activated covalent dimer[177]. In support of this theory, asymmetric ATM dimer structures displayed a partially distorted PRD, possibly indicating a step towards an active state[167,223]. The asymmetry originates from the flexible N-terminal solenoid domain, which could transduce a movement onto the kinase domain. Binding partners (e.g. Nbs1) in this region would additionally shift the balance to the active conformation.

Further, several PTMs are required for a robust ATM activation. Four autophosphorylation sites (S367, S1893, S1981, S2996) are modified upon MRN-mediated activation (**Figure 18A**)[229]. Interestingly, these sites are exclusively located in flexible loops, not resolved in the provided structure. In addition, they are distant to the dimer interface or the PRD, thus autophosphorylation plausibly has no effect on direct dimer dissociation or other conformational changes. More conceivable, these PTMs regulate the interaction with different binding partner, which in turn could induce larger movements. Therefore, all flexible loops containing the autophosphorylation sites are located on a single surface plane, creating a possibly phospho-pattern specific, and through multiple required PTMs, a highly regulated interface. With the large distance between the different modified serines, ATM could as well accommodate several interaction partners at the same time. In accordance, reports suggested interactions with various MRN components on ATM, including Nbs1 and Rad50 CCs[130,230].

Interestingly, in the case of MRNs CC domain, the distance between the phosphorylation sites fits very well to the occurrence of positively charged pockets along the closed, linear coils, as resolved by our *Ct*MRN structure (**Figure 19A, B**). Due to low sequence conservation and the lack of structural information for the full *Hs*MRN complex, both highly conserved *Ct*Tel1 (PDB: 6SI0) and *Hs*ATM (KU-55933 bound, this work) structures were aligned and the conservation of autophosphorylation sites analysed based on structural features (**Figure 19C**). In accordance, the Tel1 protein has potential autophosphorylation sites located at conserved loops as seen for human ATM (S424 ≙ S367, S1832 ≙ S1893, S1914 ≙ S1981, S2877 ≙ S2996). It is therefore well conceivable, that this interaction interface is a conserved feature to enable MRN-mediated ATM activation. In this context, a report suggesting that only the ATP-bound form of MRN, hence with closed CCs, is able to activate ATM fits very well to the proposed model[230]. MRN in an open, ring-conformation would not be able to accommodate the more or less on a single line orientated autophosphorylation sites. Further, the distances between the positively charged binding pockets on the CCs would change in the ring-conformation due to the curvature and therefore possibly disallow concerted binding to all autophosphorylation sites.

Another important PTM is the acetylation of K3016, mediated by Tip60[170]. In contrast to the reported phosphorylation sites, this modification is directly located in the PRD and therefor might destabilize the ionic interactions between K3016 and E2895 to eventually promote PRD disengagement (**Figure 18B**).

In summary, DSB-induced ATM activation requires PRD disengagement, possibly through dimer-to-monomer transition or the effect of activating factors binding and structurally altering ATM. Hence, PRD movement most likely underlies ROS-mediated ATM activation as well. In this specific

case, the reported active state of ATM is a covalently linked dimer between C2991[177]. Modelling the flexible loop harbouring this residue with Alphafold2 reveals a quite well-predicted and aligned kinase domain, with a large distance between the putative disulfide bond (**Figure 18D**). To form the disulfide bridge, the attached PRD domains would need to move drastically inwards and slightly downwards, thereby possibly resolving their inhibitory function.

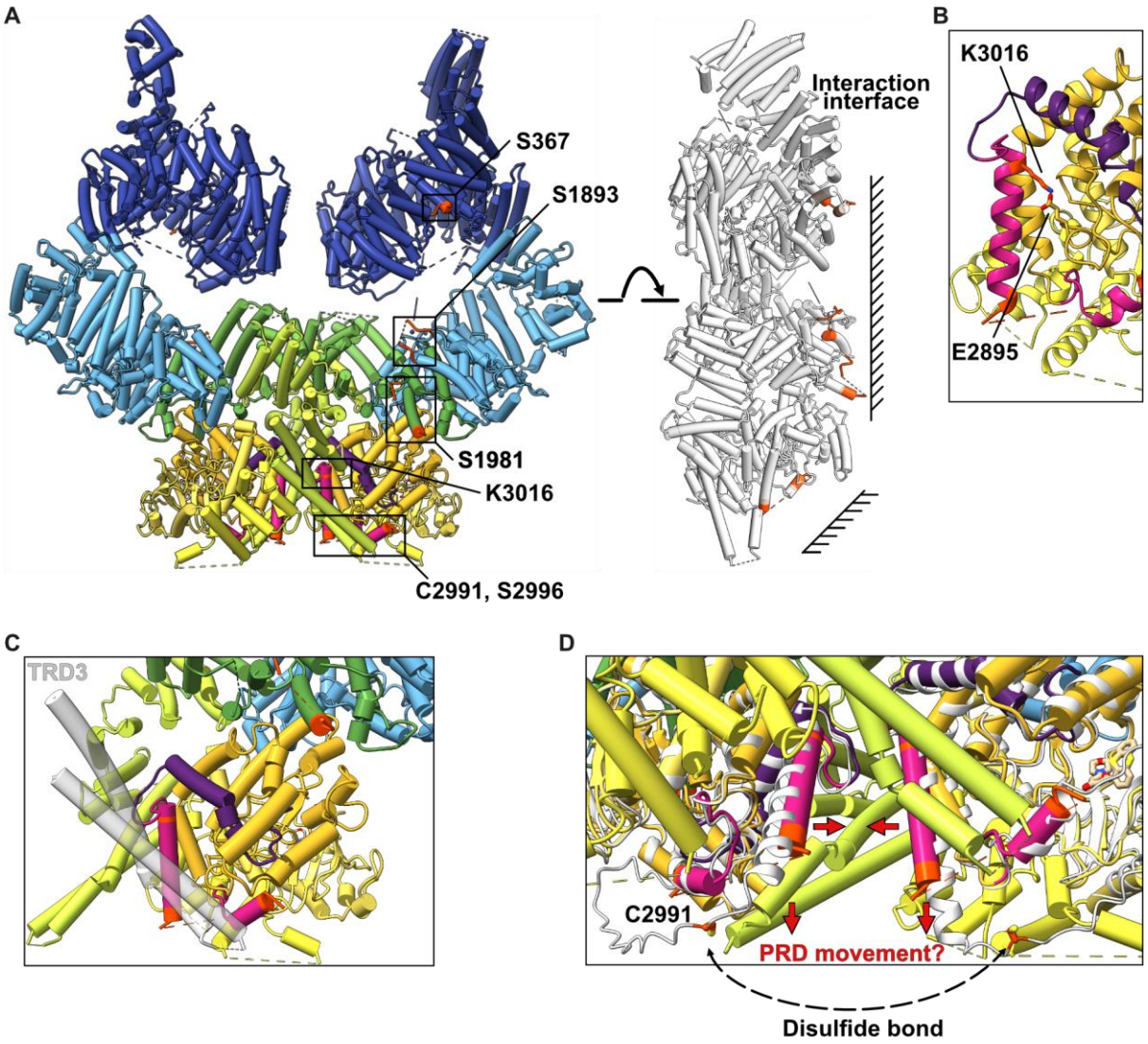

Figure 18: Model for ATM activation. Colouring according to domain architecture (see Figure 11) **A**: Left side: The four autophosphorylation-containing loops and other PTM sites (Acetylation at K3016 and disulfide bridging at C2991) (coloured orange-red) mapped to the *Hs*ATM structure (bound to KU-55933). For better visualization, two residues embracing the flexible loops are coloured respectively. Right side: Side view, the rest of ATM greyed out. For a single ATM protomer, the PTM containing loops point to an interaction plane, slightly bend towards the kinase domain. **B**: Close-up on the Tip60 acetylation site. **C**: For monomeric ATM, PRD stabilization does not involve the TRD3 domain (grey and transparent) of the other protomer. **D**: An aligned Alphafold2 model (grey) of the kinase domain reveals a large distance of the C2991 residues, for disulfide bond formation the PRD attached to this flexible loop require distinct movements.

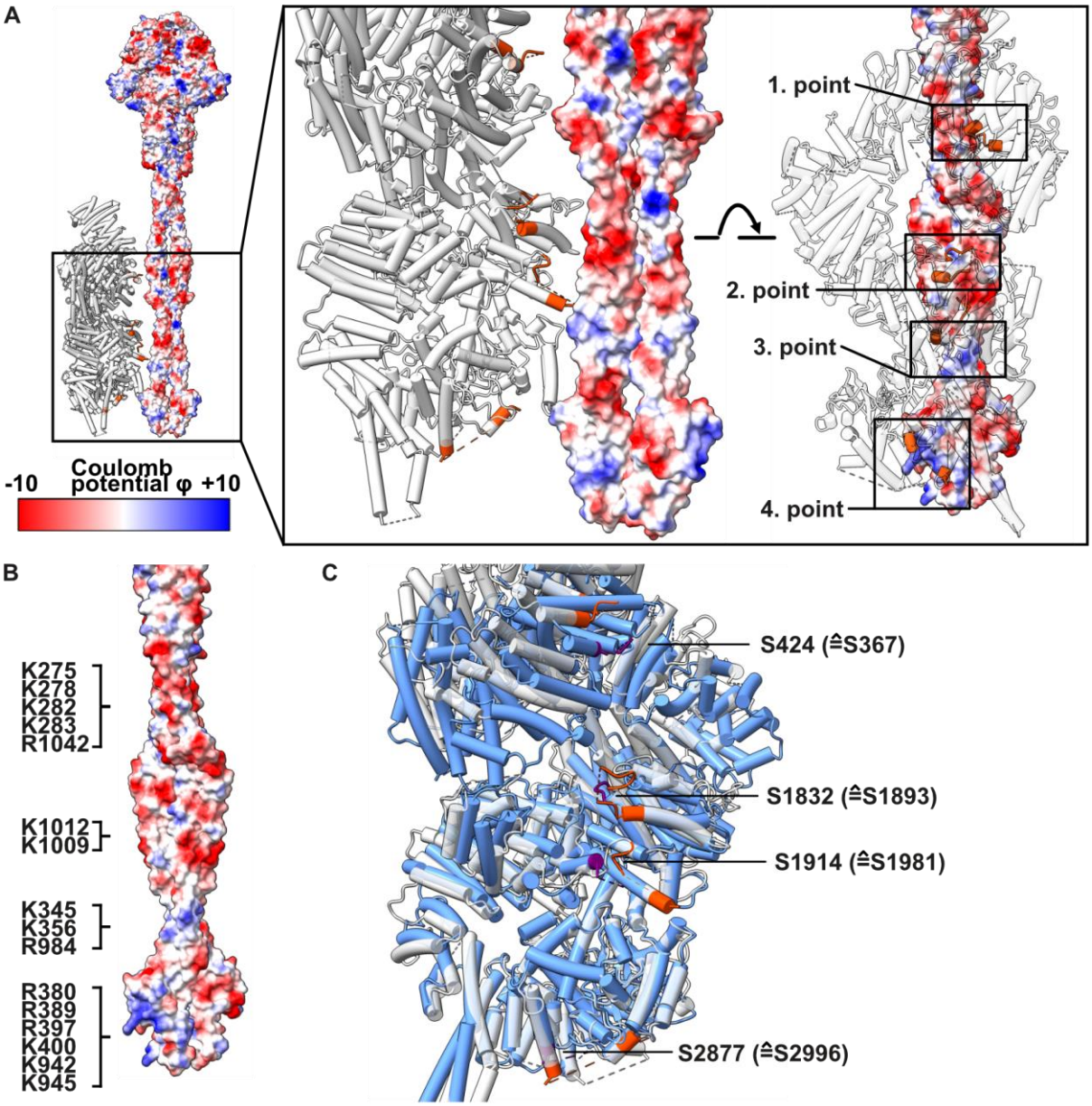

Figure 19: Detailed model for MRN-CC mediated ATM activation. *Hs*ATM grey and transparent, autophosphorylation sites orange. **A**: Left side: Large side view of *Ct*MRN (surface coloured according to Coulomb potential) binding to ATM. Right side: Magnified interface, with the interaction points on MRN highlighted in the front view. **B**: MRN CC segment alone, with the basic residues described. **C**: Comparison of the *Ct*Tel1 structure (PDB: 6SI0, blue, putative autophosphorylation sites numbered and coloured purple) and *Hs*ATM (bound to KU-55933).

3.4 Future studies

With the data presented in this work, we set an architectural framework and give a first mechanistic understanding how tethering and enzymatic functions are integrated in eukaryotic MRN. Further, we provide an unified explanation how prokaryotic MR cleaves different DNA substrates on a molecular level. Lastly, a near-complete atomic model of inhibitor-bound ATM paves the way for structure-based drug design.

Future studies are now needed to structurally clarify how eukaryotic MRN binds and cleaves DNA. This step most likely requires the additional factor CtIP to bind and activate MRN. The role of the eukaryote-specific Nbs1 subunit in this step remains elusive and must be addressed. Meanwhile, a certain homology towards the prokaryotic system allows limited conclusions for the core MR complex. The dynamics of the coiled-coils, behaving differently from the eukaryotic to the prokaryotic system, are another interesting research subject. How do they move upon DNA binding and cleavage? How can posttranslational modifications, occasionally mediated by ATM, alter their tethering and regulatory functions? Furthermore, the role of MRN oligomerization via head-head and apex-apex interactions in the context of DNA bridging and end resection needs to be addressed in detail using functional as well as structural approaches.

While the eukaryotic MRN is at the beginning of being mechanistically understood, the prokaryotic MR data ask for other studies. A main question to be answered in future is how MR loads onto DNA and recognizes DSBs. Further, the mechanism by which Mre11 relocates towards its active position remains unsolved. For bacterial MR, it is unclear if the complex oligomerizes and how it facilitates DNA tethering.

In recent years, multiple cryo-EM structures of ATM/Tel1 all showed the autoinhibited dimer. The main question in the field, how ATM can be activated by MRN is of highest importance for future structural studies. These studies might also clarify how active ATM is structurally composed: A monomer, following major rearrangements to break the hydrophobic interactions in the FAT domain or still a dimer similar to proposed ROS-activated ATM? Further, the influence of ATM phosphorylations on MRN activity remains poorly understood and needs to be clarified.

In summary, the latest technical advances in cryo-EM allowed to analyse the two central DSB factors MRN and ATM in magnificent detail, but in an isolated manner. Based on the knowledge generated in these studies, it will now be the task to look at a greater picture by combining MRN, ATM, CtIP with DNA and reconstitute the early steps of HR.

4. References

1 Hershey, A. D. & Chase, M. Independent functions of viral protein and nucleic acid in growth of bacteriophage. *J Gen Physiol* **36**, 39-56, doi:10.1085/jgp.36.1.39 (1952).

2 Watson, J. D. & Crick, F. H. The structure of DNA. *Cold Spring Harb Symp Quant Biol* **18**, 123-131, doi:10.1101/sqb.1953.018.01.020 (1953).

3 Cheng, Y. K. & Pettitt, B. M. Stabilities of double- and triple-strand helical nucleic acids. *Prog Biophys Mol Biol* **58**, 225-257, doi:10.1016/0079-6107(92)90007-s (1992).

4 Schumacher, B., Pothof, J., Vijg, J. & Hoeijmakers, J. H. J. The central role of DNA damage in the ageing process. *Nature* **592**, 695-703, doi:10.1038/s41586-021-03307-7 (2021).

5 Roos, W. P. & Kaina, B. DNA damage-induced cell death by apoptosis. *Trends Mol Med* **12**, 440-450, doi:10.1016/j.molmed.2006.07.007 (2006).

6 Khanna, A. DNA damage in cancer therapeutics: a boon or a curse? *Cancer Res* **75**, 2133-2138, doi:10.1158/0008-5472.CAN-14-3247 (2015).

7 Dietlein, F., Thelen, L. & Reinhardt, H. C. Cancer-specific defects in DNA repair pathways as targets for personalized therapeutic approaches. *Trends Genet* **30**, 326-339, doi:10.1016/j.tig.2014.06.003 (2014).

8 Norbury, C. J. & Hickson, I. D. Cellular responses to DNA damage. *Annu Rev Pharmacol Toxicol* **41**, 367-401, doi:10.1146/annurev.pharmtox.41.1.367 (2001).

9 Powell, S. & McMillan, T. J. DNA damage and repair following treatment with ionizing radiation. *Radiother Oncol* **19**, 95-108, doi:10.1016/0167-8140(90)90123-e (1990).

10 Rastogi, R. P., Richa, Kumar, A., Tyagi, M. B. & Sinha, R. P. Molecular mechanisms of ultraviolet radiation-induced DNA damage and repair. *J Nucleic Acids* **2010**, 592980, doi:10.4061/2010/592980 (2010).

11 Narayanan, D. L., Saladi, R. N. & Fox, J. L. Ultraviolet radiation and skin cancer. *Int J Dermatol* **49**, 978-986, doi:10.1111/j.1365-4632.2010.04474.x (2010).

12 Ma, B., Stepanov, I. & Hecht, S. S. Recent Studies on DNA Adducts Resulting from Human Exposure to Tobacco Smoke. *Toxics* **7**, doi:10.3390/toxics7010016 (2019).

13 Fu, D., Calvo, J. A. & Samson, L. D. Balancing repair and tolerance of DNA damage caused by alkylating agents. *Nat Rev Cancer* **12**, 104-120, doi:10.1038/nrc3185 (2012).

14 Dellarco, V. L. A mutagenicity assessment of acetaldehyde. *Mutat Res* **195**, 1-20, doi:10.1016/0165-1110(88)90013-9 (1988).

15 O'Brien, P. J., Siraki, A. G. & Shangari, N. Aldehyde sources, metabolism, molecular toxicity mechanisms, and possible effects on human health. *Crit Rev Toxicol* **35**, 609-662, doi:10.1080/10408440591002183 (2005).

16 Dasari, S. & Tchounwou, P. B. Cisplatin in cancer therapy: molecular mechanisms of action. *Eur J Pharmacol* **740**, 364-378, doi:10.1016/j.ejphar.2014.07.025 (2014).

17 Bishop, J. B. & Wassom, J. S. Toxicological review of busulfan (Myleran). *Mutat Res* **168**, 15-45, doi:10.1016/0165-1110(86)90020-5 (1986).

18 Emadi, A., Jones, R. J. & Brodsky, R. A. Cyclophosphamide and cancer: golden anniversary. *Nat Rev Clin Oncol* **6**, 638-647, doi:10.1038/nrclinonc.2009.146 (2009).

19 Thomas, C. B., Kohn, K. W. & Bonner, W. M. Characterization of DNA-protein cross-links formed by treatment of L1210 cells and nuclei with bis(2-chloroethyl)methylamine (nitrogen mustard). *Biochemistry* **17**, 3954-3958, doi:10.1021/bi00612a012 (1978).

20 Meyer-Almes, F. J. & Porschke, D. Mechanism of intercalation into the DNA double helix by ethidium. *Biochemistry* **32**, 4246-4253, doi:10.1021/bi00067a012 (1993).

21 Raney, K. D., Gopalakrishnan, S., Byrd, S., Stone, M. P. & Harris, T. M. Alteration of the aflatoxin cyclopentenone ring to a delta-lactone reduces intercalation with DNA and decreases formation of guanine N7 adducts by aflatoxin epoxides. *Chem Res Toxicol* **3**, 254-261, doi:10.1021/tx00015a011 (1990).

22 Zunino, F., Gambetta, R., Di Marco, A. & Zaccara, A. Interaction of daunomycin and its derivatives with DNA. *Biochim Biophys Acta* **277**, 489-498, doi:10.1016/0005-2787(72)90092-5 (1972).
23 Meyer, R. R. & Simpson, M. V. DNA biosynthesis in mitochondria. Differential inhibition of mitochondrial and nuclear DNA polymerases by the mutagenic dyes ethidium bromide and acriflavin. *Biochem Biophys Res Commun* **34**, 238-244, doi:10.1016/0006-291x(69)90637-8 (1969).
24 Roberts, J. D. & Kunkel, T. A. Fidelity of a human cell DNA replication complex. *Proc Natl Acad Sci U S A* **85**, 7064-7068, doi:10.1073/pnas.85.19.7064 (1988).
25 Lindahl, T. & Nyberg, B. Rate of depurination of native deoxyribonucleic acid. *Biochemistry* **11**, 3610-3618, doi:10.1021/bi00769a018 (1972).
26 Pelicano, H., Carney, D. & Huang, P. ROS stress in cancer cells and therapeutic implications. *Drug Resist Updat* **7**, 97-110, doi:10.1016/j.drup.2004.01.004 (2004).
27 Lindahl, T. Instability and decay of the primary structure of DNA. *Nature* **362**, 709-715, doi:10.1038/362709a0 (1993).
28 Fransen, M., Nordgren, M., Wang, B. & Apanasets, O. Role of peroxisomes in ROS/RNS-metabolism: implications for human disease. *Biochim Biophys Acta* **1822**, 1363-1373, doi:10.1016/j.bbadis.2011.12.001 (2012).
29 You, J. & Chan, Z. ROS Regulation During Abiotic Stress Responses in Crop Plants. *Front Plant Sci* **6**, 1092, doi:10.3389/fpls.2015.01092 (2015).
30 Wang, X. *et al.* Vitamin C and vitamin E supplementation reduce oxidative stress-induced embryo toxicity and improve the blastocyst development rate. *Fertil Steril* **78**, 1272-1277, doi:10.1016/s0015-0282(02)04236-x (2002).
31 Chatterjee, N. & Walker, G. C. Mechanisms of DNA damage, repair, and mutagenesis. *Environ Mol Mutagen* **58**, 235-263, doi:10.1002/em.22087 (2017).
32 Keszthelyi, A., Minchell, N. E. & Baxter, J. The Causes and Consequences of Topological Stress during DNA Replication. *Genes (Basel)* **7**, doi:10.3390/genes7120134 (2016).
33 Weickert, P. & Stingele, J. DNA-Protein Crosslinks and Their Resolution. *Annu Rev Biochem* **91**, 157-181, doi:10.1146/annurev-biochem-032620-105820 (2022).
34 Haber, J. E. DNA recombination: the replication connection. *Trends Biochem Sci* **24**, 271-275, doi:10.1016/s0968-0004(99)01413-9 (1999).
35 Featherstone, C. & Jackson, S. P. DNA double-strand break repair. *Curr Biol* **9**, R759-761, doi:10.1016/S0960-9822(00)80005-6 (1999).
36 Mehta, A. & Haber, J. E. Sources of DNA double-strand breaks and models of recombinational DNA repair. *Cold Spring Harb Perspect Biol* **6**, a016428, doi:10.1101/cshperspect.a016428 (2014).
37 Keeney, S. Mechanism and control of meiotic recombination initiation. *Curr Top Dev Biol* **52**, 1-53, doi:10.1016/s0070-2153(01)52008-6 (2001).
38 Schatz, D. G. & Ji, Y. Recombination centres and the orchestration of V(D)J recombination. *Nat Rev Immunol* **11**, 251-263, doi:10.1038/nri2941 (2011).
39 Kaina, B., Christmann, M., Naumann, S. & Roos, W. P. MGMT: key node in the battle against genotoxicity, carcinogenicity and apoptosis induced by alkylating agents. *DNA Repair (Amst)* **6**, 1079-1099, doi:10.1016/j.dnarep.2007.03.008 (2007).
40 Brettel, K. & Byrdin, M. Reaction mechanisms of DNA photolyase. *Curr Opin Struct Biol* **20**, 693-701, doi:10.1016/j.sbi.2010.07.003 (2010).
41 Krokan, H. E. & Bjoras, M. Base excision repair. *Cold Spring Harb Perspect Biol* **5**, a012583, doi:10.1101/cshperspect.a012583 (2013).
42 Kim, Y. J. & Wilson, D. M., 3rd. Overview of base excision repair biochemistry. *Curr Mol Pharmacol* **5**, 3-13, doi:10.2174/1874467211205010003 (2012).

43 Marteijn, J. A., Lans, H., Vermeulen, W. & Hoeijmakers, J. H. Understanding nucleotide excision repair and its roles in cancer and ageing. *Nat Rev Mol Cell Biol* **15**, 465-481, doi:10.1038/nrm3822 (2014).
44 Kunkel, T. A. & Erie, D. A. DNA mismatch repair. *Annu Rev Biochem* **74**, 681-710, doi:10.1146/annurev.biochem.74.082803.133243 (2005).
45 Li, G. M. Mechanisms and functions of DNA mismatch repair. *Cell Res* **18**, 85-98, doi:10.1038/cr.2007.115 (2008).
46 Iyer, R. R., Pluciennik, A., Burdett, V. & Modrich, P. L. DNA mismatch repair: functions and mechanisms. *Chem Rev* **106**, 302-323, doi:10.1021/cr0404794 (2006).
47 Stingele, J. *et al.* Mechanism and Regulation of DNA-Protein Crosslink Repair by the DNA-Dependent Metalloprotease SPRTN. *Mol Cell* **64**, 688-703, doi:10.1016/j.molcel.2016.09.031 (2016).
48 Larsen, N. B. *et al.* Replication-Coupled DNA-Protein Crosslink Repair by SPRTN and the Proteasome in Xenopus Egg Extracts. *Mol Cell* **73**, 574-588 e577, doi:10.1016/j.molcel.2018.11.024 (2019).
49 Kawale, A. S. & Povirk, L. F. Tyrosyl-DNA phosphodiesterases: rescuing the genome from the risks of relaxation. *Nucleic Acids Res* **46**, 520-537, doi:10.1093/nar/gkx1219 (2018).
50 Schellenberg, M. J. *et al.* ZATT (ZNF451)-mediated resolution of topoisomerase 2 DNA-protein cross-links. *Science* **357**, 1412-1416, doi:10.1126/science.aam6468 (2017).
51 Connelly, J. C., de Leau, E. S. & Leach, D. R. Nucleolytic processing of a protein-bound DNA end by the E. coli SbcCD (MR) complex. *DNA Repair (Amst)* **2**, 795-807, doi:10.1016/s1568-7864(03)00063-6 (2003).
52 Caldecott, K. W. Mammalian single-strand break repair: mechanisms and links with chromatin. *DNA Repair (Amst)* **6**, 443-453, doi:10.1016/j.dnarep.2006.10.006 (2007).
53 Caldecott, K. W. Single-strand break repair and genetic disease. *Nat Rev Genet* **9**, 619-631, doi:10.1038/nrg2380 (2008).
54 Caldecott, K. W. DNA single-strand break repair and human genetic disease. *Trends Cell Biol* **32**, 733-745, doi:10.1016/j.tcb.2022.04.010 (2022).
55 Hustedt, N. & Durocher, D. The control of DNA repair by the cell cycle. *Nat Cell Biol* **19**, 1-9, doi:10.1038/ncb3452 (2016).
56 Chang, H. H. Y., Pannunzio, N. R., Adachi, N. & Lieber, M. R. Non-homologous DNA end joining and alternative pathways to double-strand break repair. *Nat Rev Mol Cell Biol* **18**, 495-506, doi:10.1038/nrm.2017.48 (2017).
57 Burma, S. & Chen, D. J. Role of DNA-PK in the cellular response to DNA double-strand breaks. *DNA Repair (Amst)* **3**, 909-918, doi:10.1016/j.dnarep.2004.03.021 (2004).
58 Weterings, E. & Chen, D. J. The endless tale of non-homologous end-joining. *Cell Res* **18**, 114-124, doi:10.1038/cr.2008.3 (2008).
59 Sallmyr, A. & Tomkinson, A. E. Repair of DNA double-strand breaks by mammalian alternative end-joining pathways. *J Biol Chem* **293**, 10536-10546, doi:10.1074/jbc.TM117.000375 (2018).
60 Frit, P., Barboule, N., Yuan, Y., Gomez, D. & Calsou, P. Alternative end-joining pathway(s): bricolage at DNA breaks. *DNA Repair (Amst)* **17**, 81-97, doi:10.1016/j.dnarep.2014.02.007 (2014).
61 Lam, I. & Keeney, S. Mechanism and regulation of meiotic recombination initiation. *Cold Spring Harb Perspect Biol* **7**, a016634, doi:10.1101/cshperspect.a016634 (2014).
62 Lamarche, B. J., Orazio, N. I. & Weitzman, M. D. The MRN complex in double-strand break repair and telomere maintenance. *FEBS Lett* **584**, 3682-3695, doi:10.1016/j.febslet.2010.07.029 (2010).
63 Anand, R., Ranjha, L., Cannavo, E. & Cejka, P. Phosphorylated CtIP Functions as a Co-factor of the MRE11-RAD50-NBS1 Endonuclease in DNA End Resection. *Mol Cell* **64**, 940-950, doi:10.1016/j.molcel.2016.10.017 (2016).

64 Oz, R. *et al.* Phosphorylated CtIP bridges DNA to promote annealing of broken ends. *Proc Natl Acad Sci U S A* **117**, 21403-21412, doi:10.1073/pnas.2008645117 (2020).
65 de Jager, M. *et al.* Human Rad50/Mre11 is a flexible complex that can tether DNA ends. *Mol Cell* **8**, 1129-1135, doi:10.1016/s1097-2765(01)00381-1 (2001).
66 Lavin, M. F. ATM and the Mre11 complex combine to recognize and signal DNA double-strand breaks. *Oncogene* **26**, 7749-7758, doi:10.1038/sj.onc.1210880 (2007).
67 Cejka, P. & Symington, L. S. DNA End Resection: Mechanism and Control. *Annu Rev Genet* **55**, 285-307, doi:10.1146/annurev-genet-071719-020312 (2021).
68 Sturzenegger, A. *et al.* DNA2 cooperates with the WRN and BLM RecQ helicases to mediate long-range DNA end resection in human cells. *J Biol Chem* **289**, 27314-27326, doi:10.1074/jbc.M114.578823 (2014).
69 Cejka, P. *et al.* DNA end resection by Dna2-Sgs1-RPA and its stimulation by Top3-Rmi1 and Mre11-Rad50-Xrs2. *Nature* **467**, 112-116, doi:10.1038/nature09355 (2010).
70 Roy, R., Chun, J. & Powell, S. N. BRCA1 and BRCA2: different roles in a common pathway of genome protection. *Nat Rev Cancer* **12**, 68-78, doi:10.1038/nrc3181 (2011).
71 Bonilla, B., Hengel, S. R., Grundy, M. K. & Bernstein, K. A. RAD51 Gene Family Structure and Function. *Annu Rev Genet* **54**, 25-46, doi:10.1146/annurev-genet-021920-092410 (2020).
72 McIlwraith, M. J. *et al.* Human DNA polymerase eta promotes DNA synthesis from strand invasion intermediates of homologous recombination. *Mol Cell* **20**, 783-792, doi:10.1016/j.molcel.2005.10.001 (2005).
73 Li, X. & Heyer, W. D. Homologous recombination in DNA repair and DNA damage tolerance. *Cell Res* **18**, 99-113, doi:10.1038/cr.2008.1 (2008).
74 Wyatt, H. D. & West, S. C. Holliday junction resolvases. *Cold Spring Harb Perspect Biol* **6**, a023192, doi:10.1101/cshperspect.a023192 (2014).
75 Schafer, K. A. The cell cycle: a review. *Vet Pathol* **35**, 461-478, doi:10.1177/030098589803500601 (1998).
76 Asghar, U., Witkiewicz, A. K., Turner, N. C. & Knudsen, E. S. The history and future of targeting cyclin-dependent kinases in cancer therapy. *Nat Rev Drug Discov* **14**, 130-146, doi:10.1038/nrd4504 (2015).
77 Johnson, D. G. & Walker, C. L. Cyclins and cell cycle checkpoints. *Annu Rev Pharmacol Toxicol* **39**, 295-312, doi:10.1146/annurev.pharmtox.39.1.295 (1999).
78 Marechal, A. & Zou, L. DNA damage sensing by the ATM and ATR kinases. *Cold Spring Harb Perspect Biol* **5**, doi:10.1101/cshperspect.a012716 (2013).
79 Lou, Z. *et al.* MDC1 maintains genomic stability by participating in the amplification of ATM-dependent DNA damage signals. *Mol Cell* **21**, 187-200, doi:10.1016/j.molcel.2005.11.025 (2006).
80 Jungmichel, S. & Stucki, M. MDC1: The art of keeping things in focus. *Chromosoma* **119**, 337-349, doi:10.1007/s00412-010-0266-9 (2010).
81 Mattiroli, F. *et al.* RNF168 ubiquitinates K13-15 on H2A/H2AX to drive DNA damage signaling. *Cell* **150**, 1182-1195, doi:10.1016/j.cell.2012.08.005 (2012).
82 Saredi, G. *et al.* H4K20me0 marks post-replicative chromatin and recruits the TONSL-MMS22L DNA repair complex. *Nature* **534**, 714-718, doi:10.1038/nature18312 (2016).
83 Huertas, P. & Jackson, S. P. Human CtIP mediates cell cycle control of DNA end resection and double strand break repair. *J Biol Chem* **284**, 9558-9565, doi:10.1074/jbc.M808906200 (2009).
84 Zdravkovic, A. *et al.* A conserved Ctp1/CtIP C-terminal peptide stimulates Mre11 endonuclease activity. *Proc Natl Acad Sci U S A* **118**, doi:10.1073/pnas.2016287118 (2021).
85 Huertas, P., Cortes-Ledesma, F., Sartori, A. A., Aguilera, A. & Jackson, S. P. CDK targets Sae2 to control DNA-end resection and homologous recombination. *Nature* **455**, 689-692, doi:10.1038/nature07215 (2008).

86 Yu, X. & Chen, J. DNA damage-induced cell cycle checkpoint control requires CtIP, a phosphorylation-dependent binding partner of BRCA1 C-terminal domains. *Mol Cell Biol* **24**, 9478-9486, doi:10.1128/MCB.24.21.9478-9486.2004 (2004).
87 Williams, R. S., Williams, J. S. & Tainer, J. A. Mre11-Rad50-Nbs1 is a keystone complex connecting DNA repair machinery, double-strand break signaling, and the chromatin template. *Biochem Cell Biol* **85**, 509-520, doi:10.1139/O07-069 (2007).
88 Stracker, T. H. & Petrini, J. H. The MRE11 complex: starting from the ends. *Nat Rev Mol Cell Biol* **12**, 90-103, doi:10.1038/nrm3047 (2011).
89 Paull, T. T. & Gellert, M. Nbs1 potentiates ATP-driven DNA unwinding and endonuclease cleavage by the Mre11/Rad50 complex. *Genes Dev* **13**, 1276-1288, doi:10.1101/gad.13.10.1276 (1999).
90 Yoshida, T., Claverie, J. M. & Ogata, H. Mimivirus reveals Mre11/Rad50 fusion proteins with a sporadic distribution in eukaryotes, bacteria, viruses and plasmids. *Virol J* **8**, 427, doi:10.1186/1743-422X-8-427 (2011).
91 Syed, A. & Tainer, J. A. The MRE11-RAD50-NBS1 Complex Conducts the Orchestration of Damage Signaling and Outcomes to Stress in DNA Replication and Repair. *Annu Rev Biochem* **87**, 263-294, doi:10.1146/annurev-biochem-062917-012415 (2018).
92 Schiller, C. B. *et al.* Structure of Mre11-Nbs1 complex yields insights into ataxia-telangiectasia-like disease mutations and DNA damage signaling. *Nat Struct Mol Biol* **19**, 693-700, doi:10.1038/nsmb.2323 (2012).
93 Hopfner, K. P. *et al.* Structural biochemistry and interaction architecture of the DNA double-strand break repair Mre11 nuclease and Rad50-ATPase. *Cell* **105**, 473-485, doi:10.1016/s0092-8674(01)00335-x (2001).
94 Lammens, K. *et al.* The Mre11:Rad50 structure shows an ATP-dependent molecular clamp in DNA double-strand break repair. *Cell* **145**, 54-66, doi:10.1016/j.cell.2011.02.038 (2011).
95 Usui, T. *et al.* Complex formation and functional versatility of Mre11 of budding yeast in recombination. *Cell* **95**, 705-716, doi:10.1016/s0092-8674(00)81640-2 (1998).
96 Na, J. *et al.* SPRTN protease-cleaved MRE11 decreases DNA repair and radiosensitises cancer cells. *Cell Death Dis* **12**, 165, doi:10.1038/s41419-021-03437-w (2021).
97 Williams, R. S. *et al.* Mre11 dimers coordinate DNA end bridging and nuclease processing in double-strand-break repair. *Cell* **135**, 97-109, doi:10.1016/j.cell.2008.08.017 (2008).
98 Kashammer, L. *et al.* Mechanism of DNA End Sensing and Processing by the Mre11-Rad50 Complex. *Mol Cell* **76**, 382-394 e386, doi:10.1016/j.molcel.2019.07.035 (2019).
99 Paull, T. T. & Gellert, M. The 3' to 5' exonuclease activity of Mre 11 facilitates repair of DNA double-strand breaks. *Mol Cell* **1**, 969-979, doi:10.1016/s1097-2765(00)80097-0 (1998).
100 Saathoff, J. H., Kashammer, L., Lammens, K., Byrne, R. T. & Hopfner, K. P. The bacterial Mre11-Rad50 homolog SbcCD cleaves opposing strands of DNA by two chemically distinct nuclease reactions. *Nucleic Acids Res* **46**, 11303-11314, doi:10.1093/nar/gky878 (2018).
101 Shibata, A. *et al.* DNA double-strand break repair pathway choice is directed by distinct MRE11 nuclease activities. *Mol Cell* **53**, 7-18, doi:10.1016/j.molcel.2013.11.003 (2014).
102 Yamaguchi-Iwai, Y. *et al.* Mre11 is essential for the maintenance of chromosomal DNA in vertebrate cells. *EMBO J* **18**, 6619-6629, doi:10.1093/emboj/18.23.6619 (1999).
103 Park, Y. B., Chae, J., Kim, Y. C. & Cho, Y. Crystal structure of human Mre11: understanding tumorigenic mutations. *Structure* **19**, 1591-1602, doi:10.1016/j.str.2011.09.010 (2011).
104 Hopfner, K. P. & Tainer, J. A. Rad50/SMC proteins and ABC transporters: unifying concepts from high-resolution structures. *Curr Opin Struct Biol* **13**, 249-255, doi:10.1016/s0959-440x(03)00037-x (2003).
105 Hirano, T. At the heart of the chromosome: SMC proteins in action. *Nat Rev Mol Cell Biol* **7**, 311-322, doi:10.1038/nrm1909 (2006).
106 Hopfner, K. P. *et al.* The Rad50 zinc-hook is a structure joining Mre11 complexes in DNA recombination and repair. *Nature* **418**, 562-566, doi:10.1038/nature00922 (2002).

107 Williams, G. J. *et al.* ABC ATPase signature helices in Rad50 link nucleotide state to Mre11 interface for DNA repair. *Nat Struct Mol Biol* **18**, 423-431, doi:10.1038/nsmb.2038 (2011).
108 Hopfner, K. P. *et al.* Structural biology of Rad50 ATPase: ATP-driven conformational control in DNA double-strand break repair and the ABC-ATPase superfamily. *Cell* **101**, 789-800, doi:10.1016/s0092-8674(00)80890-9 (2000).
109 Seifert, F. U., Lammens, K., Stoehr, G., Kessler, B. & Hopfner, K. P. Structural mechanism of ATP-dependent DNA binding and DNA end bridging by eukaryotic Rad50. *EMBO J* **35**, 759-772, doi:10.15252/embj.201592934 (2016).
110 Deshpande, R. A., Lee, J. H. & Paull, T. T. Rad50 ATPase activity is regulated by DNA ends and requires coordination of both active sites. *Nucleic Acids Res* **45**, 5255-5268, doi:10.1093/nar/gkx173 (2017).
111 Moncalian, G. *et al.* The rad50 signature motif: essential to ATP binding and biological function. *J Mol Biol* **335**, 937-951, doi:10.1016/j.jmb.2003.11.026 (2004).
112 Chen, L. *et al.* Effect of amino acid substitutions in the rad50 ATP binding domain on DNA double strand break repair in yeast. *J Biol Chem* **280**, 2620-2627, doi:10.1074/jbc.M410192200 (2005).
113 Kissling, V. M. *et al.* Mre11-Rad50 oligomerization promotes DNA double-strand break repair. *Nat Commun* **13**, 2374, doi:10.1038/s41467-022-29841-0 (2022).
114 Alani, E., Padmore, R. & Kleckner, N. Analysis of wild-type and rad50 mutants of yeast suggests an intimate relationship between meiotic chromosome synapsis and recombination. *Cell* **61**, 419-436, doi:10.1016/0092-8674(90)90524-i (1990).
115 Zabolotnaya, E., Mela, I., Henderson, R. M. & Robinson, N. P. Turning the Mre11/Rad50 DNA repair complex on its head: lessons from SMC protein hinges, dynamic coiled-coil movements and DNA loop-extrusion? *Biochem Soc Trans* **48**, 2359-2376, doi:10.1042/BST20170168 (2020).
116 Hohl, M. *et al.* The Rad50 coiled-coil domain is indispensable for Mre11 complex functions. *Nat Struct Mol Biol* **18**, 1124-1131, doi:10.1038/nsmb.2116 (2011).
117 Wiltzius, J. J., Hohl, M., Fleming, J. C. & Petrini, J. H. The Rad50 hook domain is a critical determinant of Mre11 complex functions. *Nat Struct Mol Biol* **12**, 403-407, doi:10.1038/nsmb928 (2005).
118 Ogawa, H., Johzuka, K., Nakagawa, T., Leem, S. H. & Hagihara, A. H. Functions of the yeast meiotic recombination genes, MRE11 and MRE2. *Adv Biophys* **31**, 67-76, doi:10.1016/0065-227x(95)99383-z (1995).
119 Fulcrand, G. *et al.* DNA supercoiling, a critical signal regulating the basal expression of the lac operon in Escherichia coli. *Sci Rep* **6**, 19243, doi:10.1038/srep19243 (2016).
120 Zabolotnaya, E. *et al.* Modes of action of the archaeal Mre11/Rad50 DNA-repair complex revealed by fast-scan atomic force microscopy. *Proc Natl Acad Sci U S A* **117**, 14936-14947, doi:10.1073/pnas.1915598117 (2020).
121 Moreno-Herrero, F. *et al.* Mesoscale conformational changes in the DNA-repair complex Rad50/Mre11/Nbs1 upon binding DNA. *Nature* **437**, 440-443, doi:10.1038/nature03927 (2005).
122 Tatebe, H. *et al.* Rad50 zinc hook functions as a constitutive dimerization module interchangeable with SMC hinge. *Nat Commun* **11**, 370, doi:10.1038/s41467-019-14025-0 (2020).
123 Myler, L. R. *et al.* Single-Molecule Imaging Reveals How Mre11-Rad50-Nbs1 Initiates DNA Break Repair. *Mol Cell* **67**, 891-898 e894, doi:10.1016/j.molcel.2017.08.002 (2017).
124 Soh, Y. M., Basquin, J. & Gruber, S. A rod conformation of the Pyrococcus furiosus Rad50 coiled coil. *Proteins* **89**, 251-255, doi:10.1002/prot.26005 (2021).
125 Williams, R. S. *et al.* Nbs1 flexibly tethers Ctp1 and Mre11-Rad50 to coordinate DNA double-strand break processing and repair. *Cell* **139**, 87-99, doi:10.1016/j.cell.2009.07.033 (2009).

126 Lukas, C. *et al.* Mdc1 couples DNA double-strand break recognition by Nbs1 with its H2AX-dependent chromatin retention. *EMBO J* **23**, 2674-2683, doi:10.1038/sj.emboj.7600269 (2004).
127 Kobayashi, J. *et al.* NBS1 localizes to gamma-H2AX foci through interaction with the FHA/BRCT domain. *Curr Biol* **12**, 1846-1851, doi:10.1016/s0960-9822(02)01259-9 (2002).
128 Kim, J. H. *et al.* The Mre11-Nbs1 Interface Is Essential for Viability and Tumor Suppression. *Cell Rep* **18**, 496-507, doi:10.1016/j.celrep.2016.12.035 (2017).
129 Kobayashi, J., Antoccia, A., Tauchi, H., Matsuura, S. & Komatsu, K. NBS1 and its functional role in the DNA damage response. *DNA Repair (Amst)* **3**, 855-861, doi:10.1016/j.dnarep.2004.03.023 (2004).
130 Warren, C. & Pavletich, N. P. Structure of the human ATM kinase and mechanism of Nbs1 binding. *Elife* **11**, doi:10.7554/eLife.74218 (2022).
131 Paull, T. T. Mechanisms of ATM Activation. *Annu Rev Biochem* **84**, 711-738, doi:10.1146/annurev-biochem-060614-034335 (2015).
132 Zhang, X. & Paull, T. T. The Mre11/Rad50/Xrs2 complex and non-homologous end-joining of incompatible ends in S. cerevisiae. *DNA Repair (Amst)* **4**, 1281-1294, doi:10.1016/j.dnarep.2005.06.011 (2005).
133 Helmink, B. A. *et al.* MRN complex function in the repair of chromosomal Rag-mediated DNA double-strand breaks. *J Exp Med* **206**, 669-679, doi:10.1084/jem.20081326 (2009).
134 Milman, N., Higuchi, E. & Smith, G. R. Meiotic DNA double-strand break repair requires two nucleases, MRN and Ctp1, to produce a single size class of Rec12 (Spo11)-oligonucleotide complexes. *Mol Cell Biol* **29**, 5998-6005, doi:10.1128/MCB.01127-09 (2009).
135 Lukas, C., Falck, J., Bartkova, J., Bartek, J. & Lukas, J. Distinct spatiotemporal dynamics of mammalian checkpoint regulators induced by DNA damage. *Nat Cell Biol* **5**, 255-260, doi:10.1038/ncb945 (2003).
136 Levy, M. Z., Allsopp, R. C., Futcher, A. B., Greider, C. W. & Harley, C. B. Telomere end-replication problem and cell aging. *J Mol Biol* **225**, 951-960, doi:10.1016/0022-2836(92)90096-3 (1992).
137 d'Adda di Fagagna, F., Teo, S. H. & Jackson, S. P. Functional links between telomeres and proteins of the DNA-damage response. *Genes Dev* **18**, 1781-1799, doi:10.1101/gad.1214504 (2004).
138 Hug, N. & Lingner, J. Telomere length homeostasis. *Chromosoma* **115**, 413-425, doi:10.1007/s00412-006-0067-3 (2006).
139 Collins, K. & Mitchell, J. R. Telomerase in the human organism. *Oncogene* **21**, 564-579, doi:10.1038/sj.onc.1205083 (2002).
140 Shay, J. W. & Wright, W. E. Hayflick, his limit, and cellular ageing. *Nat Rev Mol Cell Biol* **1**, 72-76, doi:10.1038/35036093 (2000).
141 Artandi, S. E. & DePinho, R. A. Telomeres and telomerase in cancer. *Carcinogenesis* **31**, 9-18, doi:10.1093/carcin/bgp268 (2010).
142 De Boeck, G., Forsyth, R. G., Praet, M. & Hogendoorn, P. C. Telomere-associated proteins: cross-talk between telomere maintenance and telomere-lengthening mechanisms. *J Pathol* **217**, 327-344, doi:10.1002/path.2500 (2009).
143 Longhese, M. P. DNA damage response at functional and dysfunctional telomeres. *Genes Dev* **22**, 125-140, doi:10.1101/gad.1626908 (2008).
144 Bartocci, C. *et al.* Isolation of chromatin from dysfunctional telomeres reveals an important role for Ring1b in NHEJ-mediated chromosome fusions. *Cell Rep* **7**, 1320-1332, doi:10.1016/j.celrep.2014.04.002 (2014).
145 Kironmai, K. M. & Muniyappa, K. Alteration of telomeric sequences and senescence caused by mutations in RAD50 of Saccharomyces cerevisiae. *Genes Cells* **2**, 443-455, doi:10.1046/j.1365-2443.1997.1330331.x (1997).

146 Chamankhah, M. & Xiao, W. Formation of the yeast Mre11-Rad50-Xrs2 complex is correlated with DNA repair and telomere maintenance. *Nucleic Acids Res* **27**, 2072-2079, doi:10.1093/nar/27.10.2072 (1999).
147 Takata, H., Tanaka, Y. & Matsuura, A. Late S phase-specific recruitment of Mre11 complex triggers hierarchical assembly of telomere replication proteins in Saccharomyces cerevisiae. *Mol Cell* **17**, 573-583, doi:10.1016/j.molcel.2005.01.014 (2005).
148 Wu, P., Takai, H. & de Lange, T. Telomeric 3' overhangs derive from resection by Exo1 and Apollo and fill-in by POT1b-associated CST. *Cell* **150**, 39-52, doi:10.1016/j.cell.2012.05.026 (2012).
149 Rai, R. *et al.* NBS1 Phosphorylation Status Dictates Repair Choice of Dysfunctional Telomeres. *Mol Cell* **65**, 801-817 e804, doi:10.1016/j.molcel.2017.01.016 (2017).
150 Khayat, F. *et al.* Inhibition of MRN activity by a telomere protein motif. *Nat Commun* **12**, 3856, doi:10.1038/s41467-021-24047-2 (2021).
151 Cesare, A. J. & Reddel, R. R. Alternative lengthening of telomeres: models, mechanisms and implications. *Nat Rev Genet* **11**, 319-330, doi:10.1038/nrg2763 (2010).
152 Davies, O. R. *et al.* CtIP tetramer assembly is required for DNA-end resection and repair. *Nat Struct Mol Biol* **22**, 150-157, doi:10.1038/nsmb.2937 (2015).
153 Wilkinson, O. J. *et al.* CtIP forms a tetrameric dumbbell-shaped particle which bridges complex DNA end structures for double-strand break repair. *Elife* **8**, doi:10.7554/eLife.42129 (2019).
154 Andres, S. N. & Williams, R. S. CtIP/Ctp1/Sae2, molecular form fit for function. *DNA Repair (Amst)* **56**, 109-117, doi:10.1016/j.dnarep.2017.06.013 (2017).
155 You, Z. & Bailis, J. M. DNA damage and decisions: CtIP coordinates DNA repair and cell cycle checkpoints. *Trends Cell Biol* **20**, 402-409, doi:10.1016/j.tcb.2010.04.002 (2010).
156 Daley, J. M. *et al.* Enhancement of BLM-DNA2-Mediated Long-Range DNA End Resection by CtIP. *Cell Rep* **21**, 324-332, doi:10.1016/j.celrep.2017.09.048 (2017).
157 Deshpande, R. A. *et al.* DNA-dependent protein kinase promotes DNA end processing by MRN and CtIP. *Sci Adv* **6**, eaay0922, doi:10.1126/sciadv.aay0922 (2020).
158 Han, J. *et al.* ATM controls the extent of DNA end resection by eliciting sequential posttranslational modifications of CtIP. *Proc Natl Acad Sci U S A* **118**, doi:10.1073/pnas.2022600118 (2021).
159 Bennett, L. G. *et al.* MRNIP is a replication fork protection factor. *Sci Adv* **6**, eaba5974, doi:10.1126/sciadv.aba5974 (2020).
160 Wang, Y. L. *et al.* MRNIP condensates promote DNA double-strand break sensing and end resection. *Nat Commun* **13**, 2638, doi:10.1038/s41467-022-30303-w (2022).
161 Staples, C. J. *et al.* MRNIP/C5orf45 Interacts with the MRN Complex and Contributes to the DNA Damage Response. *Cell Rep* **16**, 2565-2575, doi:10.1016/j.celrep.2016.07.087 (2016).
162 Blackford, A. N. & Jackson, S. P. ATM, ATR, and DNA-PK: The Trinity at the Heart of the DNA Damage Response. *Mol Cell* **66**, 801-817, doi:10.1016/j.molcel.2017.05.015 (2017).
163 Saxton, R. A. & Sabatini, D. M. mTOR Signaling in Growth, Metabolism, and Disease. *Cell* **168**, 960-976, doi:10.1016/j.cell.2017.02.004 (2017).
164 Yamashita, A., Kashima, I. & Ohno, S. The role of SMG-1 in nonsense-mediated mRNA decay. *Biochim Biophys Acta* **1754**, 305-315, doi:10.1016/j.bbapap.2005.10.002 (2005).
165 Murr, R., Vaissiere, T., Sawan, C., Shukla, V. & Herceg, Z. Orchestration of chromatin-based processes: mind the TRRAP. *Oncogene* **26**, 5358-5372, doi:10.1038/sj.onc.1210605 (2007).
166 Jansma, M. *et al.* Near-Complete Structure and Model of Tel1ATM from Chaetomium thermophilum Reveals a Robust Autoinhibited ATP State. *Structure* **28**, 83-95 e85, doi:10.1016/j.str.2019.10.013 (2020).
167 Xin, J. *et al.* Structural basis of allosteric regulation of Tel1/ATM kinase. *Cell Res* **29**, 655-665, doi:10.1038/s41422-019-0176-1 (2019).

168 Lee, J. H. & Paull, T. T. ATM activation by DNA double-strand breaks through the Mre11-Rad50-Nbs1 complex. *Science* **308**, 551-554, doi:10.1126/science.1108297 (2005).
169 Buis, J. *et al.* Mre11 nuclease activity has essential roles in DNA repair and genomic stability distinct from ATM activation. *Cell* **135**, 85-96, doi:10.1016/j.cell.2008.08.015 (2008).
170 Sun, Y., Jiang, X., Chen, S., Fernandes, N. & Price, B. D. A role for the Tip60 histone acetyltransferase in the acetylation and activation of ATM. *Proc Natl Acad Sci U S A* **102**, 13182-13187, doi:10.1073/pnas.0504211102 (2005).
171 Sun, Y., Xu, Y., Roy, K. & Price, B. D. DNA damage-induced acetylation of lysine 3016 of ATM activates ATM kinase activity. *Mol Cell Biol* **27**, 8502-8509, doi:10.1128/MCB.01382-07 (2007).
172 Lemercier, C. *et al.* Tip60 acetyltransferase activity is controlled by phosphorylation. *J Biol Chem* **278**, 4713-4718, doi:10.1074/jbc.M211811200 (2003).
173 Tanaka, T., Halicka, H. D., Huang, X., Traganos, F. & Darzynkiewicz, Z. Constitutive histone H2AX phosphorylation and ATM activation, the reporters of DNA damage by endogenous oxidants. *Cell Cycle* **5**, 1940-1945, doi:10.4161/cc.5.17.3191 (2006).
174 Lee, J. H. & Paull, T. T. Cellular functions of the protein kinase ATM and their relevance to human disease. *Nat Rev Mol Cell Biol* **22**, 796-814, doi:10.1038/s41580-021-00394-2 (2021).
175 Stracker, T. H., Roig, I., Knobel, P. A. & Marjanovic, M. The ATM signaling network in development and disease. *Front Genet* **4**, 37, doi:10.3389/fgene.2013.00037 (2013).
176 Cid-Castro, C., Hernandez-Espinosa, D. R. & Moran, J. ROS as Regulators of Mitochondrial Dynamics in Neurons. *Cell Mol Neurobiol* **38**, 995-1007, doi:10.1007/s10571-018-0584-7 (2018).
177 Guo, Z., Kozlov, S., Lavin, M. F., Person, M. D. & Paull, T. T. ATM activation by oxidative stress. *Science* **330**, 517-521, doi:10.1126/science.1192912 (2010).
178 Zhang, J. *et al.* ATM functions at the peroxisome to induce pexophagy in response to ROS. *Nat Cell Biol* **17**, 1259-1269, doi:10.1038/ncb3230 (2015).
179 Stagni, V., Cirotti, C. & Barila, D. Ataxia-Telangiectasia Mutated Kinase in the Control of Oxidative Stress, Mitochondria, and Autophagy in Cancer: A Maestro With a Large Orchestra. *Front Oncol* **8**, 73, doi:10.3389/fonc.2018.00073 (2018).
180 Zhang, Y. *et al.* Mitochondrial redox sensing by the kinase ATM maintains cellular antioxidant capacity. *Sci Signal* **11**, doi:10.1126/scisignal.aaq0702 (2018).
181 Lim, D. S. *et al.* ATM binds to beta-adaptin in cytoplasmic vesicles. *Proc Natl Acad Sci U S A* **95**, 10146-10151, doi:10.1073/pnas.95.17.10146 (1998).
182 Li, J., Han, Y. R., Plummer, M. R. & Herrup, K. Cytoplasmic ATM in neurons modulates synaptic function. *Curr Biol* **19**, 2091-2096, doi:10.1016/j.cub.2009.10.039 (2009).
183 Rouleau, M., Patel, A., Hendzel, M. J., Kaufmann, S. H. & Poirier, G. G. PARP inhibition: PARP1 and beyond. *Nat Rev Cancer* **10**, 293-301, doi:10.1038/nrc2812 (2010).
184 Cimprich, K. A. & Cortez, D. ATR: an essential regulator of genome integrity. *Nat Rev Mol Cell Biol* **9**, 616-627, doi:10.1038/nrm2450 (2008).
185 Brown, E. J. & Baltimore, D. ATR disruption leads to chromosomal fragmentation and early embryonic lethality. *Genes Dev* **14**, 397-402 (2000).
186 Sur, S. & Agrawal, D. K. Phosphatases and kinases regulating CDC25 activity in the cell cycle: clinical implications of CDC25 overexpression and potential treatment strategies. *Mol Cell Biochem* **416**, 33-46, doi:10.1007/s11010-016-2693-2 (2016).
187 Bartek, J. & Lukas, J. Chk1 and Chk2 kinases in checkpoint control and cancer. *Cancer Cell* **3**, 421-429, doi:10.1016/s1535-6108(03)00110-7 (2003).
188 Lee, Y. C., Zhou, Q., Chen, J. & Yuan, J. RPA-Binding Protein ETAA1 Is an ATR Activator Involved in DNA Replication Stress Response. *Curr Biol* **26**, 3257-3268, doi:10.1016/j.cub.2016.10.030 (2016).

189 Delacroix, S., Wagner, J. M., Kobayashi, M., Yamamoto, K. & Karnitz, L. M. The Rad9-Hus1-Rad1 (9-1-1) clamp activates checkpoint signaling via TopBP1. *Genes Dev* **21**, 1472-1477, doi:10.1101/gad.1547007 (2007).
190 Uematsu, N. *et al.* Autophosphorylation of DNA-PKCS regulates its dynamics at DNA double-strand breaks. *J Cell Biol* **177**, 219-229, doi:10.1083/jcb.200608077 (2007).
191 Yue, X., Bai, C., Xie, D., Ma, T. & Zhou, P. K. DNA-PKcs: A Multi-Faceted Player in DNA Damage Response. *Front Genet* **11**, 607428, doi:10.3389/fgene.2020.607428 (2020).
192 Falck, J., Mailand, N., Syljuasen, R. G., Bartek, J. & Lukas, J. The ATM-Chk2-Cdc25A checkpoint pathway guards against radioresistant DNA synthesis. *Nature* **410**, 842-847, doi:10.1038/35071124 (2001).
193 Solovjeva, L. V., Svetlova, M. P., Chagin, V. O. & Tomilin, N. V. Inhibition of transcription at radiation-induced nuclear foci of phosphorylated histone H2AX in mammalian cells. *Chromosome Res* **15**, 787-797, doi:10.1007/s10577-007-1162-x (2007).
194 Herbig, U., Jobling, W. A., Chen, B. P., Chen, D. J. & Sedivy, J. M. Telomere shortening triggers senescence of human cells through a pathway involving ATM, p53, and p21(CIP1), but not p16(INK4a). *Mol Cell* **14**, 501-513, doi:10.1016/s1097-2765(04)00256-4 (2004).
195 Xu, Y. Regulation of p53 responses by post-translational modifications. *Cell Death Differ* **10**, 400-403, doi:10.1038/sj.cdd.4401182 (2003).
196 Karimian, A., Ahmadi, Y. & Yousefi, B. Multiple functions of p21 in cell cycle, apoptosis and transcriptional regulation after DNA damage. *DNA Repair (Amst)* **42**, 63-71, doi:10.1016/j.dnarep.2016.04.008 (2016).
197 Riballo, E. *et al.* A pathway of double-strand break rejoining dependent upon ATM, Artemis, and proteins locating to gamma-H2AX foci. *Mol Cell* **16**, 715-724, doi:10.1016/j.molcel.2004.10.029 (2004).
198 Imamichi, S., Sharma, M. K., Kamdar, R. P., Fukuchi, M. & Matsumoto, Y. Ionizing radiation-induced XRCC4 phosphorylation is mediated through ATM in addition to DNA-PK. *Proc Jpn Acad Ser B Phys Biol Sci* **90**, 365-372, doi:10.2183/pjab.90.365 (2014).
199 Yu, Y. *et al.* DNA-PK and ATM phosphorylation sites in XLF/Cernunnos are not required for repair of DNA double strand breaks. *DNA Repair (Amst)* **7**, 1680-1692, doi:10.1016/j.dnarep.2008.06.015 (2008).
200 Chen, B. P. *et al.* Ataxia telangiectasia mutated (ATM) is essential for DNA-PKcs phosphorylations at the Thr-2609 cluster upon DNA double strand break. *J Biol Chem* **282**, 6582-6587, doi:10.1074/jbc.M611605200 (2007).
201 Zhou, Y. *et al.* Regulation of the DNA Damage Response by DNA-PKcs Inhibitory Phosphorylation of ATM. *Mol Cell* **65**, 91-104, doi:10.1016/j.molcel.2016.11.004 (2017).
202 Kwon, S. J. *et al.* ATM-mediated phosphorylation of the chromatin remodeling enzyme BRG1 modulates DNA double-strand break repair. *Oncogene* **34**, 303-313, doi:10.1038/onc.2013.556 (2015).
203 Zhang, X. *et al.* ZEB1 confers chemotherapeutic resistance to breast cancer by activating ATM. *Cell Death Dis* **9**, 57, doi:10.1038/s41419-017-0087-3 (2018).
204 Jin, M. H. & Oh, D. Y. ATM in DNA repair in cancer. *Pharmacol Ther* **203**, 107391, doi:10.1016/j.pharmthera.2019.07.002 (2019).
205 Weston, V. J. *et al.* The PARP inhibitor olaparib induces significant killing of ATM-deficient lymphoid tumor cells in vitro and in vivo. *Blood* **116**, 4578-4587, doi:10.1182/blood-2010-01-265769 (2010).
206 Chen, C. C. *et al.* ATM loss leads to synthetic lethality in BRCA1 BRCT mutant mice associated with exacerbated defects in homology-directed repair. *Proc Natl Acad Sci U S A* **114**, 7665-7670, doi:10.1073/pnas.1706392114 (2017).
207 Hu, Y. & Guo, M. Synthetic lethality strategies: Beyond BRCA1/2 mutations in pancreatic cancer. *Cancer Sci* **111**, 3111-3121, doi:10.1111/cas.14565 (2020).

208 Petersen, A. J., Rimkus, S. A. & Wassarman, D. A. ATM kinase inhibition in glial cells activates the innate immune response and causes neurodegeneration in Drosophila. *Proc Natl Acad Sci U S A* **109**, E656-664, doi:10.1073/pnas.1110470109 (2012).
209 Hu, M. *et al.* ATM inhibition enhances cancer immunotherapy by promoting mtDNA leakage and cGAS/STING activation. *J Clin Invest* **131**, doi:10.1172/JCI139333 (2021).
210 Cannavo, E. & Cejka, P. Sae2 promotes dsDNA endonuclease activity within Mre11-Rad50-Xrs2 to resect DNA breaks. *Nature* **514**, 122-125, doi:10.1038/nature13771 (2014).
211 Hailemariam, S., Kumar, S. & Burgers, P. M. Activation of Tel1(ATM) kinase requires Rad50 ATPase and long nucleosome-free DNA but no DNA ends. *J Biol Chem* **294**, 10120-10130, doi:10.1074/jbc.RA119.008410 (2019).
212 Deshpande, R. A., Lee, J. H., Arora, S. & Paull, T. T. Nbs1 Converts the Human Mre11/Rad50 Nuclease Complex into an Endo/Exonuclease Machine Specific for Protein-DNA Adducts. *Mol Cell* **64**, 593-606, doi:10.1016/j.molcel.2016.10.010 (2016).
213 Wang, W., Daley, J. M., Kwon, Y., Krasner, D. S. & Sung, P. Plasticity of the Mre11-Rad50-Xrs2-Sae2 nuclease ensemble in the processing of DNA-bound obstacles. *Genes Dev* **31**, 2331-2336, doi:10.1101/gad.307900.117 (2017).
214 Anand, R., Pinto, C. & Cejka, P. Methods to Study DNA End Resection I: Recombinant Protein Purification. *Methods Enzymol* **600**, 25-66, doi:10.1016/bs.mie.2017.11.008 (2018).
215 Canny, M. D. & Latham, M. P. LRET-derived HADDOCK structural models describe the conformational heterogeneity required for DNA cleavage by the Mre11-Rad50 DNA damage repair complex. *Elife* **11**, doi:10.7554/eLife.69579 (2022).
216 Park, Y. B. *et al.* Eukaryotic Rad50 functions as a rod-shaped dimer. *Nat Struct Mol Biol* **24**, 248-257, doi:10.1038/nsmb.3369 (2017).
217 Lavin, M. F., Kozlov, S., Gatei, M. & Kijas, A. W. ATM-Dependent Phosphorylation of All Three Members of the MRN Complex: From Sensor to Adaptor. *Biomolecules* **5**, 2877-2902, doi:10.3390/biom5042877 (2015).
218 Gatei, M. *et al.* ATM protein-dependent phosphorylation of Rad50 protein regulates DNA repair and cell cycle control. *J Biol Chem* **286**, 31542-31556, doi:10.1074/jbc.M111.258152 (2011).
219 Gobbini, E., Vertemara, J. & Longhese, M. P. Local unwinding of double-strand DNA ends by the MRX complex promotes Exo1 processing activity. *Mol Cell Oncol* **5**, e1511208, doi:10.1080/23723556.2018.1511208 (2018).
220 Liu, Y. *et al.* ATP-dependent DNA binding, unwinding, and resection by the Mre11/Rad50 complex. *EMBO J* **35**, 743-758, doi:10.15252/embj.201592462 (2016).
221 Sharma, S. *et al.* MRE11-RAD50-NBS1 Complex Is Sufficient to Promote Transcription by RNA Polymerase II at Double-Strand Breaks by Melting DNA Ends. *Cell Rep* **34**, 108565, doi:10.1016/j.celrep.2020.108565 (2021).
222 Wang, X. *et al.* Structure of the intact ATM/Tel1 kinase. *Nat Commun* **7**, 11655, doi:10.1038/ncomms11655 (2016).
223 Baretic, D. *et al.* Structures of closed and open conformations of dimeric human ATM. *Sci Adv* **3**, e1700933, doi:10.1126/sciadv.1700933 (2017).
224 Tannous, E. A., Yates, L. A., Zhang, X. & Burgers, P. M. Mechanism of auto-inhibition and activation of Mec1(ATR) checkpoint kinase. *Nat Struct Mol Biol* **28**, 50-61, doi:10.1038/s41594-020-00522-0 (2021).
225 Xiao, J. *et al.* Structural insights into the activation of ATM kinase. *Cell Res* **29**, 683-685, doi:10.1038/s41422-019-0205-0 (2019).
226 Yang, H. *et al.* Mechanisms of mTORC1 activation by RHEB and inhibition by PRAS40. *Nature* **552**, 368-373, doi:10.1038/nature25023 (2017).
227 Chen, X. *et al.* Structure of an activated DNA-PK and its implications for NHEJ. *Mol Cell* **81**, 801-810 e803, doi:10.1016/j.molcel.2020.12.015 (2021).

228 Rao, Q. *et al.* Cryo-EM structure of human ATR-ATRIP complex. *Cell Res* **28**, 143-156, doi:10.1038/cr.2017.158 (2018).
229 Kozlov, S. V. *et al.* Autophosphorylation and ATM activation: additional sites add to the complexity. *J Biol Chem* **286**, 9107-9119, doi:10.1074/jbc.M110.204065 (2011).
230 Lee, J. H. *et al.* Ataxia telangiectasia-mutated (ATM) kinase activity is regulated by ATP-driven conformational changes in the Mre11/Rad50/Nbs1 (MRN) complex. *J Biol Chem* **288**, 12840-12851, doi:10.1074/jbc.M113.460378 (2013).

Danksagung

An dieser Stelle möchte ich mich ganz herzlich für die schöne Zeit im Labor, die vielen Möglichkeiten und Freiheiten sowie für das sehr interessante, wenn auch herausfordernde, Projekt bei meinem Doktorvater Prof. Dr. Karl-Peter Hopfner bedanken! Vielen Dank für deine professionelle Betreuung, kompetenten Rat und tolle Unterstützung bei so vielen Dingen.

Ein weiterer besonderer Dank geht an Dr. Katja Lammens, die immer ein offenes Ohr für Projektplanung und Experimentdesign hatte und mich immerzu bei cryo-EM Fragen und Problemen unterstützt hat. Weiterhin möchte ich meinen langjährigen, engen Arbeitskollegen Kristina Stakyte und Matthias Rotheneder danken für unsere fantastische Zusammenarbeit. Wir haben zusammen so viel erreicht und ich bin sehr froh, dass sie mich direkt von Anfang an in ihr Team aufgenommen haben und mir alles im für mich neuen Labor beigebracht haben. Desweitern muss ich an dieser Stelle ein riesen Dank und Lob für Brigitte Keßler aussprechen, ohne ihre enorme Hilfe bei Aufreinigungen, Klonierungen oder sonstigen Laborfragen wäre wohl vieles unbearbeitet geblieben. Ich bedanke mich bei Fabian Gut für ständigen Rat jeglicher Art und die gemeinsame Arbeit an der Etablierung neuer biochemischer Assays. An all die anderen Kollegen und Freunde im Hopfner Labor bedanke ich mich für eine so tolle Zeit, die ständige Hilfsbereitschaft und die super Atmosphäre!

Bedanke möchte ich mich auch bei den Kollaborationspartnern Christophe Jung, Wynand P. Roos, Barbara Steigenberger und dem Team von Merck KGaA um Ulrich Grädler, Thomas Fuchß und Ulrich Pehl für die tolle Zusammenarbeit und ihr Engagement.

Zu guter Letzt gilt mein ganz besonderer Dank meiner Freundin für die unendliche Unterstützung während meiner Doktorarbeit. Es war oft eine schwierige Zeit und ich bin manchmal verzweifelt, du hast mich immer wieder aufgebaut und motiviert weiterzumachen!